Synthesis of silicon- and germanium-rich phases at high-pressure conditions

D I S S E R T A T I O N

zur Erlangung des akademischen Grades

Doctor rerum naturalium
(Dr. rer. nat.)

vorgelegt

der Fakultät Mathematik und Naturwissenschaften
der Technischen Universität Dresden

von

Rodrigo Esteban Antonio Castillo Rojas

geboren am 18. November 1985 in Antofagasta (Chile)

Eingereicht am 20.04.2016

Die Dissertation wurde in der Zeit von April/2011 bis April/2016 im Max-Planck-Institut für Chemische Physik fester Stoffe angefertigt.

Verteidigt am: 18.07.2016

Gutachter: Prof. Juri Grin

Gutachter: Prof. Dr. Michael Ruck

Table of Contents

Chapter 1

Introduction

1.1 Brief history of high-pressure experiments

High-pressure experiment as we know today, started in 1909, with the first three experimental papers of Percy Williams Bridgman, related to high-pressure techniques, calibration, and compressibility [1]. The work of Bridgman had a tremendous significance considering the current state of knowledge and the available technology. For example, X-rays were recently discovered and its use in crystal structure studies had not been assumed [2]. The thermodynamic as we know it today and its equations were consolidated 30 years early and yet without practical application to real chemical systems [3]. There was no agreement on a theory of how atoms bind together to form molecules [4], and the organization of the elements in the periodic system according to the increasing atomic number had begun to assemble [5]. The most remarkable achievement of Bridgman was the design of his own high-pressure apparatus, which was able to reach up to ~10 GPa, a huge improvement with respect to the ~0.3 GPa possible with previously developed equipment. An abundance of new findings in the compressibility, electric and thermal conductivity, tensile strength and viscosity of more than 100 elements and compounds were possible thanks to the new apparatus [6]. His new discoveries and the contribution to science led him to award the Nobel Prize in physics in 1946. These findings and achievements, together with many articles that followed, established his influence on the course of modern high-pressure research. The field of high pressure now spans over a broad range of disciplines, from physics and chemistry to geoscience, planetary science and astrophysics, materials science and technology, and structural and organismal biology [7-10].

Any experiment carried out at pressures higher than atmospheric (1 atm = 0.0001 GPa), is called a high-pressure experiment. From hydrothermal synthesis (below 1 GPa) to shock-wave methods (above 500 GPa), are all considered as high-pressure experiments. The most frequently used units of pressure and their equivalence are summarized in Table 1.1.

Table 1.1 Most common units of pressure and their conversion factors. The SI unit Pa is normally used with the prefix mega (10^6) or giga (10^9).

	Pascal	Bar	Atmosphere	Torr	Pounds per square inch
	Pa	*bar*	*atm*	*Torr*	*psi*
1 Pa	1 N/m^2	10^{-5}	9.8692×10^{-6}	7.5006×10^{-3}	1.450377×10^{-4}
1 bar	10^5	10^6 dyn/cm^2	0.98692	750.06	14.50377
1 atm	1.01325×10^5	1.01325	1	760	14.69595
1 Torr	133.3224	1.333224×10^{-3}	1.315789×10^{-3}	1 mm Hg	1.933678×10^{-2}
1 psi	6.8948×10^3	6.8948×10^{-2}	6.8046×10^{-2}	51.71493	1 lb/in^2

The best way to visualize the effects of pressure is with a graphical representation of the Earth's cross-section showing the pressure as a function of depth. The standard or reference is the seal level, 1 atm (Figure 1.1). Geologists and petrologists are interested in minerals subjected to high pressures and try to reproduce the interior of the Earth. They employ such kind of scheme and they have measured with high precision the distances from the surface to the core, and the pressure-dependence at each "level".

A recent work on high-pressure high-temperature experiments on iron, led to the redetermination of the core temperature of the Earth with high accuracy. By reaching the conditions where iron is molten at 200 GPa and by extrapolation, the Earth core temperature was determined to be 6200 ± 500 K [11].

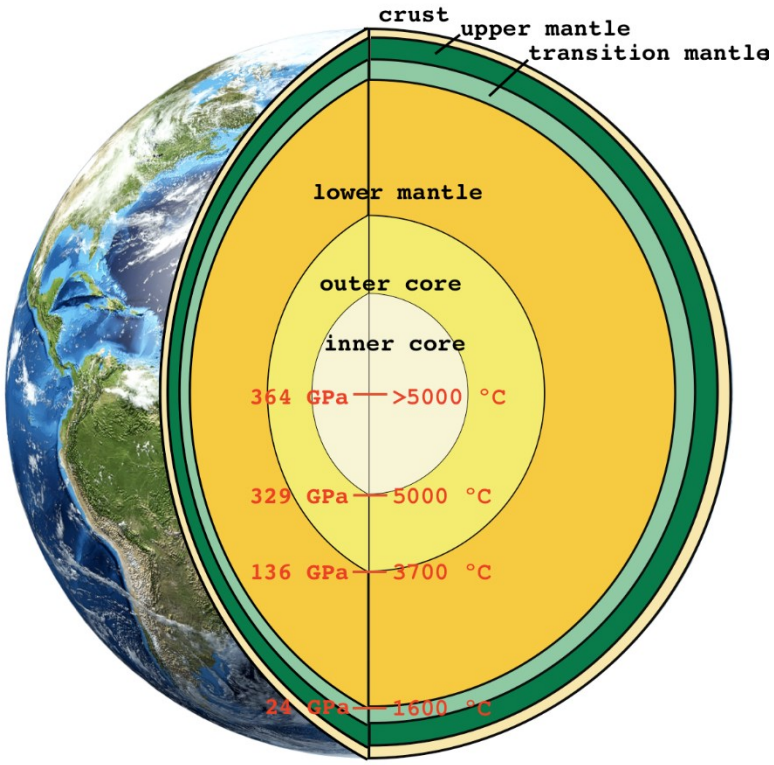

Figure 1.1 Pressures and temperatures inside the Earth.

1.2 Elements of the group IV

The group IV of the periodic system contains non-metallic, semiconducting and metallic elements. Carbon is the main component of organic and biological systems. Silicon, in the form of silicate minerals, composes over 90% of the Earth´s crust, making it the second most abundant element (28% by mass) after oxygen. It is employed mainly in steel refining and fine chemical industries, while only 10% of the elemental silicon is employed in the semiconductor electronics. Germanium is still widely used in the electronic industry and in solar cells. Tin has been historically used with copper to form the bronze alloy, while in modern applications it is used in soft solder, as a corrosion resistance for steel, and in food packaging. Lead is in a decaying curve of its uses, because of the toxicity, however one can still find lead in batteries and as a radiation shield.

The high-pressure behavior of the group IV elements [12] is summarized in Table 1.2. For carbon only one high-pressure modification is frequently observed. A wider range of different crystal structures has been discovered for silicon [13] and germanium with at least seven phases, and tin adopts four modifications [14]. The crystal structure of these elements under standard conditions are indicated by the * whereas ** specifies a high-pressure modification.

Table 1.2 Crystal structures of group IV elements at ambient- (*) and high- (**) pressure conditions.

Type	C	Si	Ge	Sn	Pb
Graphite, *hP4*	*				
Diamond, *cF8*	**	*	*	*	
β-Sn, *tI4*		**	**	**	
Fm-3m, *cF4*		**	**		*
$P6_3/mmc$, *hP2*		**	**		**
Im-3m, *cI2*				**	**

Table 1.2 reveals the so-called "Pressure – Homologue Rule" stating that, within a column in the periodic system, the high-pressure structure of an element corresponds to the normal-pressure structure of a homologous element from a higher period.

Silicon has attracted the attention of experimental and theoretical research groups long ago. At high-pressure there exists a set of crystal structures, which follow the tendency of becoming denser as pressure increases. In Figure 1.2, five high-pressure phases adopted by silicon and germanium are shown, together with the Pearson symbol and coordination number (CN) for each polymorph. The general trend is the reduction of atomic volume when the pressure is increased. At ambient temperature, the sequence of phases correspond to *cF8* → *tI4* → *hP1* → *hP2* → *cF4*. Values for atomic volume/density (in $Å^3$ and g/cm^3 respectively) in silicon vary as follow: 20.40/2.286 → 13.95/3.343 → 13.12/3.554 → 10.74/4.344 → 9.32/5.003. When temperature is involved, other metastables phases are found after quenching [15] and some additional intermediate phases have been detected upon decompression [16,17].

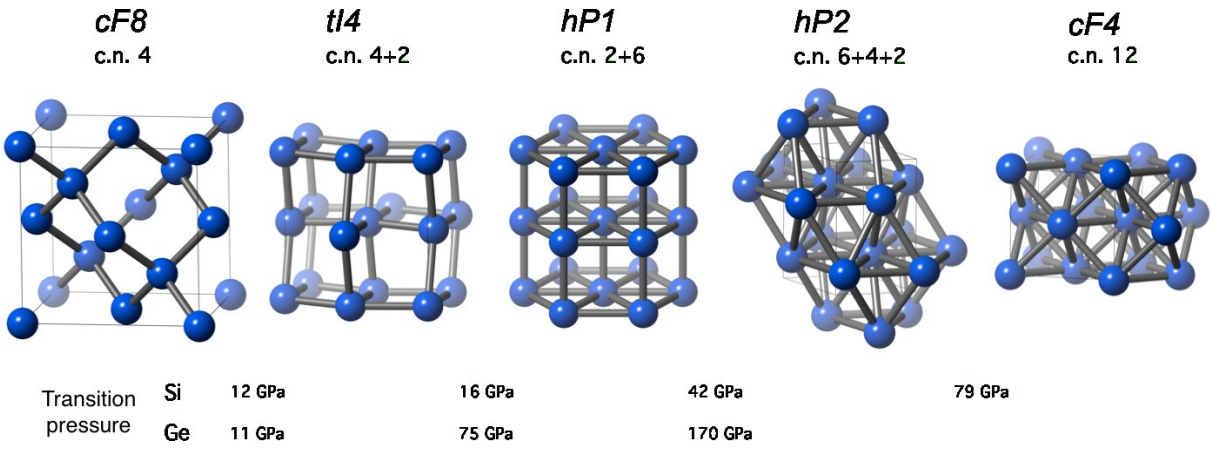

Figure 1.2 Selected crystal structures adopted by silicon and germanium observed under high-pressure condition and ambient temperature.

For germanium, the highest pressure reached in experiments is 190 GPa [18] and the *hP2* structure is still stable, although theoretical calculations predict the existence of the *cF4* at higher pressure [19].

In both cases, a continuous change to a close-packed crystal structure is evidenced along with the densification. However, there exist well-known examples of elements which undergo phase transitions to low-symmetry and surprisingly complex structures [20]. Calcium is an example of such a diversity of crystal structures when subject to increasing pressure [21].

1.3 The pressure effect on condensed phases

1.3.1 Pressure effect on chemical reactions

The effect of pressure in a chemical reaction can be understood with the aid of basic thermodynamic considerations. Taking into account the graphite (*hP4*) to diamond (*cF8*) transition, which has been one of the first experiments under high pressure conditions [22], and its corresponding tabulated thermodynamic data, $\Delta H°$ = 1.897 kJ mol^{-1} and $\Delta S° = S°(cF8) – S°(hP4)$ = 2.38 – 5.740 = –3.36 J mol^{-1}K^{-1}. The Gibbs free energy can be approximated to $\Delta G \simeq \Delta H° – T\Delta S°$ at any temperature. Therefore, under standard conditions, entropy and enthalpy favor graphite. Since $\Delta S < 0$, increases in temperature will not allow the reaction be spontaneous. Considering the pressure and its relationship to the above equation, it is known that $\Delta H = \Delta U + \Delta(PV)$, where ΔU is the change in internal energy, which is related to changes in bond energies. At a fixed ordinary pressure, $\Delta(PV) = P\Delta V$ is small because ΔV is small, since both graphite and diamond are solids and ΔV involves the change in the volume during the transition. Nevertheless, ΔV is negative because diamond is denser than graphite. Therefore, at high pressures, $\Delta(PV)$ can be made sufficiently negative that ΔH changes sign. If P is big enough ΔG will become negative and the transition becomes spontaneous. These kinds of calculation are commonly employed by theoretical chemists and is discussed in the appendix, section 5.1.

Synthesis (chemical reactions) favored under high-pressures, are nothing else than an application of the le Chatelier principle: “All structure changes under increasing pressure are necessarily accompanied by a decrease in volume”. Considering a structural transformation induced by pressure from F_1 to F_2 (F being a structural form), ΔV between the forms can be expressed as $\Delta V = \Sigma[(V/Z)F_2 – (V/Z)F_1]$ and is negative. The equation is also valid when a product is obtained under high-pressure conditions from two or more precursors. The carbon transitions [23] and the reaction for the formation of $EuSi_6$, [24,25] (Table 1.3) can be considered as examples.

Table 1.3 Calculation of ΔV for a high-pressure transformation and reaction.

	Graphite → Diamond	$EuSi_2 + 4Si \rightarrow EuSi_6$
F_1	Graphite	$EuSi_2 + 4Si$
F_2	Diamond	$EuSi_6$
VF_1, ZF_1	35.29, 2+2	252.93 + 4×160.18, 4 – 8
$\Sigma[(V/Z)F_1$	8.8225	143.3225
VF_2, ZF_2	45.38, 8	528.3, 4
$\Sigma[(V/Z)F_2$	5.6725	132.075
ΔV	-3.15	-11.2475

1.3.2 Binary metal – silicon and germanium systems: Polymorphic transitions

When reacted with alkaline-, alkaline earth- or rare-earth metals, silicon and germanium form a huge variety of binary phases at ambient conditions. Often, the tetrel-richest compounds in the systems have the composition *MTl*2 (*M* = metal, *Tl* = Si, Ge), except for chlatrates in the Ba – Si and Ba – Ge systems. Most of these phases are electron balanced according to the *8 – N* rule. Taking into account the Zintl-Klemm concept, i.e., assuming a formal transfer of the metal valence electrons to the tetrel units or framework, all these phases should behave as semiconductor and indeed they do. Additionally, extensive and systematic research at high-pressure high-temperature conditions of these compounds was done by Evers and coworkers [26,25] around 40 years ago, mainly on disilicides and digermanides [27]. These studies demonstrated that these empirical electron-counting rules are, to some extent, still valid for phases synthesized at extreme conditions.

1.4 Recent work on binary high-pressure phases containing silicon and germanium

As recently discussed, a new era of high-pressure experiments started with the work of Bridgman, by measuring physical properties of elements subjected to pressure. The observations of discontinuous changes in some of them were the first sign of pressure-induced phase transitions. After him, and with the development of the Kawai type press, a considerable large amount of sample was available to perform different kind of measurements and in this way, allowing a complete characterization of these new modifications obtained at high pressures. Then came the synthesis of new materials under pressure, increasing the number of compounds in simple binary systems, some of them with promising physical properties like the clathrates compounds in the thermoelectric field.

Clathrates are isomorphous with the known type-I gas hydrates, $G_x(H_2O)_{46}$, in which the H – O – H bonds (covalent- and hydrogen bonds) are replaced by homonuclear Si – Si or Ge – Ge bonds, and the gas molecules (G) are replaced by alkali or alkaline-earth metals [28]. The cubic structure consists of a tetraedral network of covalent bonded tetrel atoms, forming a three-dimensional assembly composed of Tl20 dodecahedra and Tl24 tetrakaidecahedra, being both connected by sharing faces. The high interest in this kind of compounds for thermoelectric applications arises from their performance i.e., its figure of merit *ZT*, defined as $ZT = S^2\sigma T/\kappa$, where *S* is the Seebeck coefficient, σ is the electrical conductivity, and κ is the total thermal conductivity. By using the concept of "phonon glass and an electron crystal" (PGEC), it means, electronic properties associated to a good semiconductor and low thermal conductivity associated with amorphous materials, stimulated the search for new materials with increased *ZT* value [29,30]. It is believed that due to resonant scattering of phonons via localized low-frequency vibrations of the encapsulated atoms, the lattice thermal conductivity is reduced, thus increasing the figure of merit [31]. The same effect has also been observed in filled skutterudites [32]. The clathrate-I Ba_8Si_{46}, a high-pressure phase, was the first superconductor consisting of a sp^3 silicon network. Since silicon atoms are four-bonded, they are electrically balanced and therefore the valence electrons coming from the barium atoms are situated in the conduction band. This excess of electrons gives many possibilities to replace silicon for electron deficient elements, and the replacement of the encapsulated atom are possible too. A huge number of derivatives of Ba_8Si_{46} have been synthesized at ambient pressure and their thermoelectric properties are reported, but it must be highlighted, that the parent structure is only accessible by high-pressure synthesis, and no transport properties have been measured on it.

In our group, several new Si-rich phases have been synthesized at high-pressure high-temperature conditions, while searching for new clathrates phases. The hexasilicides, binary compounds with composition MSi$_6$, with M = alkaline earth and rare earth metals, represent the class of Zintl compounds with excess of electrons [33,24]. Their orthorhombic crystal structure is isotypic to $EuGa_2Ge_4$ [34] and consists of three different four-bonded silicon atoms with a nearly tetrahedral coordination. The three-dimensional framework results in large channels along the [001] direction, where the metal atom is placed. Like in the Ba_8Si_{46} clathrate, the silicon atoms do not use the valence electrons coming from the metal, and according to the formula $[M^{2+}][(4b)Si^0]_6 \times 2e^-$, an excess of two electrons per formula unit is present, resulting in a metal-like conduction.

A second family of compounds succeeded in our group are the trisilicides, binary phases composed of an alkaline-earth or a rare-earth metal and silicon in the ratio 1:3 [35]. They crystallize in a new type of crystal structure, the $CaGe_3$-type [36]. Its structure comprises layers of silicon atoms separated by the metal atoms. The two independent silicon atoms are present in form of dimers, located parallel and perpendicular to the [001] direction, resulting in infinite dumbbells along the plane. Beside the new prototype of crystal structure represented by these compounds, and the rather unusual connectivity found for the silicon atoms, they also show superconducting behavior with moderately strong phonon-electron coupling.

Pentasilicides, compounds with composition MSi$_5$, were also successfully synthetized at high-pressure high-temperature conditions, for M = Ce and Gd [37]. They are isostructural to $LaGe_5$ [38] and the most interesting feature of these is the bonding situation between the silicon atoms. Two symmetry independent silicon atoms are occupying position *2d* and *8l* of the space group *Immm*, one having a 3+2 coordination, as in the case of trisilicides, which is a quite unusual coordination for silicon, while the other silicon has eight equivalent interatomic distances to silicon atoms, an even more unusual coordination sphere for an element of group IV. Such exotic bonding patterns demanded physical properties measurements and was an excellent candidate for quantum chemical calculations, especially chemical bonding analysis. The study revealed a non-classical chemical bonding setting for the silicon with the eight neighbor atoms, involving the participation of the semi-core states of the rare-earth atom, creating multicenter interactions. A similar bonding situation was observed in the Ce_2Si_7 compound [37]. A complete characterization of the family MGe$_5$ (M = La, Nd, Sm, Gd, Tb) was performed [39]. These pentagermanides, which adopt the same crystal structure, decompose under ambient pressure at temperatures between 500 and 700 K, and the Sm and Nd compounds transform to another metastable phase with slightly deficient germanium content [40].

1.5 Goal of the present work

The main purpose of the present work is the preparation of new high-pressure phases with high Ge or Si content, investigation of crystal structures and their relation to the physical properties. The above-described high-pressure phases were obtained mainly with silicon at pressures in the range 3 – 10 GPa, and temperatures up to 1600 K. The expectation is that in analogous germanium systems using higher pressures around 16 GPa, new metastables phases will be stabilized and can be retained at ambient conditions, by quenching the samples.

Chapter 2

Experimental Techniques

2.1 Preparation of precursors

All sample handling was performed in the controlled atmosphere of an Ar-filled glove box (MBraun), monitoring the partial pressure of H_2O and O_2 and keeping the values below 1.0 ppm. Sample handling includes weighting, melting and grinding of the starting materials, as well as the assembling of octahedrons for high-pressure reactions, and finally preparation of the already pressed samples for the different types of analysis. Chemicals used for the preparation of the precursor materials are summarized in Table 2.1. In all cases, an excess of 1% of the metal element was added in order to account for the high vapor pressure of the metals upon melting.

Table 2.1 Elements used for the synthesis of compounds in the present work.

Element	Physical State	Company	Purity (%)
Si	Lump	Chempur	99.999
Ge	Lump	Chempur	99.9999
Sr	Crystalline dendritic pieces	Alfa Aesar	99.95
Ba	Distilled dendritic pieces	Alfa Aesar	99.9
Eu	Rod	AMES Lab	99.9

2.1.1 Arc melting

The arc melting furnace is located inside the glove box, and is the principal device used in the present thesis for the synthesis of the precursor samples. Direct reaction of the elements is performed on a water-cooled copper heart, with the aid of a tungsten electrode that can reaches up to 3500 °C in a short time. After each melting experiment, the sample is cooled to room temperature, turned and then melted again to ensure homogeneity

Normally three times five-to-ten seconds of melting is enough to get a homogenous mixture of the desired composition.

2.1.2 High-frequency melting

A high-frequency inductive furnace is available in the glove box and used mainly to “pre-react” the samples, which will be further annealed. The samples are placed in a crucible featuring metallic conductivity (glassy carbon or metal) and placed inside a copper coil with a 6 turn spiral. The current induces resistive heating of the container and the sample is molten. The temperature is measured by an IR pyrometer focused on the container surface. This synthetic route for precursor materials is especially useful when metals with a high vapor pressure have to be molten together with other elements.

2.2 High pressure methods

Different methods and techniques are used for generating high pressure. They can be classified depending on the amount of employed sample. Basically, the higher the pressure, the lower the volume of the sample. Pressures up to 500 GPa can be reached with the shockwave method, in which a high energy wave, normally coming from a detonation, travels inside the sample causing an almost instantaneous rise in pressure [41]. Pressures higher than 300 GPa are possible thanks to the diamond anvil cell, the most common and available method for studying the behavior of materials under pressure by recording X-ray images or any other type of optical measurement, usually with synchrotron radiation, but also available for "in-house-laboratories". Particles of the size of a single-crystal are needed for such experiments, and novel phase transitions and crystal structures can be found. However, the small amount of sample impeded some measurements of the physical properties. In contrast, the multi-anvil apparatus can achieve pressures of ~16 GPa with a sample volume of 3-5 mm^3 or ~10 GPa for sample volume of 10-12 mm^3. Such amount of sample is enough for phase identification and characterization. In the preparation of the samples presented in this thesis, the multi-anvil device was employed.

2.2.1 Multianvil device

The multianvil apparatus is the widely used device for the synthesis of large volume samples under high pressures. Several variations have been developed, one of them established by Walker et al. [42] which is available at the MPI CPfS together with a 1000 tons press, both acquired from the Max Voggenreiter Company [43]. A very descriptive explanation regarding the arrangement and operation of the press, the module and the sample assemble was given by Huppertz [44]. The Walker module consists of a cylindrical vessel in which three tool-steel wedges (the anvils) are accommodated at the bottom forming a nest, in which a cubic arrangement containing the octahedron inside is positioned along the [111] axis (Figure 2.1). Three additional wedges are placed on top, leaving a gap with the bottom wedges. A pressure distribution plate is positioned on top and the Walker module is ready to be pressed under the 1000 tons hydraulic press installed in the laboratory. The load on the Walker module forces the upper wedges towards the lower set, forcing the tungsten carbide (WC) cubes to converge to the sample cavity. Thus, quasi-hydrostatic pressure is achieved in the center of the assembly, where the sample is located. The central octahedron is assembled as follows: the sample, as fine powder, is loaded into a container machined from hexagonal boron nitride (*h*-BN). The crucible is placed in a cylindrical resistance heater, typically made of graphite, with molybdenum plates contacting both ends of the tube with the tungsten carbide cubes. In order to isolate the furnace against the Cr_2O_3-doped MgO octahedron, a ZrO_2 sleeve surrounds its inner part. The eight truncated WC cubes are arranged around the octahedron, fitting the triangular face (the truncated corners) onto the octahedron faces and keeping a distance between adjacent cubes trough the gaskets, which have to be fixed on the cubes (Figure 2.2). Depending on the octahedral edge length (OEL) and the truncation edge length (TEL), one can achieve different pressures. The common set for OEL/TEL used in our laboratory are 18/11, which allows to load a force of 600 tons (~10 GPa and 1500 K), and 14/8, in which up to 800 tons can be loaded (~16 GPa and 2000 K). Again, these setups allow for the synthesis of relatively large sample volume. The pressure is calibrated prior to the experiments, by in-situ monitoring of the resistance changes of bismuth. Bismuth is an element with well-known phase transitions at relatively low pressures. It transforms from the As-type to Bi-II at 2.5 GPa, then to Bi-III

at 2.7 GPa and finally to bbc at 7.7 GPa. All these transitions are reproducible and abrupt and can be followed by the changes of electrical conductivity [45]. Several runs at different conditions using thermocouples calibrate the temperature. Regarding the time, around four hours are needed to reach the maximum pressure in the 18/11 setup, and around five hours in the 14/8 one. After the desired pressure is achieved, the sample starts to be annealed for a typical period of one hour followed by quenching to room temperature. The decompression takes normally three times longer than compression. This usual procedure for high-pressure high-temperature synthesis can be adjusted to the expected product, for instance, when single crystals are desired. Longer times of annealing or cooling can be programmed, usually a weekend is used for this purpose. The decompression ratio can also be changed when, for example, a highly brittle sample is obtained. In such cases slow decompression needs to be programmed in order to avoid cracks inside the sample.

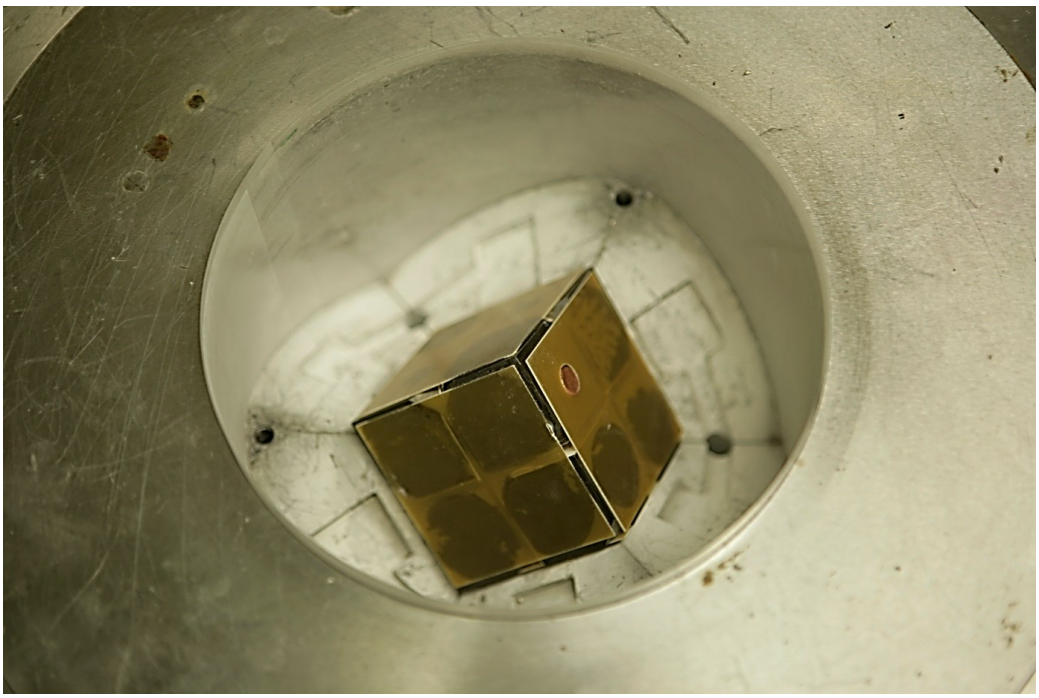

Figure 2.1 Cubic arrangement containing the sample, resting on the nest formed by the three wedges. View along a three-fold axes of the central cube and the inner octahedron.

The multianvil press uses force magnification to amplify pressure by reducing the area over which the force is applied, according to $P = F/A$. For instance, a typical multianvil could load 1000 ton (9806650 N) onto a 10 mm octahedron, with a surface of 346.41 mm^2, to produce a pressure of 28.31 GPa inside the sample, while the pressure in the hydraulic ram is 0.3 GPa. Therefore, using smaller assemblies can increase the pressure in the sample. The load that can be applied is limited by the compressive yield strength of the WC cubes, especially for heated experiments.

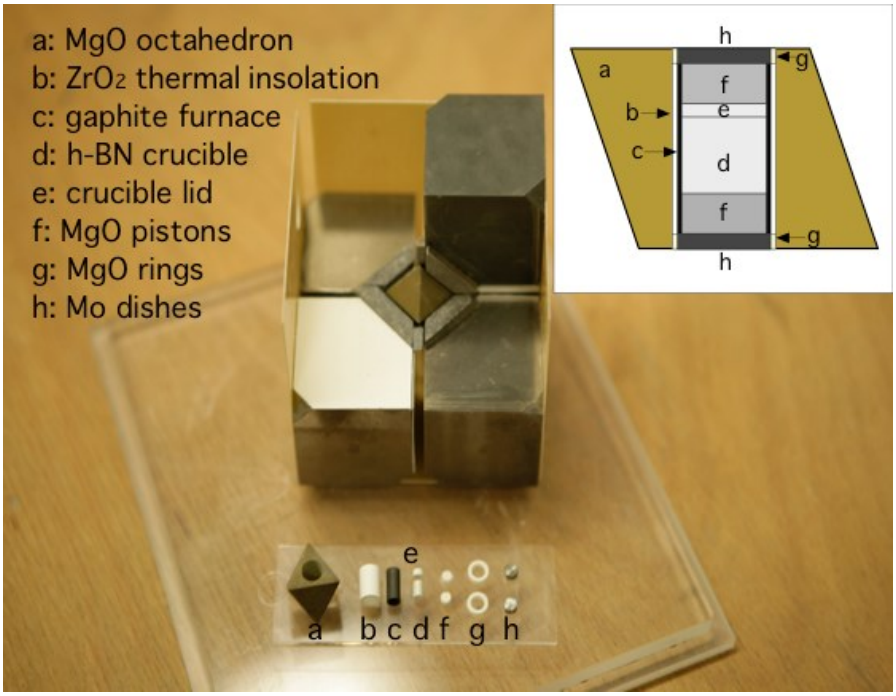

Figure 2.2 Construction of the cubic arrangement with eight truncated WC cubes and the central octahedral container. In the inset a cross-section of the octahedron is schematically shown. The labelling corresponds to the items shown in the picture (a – h).

2.3 Characterization methods

2.3.1 X-ray methods

2.3.1.1 Powder X-ray diffraction

Powder X-ray diffraction (PXRD) is a technique widely used in materials characterization. Diffraction occurs when the Bragg´s law is satisfied, and the resulting X-ray diffraction patterns are characteristic for each substance. Data collection was performed in transmission mode with an Image Plate Guinier Camera Huber G670 diffractometer, equipped with an image plate detector and a Ge(111)-monochromator. Every sample was measured in the range $3° \leq 2\theta \leq 100°$, with a step width of 0.005°, and 6 x 30 min scans. Polycrystalline powder samples are sieved to gain a particle size less than 40 μm. The sample is dispersed between two polyamide foils (Chemplex) and fixed with an o-ring on the sample holder. This setup prevents possible oxidation of the sample and water or moisture contaminations. Samples containing europium were measured with Co $K\alpha 1$ (λ = 1.788996(1) Å) radiation. For the rest of the samples, Cu $K\alpha 1$ (λ = 1.5405929(5) Å) radiation was employed. Analysis of powder patterns was done with an integrated suite of programs, WinXPow [46]. For lattice parameters refinement, the internal standard LaB_6 [47] (a = 4.15683(9) Å) was added. Adjustment of reflection positions based on the internal standard reflections, and final least-squares refinement of the lattice parameters was done with the WinCSD crystallographic package [48]. For full-profile refinements, the measurements were carried out with a STOE-STADIP-MP diffractometer, in Bragg-Brentano geometry, equipped with a position sensitive detector (PSD) and a Ge(111)-monochromator, using the Cu $K\alpha 1$ radiation. The range of measurement was $3° \leq 2\theta \leq 120°$, with a step width of 0.02°, and 4 x 10 h scans. High-resolution synchrotron X-ray powder diffraction experiments were available

at the beamline ID31 of the European Synchrotron Radiation Facility (ESRF) in Grenoble. For data collection, a quartz capillary (diameter = 0.5 mm) was filled with the sample and sealed in Ar atmosphere. A multi-analyzer stage with nine detectors, each preceded by a Si (111) crystal, was employed in Debye-Scherrer geometry, and the wavelength was determined for each experiment by measuring Si or LaB_6 standards. The exact values for each experiment are given in the corresponding chapters. Usually, the measurement range was $1° \leq 2\theta \leq 44°$, with step width of 0.001°. In all cases, the refinements were performed by the Rietveld method as implemented in the Jana2006 program [49] or WinCSD. For visualization of crystal structures, the programs Atoms [50], Diamond [51], and CrystalMaker [52] were employed.

2.3.1.2 Single-crystal X-ray diffraction

For single crystal X-ray diffraction experiments, suitable size and shape single crystals were picked and mounted on the top of glass capillaries. Data collection at room temperature was performed with a Rigaku AFC 7 diffractometer equipped with a Saturn 724 and CCD detector, employing monochromated Mo-$K\alpha$ radiation (λ = 0.71073 Å). Absorption correction was performed by a multi-scan procedure. Structure solution and refinements were done either by the SHELXS-97 and SHELXL-97 programs [53], integrated in the WinGX package [54], or with the WinCSD crystallographic package.

2.3.1.3 X-ray absorption spectroscopy

X-ray absorption spectra were recorded for europium containing samples by performing extended X-ray absorption fine structure (EXAFS) scans at the A1 beamline of DESY. The photon absorption of Eu was recorded at the energy of the L_3 line at 6977 eV, together with a Eu_2O_3 reference (Eu^{3+}). Scans in the range 6900 eV $\leq E \leq$ 7300 eV with a constant step width of 0.2 eV were registered and the X-ray absorption near edge structure (XANES) region was employed for further interpretations and analysis.

2.3.2 Microstructure and electron microscopy

2.3.2.1 Metallography

Metallographic characterizations were performed on cross-sections of approx 0.1 mm² which were mounted in electrically conductive phenolic resin (PolyFast, Struers) suitable for microstructure analyses on scanning electron microscope (SEM). Cross-section preparation were realized by grinding with SiC down to 6 µm abrasive particle size succeeded by two or three steps of polishing with minimal diamond particle size of 1/4 µm. Chemical-mechanical finishing with Al_2O_3 or SiO_2 suspension were carried out for the germanium containing samples.

2.3.2.2 Optical and Scanning Electron Microscopy

The samples were investigated by a light-optical polarization microscope (Zeiss Axio Plan 2), as well as by a Philips XL 30 Scanning Electron Microscope, employing a LaB_6 cathode. After careful inspection, sample composition was determined by Energy Dispersive X-ray Spectroscopy (EDXS), performed with an attached EDAX Si (Li) detector, on the polished samples. Accurate composition determination was

carried out by means of wavelength dispersive X-ray spectroscopy (WDXS, Cameca SX 100). Ten points are selected from the sample and their composition quantified with the aid of standard references. Depending on the sample composition, either the elements or binary phases were used as reference materials. When single crystals needed to be subject of chemical analysis, EDXS was the chosen method. For that purpose, the single crystals were dismounted from the capillary (once their diffraction intensities have been collected), washed with water-ethanol solution, and fixed onto double-coated carbon conductive tabs, while the other surface was fixed to the aluminum sample holder.

2.3.2.3 TEM

Transmission Electron Microscopy and manually controlled diffraction tomography were performed on a FEI TECNAI 10 (100 kV) microscope, equipped with a 2k CCD camera (TemCam-F224HD, TVIPS). The selected area electron diffraction (SAED) mode was used for tomography data collection. The tilt sequence at steps of 1° was performed manually in a total tilt range of 121° (−60° to 60°, step of 1°) using a standard double-tilt holder (GATAN). The collected series data was stored as a set of files in TIF format, converted into MRC format stacks, and further processed for reconstruction of the diffraction volume, using the ADT3D software package [55]. After indexing the spots in reciprocal-space, the intensities were integrated and stored as standard *hkl*-files for processing by X-ray diffraction software.

2.3.3 Thermal analysis

2.3.3.1 DSC

Metastable high-pressure phases often transform to a thermodynamically stable form at relatively low temperatures [56]. In order to investigate this phenomenon, Differential Scanning Calorimetry (DSC) was applied. DSC measurements were carried out in a Netzsch DSC 404C apparatus, employing an E-type thermocouple, with a heating and cooling rate of 10 K/min, from room temperature to 50 – 100 K above the *liquidus* of the binary phase diagram for the given sample composition. Pieces of samples of 10 – 20 mg were placed into alumina crucibles and heated/cooled under argon atmosphere. After the cycle, no reaction with the crucible was observed, and almost the same amount of sample was recovered for further identification. The peak onset temperature values were used for interpretation. The thermodynamically stable form is usually lower in energy in comparison to the metastable one, and thus the transition during the heating shows an exothermic peak in the DSC curve. Once the ambient pressure form is reached the sample behaves as indicated by the corresponding phase diagram.

2.3.4 Physical properties measurements

2.3.4.1 Magnetic susceptibility

Magnetic susceptibility measurements were carried out with a SQUID magnetometer (MPMS XL-7, Quantum Design) on bulk polycrystalline samples. Diverse external fields between 100 Oe and 70 kOe were applied in the temperature range 1.8 – 400 K, in order to determine the magnetic behavior of the samples. Paramagnetic impurities were estimated and corrected applying the Honda-Owen

correction. In case of superconducting compounds, geometrical factors of the sample were taken into account for the demagnetization effect, when the shape of the sample allowed it.

2.3.4.2 Electrical resistivity

Electrical resistivity measurements were carried out in the temperature range 2 – 350 K, by a standard ac four-probe technique (PPMS, Quantum Design). For this purpose, a bar-shaped piece of sample with dimensions of 4 x 2 x 2 mm^3 is necessary, giving a typical inaccuracy of $\pm$ 20% due to the contact geometry uncertainty. However, the dimensions of the samples obtained by high-pressure synthesis are clearly below such limit. Therefore, a piece of sample as big as possible is used and contacted for the measurement. However, due to the irregular shape and inaccurate dimensions, the estimated error is of the order of $\pm$ 40% and it is better to call the measured quantity resistance instead of resistivity. The second possible solution is to grind and mix two or three samples coming from different high-pressure experiments and cold-press them to an ideal shape and size. In both cases the shape of the experimentally obtained curves are the same, but differences up to ten times in the absolute value of the electrical resistivity were detected when bulk and pressed samples are compared.

2.3.4.3 Specific heat

The heat capacity is a basic quantity for the determination of other thermodynamic parameters as well as material properties. A complete characterization of the superconducting properties of the compounds prepared in the present work was done by specific heat measurements, as well as in the case of magnetic compounds. For that purpose, the specific heat measurements were done in a relaxation-type method (PPMS, Quantum Design) on irregular shape bulk samples (10 – 20 mg).

2.3.5 Electronic structure calculations

Electronic band structure calculations in the framework of the density functional theory (DFT) were performed in order to complement and understand the observed experimental behavior. For that purpose, two different approaches were employed; the elk code [57] and the Stuttgart TB-LMTO-ASA package [58]. In both programs, the local density approximation (LDA) was used. With the converged calculation, chemical bonding analysis in k-space was performed by calculating the corresponding *density of states* (DOS) and *band dispersions*, as well as chemical bonding analysis in real space by means of the topological analysis of the electron density according to Bader [59], and the electron localizability indicator [60] implemented in the DGrid program [61]. In all cases, the experimental structural parameters were employed for the calculations.

The elk code is an implementation of the full potential (FP) all-electron augmented planewave [62] method with local orbitals, being one of the most accurate computational schemes for solid-state Kohn-Shan DFT [63]. In such a scheme, the lattice space is divided into interstitial region (IR) and non-overlapping atomic muffin-tin (MT) spheres centered at atomic positions. The basis set comprises plane waves and atomic orbitals, respectively.

In the Tight-Binding Linear Muffin Tin Orbital Atomic Sphere Approximation, TB-LMTO-ASA, the electronic structure of materials can be calculated quite fast and with high accuracy. In the method,

the orbitals are expanded in terms of the angular momentum index around each atom and can be considered crystal extensions of atomic orbitals. During a typical calculation, as in the previous case, crystals are divided into regions (muffin tins) around each atom where the LMTO basis is expanded, and interstitial regions outside of the muffin tins. In the LMTO-ASA case, the system must be closed-packed, thus producing a compact basis set leading to efficient calculations [64]. In the calculations done in this work, the Barth-Hedin exchange potential was employed.

Chapter 3
Results and Discussion

3.1 $Ba_{8-x}Si_{46}$

The superconducting binary clathrate-I $Ba_{8-x}Si_{46}$ [65-67] constitutes the prototype for a number of ternary compounds in which silicon is typically substituted by a group 13 or a transition metal element. From the chemical point of view, the composition of clathrate $Ba_{8-x}Si_{46}$ may be interpreted within the *8 – N* rule and the Zintl concept as $[Ba^{2+}]_{8-x}[(4b)Si^{0}]_{46}\times(16-2x)e^{-}$, i.e., the excess electrons induce a metal-like behavior in electronic transport, which is in agreement with the superconducting properties [68]. However, so far the measurements on $Ba_{8-x}Si_{46}$ have been focused on properties associated to superconductivity such as magnetic susceptibility or electrical conductivity [69]. Recently, the phonon propagation of $Ba_{7.5}Si_{46}$ was investigated experimentally by means of inelastic X-ray scattering in combination with ab-initio DFT calculations [70]. Nevertheless, a complete picture of the electronic and thermal transport properties is still missing. In order to explore the suitability of silicon – the more abundant analog of germanium – for use in thermoelectric clathrate materials, knowledge of the transport properties of $Ba_{8-x}Si_{46}$ is required as a reference for understanding the physical properties of multicomponent clathrates with low substitution levels.

3.1.1 Preparation

Preparation and handling of materials for high-temperature high-pressure synthesis were performed in the inert atmosphere of argon-filled glove boxes. The precursor with nominal composition Ba:Si = 8:46 is prepared by arc melting of elemental Ba and Si. In order to account for the mass loss during the melting process, a mass excess of 1 % barium has been added. The samples were ground and loaded in *h*-BN crucibles and enclosed in MgO octahedrons. Various conditions for temperature and pressure were applied in the range 1100 – 1500 K and 3 – 10 GPa. The experiments were carried out for one hour of annealing followed by quenching (cooling with the equipment) to room temperature before decompression. In order to avoid or reduce the formation of cracks, the pressure program was modified, and the samples were slowly decompressed within twelve hours.

3.1.2 Results

Among all attempts to get the pure and crystalline phase Ba_8Si_{46}, the optimal conditions for the synthesis were found to be at 5 GPa and one hour of annealing at 1200 K. The brittleness of Ba_8Si_{46}, made it impossible to separate the crucible from the sample without breaking it into small pieces. Therefore, a different approach had to be employed. It was decided to polish the whole cylindrical assemble (crucible + sample) for removing the container and, at the same time, giving the required shape to the specimen (Figure 3.1.1a). After several attempts of shaping the brittle polycrystalline material, a parallelepiped-shaped bulk specimen was obtained by removing the *h*-BN crucible with silicon carbide paper (SiC, grit 4000) and a polishing machine (LaboPol-21) operated at 250 rpm with water as coolant. Finally, a specimen of the dimensions $3.35\times2.08\times1.85$ mm^3 could be contacted for the measurements (Figure 3.1.1b).

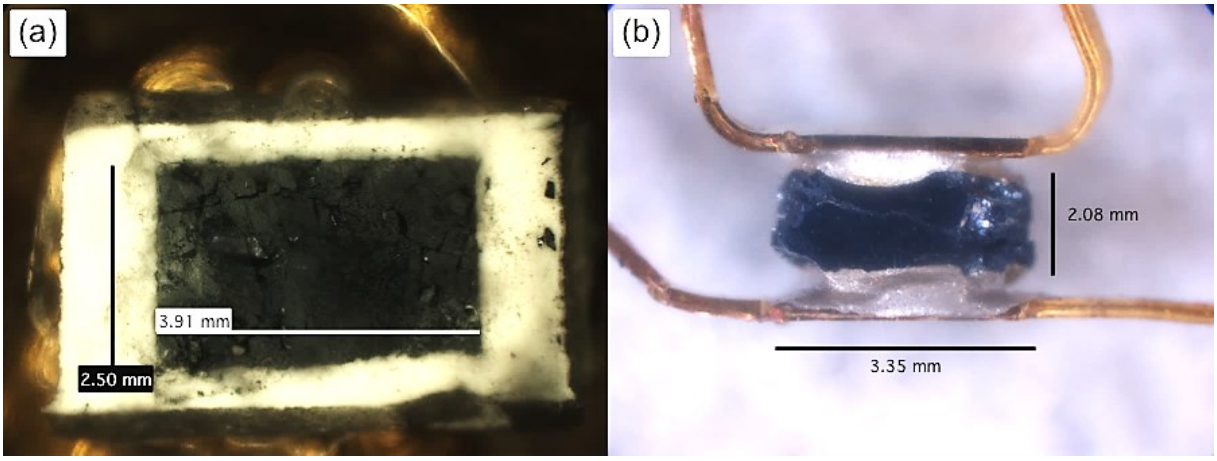

Figure 3.1.1 $Ba_{8-x}Si_{46}$ specimen (a) prepared with the standard decompression program, and (b) prepared with the extra slow pressure-release program, showing the contacts for the measurements.

3.1.2.1 Thermal behavior and crystal structure refinement

According to the DSC experiment combined with the X-ray powder diffraction characterization of its products, the main phase decomposes exothermally at 884 K (Figure 3.1.2) into $BaSi_2$ and Si which are the stable phases at ambient pressure according to the phase diagram. These findings reveal the metastable character of the clathrate-I phase and are in agreement with an earlier temperature dependent X-ray powder diffraction study [71].

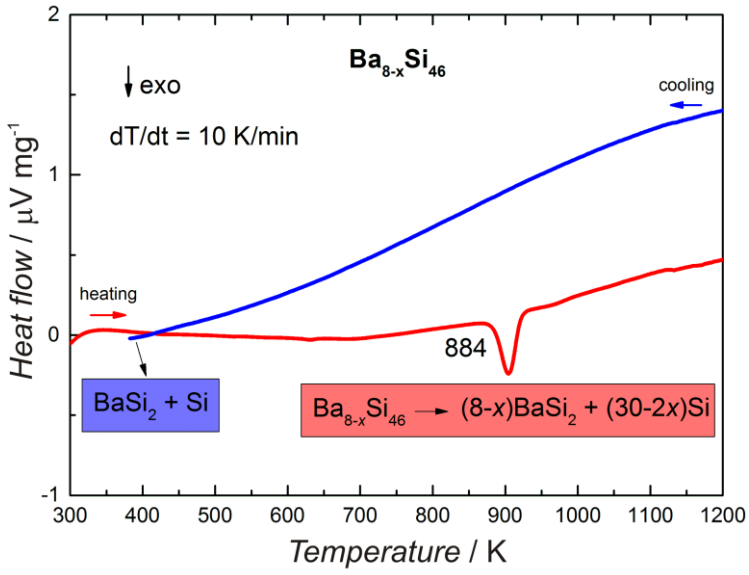

Figure 3.1.2 Differential scanning calorimetry of $Ba_{8-x}Si_{46}$. The irreversible transition to the disilicide and silicon, occurring during the heating cycle, reveals the metastable character of the sample.

The X-ray powder diffraction experiment reveals the presence of crystalline phases in the product. The major phase is the clathrate-I, in addition α-silicon Si (*c*F8) was observed as a minority phase (Figure

3.1.3), being well in agreement with the metallographic data (Figure 3.1.4). The average of 9 point analyses applying the WDXS technique results in the following concentrations: Ba - 42.9(2) mass.% , Si - 57.4(3) mass.%, i.e., the analytical total amounts to 100.3 (2) mass.%. This corresponds to the composition $Ba_{7.0(1)}Si_{46}$.

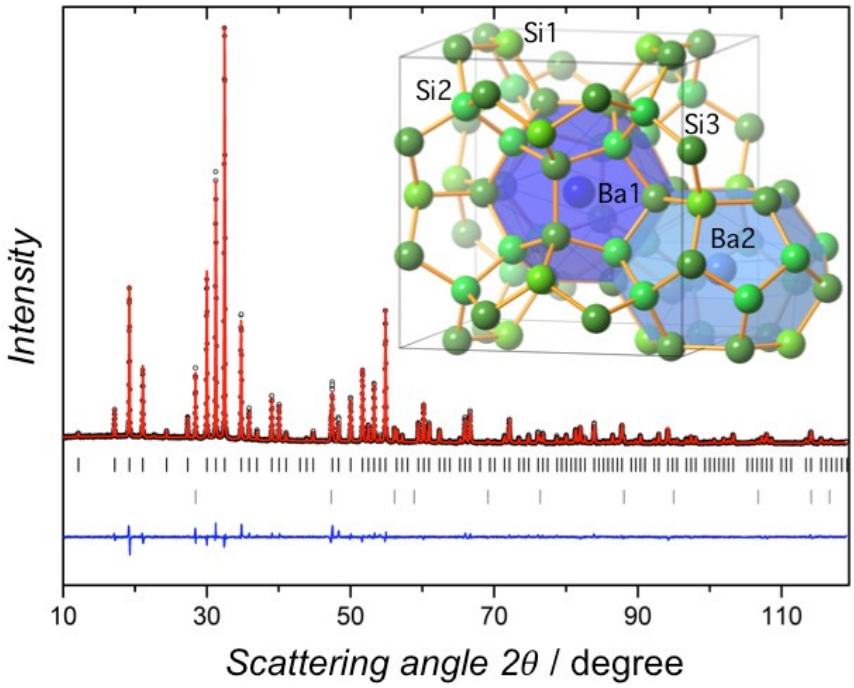

Figure 3.1.3 X-ray powder diffraction pattern of $Ba_{8-x}Si_{46}$ together with the crystal structure model obtained from the refinement. Black points and red lines correspond to the observed and calculated intensities, respectively. Vertical tick marks correspond to reflection positions and the difference between the observed and calculated intensities is shown as blue.

3.1.2.2 Chemical composition

Barium deficiency in type-I Ba_8Si_{46} clathrate is a well-known issue [72]. The composition of the material used for physical properties measurements was determined by Rietveld refinement (Figure 3.1.3). The crystallographic information and data collection details are listed in Table 5.1, the final atomic coordinates and isotropic displacement parameter are shown in Table 5.2 and selected interatomic distances are in Table 5.3. The crystal structure is shown in the inset of Figure 3.1.3. Similar values for the ADP of silicon atoms indicate the absence of defects within the three-dimensional framework. The Ba1 position is only partially occupied. The refinement of the occupancy factor for this position was stable despite the expected correlation between the occupation factor of barium positions and the scale factor (Ba delivers the main contribution to most diffraction intensities in this compound). The structure refinement yields the composition $Ba_{7.27(1)}Si_{46}$.

By reviewing the published work on the Ba_8Si_{46} clathrate, a correlation of composition, lattice parameter and superconducting transition temperature becomes evident. In order to have an additional estimation of the Ba content, the published data was plotted in the form of lattice parameter as a function of composition (Figure 3.1.5).

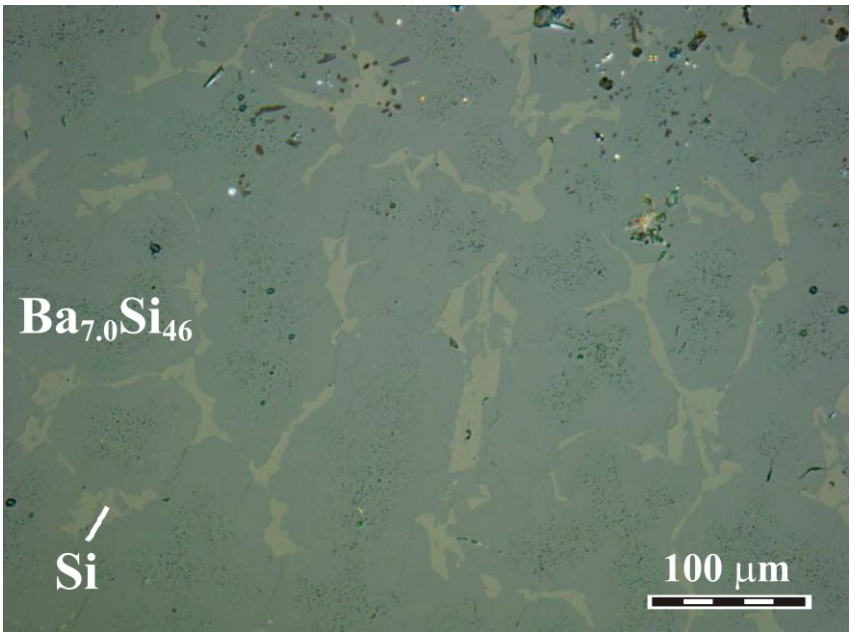

Figure 3.1.4 Optical images of the sample $Ba_{8-x}Si_{46}$ obtained with polarized light. The microstructure is composed of the clathrate as a main phase and small domains of silicon.

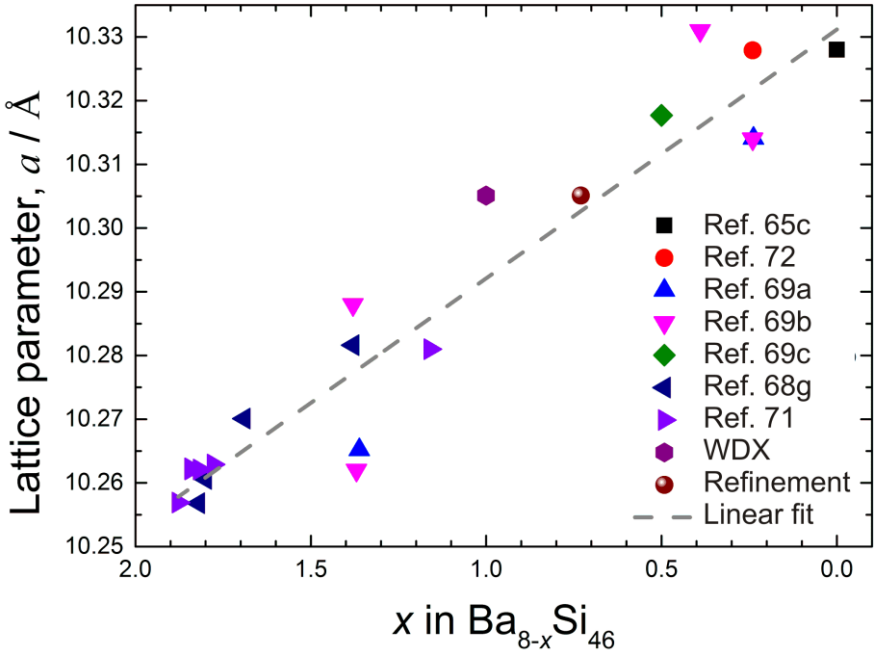

Figure 3.1.5 Lattice parameter *a* of the clathrate phase $Ba_{8-x}Si_{46}$ as a function of the experimentally determined barium content (references indicated in the legend). The gray dashed line represents the linear equation obtained by least squares refinement.

The least squares refinement of previous results yields the equation $a = 10.01864 + 0.03907(8-x)$, which gives with the experimentally obtained lattice parameter (a = 10.3051 Å) the total composition

$Ba_{7.3(1)}Si_{46}$. The values of the barium content obtained from the structure refinement, from the WDX analysis and from the lattice parameters are equal within a few estimated standard deviations. Thus, the composition of the prepared compound amounts to $Ba_{7.2(1)}Si_{46}$ by averaging the values above.

3.1.3 Physical properties

The mechanical stability of the manufactured specimen was high enough for shaping the sample for physical properties measurements. Great care was taken to discard those specimens which were damaged during the synthesis procedure or in the course of subsequent preparation steps. Only two pieces cut from the as-grown cylindrical ingots were found to exhibit low resistivity values, other showed at least tenfold higher values. This finding is attributed to the brittleness of $Ba_{7.2}Si_{46}$ so that the material is predisposed to develop micro-cracks, which tamper with electrical conductivity. The thermal conductivity and the Seebeck coefficient were determined simultaneously. Due to the small sample size, two gold-plated copper disc holding (heater/hot thermometer and heat sink/cold thermometer, respectively) were glued to the sample with silver-filled epoxy raisin (Figure 3.1.1b). The temperature jumps between discs and sample are expected to be sufficiently small for the investigated temperature gradient, but the error for the electrical resistivity in this two-point setup is expected to be disproportionate. Therefore, conductivity was separately determined with a four-point arrangement using 25 μm Pt wires (estimated inaccuracy ± 10%).

3.1.3.1 Magnetic susceptibility

The high-field magnetic susceptibility of $Ba_{7.2}Si_{46}$ shows only a weak temperature dependence (Figure 3.1.6). The value for $T \rightarrow 0$ corrected for ferromagnetic impurities amounts to $+9.2\times10^{-4}$ emu mol^{-1}, indicating a sizable Pauli-paramagnetic contribution χ_P. Adopting a value χ_{dia} = -4.0×10^{-4} emu mol^{-1} (Ba^{2+}, Si^0) [73,74] for the diamagnetic contributions, χ_P = $+13.2\times10^{-4}$ emu mol^{-1} may be derived. Within the free electron approximation, this value would correspond to an electronic density of states (DOS) of 41 states eV^{-1} $f.u.^{-1}$ at the Fermi level. Below, we derive a significantly larger DOS from the electronic specific heat coefficient γ_n. This indicates that our estimate for χ_{dia} is too small. Therefore, it is reasonable to assume that additional large diamagnetic Larmor-type contributions are present in $Ba_{7.2}Si_{46}$, as commonly observed for clathrate-type atomic patterns [75,76].

Below 8.2 K, the compound becomes superconducting as signaled by a sharp transition to a state with large diamagnetic response (Figure 3.1.6, inset). The shielding fraction measured after zero-field cooling is close to unity while the Meissner effect signal in field-cooling is much less (both uncorrected for demagnetization). The incomplete Meissner flux repulsion is attributed to the pinning of flux lines in this type-II superconductor.

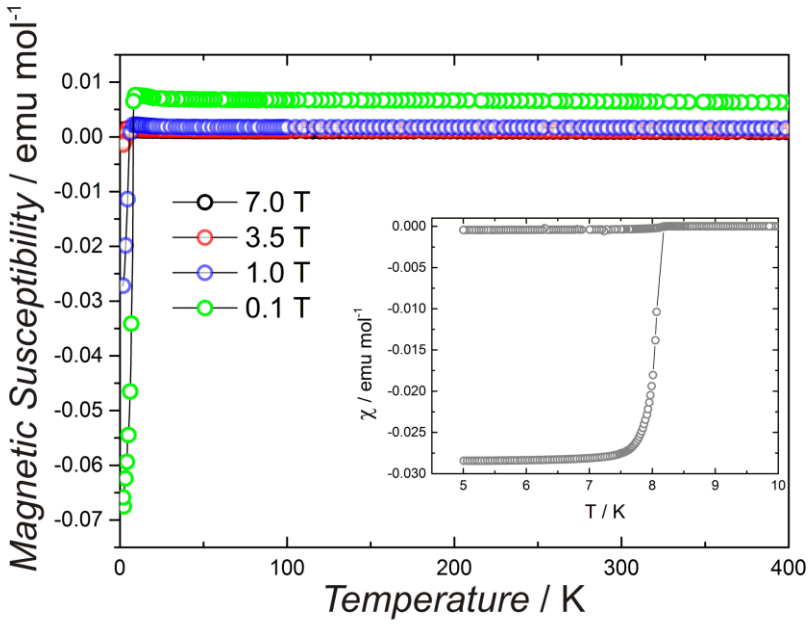

Figure 3.1.6 Magnetic susceptibility of $Ba_{7.2}Si_{46}$ at different magnetic fields. The Meissner effect is shown in the inset.

3.1.3.2 Specific heat

The difference of the specific heat, $\Delta Cp(T,B_{ext}) = Cp_{,s} - Cp_{,n}$ ($Cp_{,s}$ and $Cp_{,n}$ being the specific heat in the superconducting and normal state, respectively) measured in different magnetic fields up to B_{ext} = 4 T is given in Figure 3.1.7. The results are similar to those of independently performed earlier measurement [77]. The midpoint of the step-like (second-order) transition in zero field is at Tc(mid) = 8.08(1) K and the relative size $\Delta Cp/T$c(mid) amounts to 266 mJ mol^{-1} K^{-2}. The ratio $\Delta Cp/\gamma_n T$c of 1.86 indicates a moderately enhanced electron-phonon coupling. For the temperature range measured in our study ($T > 2.0$ K), the $\Delta Cp(T)$ in zero field is well described by the phenomenological alpha model [78] with $\alpha = \Delta_0/k_B T$c ≈ 2.00(5) and γ_n` = 134 mJ $mol^{-1}$ $K^{-2}$, i.e., with a single conventional s-wave gap function for moderately enhanced electron-phonon coupling. For the determined value of $\alpha$, a ratio $\Delta Cp/\gamma_n T$c of 1.82 is expected. This ratio and the value of $\gamma_n$` are in fair agreement with the values reported above. Although it was already reported that $\Delta Cp(T)$ is well described by this model, the previous data down to 0.4 K called for the presence of an additional gap contribution with a small weight of 10% and very small α, i.e., for a two-gap scenario with a small admixture of a band with small gap-to-Tc ratio. Although the present measurement do not evidence a second contribution, our results agree with the earlier conclusions [77] since the contribution of the second gap becomes significant only below the minimum temperature of the current data.

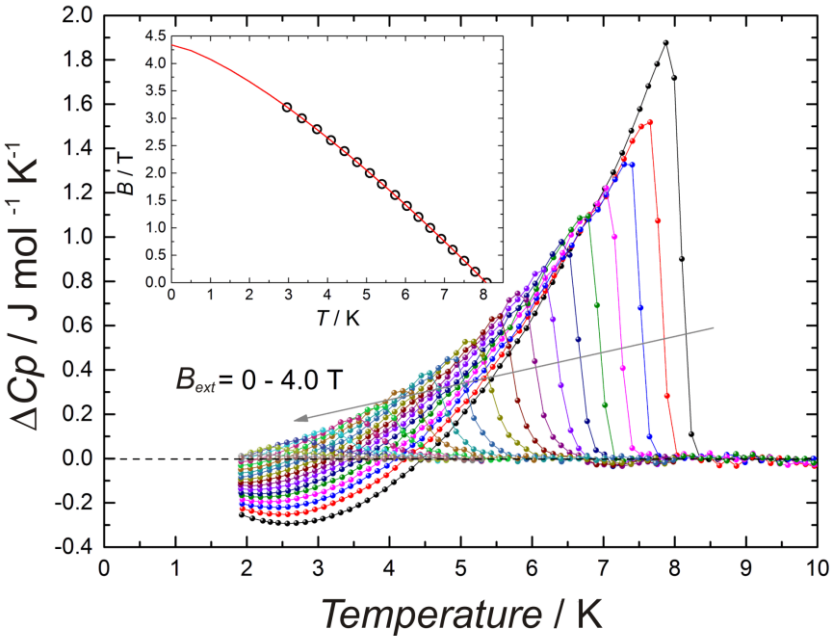

Figure 3.1.7 Difference specific heat, $\Delta Cp(T)$ of $Ba_{7.2}Si_{46}$ at low temperatures. The inset shows the $B_{c2}(T)$ relationship.

The midpoint transition temperature Tc as a function of field B_{ext} was determined by fitting the transitions in $Cp(T,B_{ext})$ including a Gaussian broadening. The relationship $B_{c2}(T)$ is given in the inset of Figure 3.1.7. It is well fitted by the phenomenological formula $B_{c2}(T) = B_{c2}(0) - (T/Tc(0))^{\alpha}$ with the parameter values $\alpha = 1.34(1)$ and $B_{c2}(0) = 4.34(2)$ T. Alternatively, the Werthamer-Helfand-Hohenberg (WHH) extrapolation $B_{c2}(0) = -0.693 \times Tc \times dB_{c2}/dT\,|_{T=Tc}$ results in $B_{c2}(0) = 3.85(2)$ T. These $B_{c2}(0)$ values are significantly lower than the reported 5.75 T derived from the specific heat data using the WHH extrapolation [77]. This might be due to a lower concentration of point defects (higher residual resistance ratio) and, consequently, weaker flux-line pinning in the present sample.

The specific heat of $Ba_{7.2}Si_{46}$ in the normal conducting state (at magnetic fields $B > B_{c2}$) in the temperature range 1.9 – 10.3 K is not sufficiently well described by the standard ansatz $Cp(T) = \beta T^3 + \gamma_n T$. Here, βT^3 is the lattice term in the Debye approximation and $\gamma_n T$ is the conduction electron Sommerfeld term. Instead, the fit improves significantly when adding an Einstein term (Figure 3.1.8), a fact well known for clathrates with heavy guest atoms in a rigid host lattice [79 and references therein, 80], and nicely revealed by plotting the specific data in the form CpT^{-3} *vs* T (Figure 3.1.8, inset). The obtained Einstein term has a spectral weight of 10.8 R (R = molar gas constant $N_A k_B$, formally corresponding to 3.6 atoms per formula unit with three degrees of freedom each) and a characteristic temperature $\Theta_E = 78.3(6)$ K, the latter being in good agreement with the first peak in the phonon DOS (at ≈ 7 meV = 81 K [77]). Also, the value for Θ_E from the Cp data agrees fairly well with the large ADP of the Ba atoms ($\Theta_{E,calc} = 72$ K) evidenced by crystal structure refinement (cf. Table 5.2, and [69,71]). The remaining parameters of the fit are $\gamma_n = 143(1)$ mJ mol^{-1} K^{-2}, and $\beta = 2.25(5)$ mJ mol^{-1} K^{-4} (corresponding to a Debye temperature of 352 K for the remaining 3×54 – 10.8 = 3×50.4 degrees of freedom). The Sommerfeld coefficient γ_n is in excellent agreement with the earlier reported one of 144 mJ mol^{-1} K^{-2} [65] and corresponds to an electronic DOS of 61 states eV^{-1} f.u.$^{-1}$ at the Fermi level.

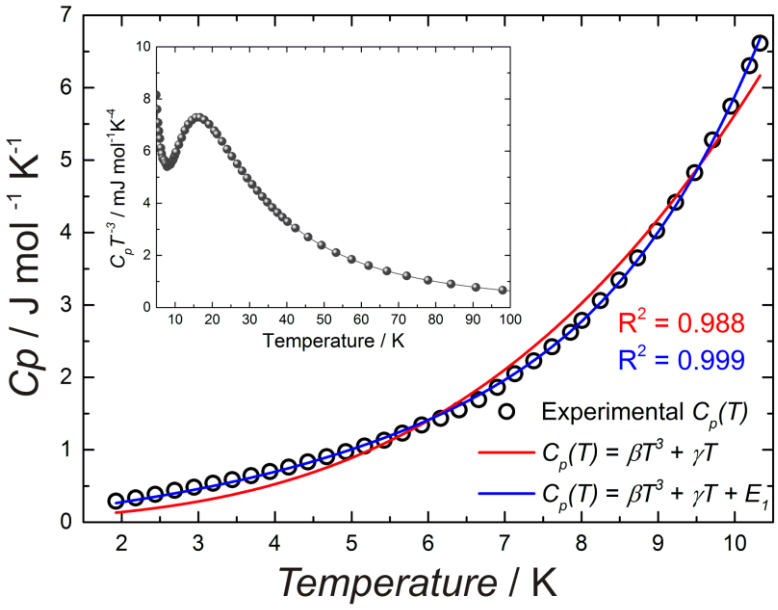

Figure 3.1.8 Specific heat in the low temperature range (open circles) measured in an overcritical field $B_{ext} > B_{c2}$. The lines represent the two models employed during the fitting of the experimental data. The simple Debye model (red line) was not sufficient, thus an Einstein term was added, improving the description of the data (blue line). The specific heat is plotted in the form CpT^{-3} vs T, revealing the possible Einstein-like contribution (bell-shaped anomaly).

3.1.3.3 Electrical resistivity

The DOS values at the Fermi level obtained experimentally are both larger than the theoretically calculated (all-electron fully relativistic approach) 20 states eV^{-1} $f.u.^{-1}$ [81] and fit better to the simpler TB-LMTO-ASA calculation with 30 states eV^{-1} $f.u.^{-1}$ (Figure 3.1.9). The reasons of this discrepancy are under investigation.

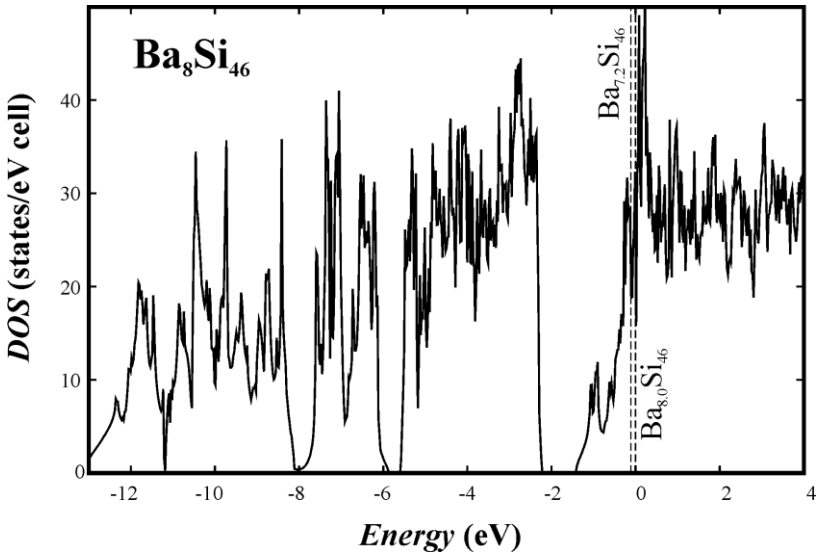

Figure 3.1.9. Electronic DOS calculated for the composition Ba_8Si_{46} with the position of the Fermi level for the experimental composition $Ba_{7.2}Si_{46}$ is estimated in the rigid-band approximation.

Well in agreement with the electronic balance mentioned in the introduction and the calculated electronic DOS, $Ba_{7.2}Si_{46}$ reveals metallic behavior in electronic transport, and the electrical resistivity increases with temperature (Figure 3.1.10). The absolute values of the resistivity are high being probably additionally influenced by the two-phase microstructure of the measured specimen. The size of the temperature-dependent part ($\rho_{300K} - \rho_0 \approx 3$ μΩ m) is of the order which is often observed for ternary intermetallic compounds with high density of states at the Fermi level.

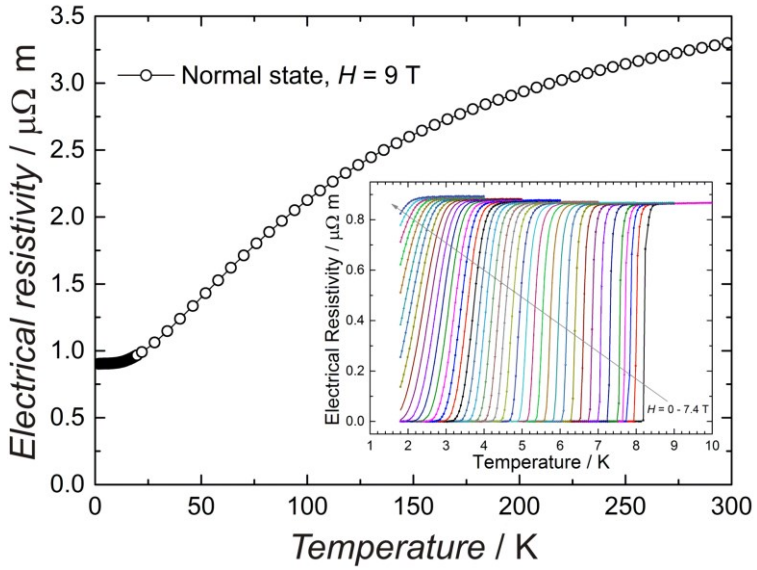

Figure 3.1.10 Electrical resistivity, $\rho(T)$ of $Ba_{7.2}Si_{46}$ in the normal state ($B_{ext} > B_{c2}$). The inset shows the dependence of $\rho(T)$ with the applied magnetic field.

In the absence of an external magnetic field, the transition to the superconducting state is evidenced (Figure 3.1.11). The superconducting transition width was evaluated (10 – 90%) to be 0.06 K and is considerably broadened to 1.78 K at 5 T, affecting also the *Tc* onset (Figure 3.1.11, inset). The *B* – *T* phase diagram for $Ba_{7.2}Si_{46}$, corresponding to temperatures with the onset, midpoint and zero resistivity, for the different magnetic fields is plotted in the inset of Figure 3.1.11. The visual inspection of the plot indicates that any of the three curves follow a parabola and thus, cannot be well described by the power-law, as in the case of the specific heat data. This may be another indication of the two-gap superconducting mechanism, reported for the clathrate Ba_8Si_{46}. On the other hand, applying the WHH extrapolation to the data, and using the first four points for the dB_{c2}/dT value, the upper critical field is found to be 3.80, 3.72 and 3.65 T, for the onset, midpoint and zero values of resistivity, respectively, which is in excellent agreement with $B_{c2}(0)$ found by the specific heat measurements ($B_{c2}(0) = 3.85(2)$ T).

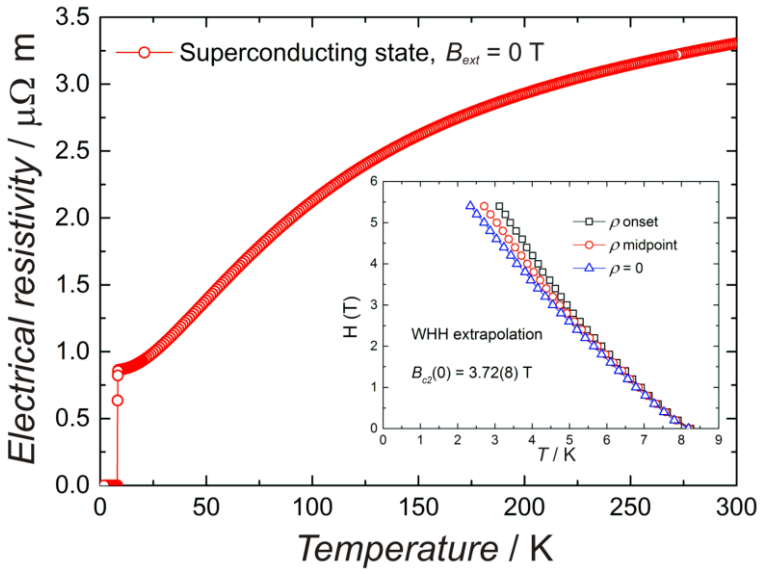

Figure 3.1.11 Electrical resistivity of $Ba_{7.2}Si_{46}$ in the superconducting state. The *B_{c2}(T)* relationships are shown in the inset.

3.1.4 Thermoelectric properties

The thermoelectric properties of $Ba_{7.2}Si_{46}$were investigated by performing measurements on the specimen shown in Figure 3.1.1b. The electrical resistivity, thermopower, thermal conductivity, and figure of merit are shown in Figure 3.1.12. The very good electrical conduction (metal-like, and superconducting below 8.2 K) and the low thermopower, caused by the excess electrons, mainly contribute to the resulting low thermoelectric figure of merit, *ZT*. In general, clathrates are considered promising thermoelectric materials because of the possibility to decrease the thermal conductivity. Contrary to this expectation, the thermal conductivity exhibits considerably high values in $Ba_{7.2}Si_{46}$. The reason for that behavior may be related directly to the different contributions to the total thermal conductivity, and thus, to the crystal structure pattern. This will be analyzed in detail below.

By applying the Wiedemann-Franz law, the total thermal conductivity of $Ba_{7.2}Si_{46}$ was decomposed into lattice and electronic contributions (Figure 3.1.13). As stated above, the total conductivity, with more than 6 W K^{-1} m^{-1} at room temperature, is remarkably high in comparison with other barium-containing clathrates. Especially large is the lattice contribution. For comparison, in the binary $Ba_8Ge_{43}\square_2$, experimental data cover a range between 2.0 and 2.8 W K^{-1} m^{-1} at room temperature depending on the ordering level of the vacancies in the crystal structure [82]. In the ternary clathrates $Ba_8Ga_{16}Ge_{30}$ and $Ba_8Au_{5.3}Ge_{40.7}$ it drops even below 1.0 W K^{-1} m^{-1} at room temperature caused – in particular – by additional dative bonding between Ba and electronegative transition metal [68d,82]. Also the gold-substituted $Ba_8Au_xSi_{46-x}$ with 1.0 – 2.5 W K^{-1} m^{-1} (depending on x) at room temperature shows much smaller thermal conductivity than the binary clathrate $Ba_{7.2}Si_{46}$ [83]. One of the reasons for the large lattice thermal conductivity is the absence of defects in the silicon framework. Another reason is the chemical bonding in this compound. This was studied applying the electron-localizability approach.

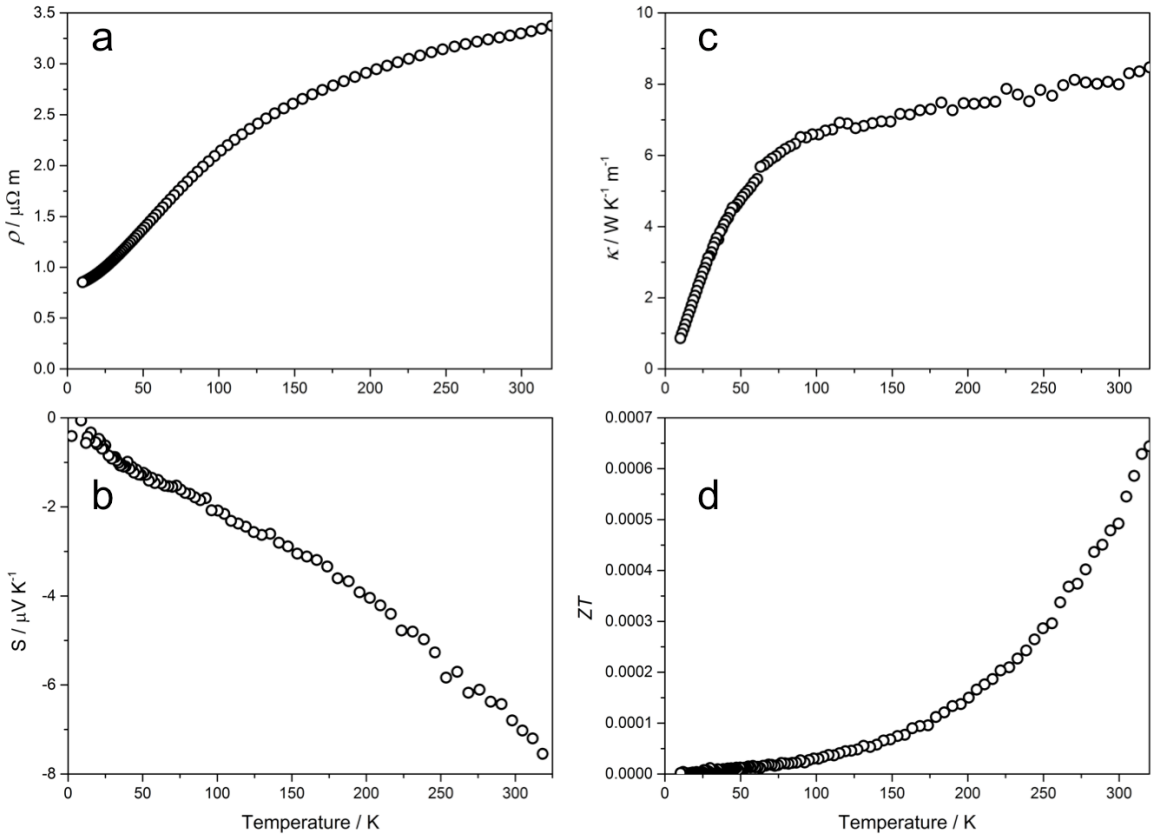

Figure 3.1.12 Low-temperature thermoelectric properties of $Ba_{7.2}Si_{46}$ sample: (a) electrical resistivity, (b) thermopower (Seebeck coefficient), (c) thermal conductivity, and (d) thermoelectric figure of merit, *ZT*.

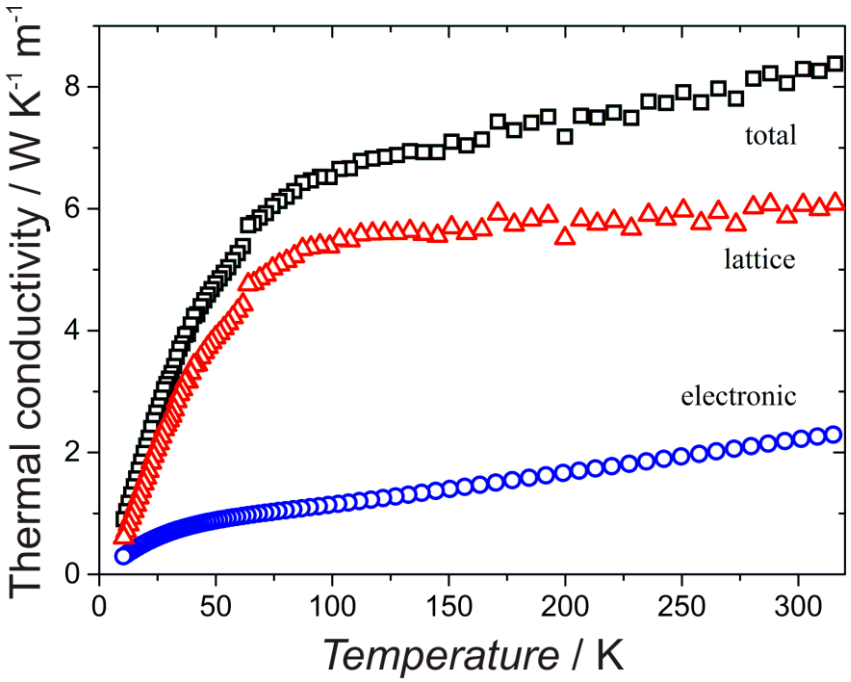

Figure 3.1.13 Total, lattice and electronic thermal conductivity, κ of $Ba_{7.2}Si_{46}$ vs temperature.

3.1.5 Chemical bonding

The distribution of the electron-localizability indicator (ELI-D) reveals maxima between the silicon atoms forming two-center covalent bonds within the polyanionic framework (Figure 3.1.1.14, top). The last (6th shell) of the barium atoms is not visible in the distribution indicating substantial charge transfer from the Ba cations to the anionic silicon framework. No maxima of ELI-D were found between the silicon atoms in the 6*d* position and the Ba1 atoms in Ba_8Si_{46}. This finding is in contrast to the results for $Ba_8Au_6Si_{40}$ which – as expected from findings for $Ba_8Au_6Ge_{40}$ [68d]) – shows ELI-D maxima between Ba and Au. Such "simplification" of the bonding in the binary clathrate, when compared with the ternary varieties, together with the smaller atomic mass of silicon, seems to be the main reason for the large lattice thermal conductivity. It behaves similar to the thermal conductivity of the elements of the group 14, for which the values decrease in the sequence C – Si – Ge [84].

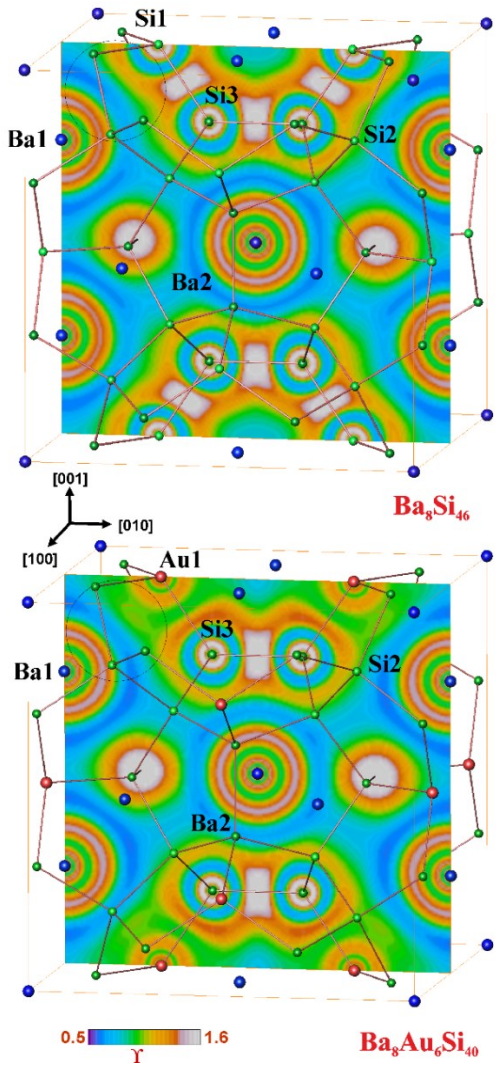

Figure 3.1.14. Distribution of the electron-localizability indicator ELI-D in the (100) plane for Ba_8Si_{46} and $Ba_8Au_6Si_{40}$. ELI-D maxima between the silicon or between the Si and Au atoms reveal the covalent bonding within the polyanionic framework. The ionic interaction between the framework and the Ba cations is visualized by the absence of the 6th shell for the Ba species in both compounds and by the additional absence of the ELI-D maxima between Ba and Si in Ba_8Si_{46}. The dative framework-barium (Au – Ba) interaction is found from the ELI-D maxima in $Ba_8Au_6Si_{40}$ and is absent in Ba_8Si_{46}.

3.1.6 Conclusions

The electronic and thermal transport of the binary clathrate $Ba_{8-x}Si_{46}$ has been studied on bulk polycrystalline specimen with the composition $Ba_{7.2}Si_{46}$. The superconducting transition is observed at a slightly higher temperature of 8.2 K as reported earlier. In agreement with simple electron counting and the analysis of the chemical bonding, $Ba_{7.2}Si_{46}$ reveals metallic character of the electronic transport. The thermal conductivity is remarkably high in comparison with the binary germanium analog and the ternary substitution varieties of germanium and silicon. The reasons for the enhanced lattice thermal conductivity are the ordered atomic arrangement in the polyanionic framework and the simple (in comparison to the ternary variants) heterodesmic bonding in $Ba_{7.2}Si_{46}$ which is characterized by charge transfer from Ba to the framework and covalent interaction within the framework.

3.2 $BaGe_6$ and $BaGe_{6-x}$

During attempts to fill the voids in the clathrate $Ba_8Ge_{43}\square_3$ with germanium by applying high-pressure high-temperature conditions, a new phase was found in the system Ba – Ge. As shown in Figure 3.2.1, from 10 GPa on, a completely new set of reflections was detected, in which the x-ray powder pattern turned out to be similar to that of $SrGe_{5.5}$ [85]. The indexing, based on the lattice parameters of $SrGe_{5.5}$, succeeded in an orthorhombic unit cell. The space group *Cmcm* could be easily derived from the extinction conditions, in agreement with the strontium homologue. However, a few reflections remained unindexed (Figure 3.2.1, bottom), even when the sample was single phase, thus a detailed analysis of the crystal structure, requiring single crystal diffraction data, was performed.

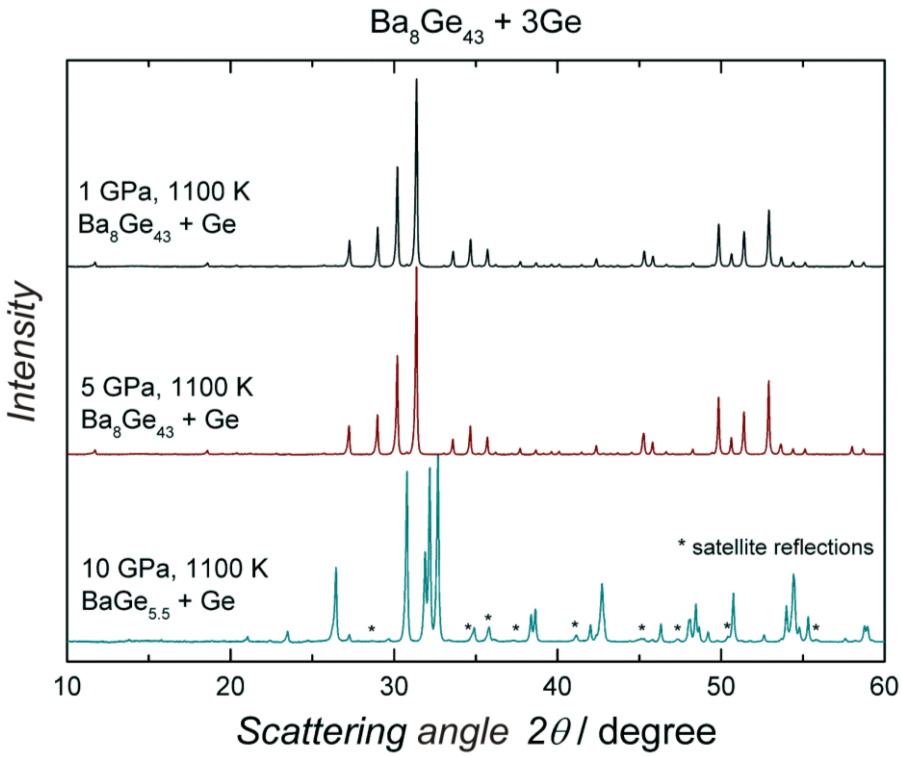

Figure 3.2.1 X-ray powder diffraction patterns of mixtures Ba_8Ge_{43} + 3Ge, subject to different conditions of HPHT. At 10 GPa and 1100 K, a new set of reflections appeared. The low intensity reflections marked by * were not included during the indexing procedure.

3.2.1 Preparation, chemical composition and thermal behavior

Sample handling was performed in the inert atmosphere of glove boxes. The precursor samples with nominal composition Ba:Ge = 1:5.6 were prepared by arc melting of high-purity elements (see Table 2.1). In order to compensate for the high vapour-pressure of barium, an excess of 1% was added to the initial mixture. The resulting mixture of Ba_8Ge_{43} and Ge was ground loaded into the *h*-BN crucible and subject to different conditions of high-pressure and high-temperature (Figure 3.2.2). The optimal conditions for the formation of $BaGe_{5.6}$ were found to be in the pressure range 10(1) - 15(2) GPa and at temperatures between 773(50) to 1473(120) K, respectively, as determined by x-ray powder diffraction experiments. The typical procedure for HPHT treatment includes the increase of pressure

for three hours and a constant value for one hour of annealing. After the thermal treatment, the internal water-cooling of the Walker module quenches the sample, and the pressure is decreased during nine hours to ambient conditions. In order to grow single crystals, the annealing procedure included 10 minutes of heating at 1073 K followed by cooling down to 973 K within 10 hours. When the mixture is treated at 15 GPa and 1300 K, two new phases were found to coexist, namely $BaGe_6$ and $BaGe_5$ in a new modification (chapter 3.5).

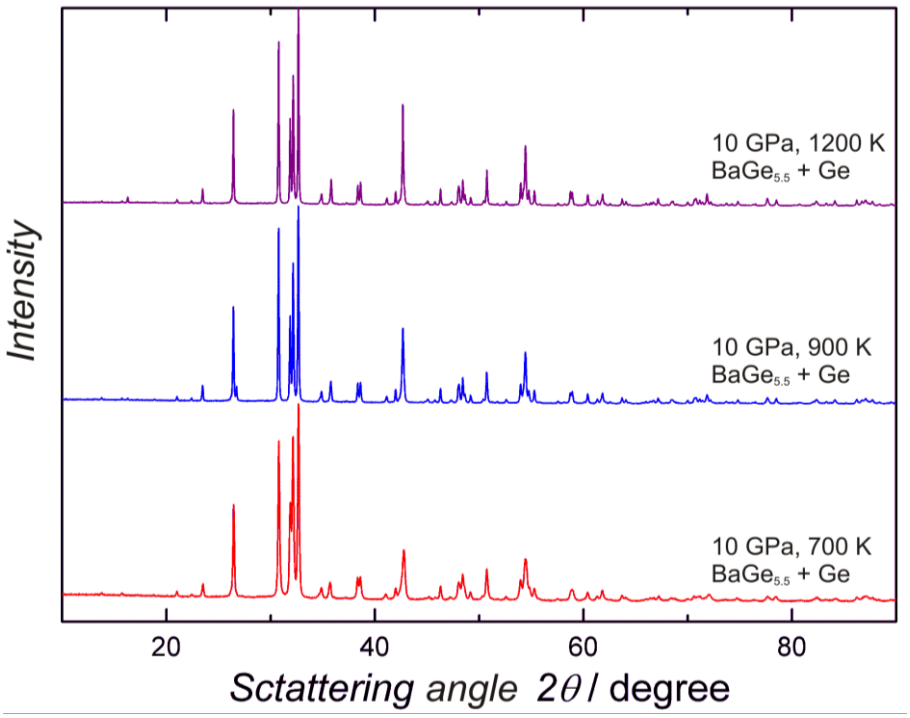

Figure 3.2.2 X-ray powder diffraction patterns of mixtures Ba_8Ge_{43} + Ge, subject to different temperatures at constant pressure.

A piece of sample recovered from the same ingot for growing single crystals, was prepared for metallographic inspection. Optical examination revealed a single phase (Figure 3.2.3) and chemical analysis by means of WDX spectroscopy performed on ten different points suggest a composition $Ba_{1.00(1)}Ge_{5.4(8)}$. This composition will be used as a reference for later refinements.

Upon heating at ambient pressure (Figure 3.2.4), $BaGe_{6-x}$ undergoes an irreversible decomposition into Ge and the normal-pressure modification of $BaGe_5$ at approximately 689 K, as evidenced by annealing sample at 773 K for two days (Figure 3.2.5). On further heating, the DSC curve shows the same transitions as $BaGe_5$ [86], ending with Ba_6Ge_{25} and Ge after several transformation reactions (Figure 3.2.6).

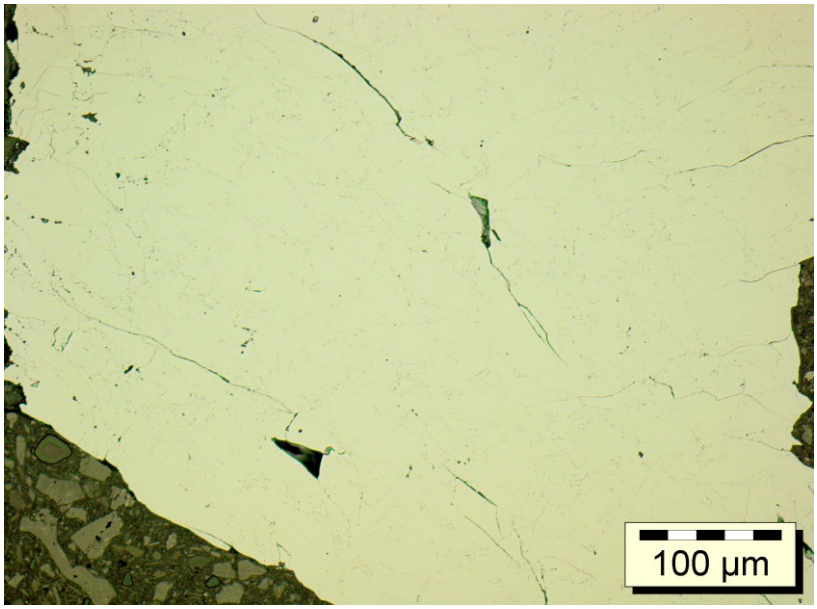

Figure 3.2.3 Optical microscopy image (bright-field) of the $BaGe_{5.6}$ sample prepared for the single crystals growth, under HPHT conditions, showing a single phase with composition $Ba_{1.00(1)}Ge_{5.54(8)}$.

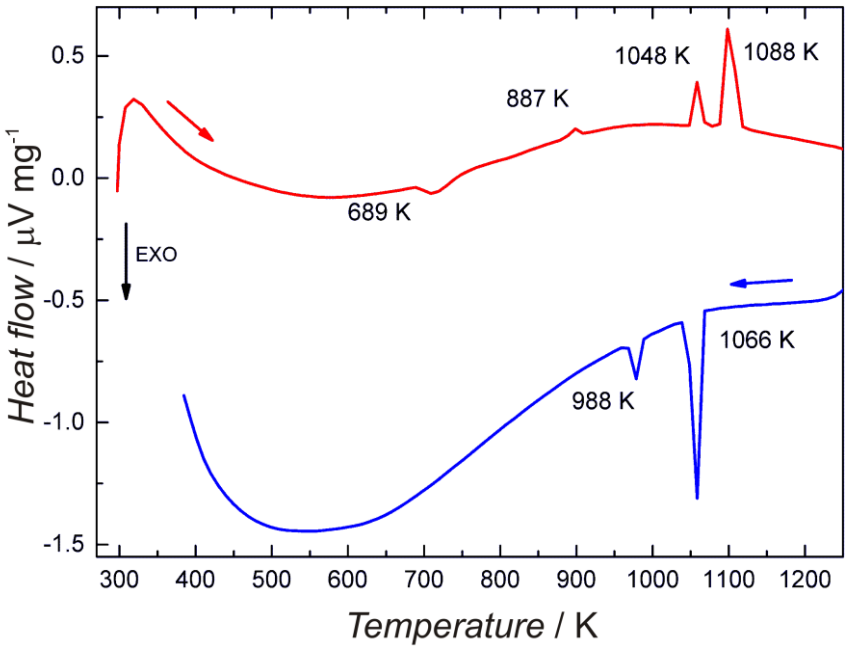

Figure 3.2.4 Thermal behavior of $BaGe_{6-x}$. For all effects, onset temperatures are given. The exothermic and irreversible effect at 689 K corresponds to the decomposition $BaGe_{6-x} \rightarrow BaGe_5 + (1-x)Ge$. $BaGe_5$ transforms into Ba_6Ge_{25} and Ge at 887 K. At 1048 K, Ba_6Ge_{25} and Ge react to form Ba_8Ge_{43} and then it decomposes peritectically at 1088 K into Ba_6Ge_{25} and Ge.

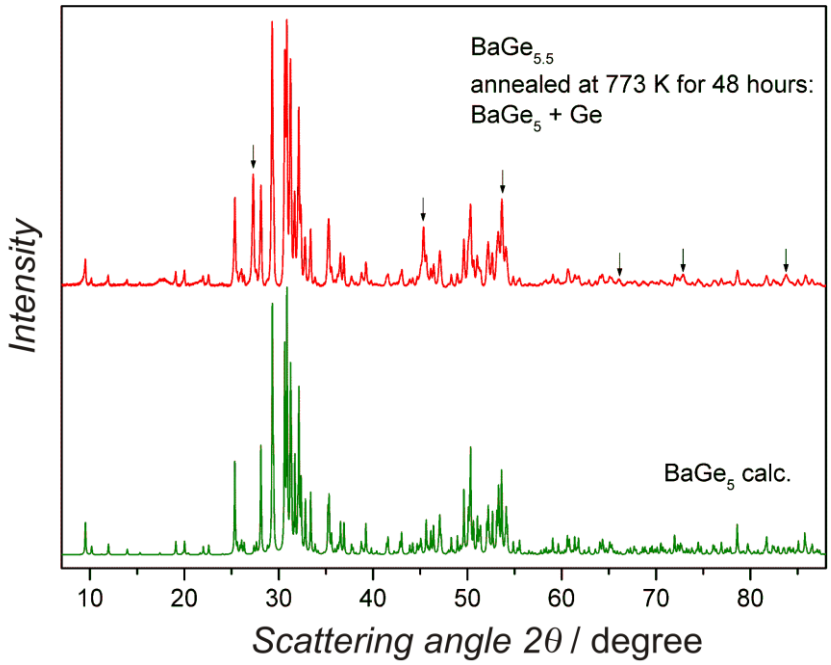

Figure 3.2.5 X-ray powder diffraction diagram (red lines) of the two-phase sample containing $BaGe_5$ and α-Ge as obtained by thermal decomposition of $BaGe_{6-x}$ (x = 0.5) at 773 K for 48 h. Reflections attributed to α-Ge are marked by arrows. The lower diagram shows the calculated diffraction pattern for the ambient pressure modification of $BaGe_5$ (green lines).

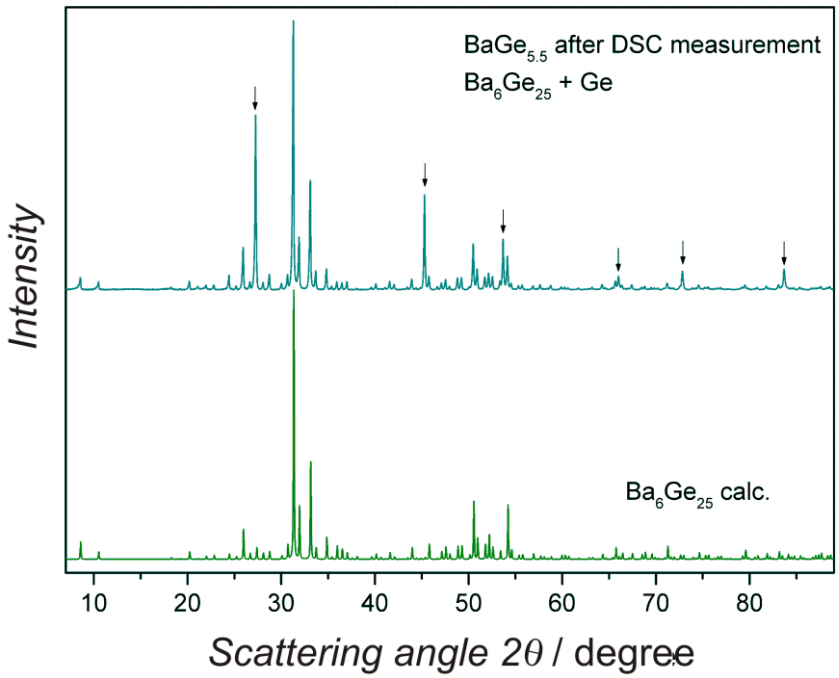

Figure 3.2.6 X-ray powder diffraction diagrams (top) of $BaGe_{6-x}$ after the heating and cooling cycle. The calculated diagram of Ba_6Ge_{25} is plotted (bottom) to identify the main phase. Additional lines correspond to Ge and are indicated by arrows (top).

3.2.2 Crystal structure of $BaGe_6$

Refinement of powder X-ray diffraction data using full profiles (Figure 3.2.7) evidences that $BaGe_6$ is isotypic to the binary silicon compounds MSi_6 (*M* = Ca, Sr, Ba; Eu) [24,33] and the ternary phase $EuGa_2Ge_4$ [34]. The atomic arrangement comprises three symmetry-independent four-bonded germanium atoms, which form infinite zig-zag chains along the [100] direction. These one-dimensional building units are interconnected to a three-dimensional network. The resulting tubular voids house the barium atoms. The shortest Ge – Ge distances from 2.48(4) to 2.63(3) Å within the network are consistent with the values usually observed in Ge-rich intermetallic compounds [38,39,36]. According to the Zintl concept, the electron balance of this connectivity pattern correspond to $BaGe_6$ = $[Ba^{2+}][(4b)Ge^0]_6 \times 2e^-$ revealing two excess electrons per formula unit. This is a quite remarkable finding since clathrates with germanium as majority component usually reveal chemical compositions which are charge balanced. Structural data of $BaGe_6$ are reported in Tables 5.4 – 5.6, in appendix.

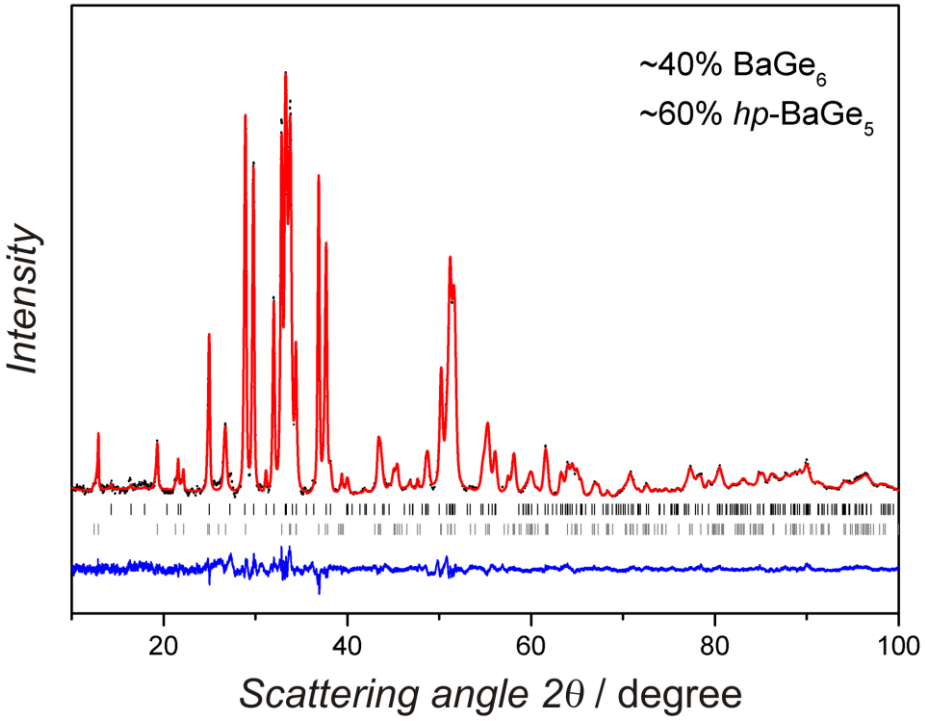

Figure 3.2.7 X-ray powder diffraction diagram (black points) of the two-phase sample containing $BaGe_5$ and $BaGe_6$ as obtained high-pressure high-temperature treatment of the sample $BaGe_{6-x}$ (x = 0.5) at 15 GPa and 1300 K. The calculated pattern is shown in red, the difference between computed and measured intensities in blue. Line positions of possible reflections are indicated by tick marks.

3.2.3 Crystal structure of $BaGe_{6-x}$

3.2.3.1 Commensurate approximation

For the germanium-poorer compound $BaGe_{6-x}$, the strongest X-ray diffraction reflections of single crystals indicate an orthorhombic unit cell which is similar to that of $BaGe_6$: *b* and *c* axis of $BaGe_{6-x}$ are larger by 4% and 3%, respectively, while the *a* axis is 12% shorter. However, long-time X-ray diffraction exposures around the substantially shorter [100] direction reveal a second set of reflections with lower

intensities (labelled as satellites in Figure 3.2.8). In first approximation, the positions of these extra spots are compatible with a seven-fold superstructure along [100].

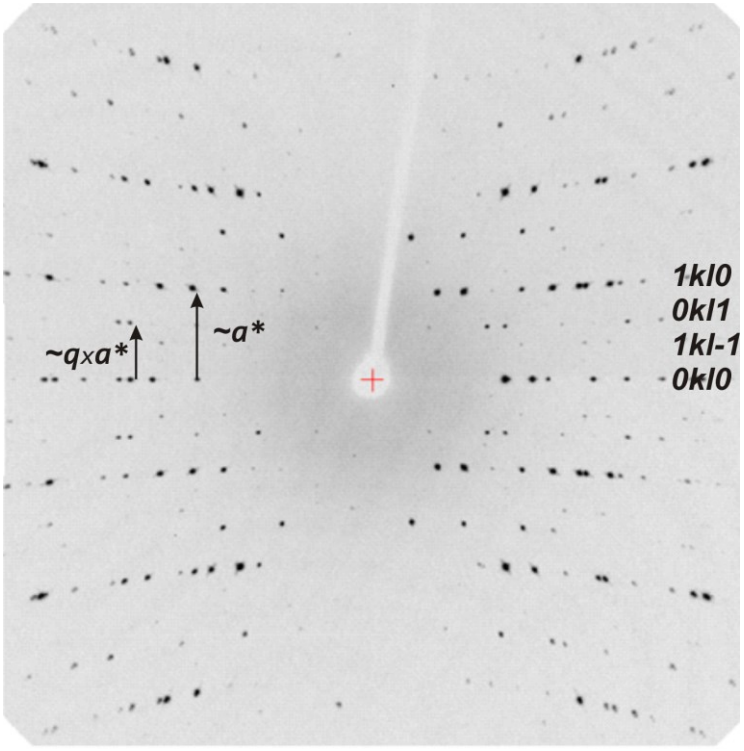

Figure 3.2.8 Axial oscillation photo around [100] of $BaGe_{6-x}$. The indexing refers to the structure description in 3+1 dimensions. Main reflections are marked as *0kl0* and *1kl0*, respectively; *0kl1* and *1kl-1* indicates satellite reflections.

The solution assuming a commensurate superstructure to the $BaGe_6$ motif succeeds in the composition Ba_7Ge_{39} and the space group $Cmc2_1$ (Tables 5.7 – 5.10). The projection along [010] shows that this atomic arrangement with composition Ba_7Ge_{39} provides characteristic defects at some Ge1 positions of the $BaGe_6$ motif plus displacements of the surrounding framework atoms (Figure 3.2.9). The majority of the germanium atoms establish four short contacts, but the species around the end of the chain fragments form only three short connections. Longer Ge – Ge contacts of these atoms amount to 3.017(9) Å and will not be considered here. In comparison to $BaGe_6$, the altered composition and the modified connectivity of the model for $BaGe_{6-x}$ results in a significant reduction of the electron excess according to $[Ba^{2+}]_{7/7}[(3b)Ge^{1-}]_{12/7}[(4b)Ge^{0}]_{27/7}\times 2/7e^{-}$.

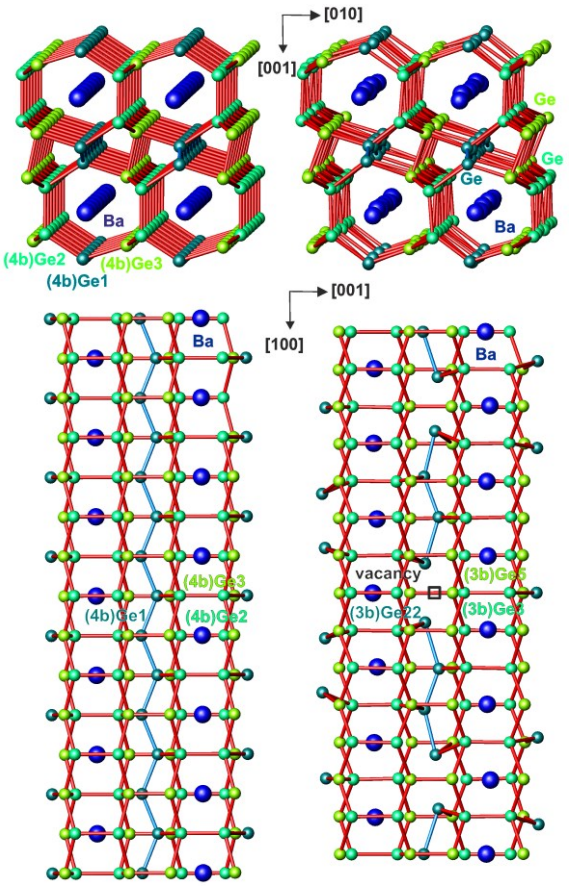

Figure 3.2.9 Crystal structures of $BaGe_6$ (left) and the commensurate model of $BaGe_{6-x}$ (Ba_7Ge_{39}, right). The germanium zig-zag chain of $BaGe_6$ which is fragmented in Ba_7Ge_{39} is shown in cyan. Other short Ge – Ge contacts are indicated red.

However, the three-dimensional description of $BaGe_{6-x}$ remains imperfect, e.g., with respect to the large range of displacement parameters resulting for the germanium atoms (Table 5.9). Moreover, the exact positions of the superstructure reflections diverge slightly from a commensurate periodicity which is another indication for the inadequacy of the commensurate model.

For advancing to a four-dimensional (3D + 1D) description of the modulation, single-crystal diffraction intensities of the substructure are assigned to indices of the type (*hkl0*) and the weaker superstructure reflections are interpreted as satellites of index (*hklm*) with $m = \pm 0, 1, 2, 3$. The reflections which are classified as observed comply with the additional extinction condition *hk0m*: *m* = 2n yielding the four-dimensional superspace [87] group *Cmcm*(α00)00s (Table 5.11).

For precise determination of lattice parameters and modulation vector, powder synchrotron X-ray diffraction data are analysed. With a^* being the reciprocal lattice vector of the substructure, the refined modulation vector correspond to $q = 0.5700(1)a^*$ in comparison to the value of $4/7a^*$ ($0.5714a^*$) for the identity period of the sevenfold commensurate supercell.

3.2.3.2 Incommensurate approximation

The crystal structure solution of the incommensurate model starts in the three-dimensional space group *Cmcm* using direct methods and the single-crystal X-ray diffraction intensities of the main reflections. Thorough analysis of the resulting $EuGa_2Ge_4$-like atomic pattern [34] reveals additional maxima of the difference electron density above and below the Ge1 position in [100] direction (Figure 3.2.10, top). Describing these features by introducing the additional germanium position Ge4, the modulation parameters are obtained by least squares refinements in the super-space group *Cmcm*(α00)00s using all reflections (including satellites up to 3. order). Refinements proceed by including atomic coordinates and their symmetry-allowed positional modulation amplitudes as well as the atomic displacement parameters in anisotropic approximation. At this stage, the symmetry-allowed occupational modulation amplitudes for the Ge1 and Ge4 position are included. The calculation range for the occupation modulation amplitudes are obtained from the distribution of the electron density in the (*x1,x4*) plane for the Ge1 and Ge4 positions (Figure 3.2.10, top and bottom, respectively).

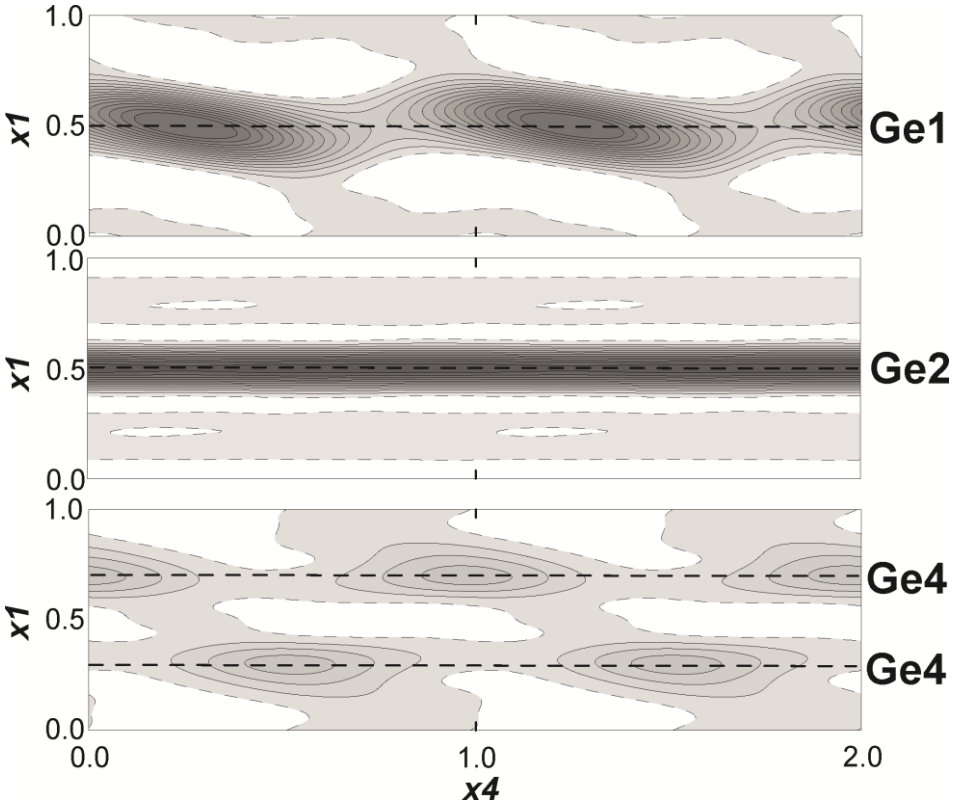

Figure 3.2.10 Difference electron density in the *x1,x4* plane for the positions Ge1, Ge4 (defect occupation, top and bottom, respectively) and – for comparison – Ge2 (full occupation, middle) in $BaGe_{6-x}$. The isolines are drawn with a step size of 25 e/Å. The dashed lines indicate the positions of the atoms Ge1 (x = 0.5, y = 0.7477, z = 0.5363), Ge2 (x = 0.5, y = 0.07334, z = 0.35026) and Ge4 (x = 0.5 $\pm$ 0.187, y = 0.7557, z = 0.5132).

For the least-squares refinements of the modulated crystal structure, the Crenel-function technique [88] is applied as implemented in the program package WinCSD [48]. Final refinements include atomic coordinates, their positional modulation amplitudes, atomic displacement parameters and

occupational modulation amplitudes (Tables 5.12 – 5.14). The refinement yields a residual value of R_F = 0.036, and the resulting interatomic distances (Figure 3.2.11) fall into the range from 2.346 Å to 2.861 Å. The total composition of the unit cell in non-commensurate description corresponds to $BaGe_{6-x}$ with x = 0.49, so that the incommensurate description resembles the electron-precise situation $[Ba^{2+}][(3b)Ge^{1-}]_{4x}[(4b)Ge^{0}]_{6-x}\times 0e^{-}$ (x = 0.5) within the experimental uncertainty.

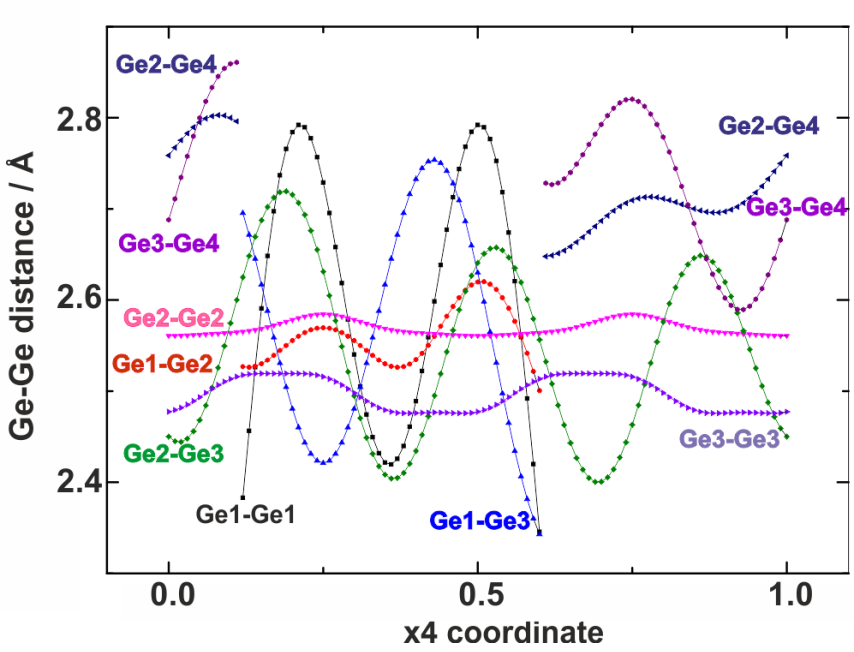

Figure 3.2.11 Ge – Ge distances in $BaGe_{6-x}$ (x = 0.5) as a function of the coordinate *x4*.

3.2.4 Chemical bonding and electronic structure in $BaGe_6$ and $BaGe_{6-x}$

The chemical bonding of $BaGe_6$ and $BaGe_{6-x}$ is characterized in direct space by quantum chemical calculations of the electron localizability indicator (ELI). Non-interacting atoms would exhibit spherical symmetry of the ELI distribution while variations, especially in the valence region, are fingerprints of atomic interactions, i.e., covalent bonds or lone pairs. The ELI distribution in $BaGe_6$ reveals that the 6th shell of Ba is basically not visible (Figure 3.2.12, top). This finding is attributed to a substantial charge transfer from barium to the electronegative germanium framework. Around the germanium atoms, five ELI-D attractors are observed. Four of these, which are located close to the shortest Ge – Ge contacts, visualize covalent interactions of the germanium atoms. Beside these four attractors, additional maxima are found for each germanium atom (red in Figure 3.2.12, bottom). Such features are absent in the corresponding ELF distribution of the isotypic electron-precise compounds $EuGa_2Ge_4$ [34]. Thus, these features are assigned to the electron excess of $BaGe_6$.

The ELI-D distribution in Ba_7Ge_{39} (as a commensurate model for $BaGe_{6-x}$) reveals essentially the same charge transfer from barium to the germanium framework as in $BaGe_6$ (Figure 3.2.13, top). Only four ELI-D attractors are observed around each germanium atom (Figure 3.2.13, bottom). Most of these are located close to Ge – Ge contacts visualizing two-centre bonds. However, some of the attractors are monosynaptic, i.e. their basins contact only the core basin of one germanium atom, thus visualizing three-bonded germanium atoms with lone-pair-like features.

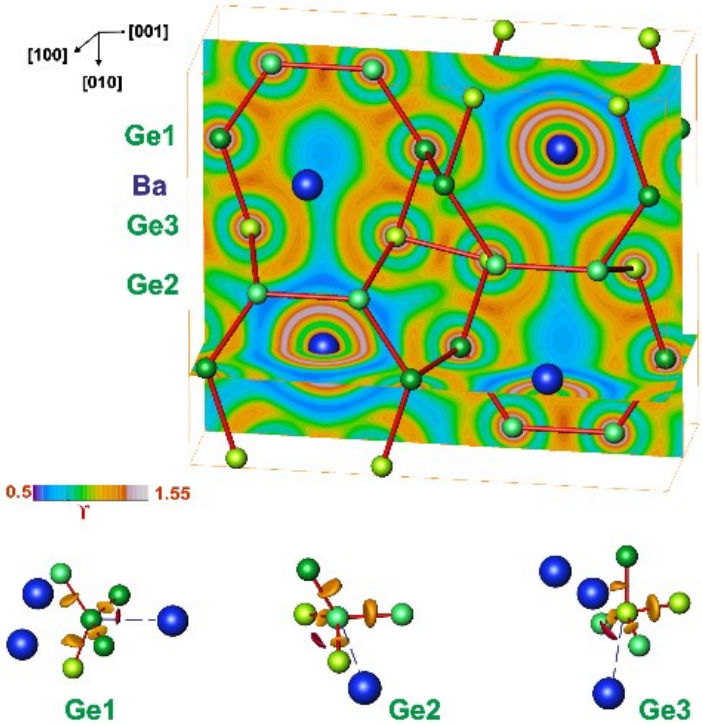

Figure 3.2.12 Electron localizability indicator (ELI-D) in $BaGe_6$: (top) distribution in planes perpendicular to the directions [100] and [010]; (bottom) isosurfaces around the germanium atoms.

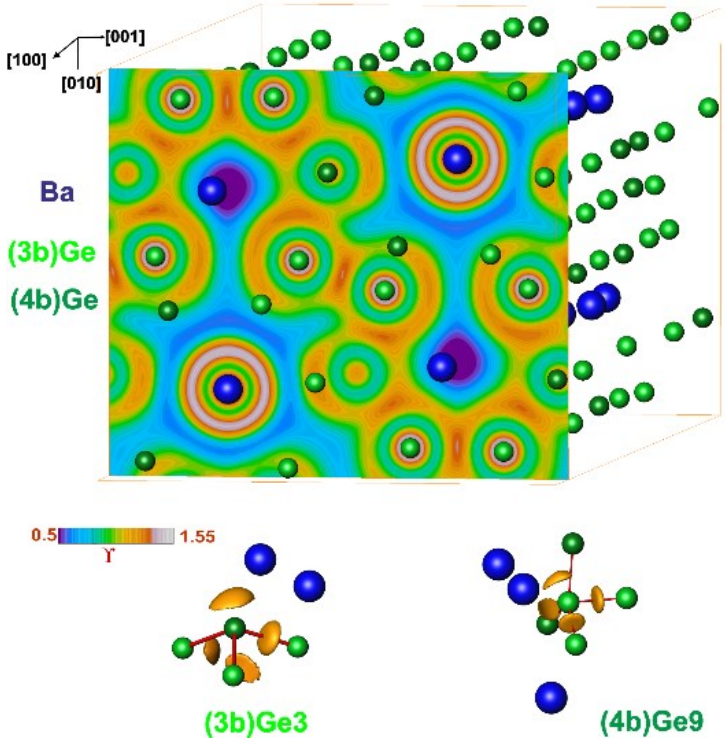

Figure 3.2.13 Electron localizability indicator (ELI-D) in Ba_7Ge_{39} as a commensurate model for $BaGe_{6-x}$: (top) distribution in the plane perpendicular to [100]; (bottom) isosurfaces around a selected three- (left) and four-bonded (right) germanium atom, respectively. The numbering of the germanium atoms refers to that of Table 5.8.

The electronic density of states (DOS) for $BaGe_6$ reveals a high density of states at the Fermi level and a rudimentary pseudogap at E ≈ -0.6 eV (Figure 3.2.14, top). The top of the valence band is mainly formed by Ge(p) states, and more than half of these are contributed by Ge1, implying the important role of these atoms in the electrical conductivity of the compound.

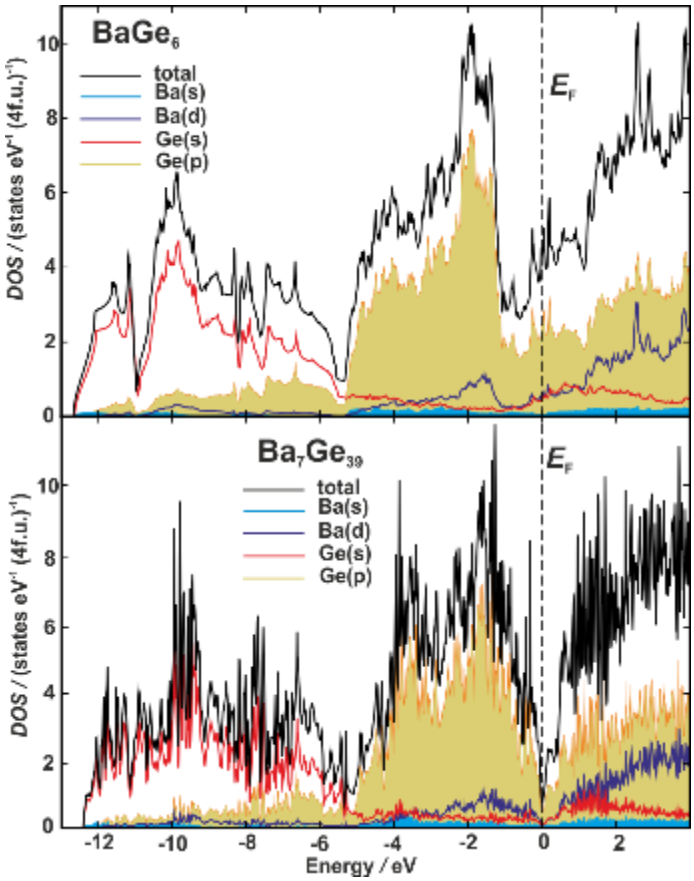

Figure 3.2.14. Electronic density of states for $BaGe_6$ (top) and the commensurate model of $BaGe_{6-x}$ (Ba_7Ge_{39}, bottom). The DOS of $BaGe_{6-x}$ is scaled to one Ba atom as in $BaGe_6$, i.e., one formula unit of Ba_7Ge_{39} is renormalized to $Ba_{7/7}Ge_{39/7}$ or $BaGe_{5.57}$.

The formation of defects in $BaGe_{6-x}$ (Ba_7Ge_{39}) does not only shift the Fermi level to lower energies, but opens also a pronounced pseudo-gap by reducing the DOS around the Fermi level by a factor of three in comparison to $BaGe_6$ (Figure 3.2.14, bottom). These changes close to E_F are in full accord with a substantial reduction of the electron excess by the vacancy formation.

3.2.5 Physical properties

3.2.5.1 Magnetic susceptibility

In agreement with the observed systematics of the electronic density of states, the high-field magnetic susceptibility $\chi(T) = M/H$ of $BaGe_{6-x}$ (Figure 3.2.15) is negative indicating diamagnetic behavior. The

value χ_0 of -120(10)×10^{-6} emu mol^{-1} at T = 0 is in fair agreement with the sum of the diamagnetic increments which results in -90×10^{-6} emu mol^{-1} for $BaGe_{6-x}$ (x = 0.5). These results evidence diamagnetic, and thus, semiconducting behaviour of the Ge-deficient sample.

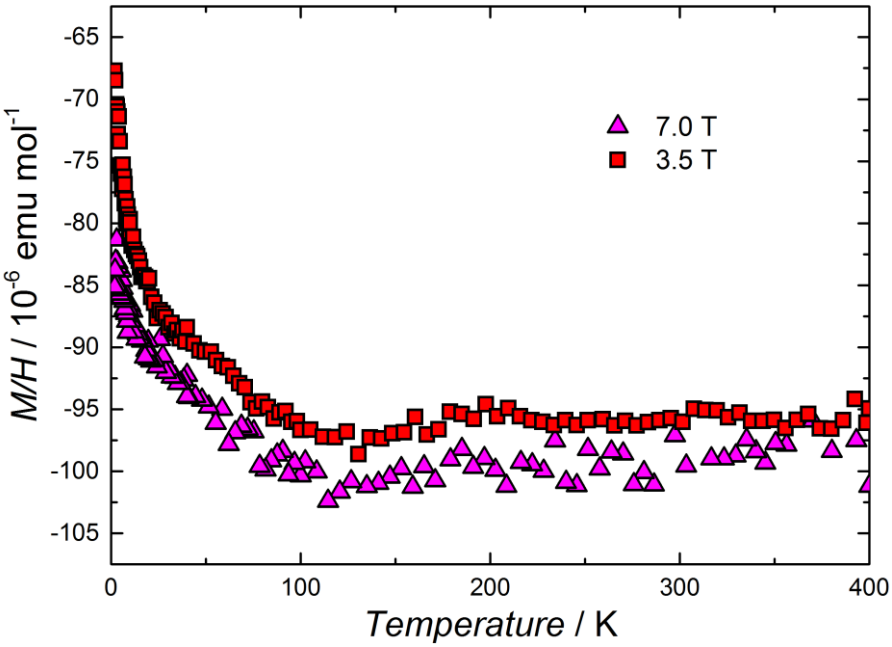

Figure 3.2.15 Molar magnetic susceptibility of $BaGe_{6-x}$ vs temperature, at high magnetic fields.

3.2.5.2 Electronic and thermal transport

Consistently, the electrical resistivity $\rho(T)$ decreases slightly and almost linearly with temperature (Figure 3.2.16, a) indicating a semiconducting characteristic. The high absolute value indicates a strongly doped (defects, impurities) semiconductor with the result that also the Seebeck coefficient S_{300K} is reduced to a value of 10 μVK^{-1} which would be more typical for a metallic conductor (Figure 3.2.16, b). The thermal conductivity $\kappa(T)$ of the modulated framework ensemble (κ_{300K} = 1.7 $Wm^{-1}K^{-1}$) is low (Figure 3.2.16, c) and of the typical order found in cage compounds, e.g., clathrates like $Ba_8Ni_{3.5}Ge_{42.1}\square_{0.4}$ (□ represents a vacancy) [82]. The resulting thermoelectric figure of merit, $ZT = S^2 \times T/(\kappa \times \rho)$ remains small because the effects caused by the high charge-carrier concentration clearly overcompensate the beneficial contribution of the low thermal conductivity (Figure 3.2.16, d).

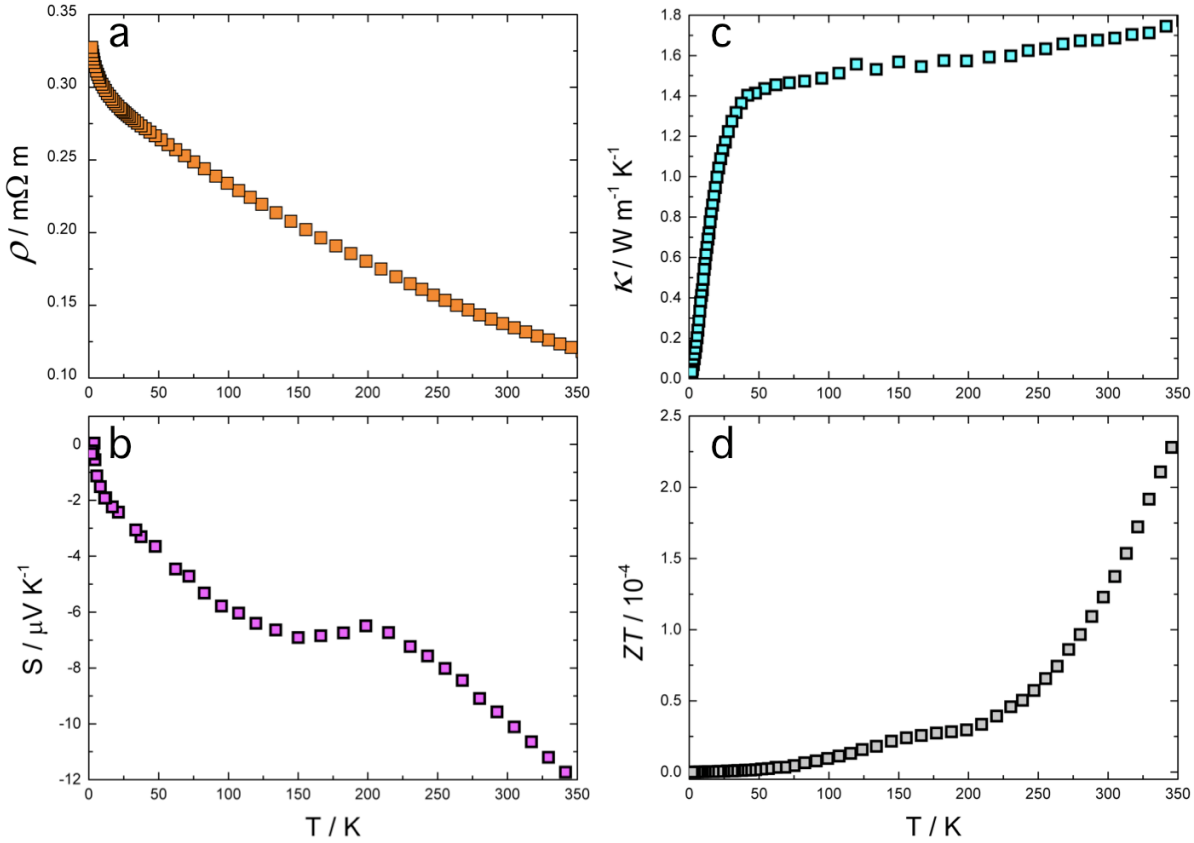

Figure 3.2.16. Electronic and thermal transport properties of $BaGe_{6-x}$ at temperatures between 2 K and 353 K.

3.2.6 Conclusions

The crystal structures of $BaGe_6$ and $BaGe_{6-x}$ (x = 0.5) exhibit a clear interdependence of network topology and electron balance. $BaGe_6$ features four-bonded framework atoms and a surplus of electrons, a situation more frequently observed for silicon-rich compounds [24a, 33]. In $BaGe_{6-x}$, those germanium atoms which engird the defects are three-bonded. The simultaneous localization of excess electrons in lone pairs provides efficient electron traps and, thus, an effective decoupling of electrical and thermal conductivity. Although similar phenomena have already been observed in phases like the structurally related $SrGe_{5.5}\square_{0.5}$ [85] or type-I clathrates like $K_8Ge_{44}\square_2$ [89], the arrangement of defects normally preserves conventional three-dimensional symmetry. The unique feature of $BaGe_{6-x}$ is that the requirements for an electron-precise phase according to the *8 – N* and the Zintl concept are fulfilled by the formation of lattice defects exhibiting incommensurate modulations of atomic positions and site occupation.

3.3 *hp*-$BaGe_5$

At ambient pressure, $BaGe_5$ is obtained via decomposition of Ba_8Ge_{43} at low temperature. It crystallizes in the orthorhombic space group *Pnma* (no. 53) with lattice parameters *a* = 10.727(1), *b* = 9.2844(7), *c* = 14.794(1) and represents a new type of intermetallic clathrate. Because of the unique manner to obtain this phase, it was not possible to grow single crystals and the structure solution was performed by applying direct methods on powder X-ray diffraction data. Since the powder pattern comprises a huge number of lines exhibiting significant overlap, the space group was determined with the aid of electron diffraction data [86].

The present chapter introduces, a new high-pressure modification of $BaGe_5$, from now on referred as *hp*-$BaGe_5$, which was observed in attempts to synthesize $BaGe_6$. Later it was successfully obtained as a phase pure material and fully characterized.

3.3.1 Preparation and chemical composition

The precursor samples with nominal composition Ba_6Ge_{25} were prepared by induction melting of a stoichiometric mixture of the high-purity elements (see Table 2.1) in sealed tantalum ampoules. Around 40 mg of the stoichiometric mixture Ba_6Ge_{25} + 5Ge were loaded into the *BN*-crucible and subject to different conditions of high-pressure and high-temperature. Optimal pressure and temperature ranges for the formation of *hp*-$BaGe_5$ were found to be at 15 (2) GPa and between 900(90) K and 1200(120) K, respectively, as indicated by x-ray powder diffraction experiments. In Figure 3.3.1 powder patterns of products synthesised at different pressures are shown.

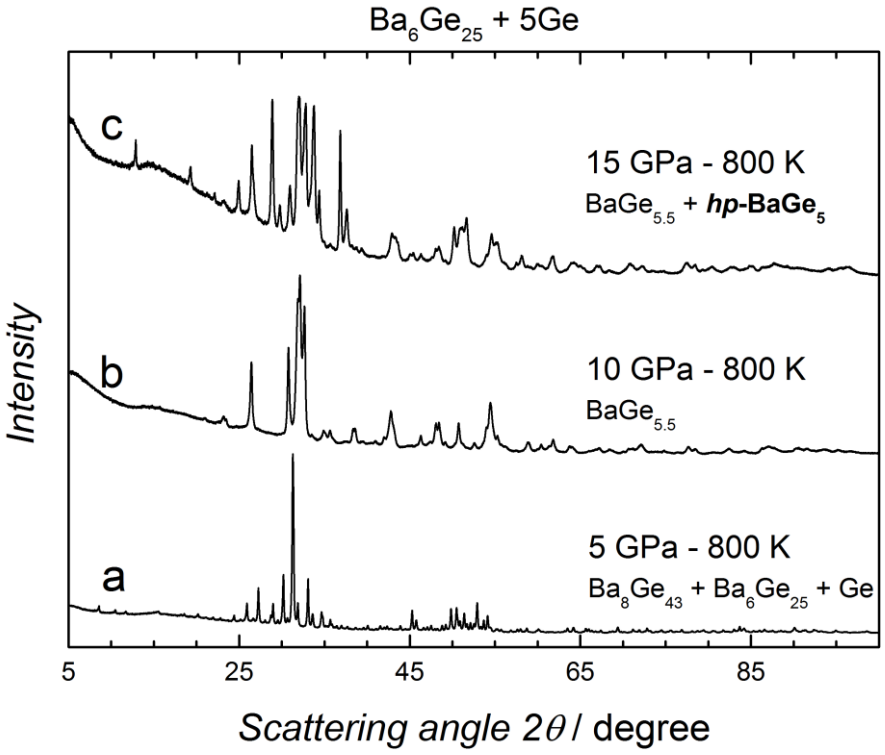

Figure 3.3.1 Powder x-ray diffraction patterns of mixtures Ba_6Ge_{25} + 5Ge, subject to different pressures at constant temperature.

They evidence that the new phase is obtained at 15 GPa. Once the pressure was determined, different conditions of temperature were tried, as shown in Figure 3.3.2. The chosen synthesis conditions for sample production were set to 15 GPa and 1100 K. Because of the reflection overlap, indexing of the powder diffraction pattern was not possible and therefore, a TEM study started.

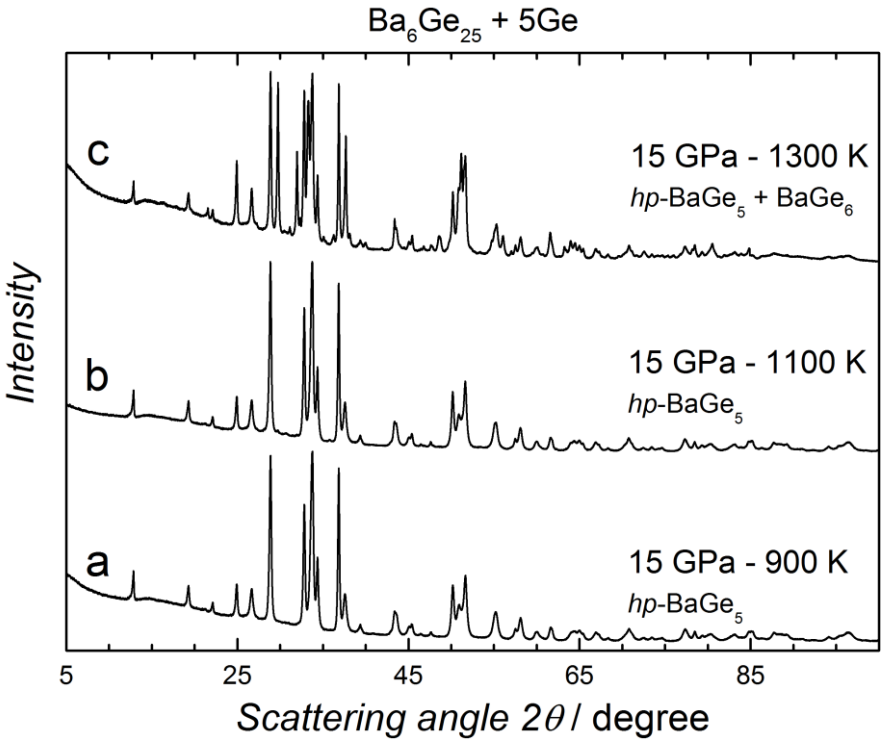

Figure 3.3.2 Powder x-ray diffraction patterns of mixtures Ba_6Ge_{25} + 5Ge, subject to different temperatures at constant pressure.

Optical inspection of a polished sample revealed a single phase, as shown in Figure 3.3.3. Wavelength-dispersive X-ray spectroscopy measurements on the specimen indicate the composition $Ba_{0.9(1)}Ge_{5.1(1)}$ which corresponds within experimental uncertainty to the ratio Ba:Ge of 1:5.

3.3.2 TEM study and indexing

Focused ion beam (FIB) is a unique technique for preparing thin cross-sections with defined crystallographic orientations in small particles or grains, which is difficult to achieve with other techniques, in particular for the materials which easily deform mechanically, as in the present case. The observable main cleavage plane (010) of *hp*-$BaGe_5$ facilitated the orientation procedure for the FIB cuts.

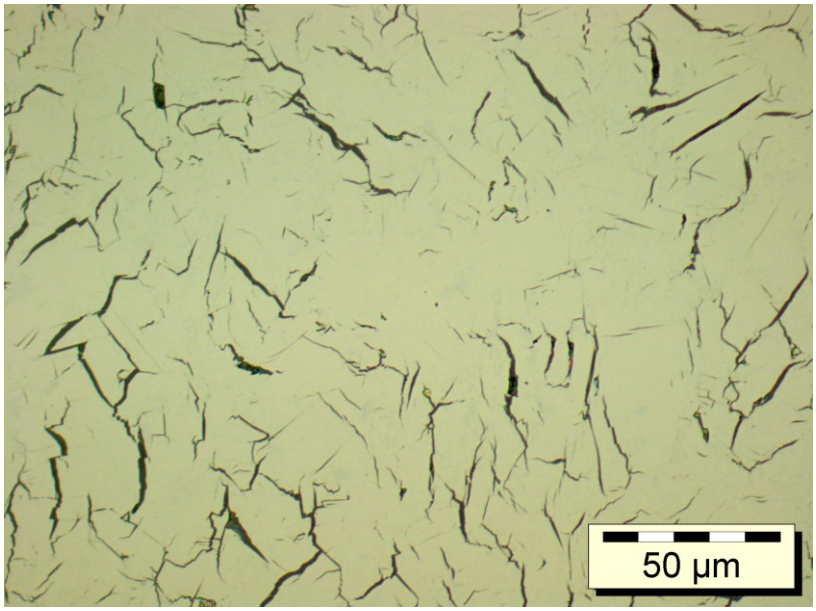

Figure 3.3.3 Optical microscopy image (bright-field) of the *hp*-$BaGe_5$ sample prepared at HPHT conditions, showing a single phase with composition $BaGe_5$. The black sections are cracks formed during the preparation for metallography.

A preliminary transmission electron microscopy experiment reveals diffuse diffraction patterns of the powdered particles indicating mechanical deformation of crystallites. Therefore, two specimens for TEM study were prepared by the FIB cutting. Thin cross-sections were prepared by FIB using an FEI Quanta 200 3D dual beam (SIM/SEM) device (FEI, Germany) equipped with an *Omniprobe* micro-manipulator. For this purpose, a piece of the bulk material was attached with conductive glue on an aluminum SEM holder with the cleavage surface at the top. One cut was prepared perpendicular to the [010] plane. For electron diffraction tomography, a second slice was cut. A protective layer of platinum with a thickness, height and length of about 1.5 µm, 2 µm and 20 µm, respectively, was deposited on the selected region with both cuts using an accelerating voltage of 30 kV and a current of 0.1 nA. Each cross-section (1.5 mm thickness) was cut by applying a Ga ion beam using an acceleration voltage of 30 kV and a current of 5–0.5 nA. The prepared thin cut was transfered onto a copper *Omniprobe* TEM holder using the in situ lift-out technique [90]. After the lift-out, the cross-section was thinned down to a thickness of about 60 nm (by applying an acceleration voltage of 30 kV with currents of 1–0.01 nA of the Ga ion beam (Figure 3.3.4).

Electron diffraction tomography analysis was carried out on the FIB-manufactured specimens. A thin region of a crystal (slice 2, cf. above, thickness ca. 60 nm) was chosen for data acquisition. The crystal area selected filled the full aperture area (diameter of about 440 nm; Figure 4b). The electron diffraction tomography study suggested a body-centered orthorhombic structure with approximate lattice parameters a = 8.3 Å, b = 4.8 Å, c = 13.8 Å, $\alpha = \beta = \gamma \approx 90°$ (see Figures 5a-c), determined without symmetry restrictions. After indexing the spots of reciprocal space, the intensities were integrated and stored as standard *hkl* files (582 measured of which 201 are symmetry independent reflections). Final lattice parameters (Table 5.15) were obtained by refinement of X-ray powder diffraction data employing LaB_6 as internal standard.

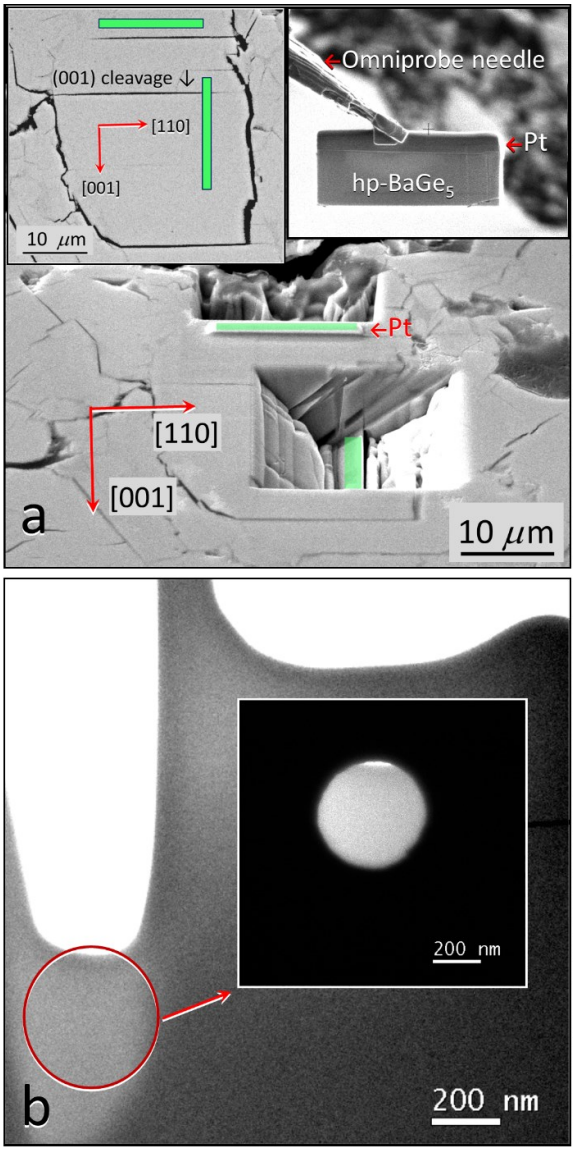

Figure 3.3.4 (a) SEM images of *hp*-BaGe$_5$ (metallographic sample), showing the positions of two oriented FIB cross-sections (marked green) parallel or perpendicular to the (001) cleavage fracture. The top inserts show the metallographic surface before the focussed ion beam (FIB) experiment (left) and one lift-out cross section (right). (b) TEM image of the FIB cut, showing the SAED region used for electron diffraction tomography. The insert shows the same region with the SAED aperture.

3.3.3 Crystal structure

Extinction conditions were derived from the SAED patterns (Figures 5.5 d-f) and are in agreement with space groups *Imma*, *I2ma* or *Im2a*: *0kl*, *k+l = 2n*; *h0l*, *h+l = 2n*; *hk0*, *h*, *k = 2n*; and *hkl*, *h+k+l = 2n*. The centrosymmetric space group *Imma* was chosen for crystal structure solution using the SIR2011 program [91], on basis of the 3D electron diffraction intensity data of 211 symmetry independent reflections and refined with the Shelx software [53]. The value for the residual *R* amounts to 0.31. This value is relative high but normal for raw electron diffraction data [92].

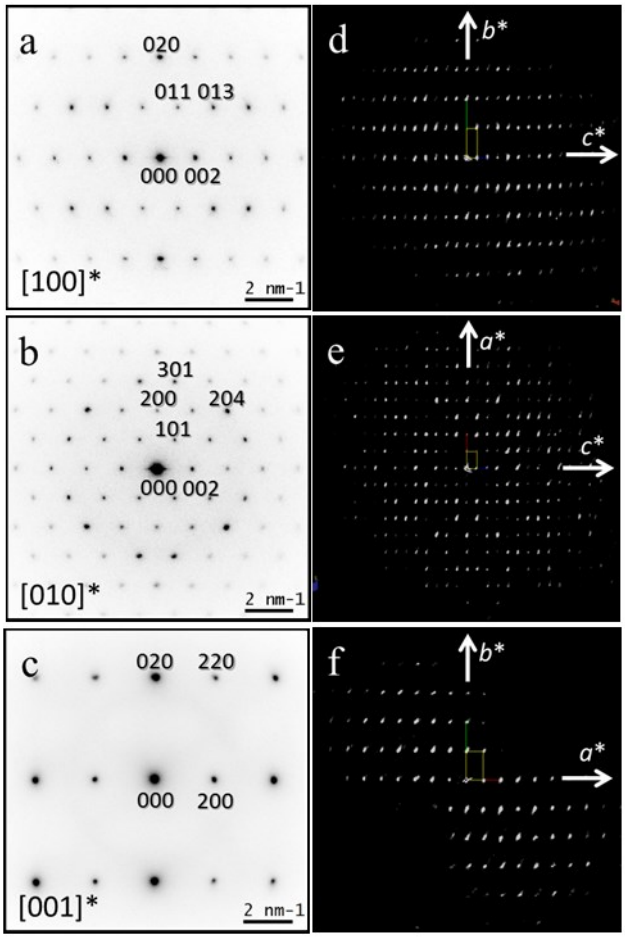

Figure 3.3.5 Electron diffraction of *hp*-$BaGe_5$: SAED images along [100]* (a), [010]* (b) and [001]* (c) directions; projections of the 3D diffraction patterns (reciprocal volume) along [100]* (d), [010]* (e) and [001]* (f) directions used for crystal structure determination.

The structure model was finally refined using the Rietveld method on basis of high-resolution X-ray powder diffraction synchrotron data (Figure 3.3.6).

Refined lattice parameters, atomic coordinates and displacement parameters in isotropic description are listed in Tables 5.15 and 516. Selected interatomic distances are in Table 5.17 and the crystal structure is shown in Figure 3.3.7.

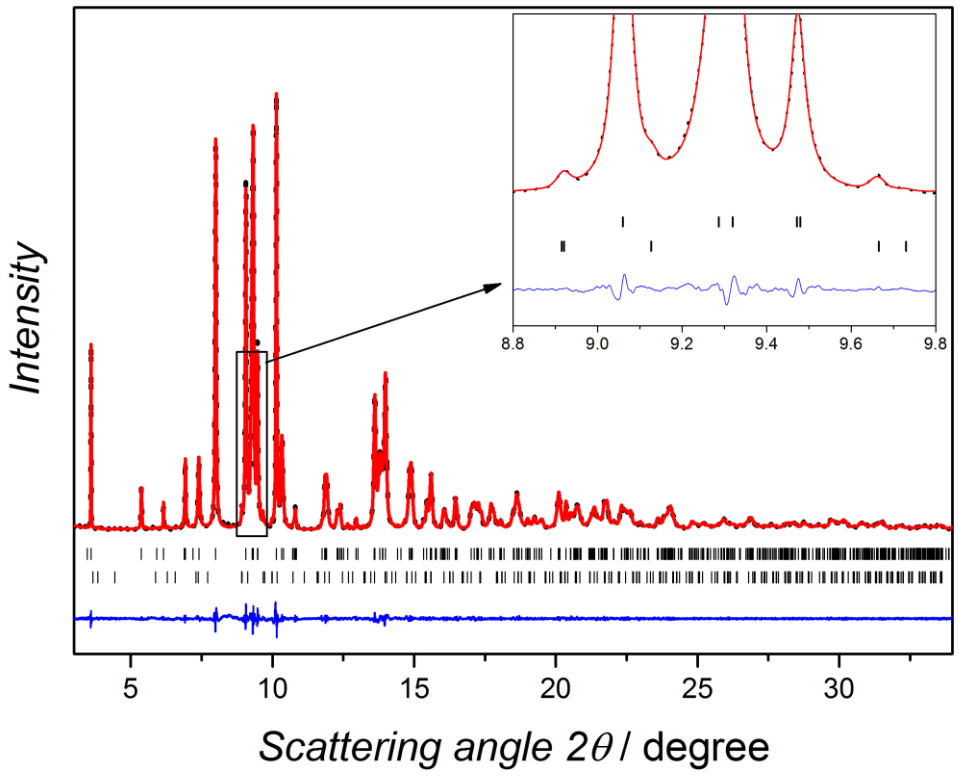

Figure 3.3.6 Rietveld refinement performed on synchrotron X-ray powder diffraction data (λ = 0.43046 Å). Reflection positions are marked by vertical ticks (upper row: *hp*-$BaGe_5$, bottom row: $BaGe_3$ (3 mass%, $CaGe_3$-type crystal structure), the observed intensities are displayed as black points, the calculated pattern as a red curve. The differences between observed and calculated intensities are shown in blue. Selected reflections of the minority phase $BaGe_3$ are visualized in detail in the inset.

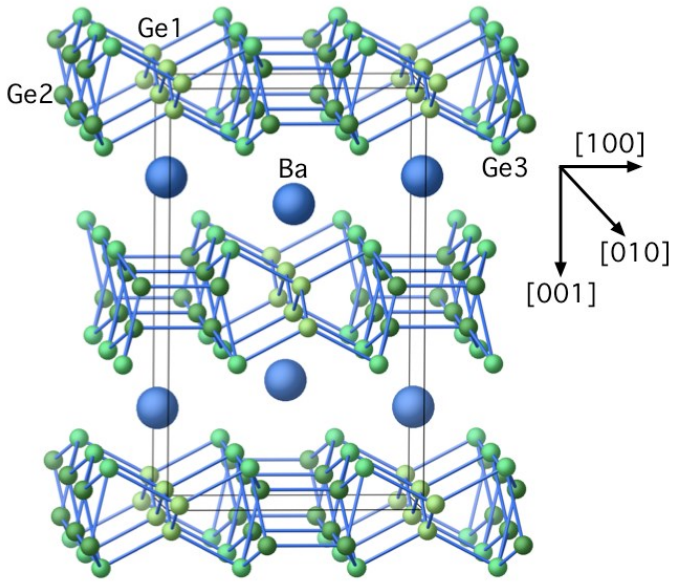

Figure 3.3.7 Crystal structure of *hp*-$BaGe_5$ in a view along [010] showing interatomic distances up to 2.68 Å within the germanium layer.

Two-dimensional slabs of Ge atoms are separated by corrugated layers of the barium atoms, revealing a pronounced anisotropy of the crystal structure. The germanium layers contain six-membered rings, one of them in boat conformation with four Ge atoms forming the base and two independent Ge3 atoms shape the *fore* and *aft*. These rings are interconnected to double chains oriented along the [010] axis. Condensation via the Ge1 zig-zag chains along [010] axis results in double layers perpendicular to the *c*-axis. In this manner, all germanium atoms adopt four short Ge-Ge distances. Ge1 is coordinated in form of a distorted tetrahedron (2 × *d*(Ge1-Ge3) = 2.5933(6) Å and 2 × *d*(Ge1-Ge1) = 2.6690(5) Å). Ge2 shows also four short distances within an tetrahedron (1 × *d*(Ge2-Ge2) = 2.5600(7) Å + 1 × *d*(Ge2-Ge3) = 2.6080(7) Å + 2 × *d*(Ge2-Ge3) = 2.6843(4) Å) with two additional longer distances [*d*(Ge2–Ge2) = 2.9049(5) Å]. Finally, Ge3 forms an irregular coordination polyhedron derived from a ψ-pyramid (1 × *d*(Ge3-Ge1) = 2.5933(6) Å + 1 × *d*(Ge3-Ge2 = 2.6080(7) Å + 2 × *d*(Ge3-Ge2) = 2.6843(4) Å). The latter two atoms exhibit a pronounced similarity of the interconnection patterns to the Al and Ge atoms in β-BaAl$_2$Ge$_2$ [93] (Figure 3.3.8, left). The coordination polyhedron of the Ba atoms can be described as intermediate between β-BaAl$_2$Ge$_2$ and BaGe$_6$, as depicted in Figure 3.3.8.

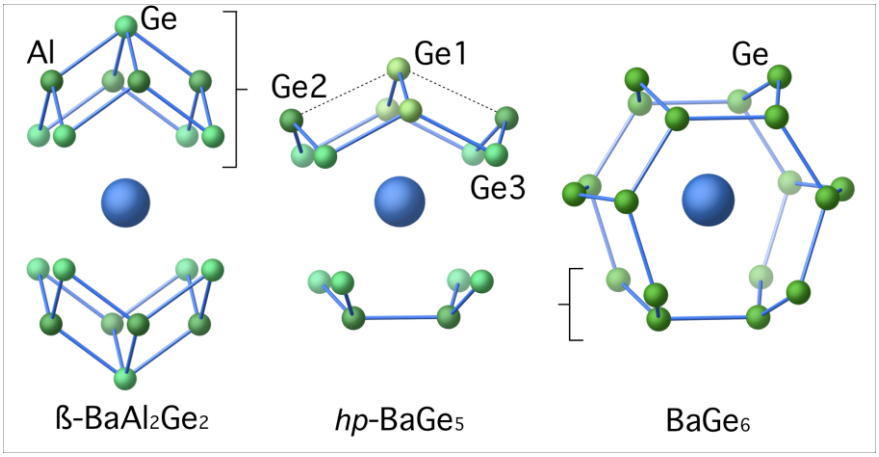

Figure 3.3.8 Coordination polyhedral of Ba (blue sphere) in β-BaAl$_2$Ge$_2$ (left), *hp*-BaGe$_5$ (middle) and BaGe$_6$ (right). The asymmetric environment of the Ge3 atom in *hp*-BaGe$_5$ is similar to that of Ge found in β-BaAl$_2$Ge$_2$. The coordination polyhedron of Ba in *hp*-BaGe$_5$ contains fragments of both, β-BaAl$_2$Ge$_2$ and BaGe$_6$.

3.3.4 Thermal behavior

The thermal behavior investigated by DSC measurement revealed three exothermic effects with onset temperatures of 469, 573.5, and 676.6 K in the heating curve (Figure 3.3.9).

The first exothermic effect is assigned to a transition to a new, hitherto uncharacterized phase with a composition close to BaGe$_5$. Since this effect is irreversible and exothermic, the new *hp*-BaGe$_5$ is a metastable high-pressure phase. The second exothermic effect represents the decomposition into a mixture of Ba$_8$Ge$_{43}$ and Ba$_6$Ge$_{25}$, and the third exothermic effect indicates reaction of the clathrate mixture yielding the ambient pressure modification BaGe$_5$. On further heating, the thermal behaviour corresponds to that of ambient pressure BaGe$_5$ [86] and consists of three endothermic effects occurring at 866, 1046 and 1082 K. These are attributed to the transformation of BaGe$_5$ into Ba$_6$Ge$_{25}$ and Ge, the formation of Ba$_8$Ge$_{43}$ and finally the peritectic decompositions of Ba$_8$Ge$_{43}$ into Ge and the

corresponding melt, respectively. Figure 3.3.10 shows the powder x-ray patterns of all obtained products.

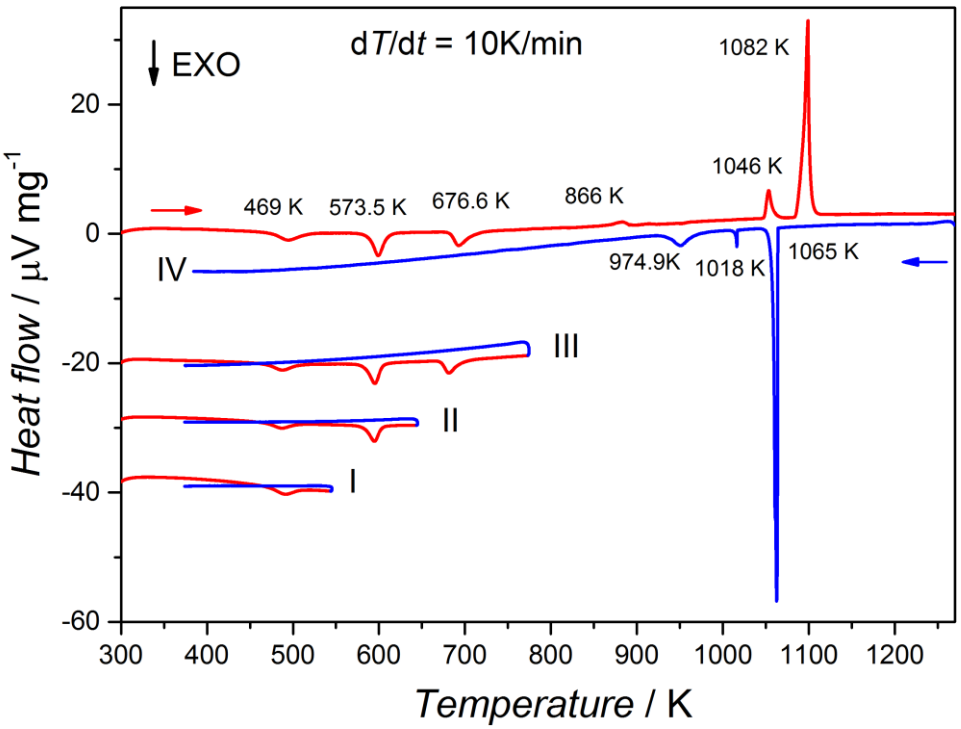

Figure 3.3.9 Thermal behaviour of *hp*-$BaGe_5$ in different temperature ranges. Heating is indicated by red and cooling by blue lines.

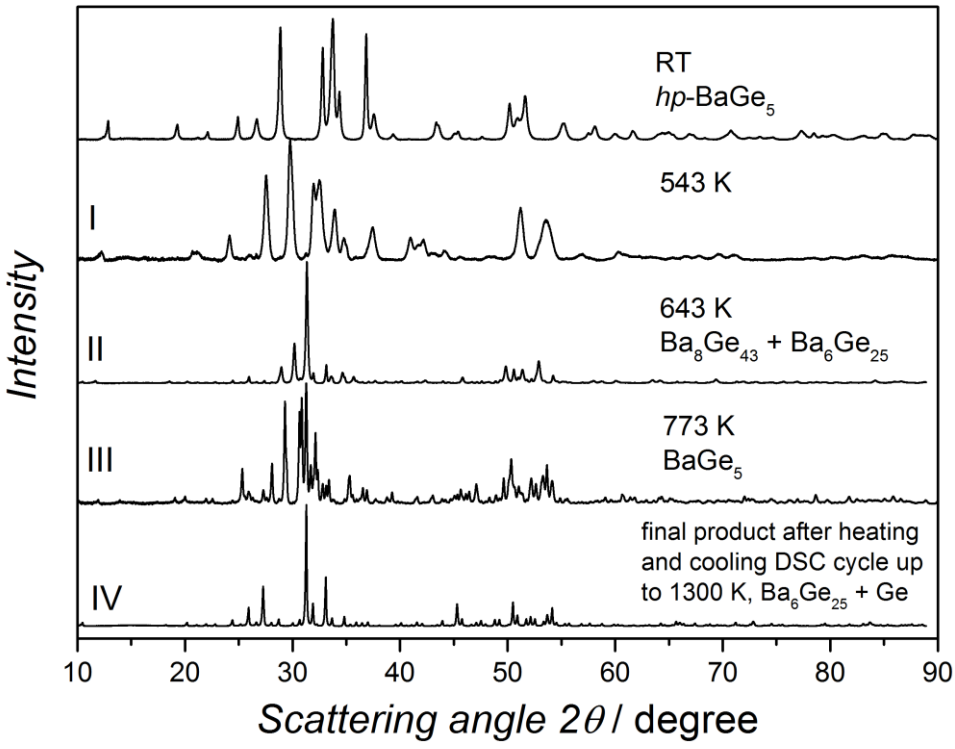

Figure 3.3.10 X-ray powder diffraction patterns of *hp*-$BaGe_5$ and its decomposition products obtained by DSC measurements. The labelling (I – IV) corresponds to the thermal cycles indicated in Figure 3.3.9.

3.3.5 Chemical bonding analysis

Details of the organization of chemical bonding in *hp*-BaGe$_5$ were obtained from the analysis of atomic interactions in real space within the electron localizability approach. Integration of the electron density within atomic basins - defined in accordance with the QTAIM technique [59] - yields effective charges amounting to Ge1$^{0.28-}$, Ge2$^{0.16-}$, Ge3$^{0.28-}$, and Ba$^{1.16+}$ (Figure 3.3.11) with the average charge on a germanium atom of -0.24. Assuming a complete transfer of the Ba valence electrons to the Ge substructure, a balance [Ba^{2+}][Ge$^{0.4-}$]$_5$ would be expected. The finding of experimental charges being significantly smaller than those calculated on basis of the complete ionic balance given above indicates that charge transfer represents only part of the atomic interactions which are responsible for the bonding organization in *hp*-BaGe$_5$.

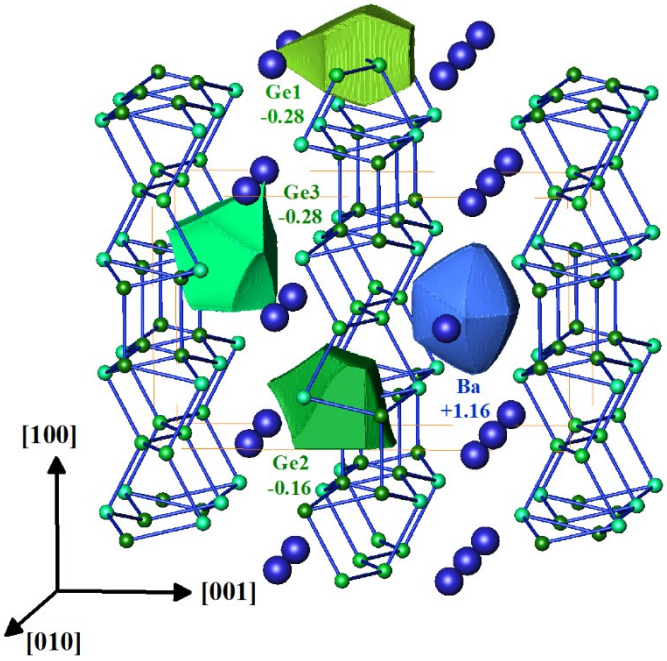

Figure 3.3.11 QTAIM atoms and their effective charges in *hp*-BaGe$_5$.

Assuming that the crystal structure obeys the Zintl-Klemm concept, a framework containing solely four-bonded tetrel atoms does not require additional electrons for its stabilization. A clear example of such electronic counting reveals the (*cF*136) modification of Ge [94]. Even containing large voids, the clathrate-II-type Ge framework □$_{24}$Ge$_{136}$ exists also without the filler atoms because of the full electronic balancing: [(4b)Ge^0]$_{136}$ = [(4b)Ge^0]$_8$[(4b)Ge^0]$_{32}$[(4b)Ge^0]$_{96}$. Introducing additional electrons into similar clathrate-II-type framework is completely or partially compensated by formation of the defects within the framework, the neighbouring atoms are three-bonded: K$_8$Ge$_{44}$ = [K^{1+}]$_8$[(3b)Ge^{1-}]$_8$[(4b)Ge^0]$_{36}$□$_2$ [95], and Ba$_8$Ge$_{43}$ = [Ba^{2+}]$_8$[(3b)Ge^{1-}]$_{12}$[(4b)Ge^0]$_{31}$□$_3$ × 4e [96], respectively. An alternative way is presented in the ambient pressure modification of BaGe$_5$ = [Ba^{2+}][(3b)Ge^{1-}]$_2$[(4b)Ge^0]$_3$ [86] or in Ba$_6$Ge$_{25}$ = [Ba^{2+}]$_6$[(3b)Ge^{1-}]$_8$[(4b)Ge^0]17 × 4e- [97], where a part of Ge atoms become three-bonded just by the topology of the framework without vacancy formation. The high-pressure modification of BaGe$_5$ represents the third way adapting a four-bonded Ge framework to the presence of excess electrons. This is visualized by the analysis of the electron localizability indicator.

The distribution of ELI-D (Figure 3.3.12, top) in the vicinity of Ba is non-spherical and shows structuring in the 5th shell which indicates participation of these electrons (5d) in the bonding interactions. Furthermore, ELI-D reveals maxima between the Ge atoms and their closest neighbours. Four maxima on Ge1-Ge contacts confirm its four-bonded character derived from the interatomic distances (Figure 3.3.12, bottom left). The ELI-D around Ge2 shows five attractors (Figure 3.3.12, bottom middle), four of them are located close to the Ge2-Ge contacts and have populations between 0.7 and 1.7 electrons. The fifth one is located within the quadrangle Ba-Ge3-Ge2-Ge3-Ba in direction to the second next Ba neighbour and indicates a lone-pair-like interaction between Ge2 and Ba. Despite the 5th shell of Ba is structured in the direction of this attractor (Figure 3.3.12 top), the lone-pair character of the interaction predominates, as indicated by the finding that the basin of this attractor is by more than 95% located within the atomic basin of the Ge2 atom. Following the four short Ge-Ge distances, the ELI-D distribution around Ge3 (Figure 3.3.12, bottom right) has five maxima, four on the Ge-Ge contacts or close to them, and the fifth one – similarly to Ge2 – in direction of the closest Ba atom, indicating again a lone-pair-like interaction in this region of the crystal structure. The lone-pair character of this interaction is even more pronounced than that of Ge2: the basin is located completely within the QTAIM basin of Ge3.

The disynaptic attractors on the Ge1–Ge contacts are well in agreement with four-bonded tetrel atom. This is supported by the integration of the electron density in the bonding basin yielding 3.8 electrons per Ge1 atom ($Ge^{+0.2}$), i.e. being close to the count for Ge^0 and having in good approximation 2c-2e bonds in this part of the crystal structure. Integrating the electron density within the bonding basins on the Ge2–Ge contacts yields 4.2 electrons per Ge atom ($Ge^{-0.2}$). The same operation for the Ge3-Ge contacts yields 5.05 electrons per Ge atom ($Ge^{-1.05}$). Thus the atoms Ge1 and Ge2 with the tetrahedron-like homoatomic coordination have the expected electron counts close to Ge^0; the Ge3 atom with one clear lone-pair is roughly Ge^{-1}, yielding the electron balanced: $[Ba^{+2}][(4b)Ge1^0][(4b)Ge2^0]_2[Ge3^{-1}]_2$. This result is in good agreement with the finding that the Fermi level is located in a pseudo-gap of the electronic DOS (Figure 3.3.13b).

3.3.6 Magnetic susceptibility and electrical resistivity

Consistently with the findings of the bonding analysis and the calculated band structure, the electrical resistivity of *hp*-$BaGe_5$ (Figure 3.3.14) increases almost linearly with temperature for T > 50 *K* indicating a metal-type electronic transport behaviour. Below 50 K a parabolic behaviour is observed and around 10 K and below the resistivity is constant. A small magnetoresistance effect was detected when an external magnetic field was applied during the measurement, yielding basically the same shape for the curve but with values of resistivity becoming larger below 150 K with the largest difference at 2 K (Figure 3.3.14, inset).

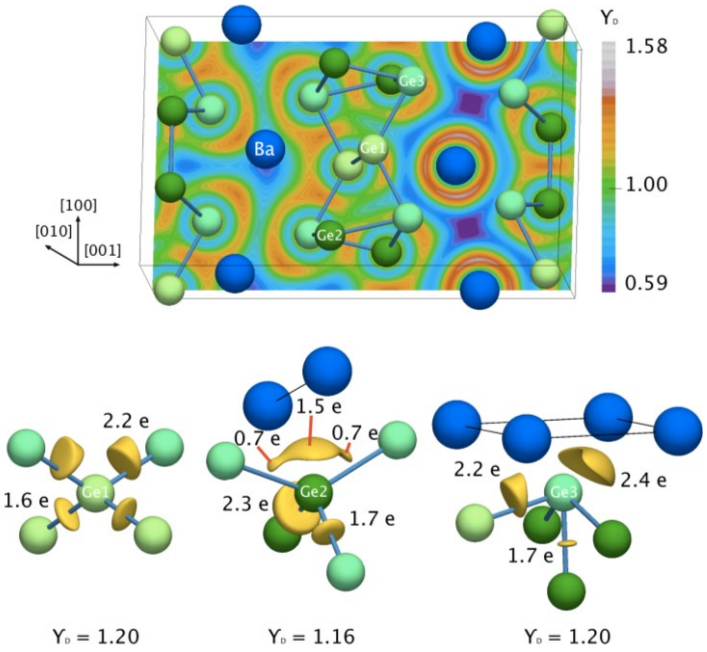

Figure 3.3.12 Electron localizability indicator (ELI-D) in *hp*-BaGe$_5$. The shortest Ge–Ge distances (2.56 to 2.68 Å) are shown as light-blue lines. The ELI-D isosurfaces around Ge atoms visualize positions of attractors on Ge-Ge contacts and their location with respect to the neighboring Ba atoms (interconnected by black lines).

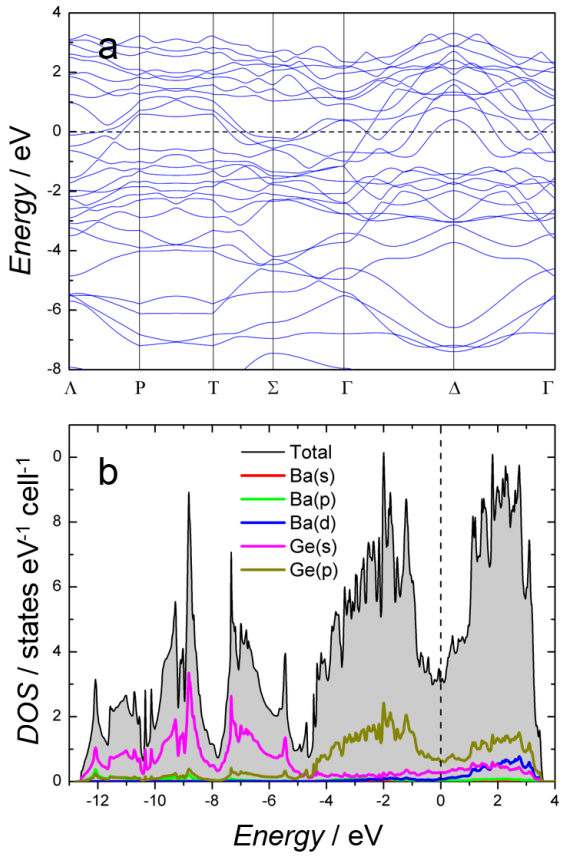

Figure 3.3.13 Electronic structure of *hp*-BaGe$_5$: (a) total band structure; (b) calculated total electronic density of states (DOS) together with the orbital-resolved contributions.

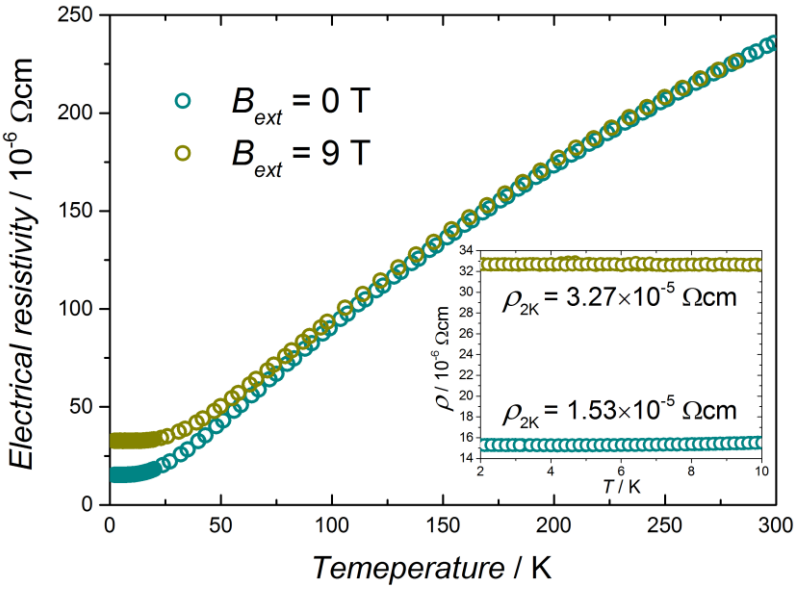

Figure 3.3.14 Electrical resistivity (ρ) of *hp*-$BeGe_5$ as a function of temperature measured with and without external magnetic field. A zoom to the data in the low-temperature range is displayed in the inset to highlight the magnetic field dependence.

The magnetic susceptibility is nearly independent of temperature under strong fields, showing diamagnetic behaviour in the whole temperature range, with an increase toward low temperatures likely caused by traces of paramagnetic impurities (Figure 3.3.15). Consistent with this observation, the susceptibility at low field shows a positive value, indicating the presence of minor ferromagnetic impurities. Taken these into account by the Honda-Owen extrapolation results in approximately 5.6 ppm of an iron-containing impurity. The observed value of 96×10^{-6} emu mol^{-1} at 300 K is in good agreement with the sum of the core diamagnetic contributions amounting to 110.5×10^{-6} emu mol^{-1}.

3.3.7 Conclusions

The new modification of $BaGe_5$ was synthesized at elevated pressure and in a range of temperatures; 15 GPa and 900 - 1200 K. The reduction of the atomic volume from the ambient to the high-pressure form of $BaGe_5$, expressed as $\Delta V = V_{hp\text{-}BaGe_5}/Z - V_{BaGe_5}/Z$, amounts to ΔV = -7.9 $Å^3$. Thus, the structure adopted under high-pressure is favored according to the small compression with respect to the ambient pressure modification. According to the thermal behavior, a monotropic decomposition takes place at relatively low temperature into a hitherto unknown modification with poor germanium content, which is at the same time, another metastable phase.

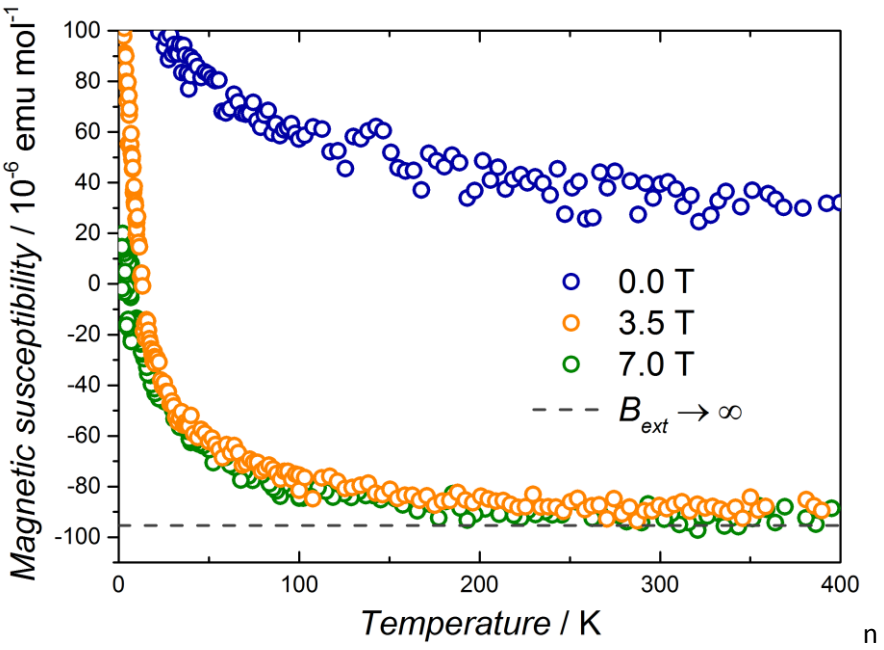

Figure 3.3.15 Magnetic susceptibility of *hp*-BeGe$_5$ as a function of temperature measured at different fields. Gray dashed line represents the extrapolation at infinite field.

The layered structure is composed of three symmetry-independent germanium atoms. Ge1 and Ge2 atoms show classical nearly tetrahedral environment with four closest neighbors, while Ge3 is also four-bonded but in an irregular coordination polyhedron derived from a ψ-pyramid. Detailed analysis of the chemical bond in direct space, revealed four attractors for both, Ge1 and Ge2, indicating a covalent interaction. Taking into account the integration of the electron density within the atomic basins, both species are uncharged. In contrast, the Ge3 atom stands for -1. The resulting charge balance is Ba[Ge^0]$_1$[Ge^0]$_2$[Ge^{-1}]$_2$ in accordance with the Zintl-Klemm concept.

Regarding physical properties, a metal-type behavior was observed by electrical resistivity measurements. Magnetic susceptibility measurements indicated that *hp*-BaGe$_5$ is diamagnetic with a value that can be attributed to the negatively charged Ge3^{-1}.

3.4 $BaGe_3$

The binary high-pressure phase $BaGe_3$ was recently reported [98]. It was synthesized in the pressure range 3 – 13 GPa at temperatures between 773 and 1473 K. The compound crystallizes in the hexagonal crystal system, and was described as isotypic to $BaSn_3$ [99]. The new phase exhibits metal-like electronic transport properties and becomes superconducting below 4.0 K.

During the synthesis of the high-pressure form of the binary $BaGe_5$ phase, additional sets of reflections were detected in the powder X-ray diffraction pattern (Figure 3.3.6 in chapter 3.3). According to metallographic inspection, the side phase had the composition ratio Ba:Ge 1:3, however their reflections could not be assigned to the earlier described hexagonal phase. Thus, a new set of experiments was performed aiming to synthesize the new modification of $BaGe_3$ at the synthesis conditions of $BaGe_5$.

3.4.1 Synthesis and crystal structure

The starting parameters were set to a pressure of 15 GPa and an annealing temperature of 1473 K during one hour before quenching. The precursor materials were a mixture of $BaGe_2$ and Ge in the stoichiometric ratio Ba:Ge 1:3. The elements were molten in the arc-melter, adding an excess of 1% of barium to take into account the mass loss due to the high vapor-pressure of this. All the processes were performed in an Ar-filled glove box, including the sample preparation for the high pressure experiments.

The first sample obtained at high-pressure was analyzed by X-ray powder diffraction, which showed a complex powder diagram composed of a mixture of different high-pressure phases in the Ge-rich side of the Ba – Ge system; $BaGe_5$, $BaGe_6$, $BaGe_{6-x}$ and $BaGe_3$. The next experiment was performed at a lower annealing temperature, 1273 K and the obtained X-ray diffraction powder pattern seemed less complex, with apparently a single new phase, as indicated in Figure 3.4.1, top. Lowering the pressure, the product obtained is the already reported hexagonal modification (Figure 3.4.1, bottom) in a wide range of temperatures.

The powder X-ray diffraction pattern of the new modification (Figure 3.4.1, top) could be successfully indexed in the tetragonal crystal system, with lattice parameters a = 7.8242(3), c = 12.784(1). The crystal structure type was assigned based on the similarities of the lattice parameters and the intensity pattern of the diffraction data with those of the recently published $CaGe_3$ [36]. The structure model was refined by the Rietveld method on basis of synchrotron X-ray diffraction data. The refinement results and the crystal structure are shown in Figure 3.4.2 and 3.4.3, respectively, while the crystallographic data and atomic positions with isotropic ADP are shown in Tables 5.18 – 5.20.

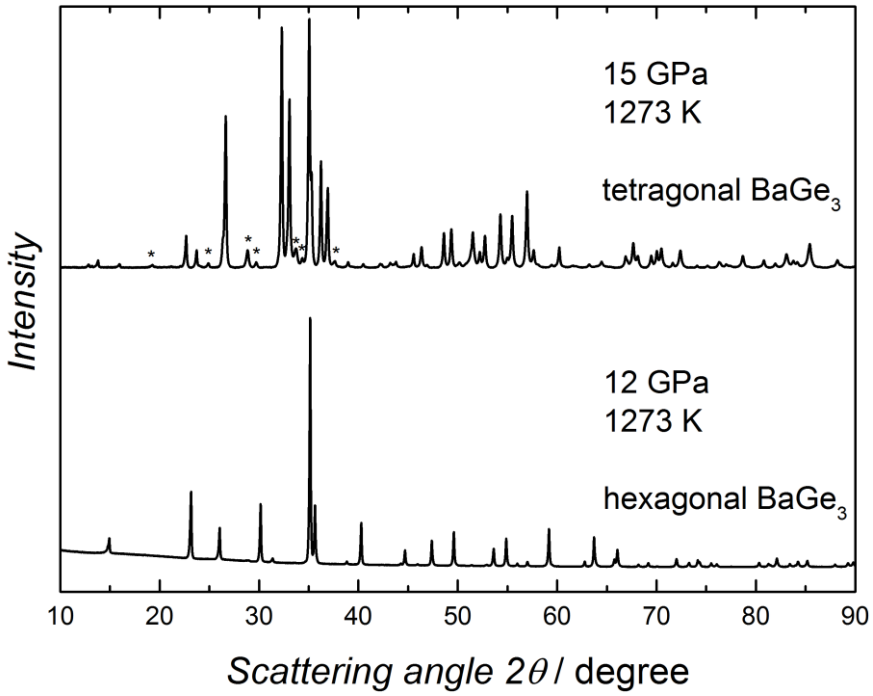

Figure 3.4.1 X-ray powder diffraction patterns of $BaGe_3$ synthetized at different conditions. The new modification (top) was obtained at 15 GPa (together with a small amount of *hp*-$BaGe_5$, indicated by stars) and the hexagonal modification (bottom) was obtained at 12 GPa.

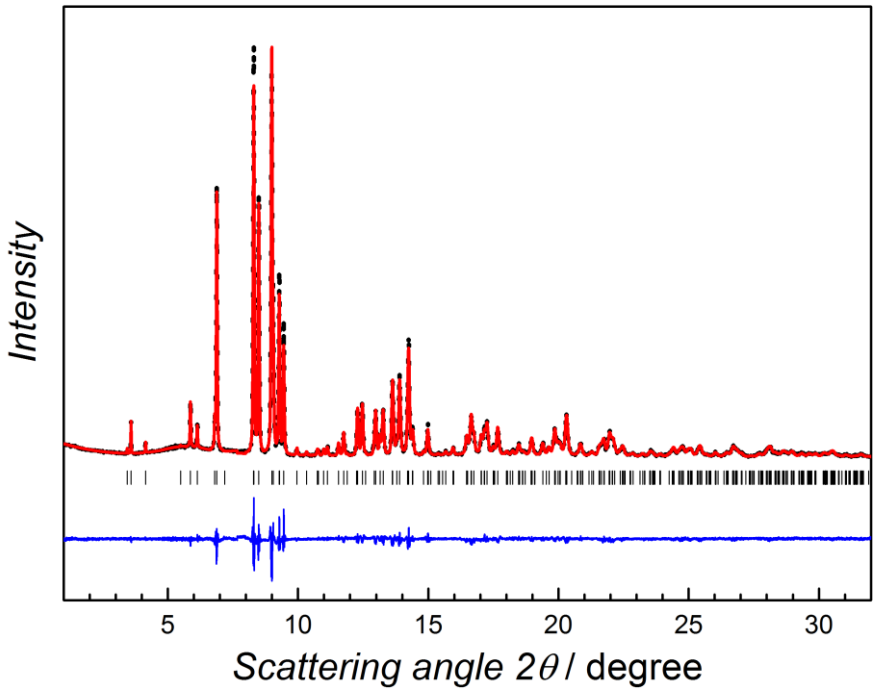

Figure 3.4.2 X-ray powder diffraction pattern of $BaGe_3$. The data collection was done at the beamline ID22 of the ESRF, with a wavelength λ = 0.40066 Å. Black points and red lines correspond to the observed and calculated intensities, respectively. Vertical tick marks correspond to reflection positions and the difference between observed and calculated intensities is shown as blue.

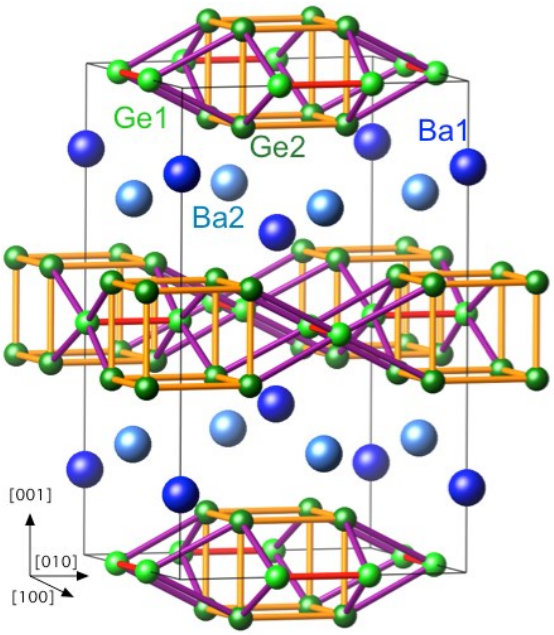

Figure 3.4.3 Crystal structure of $BaGe_3$. The color legend for the bonding is: Ge1 – Ge1 = red, Ge1 – Ge2 = violet, Ge2 – Ge2 = orange. The same code is used in the following Figures.

The crystal structure of the tetragonal modification of $BaGe_3$ is isotypic to $CaGe_3$ and the trisilicides [35,100], and consists of two-dimensional germanium units separated by barium atoms. The Ge layers comprise units of two Ge dimers parallel to [001] in the form of square prisms (orange) that are braced by Ge1 pairs (red) in two perpendicular orientations, resulting in infinite slabs of condensed dumbbells. The interatomic distances of the five-bonded Ge atoms are compatible with covalent bonds present in Ge-rich binary compounds.

The coordination sphere for each of the symmetry-independent Ba and Ge atoms was analyzed by the method proposed by G. Brunner and D. Schwarzenbach [101], which consists of adding all the surrounding atoms with a weighting scheme, i.e., if the shortest distance to a neighboring atom is set equal to 1.0, then further atoms are found at distances between 1.0 and 1.3, [102]. The resulting histograms are shown in Figure 3.4.4. It is deduced that the coordination sphere for both Ba atoms is 12 (4+4+4 and 4+8 for Ba1 and Ba2, respectively), Ba1 being surrounded on one side by a distorted square antiprism formed by 8 Ge1-Ge2 contacts and on the opposite direction by a square planar made of Ge2-Ge2 contacts. Ba2 is surrounded by two Ge6 trigonal-prismatic units that are in staggered conformation with the metal atom sitting at the center. In the case of the Ge atoms, both have 5 closest neighbors in form of a square prism, the Ge2 atom in irregular shape. The four coordination polyhedrons are shown in Figure 3.4.5.

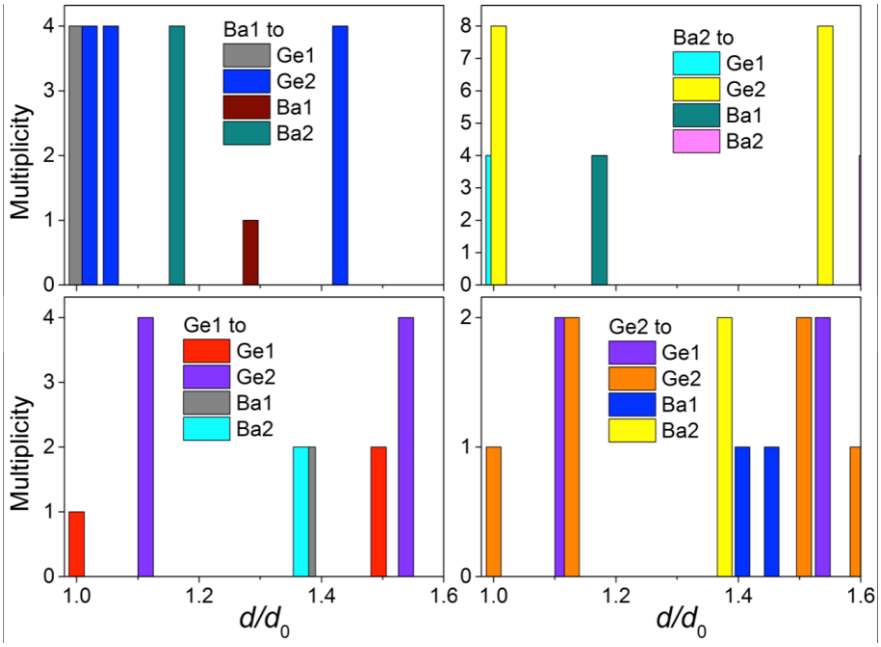

Figure 3.4.4 Connectivity histograms for each atom in the crystal structure of $BaGe_3$. The color legend is the same as in Figure 3.4.3.

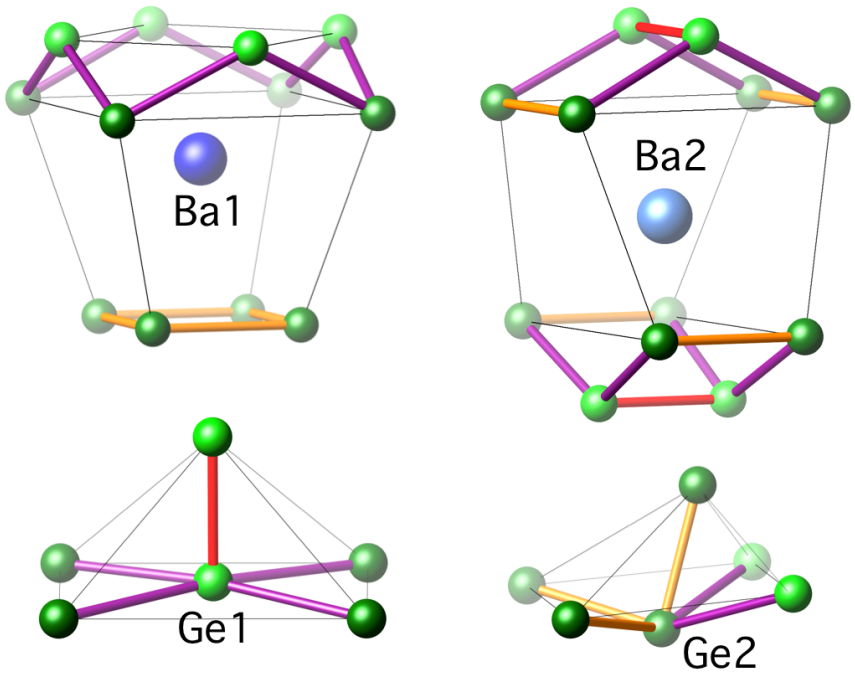

Figure 3.4.5 Coordination polyhedrons for the two symmetry independent Ba and Ge atoms. The color legend is the same as in Figure 3.4.3.

According to the *8-N* rule, there must be a total of 10/3 bonds between the Ge atoms forming the anionic framework. Such unbalanced condition may imply a metallic behavior in the electronic transport properties.

Clearly, the standard electron counting rules do not hold for $BaGe_3$ in this modification, and its chemical bonding situation and electron distribution will be investigated carefully by advanced quantum chemical calculations.

3.4.2 Quantum chemical calculations

Topological analysis of the electron density by means of the QTAIM technique [59] in $BaGe_3$, evidences charge transfers from the Ba atoms to the Ge layers (Figure 3.4.6). Similar to *hp*-$BaGe_5$, the charge transfer is not the full oxidation state expected for barium atom (Ba^{2+}), indicative that additional interactions must be present in the organization of the crystal structure.

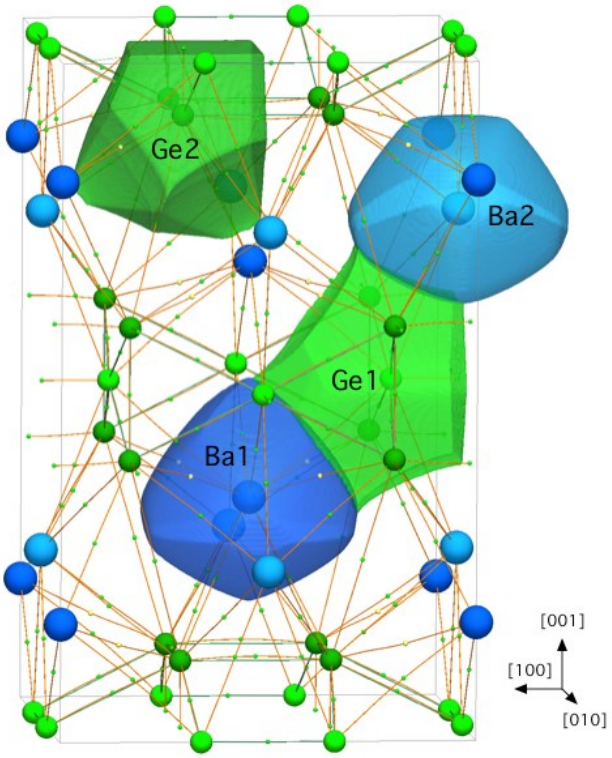

Figure 3.4.6 QTAIM atoms in *t*-$BaGe_3$. The orange lines represent the bond paths and the small green and yellow spheres located in the bonds paths represent the bond critical points.

The complex and unique distribution of the Ge atoms within the layers, which yield five short Ge – Ge interactions (according to the interatomic distances) is investigated by the electron localizability indicators, in the ELI-D representation [60]. The penultimate shell of both Ba atoms deviate from spherical symmetry, as shown in Figure 3.4.7 a. This is strong evidence for their participation in covalent interactions with the surrounding Ge layers. In Figure 3.4.7 b, the Ba atoms were removed in order to better visualize the Ge layers. The three slices normal to the [001] direction show different sections of the Ge layers. High Υ values are observed between the closest Ge – Ge connections representing covalent interactions. Additional maxima of Υ are detected around both Ge atoms

representing lone-pairs which are oriented in direction of the Ba atoms. In analogy to earlier findings on *hp*-$BaGe_5$ and $EuGe_3$ (chapter 3.6) this is a fingerprint of multicenter bonding. Additional insight into the bonding attractors is given in chapter 3.5.

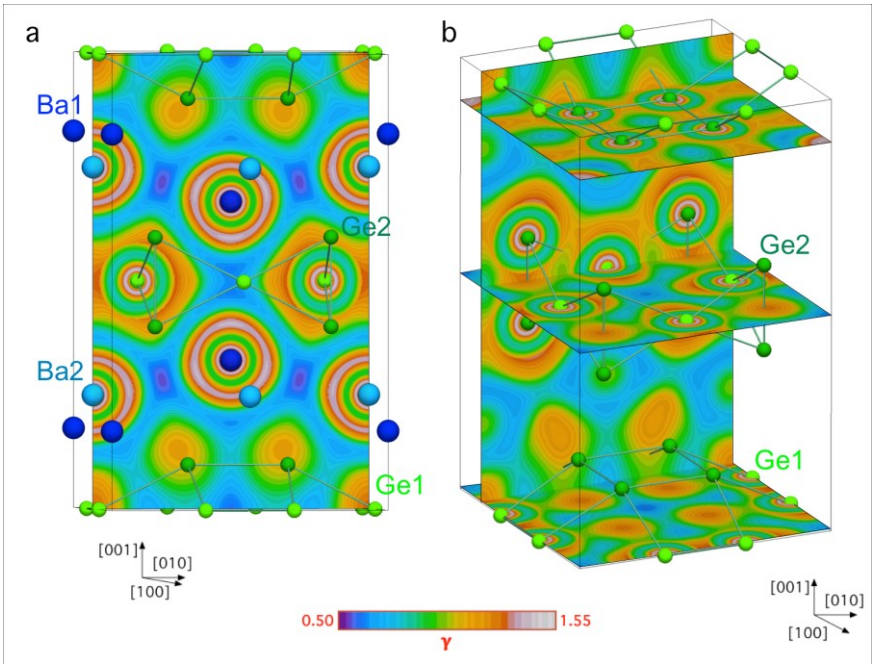

Figure 3.4.7 ELI-D picture of $BaGe_3$: (a) Structuring of the penultimate shell of Ba atoms; (b) bonding attractors in the Ge layers. Ba atoms were removed for better visualization.

3.4.3 Physical properties

3.4.3.1 Magnetic susceptibility

Magnetic susceptibility measurements were performed on different samples of $BaGe_3$. At zero magnetic field, the sample becomes superconducting at *Tc* = 6.5 K (Figure 3.4.8). By plotting the volumetric susceptibility, uncorrected for geometrical factors, the superconducting volume fraction amounts to > 100% (Figure 3.4.8, inset), which indicates the bulk superconductivity.

At high magnetic fields $BaGe_3$ shows diamagnetic behavior in the whole temperature range, as indicated by the negative susceptibility (Figure 3.4.20). Taking into account the Curie-law-like contributions to the magnetic susceptibility due to minor paramagnetic impurities, the value extrapolated at T = 0 K amounts to -76×10^{-6} emu mol^{-1}, which is a slighter lower than the value predicted by the diamagnetic contribution of -66.8×10^{-6} emu mol^{-1}.

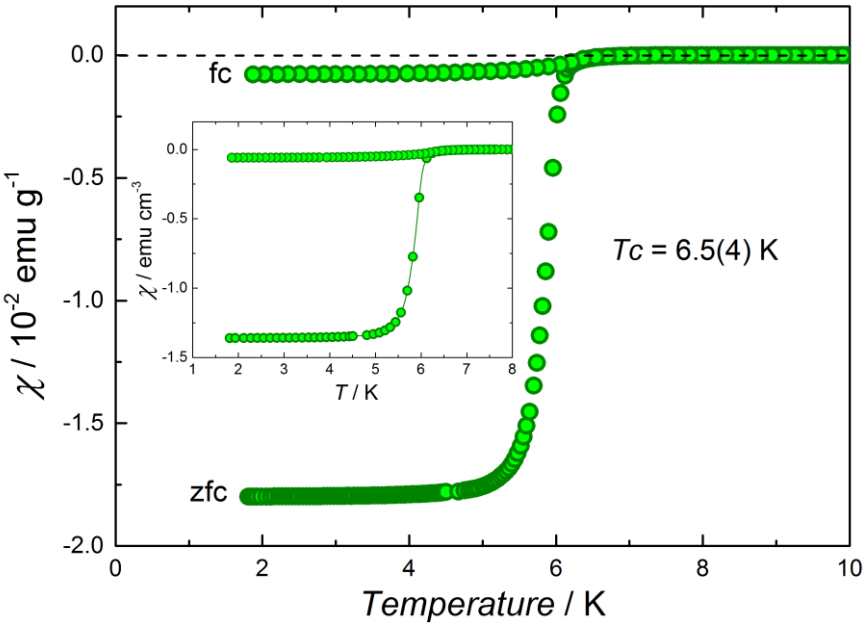

Figure 3.4.8 Zero-field magnetic susceptibility of $BaGe_3$. The superconducting state with *Tc* = 6.5 K is clearly indicated by the Meissner effect. The superconducting volume fraction is shown in the inset.

Magnetic susceptibility measurements were performed on several samples originated from different high-pressure synthesis (all of them at the same conditions), and most of the resulting samples showed broad reflections in their X-ray powder diffraction pattern. Accordingly, the magnetic measurements evidenced broad transitions, where it was not possible to extract reliable information. This is attributed to high strain which is induced during the high-pressure high-temperature synthesis. On the other hand, few experiments resulted in "good-quality" samples, i.e., their X-ray powder diffraction patterns showed sharper reflections, and the magnetic measurements produced sharper transitions, as shown in Figure 3.4.8. Thus, it was decided to measure magnetic susceptibility first and its quality was evaluated by its transition jump. In this way, enough sample was saved in order to perform further characterization, such as specific heat measurements at low temperatures. After all this, the samples were prepared for X-ray diffraction characterization and, as expected, single crystalline phase was obtained. By doing this procedure, an interesting relation was found for the different modifications of $BaGe_3$ and is discussed in 3.4.5.1.

3.4.3.2 Specific heat

The measurement performed on the best specimen resulted in a smooth curve (Figure 3.4.9). The anomalies expected for superconducting materials appear (second-order phase transition) and can be distinguished in the low temperature range (Figure 3.4.9, inset). The jump from the normal-state to the superconducting-state is not sharp, however, the measurement is useful for additional analysis.

In the low temperature range, the specific heat was measured at different magnetic fields (Figure 3.4.10). At 800 mT the superconductivity seems to vanish completely, and thus, those data points are employed for further analysis of the normal state. The specific heat is usually described as a contribution of two main terms; $Cp = \gamma T + \beta T^3$, however, this model fitted to the data points shows

significant discrepancies. This is better visualized by inspecting the data in the form CpT^{-1} vs T^2, in which the data points measured at 800 mT (overcritical field) would behave as a straight line (Figure 3.4.11).

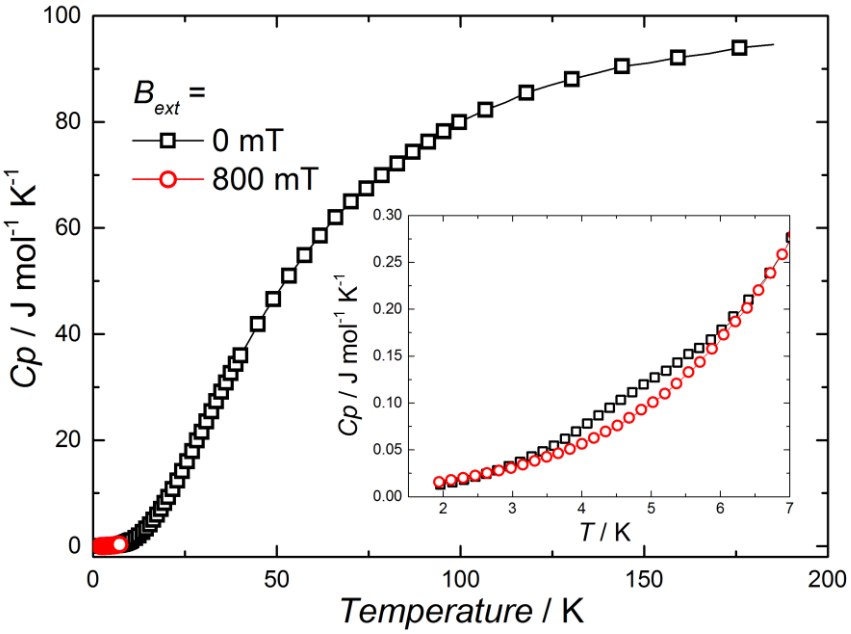

Figure 3.4.9 Specific heat measured in the temperature range 2 – 200 K. The black curve represents the measurement in absence of an external magnetic field, while the red curve indicates a measurement in an external magnetic field of 800 mT. The inset shows the low-temperature region.

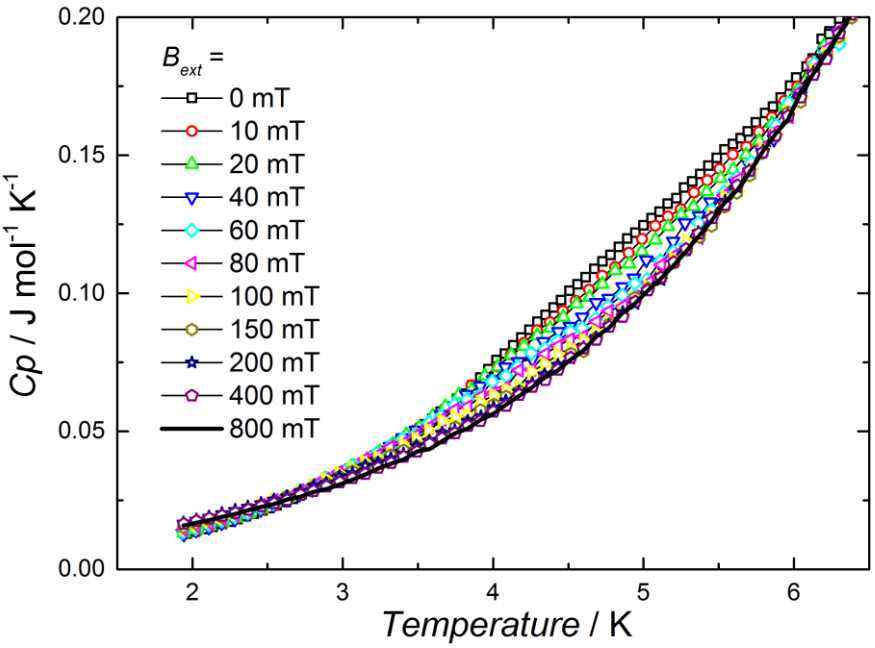

Figure 3.4.10 Specific heat measurements at different magnetic fields. At 800 mT the superconducting-state is completely suppressed.

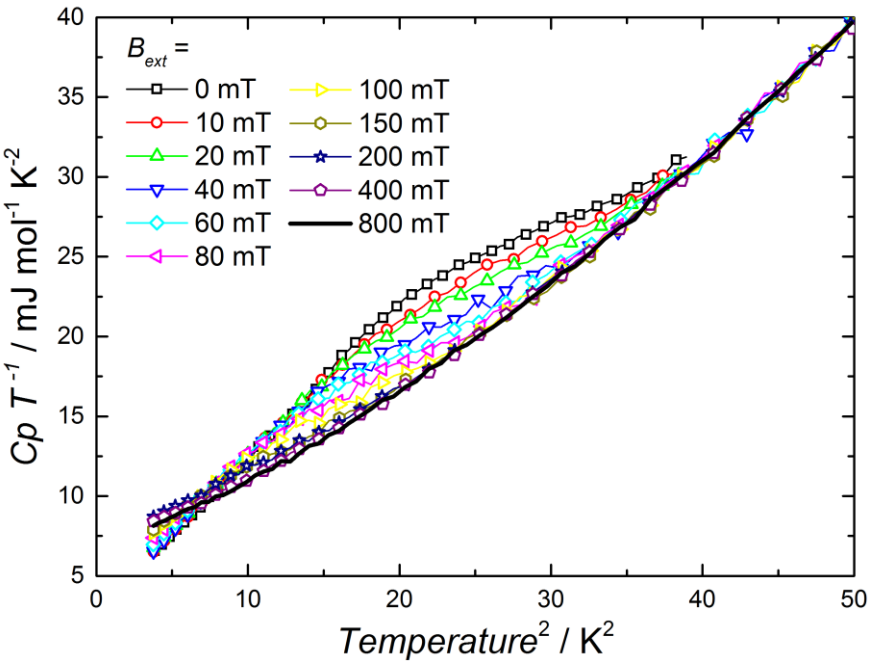

Figure 3.4.11 Specific measurement (from Figure 3.4.10) in the form CpT^{-1} vs T^2. The deviation from a straight line is of the normal-state (B_{ext} = 800 mT) evident for $T^2 < 20$ K^2, which indicates that the simple model $Cp = \gamma T + \beta T^3$ is not sufficient for the precise description of the data points.

The tiny deviation from the idealized model consisting of the two main components (Sommerfeld T-dependent term and Debye T^3-dependent term), can be properly described by adding an extra T^5-dependent term. Thus, the normal state specific heat data between 2.0 and 7.0 K (Figure 3.4.12) are finally modeled by $Cp = \gamma T + \beta T^3 + \delta T^5$, where $\beta T^3 + \delta T^5$, represent the first terms of the harmonic lattice approximation for the phonon contribution. The fit results in γ = 6.32 mJ mol^{-1} K^{-2}, and β = 0.41 mJ mol^{-1} K^{-4}, with an initial Debye temperature of $\theta_D(0)$ = 266 K. Similarly, the reduced specific heat jump amounts to $\Delta Cp/\gamma Tc$ = 1.3, significantly lower than the predicted by the BCS theory.

The upper critical field was also evaluated from these measurements, by using the difference in the specific heat between the superconducting- and normal-state data (Figure 3.4.13). The curves were modeled by a step-like function, and thus its midpoint of the left-half curves were obtained as the Tc. Then, the Werthamer-Helfand-Hohenberg (WHH) [103] extrapolation was employed to estimate the upper critical field for T = 0 K, $B_{c2}(0) = -0.693 \times Tc \times dB_{c2}/dT \,|_{T=Tc}$ with dB_{c2}/dT = 70.99 mT K^{-1}, resulting in 315 mT.

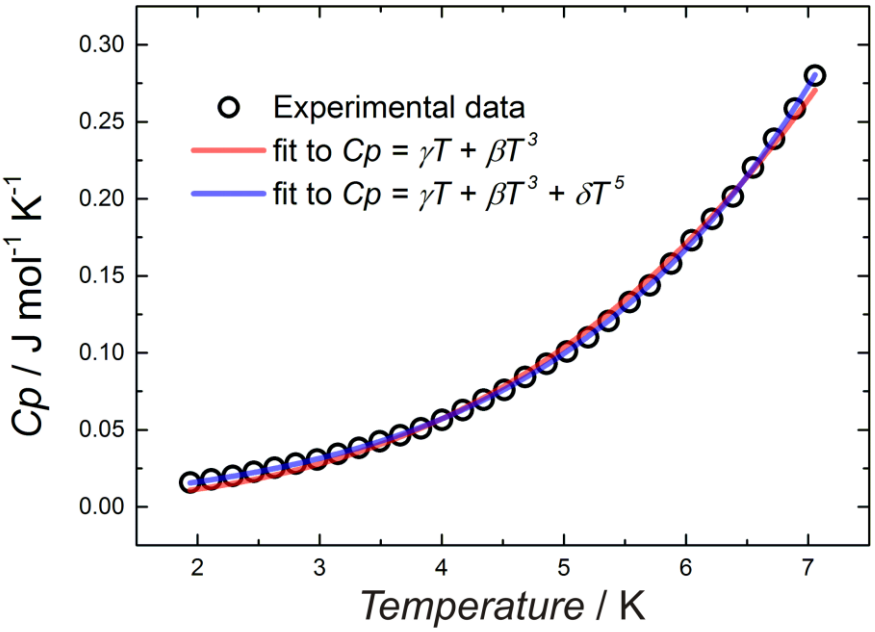

Figure 3.4.12 Specific heat in the normal state (B_{ext} = 800 mT) of $BaGe_3$. The fit including a harmonic approximation improves (blue line) the model of the standard Sommerfeld and Debye description (red line).

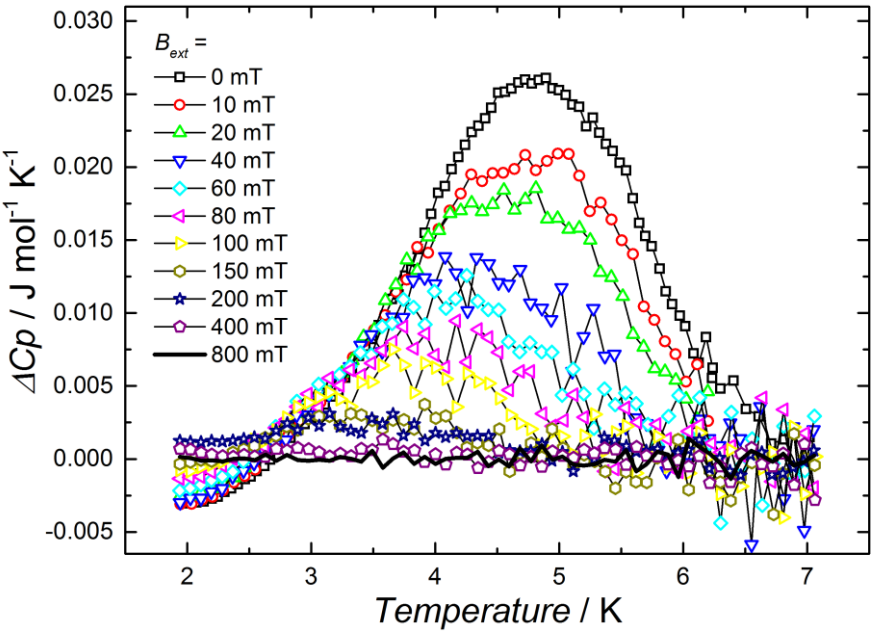

Figure 3.4.13 Difference specific heat of $BaGe_3$. The bell-shape curves were modeled by a step-like function applied to the right-side of the bell, and their midpoints were extracted as *Tc* for the WHH extrapolation.

3.4.4 Structural and bonding properties of $BaGe_3$ in the *hP8* form

In order to compare the above determined physical properties of $BaGe_3$ (in the t*I*32 form, from now on, *t*-$BaGe_3$), the hexagonal modification was synthesized (from now on, *h*-$BaGe_3$) and its physical properties measured and analyzed. In this way, the impact of polymorphism on the superconducting properties can be investigated.

h-$BaGe_3$ was successfully obtained at the earlier reported conditions [98] as shown in Figure 3.4.14, left. Its crystal structure was refined and the model presented in Figure 3.4.14 right, agrees well with the published data. Crystal structure details are reported in Tables 5.21 – 5.23.

The thermal stability of *h*-$BaGe_3$ and *t*-$BaGe_3$ was investigated by means of DSC analysis at ambient pressure and the results are shown in Figure 3.4.15. The hexagonal modification starts to decompose at 614 K and the tetragonal at 602 K. This last peak has a shoulder with a temperature determined at the peak maximum of 628 K, which coincides with the peak maximum of the unique exothermic effect in *h*-$BaGe_3$. At the end of the DSC measurement, the products are in both cases a mixture of Ba_6Ge_{25}, $BaGe_2$ and Ge. Since these effects do not occur during upon cooling, they are classified as monotropic transitions and evidence the high-pressure metastable nature in both compounds.

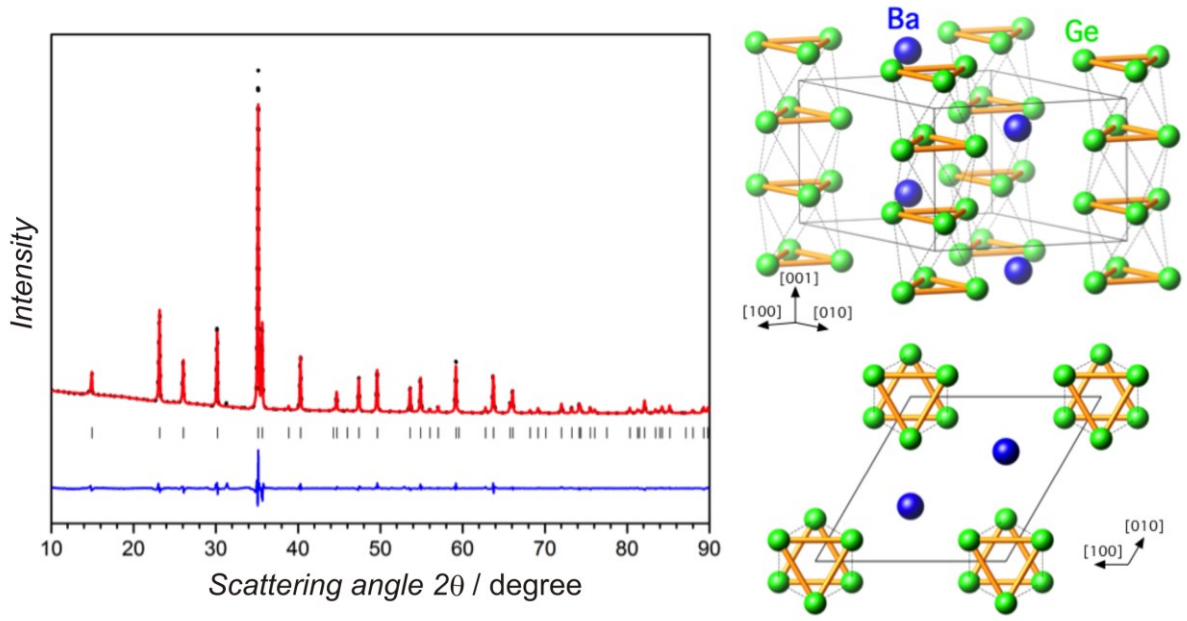

Figure 3.4.14 X-ray powder diffraction pattern of *h*-$BaGe_3$ (Cu $K\alpha 1$ λ = 1.540562 Å). Black points and red lines correspond to the observed and calculated intensities, respectively. Vertical tick marks correspond to reflection positions and the difference between observed and calculated intensities is shown in blue. The color code of the crystal structure is employed in the following figures that contain the *h*-$BaGe_3$ structure.

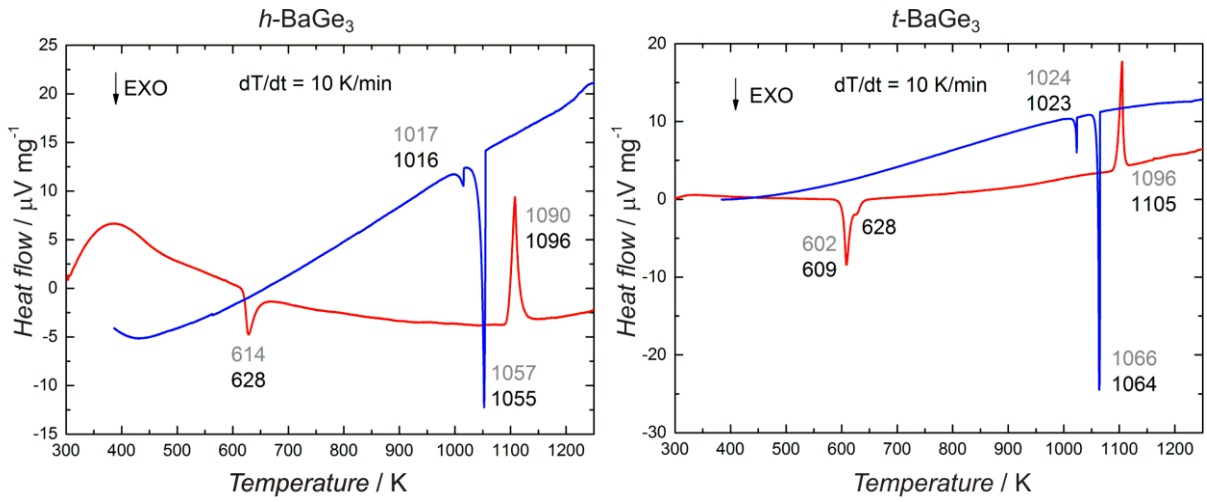

Figure 3.4.15 DSC of *h*-$BaGe_3$ (left) and *t*-$BaGe_3$ (right). The red and blue lines represent the heating and cooling, respectively, at a ratio of 10 K/min. In both cases, the inset temperatures of all peaks are shown in gray and the temperatures at the peak maximum are shown in black.

In order to clarify the chemical reactions involved during exothermic effects in both modifications, annealing experiments as well as in-situ XRD measurements were performed. The results reveal that *h*-$BaGe_3$ decomposes into Ba_6Ge_{25} + $BaGe_2$ + Ge (Figure 3.5.16), while *t*-$BaGe_3$ transforms first into $BaGe_2$ and Ge and then this mixture produces Ba_6Ge_{25}, with the consequence that Ba_6Ge_{25} and $BaGe_2$ are co-resident (Figures 3.5.17 and 3.5.18).

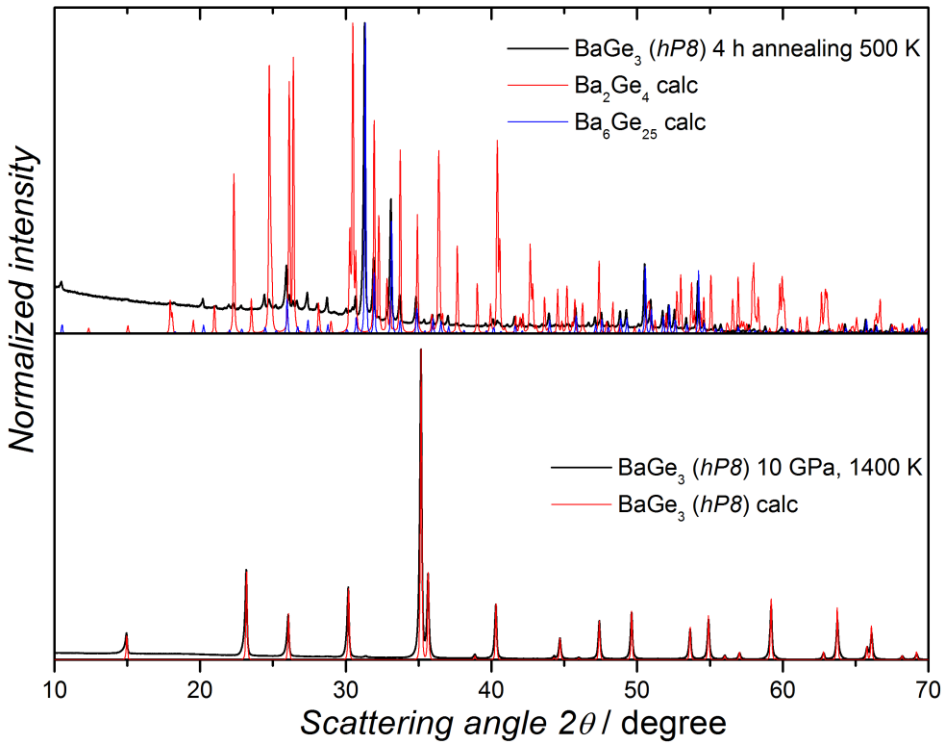

Figure 3.5.16 X-ray powder diffraction pattern of *h*-$BaGe_3$ (bottom) and the product obtained after annealing *h*-$BaGe_3$ at 500 K during four hours (top).

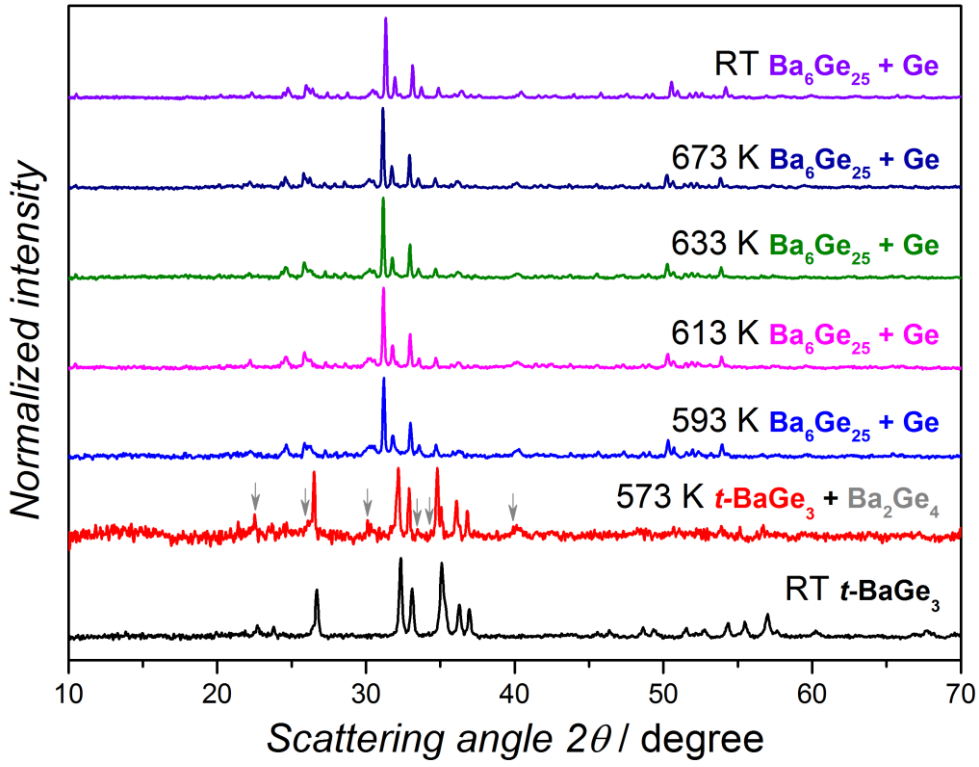

Figure 3.5.17 In-situ X-ray powder diffraction patterns of *t*-$BaGe_3$ sample upon heating.

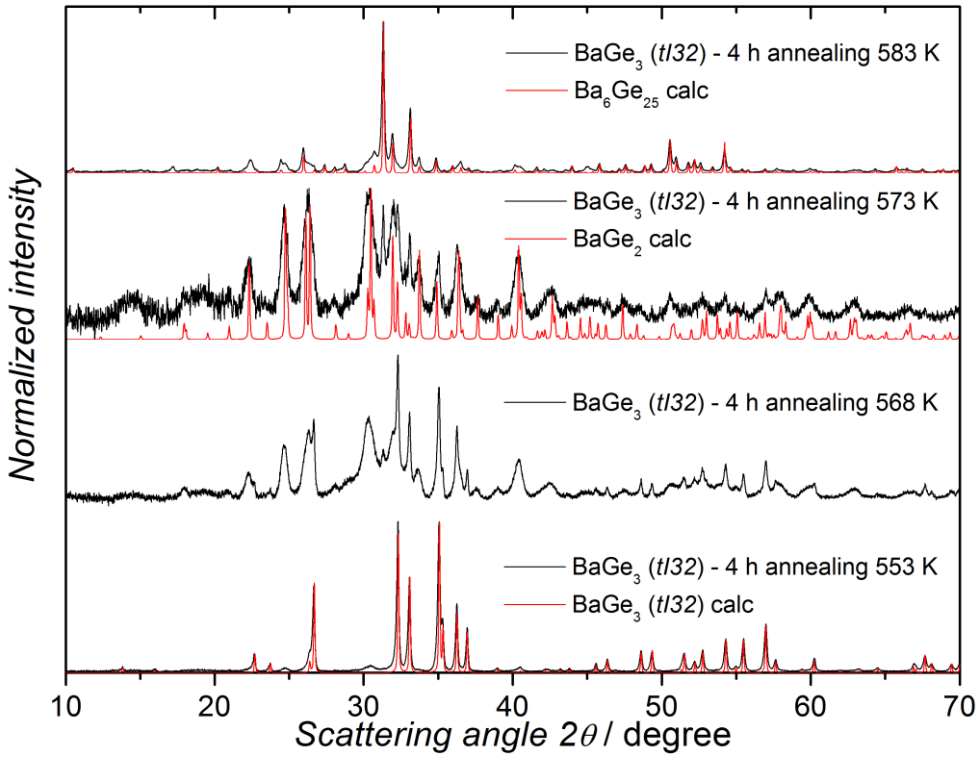

Figure 3.5.18 X-ray powder diffraction pattern of *t*-$BaGe_3$ and the product obtained after annealing *t*-$BaGe_3$ at different temperatures.

The chemical bonding of *h*-$BaGe_3$ was discussed by Fukuoka *et al.* [98] by means of band structure calculations, density of states, crystal orbital Hamilton population and the electron localization function, yielding the conclusion that strong bonded Ge – Ge interactions are present within the triangle (short distance) and a weak interaction between the Ge atoms of adjacent layers (long distance). In order to compare the modifications, the QTAIM atoms and the ELI-D were calculated for this structure. The results are shown in Figure 3.4.19.

Integration of the electron density within the atomic basins yields the effective charges +1.2 and -0.4, for Ba and Ge, respectively, which are basically the same number as for the tetragonal case (+1.2, +1,1, -0.4, -0.4 for Ba1, Ba2, Ge1 and Ge2, respectively).

Concerning the volume of the atomic basins, the computed quantities are 27.44 and 24.54 $Å^3$ for Ba and Ge respectively. Compared to the tetragonal situation, the average over the two distinct barium is slightly reduced (27.34 $Å^3$, 27.91 and 26.78 $Å^3$ for Ba1 and Ba2, respectively), while for the germanium atoms, the volumes are reduced in a considerably way to 22.85 for Ge1 and 23.89 $Å^3$ for Ge2. Thus, the formation of *t*-$BaGe_3$ from *h*-$BaGe_3$ is associated with a reduction of the volume per formula unit from 101.1 to 97.95 $Å^3$, as expected for a polymorph synthetized at higher pressure.

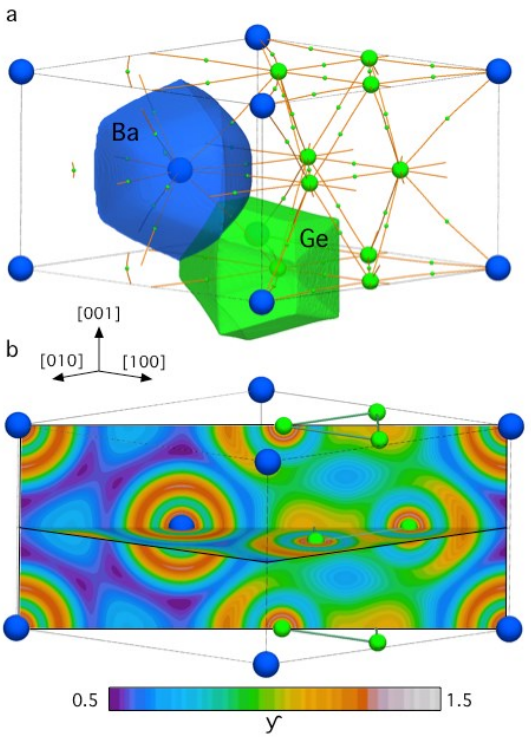

Figure 3.4.19 (a) QTAIM atoms together with the bond paths (orange lines) and bond critical points (small green spheres) and (b) ELI-D pattern of *h*-$BaGe_3$.

The ELI-D picture in the plane normal to [001] is similar to the reported ELF [98]. Perpendicular to [001], the structuring of the penultimate shell of the Ba atom is noticeable, suggesting the participation of this atom in the bonding. Especially in the same plane where Ge – Ge bonding attractors are present, strong structuring of the penultimate shell indicates multicenter bonding, similar to the tetragonal

case. Regarding the Ge3 units, high Υ values are observed between the Ge atoms in the Ge3 unit, and even higher values are around the regions located at each corner of the triangle made of Ge, in a lone-pair shape.

The computed volume of the ELI-D core basins are 21.63 and 17.51 Å^3 for Ba and Ge, respectively. With respect to the tetragonal structure (22.22 and 21.30 Å^3 for Ba1 and Ba2, 12.51 and 13.72 Å^3 for Ge1 and Ge2), the Ba atoms adopt almost the same (in average) volume, indicating that the reorganization of the Ge partial structure does not affect the electronic environment of the barium atoms. However, the core volume of the ELI-D basins of the Ge atoms is strongly reduced from the hexagonal to the tetragonal structure, pointing to a substantial reorganization of the bonding electrons, in agreement with the change in the coordination number and the bonding distances.

3.4.5 Physical properties of *h*-$BaGe_3$

3.4.5.1 Magnetic susceptibility and electrical resistivity

Magnetic susceptibility measurements indicate diamagnetic behavior in the whole temperature range investigated. Alike the tetragonal form, the corrected magnetic susceptibility extrapolated to T = 0 K amount to -98×10^{-6} emu mol^{-1}, lower than the value found for *tI32*. Two samples of both modifications were employed to compare the magnetic susceptibility, as shown in Figure 3.4.20. The magnetic susceptibility is well defined for both forms, so that one can distinguish the polymorph by inspecting the plot. The effect observed for the *tI32* form below T = 200 K cannot be attributed to a structural phase transition since no similar anomalies were detected in the specific heat. Thus, it may be due to an electronic effect.

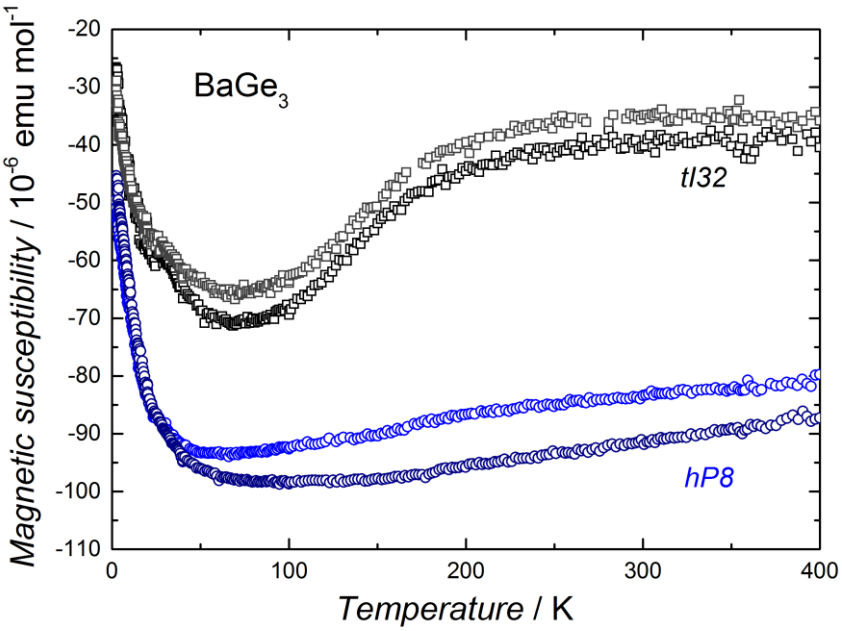

Figure 3.4.20 Temperature dependence of the magnetic susceptibility of $BaGe_3$ (B_{ext} > B_{c2}). Four different samples were employed: two *tI32* (black and gray) and two *hP8* (blue and dark blue).

Within the free-electron model, the total susceptibility, χ_0, at $T = 0$ is a sum of diamagnetic closed-shell contributions and Pauli-paramagnetism, from conduction electrons. Assuming that the difference of χ_0 of the two phases in exclusively due to this last influence, the estimated density of states of the *tI32* form is higher by 0.7 states eV^{-1} $f.u.^{-1}$ than that of the *hP8* modification, which is in agreement with the band structure calculations: 1.85 and 1.32 states eV^{-1} $f.u.^{-1}$ for the *tI32* and *hp8* modification, respectively. Additionally, by inspecting the DOS (Figure 3.4.27), the rise of $\chi(T)$ for the *tI32* polymorph hints to a sharp structure of the DOS a few meV above E_F.

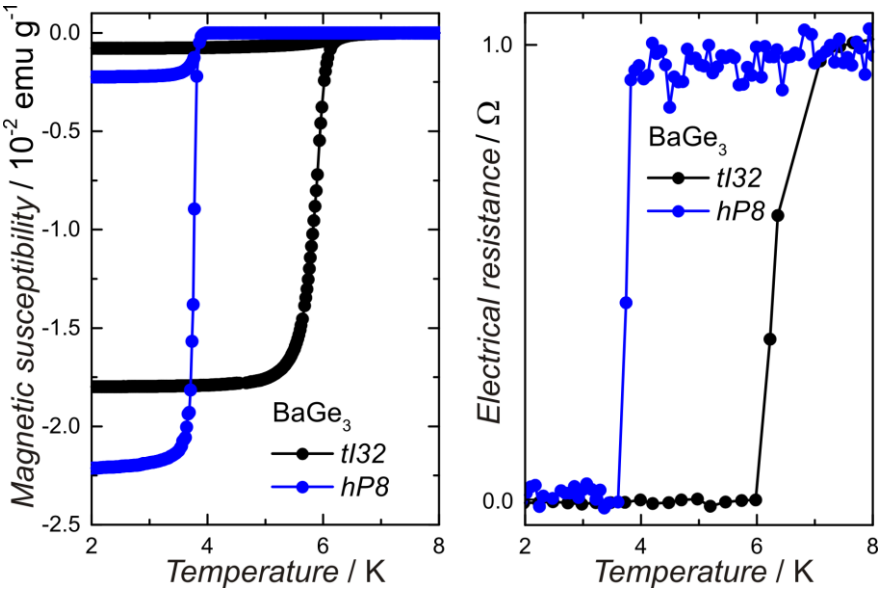

Figure 3.4.21 Temperature dependence of the magnetic susceptibility (left) and electrical resistance (right) of *h*-$BaGe_3$ (blue) and *t*-$BaGe_3$ (black). The Meissner effect is observed at 3.9(2) K. The inset shows the dependence up to room temperature at high magnetic fields.

3.4.5.2 Specific heat

The specific heat of *h*-$BaGe_3$ from 2.0 K to room temperature, measured in the overcritical field of 150 mT, is shown in Figure 3.4.22. Similar to *t*-$BaGe_3$, at high temperature it reaches the almost constant value predicted by the classical theory (Dulong-Petit´s law), $C = 3NR$, N being the number of atoms in the unit cell and R the universal gas constant.

In the low temperature range, the sample becomes a superconductor at Tc = 3.9(2) K (from diamagnetic susceptibility measurements, Figure 3.4.21). The specific heat as a function of temperature (at different magnetic fields) is shown in Figure 3.4.23.

As for *t*-$BaGe_3$, the experimental data points were fitted first to the standard model (Sommerfeld + Debye) and then to the harmonic approximation that significantly improved the description. The addition of the δT^{-5} term is justified by inspection of the data plotted in Figure 3.4.24, in which the measured data deviates from a straight line at low temperature.

The results of the fit $Cp = \gamma T + \beta T^3 + \delta T^5$, are: $\theta_D(0)$ = 205 K, from β = 0.90 mJ mol^{-1} K^{-4}, and a dressed density of states at E_F of 1.87 states eV^{-1} $f.u.^{-1}$ from γ = 4.4 mJ mol^{-1} K^{-2}. As expected, the Debye

temperature is lower in this quasi unidimensional structure, compared to the layered structure of the tetragonal modification. The ratio $\Delta Cp/\gamma Tc$ amounts to 1.49, indicating a weak electron-phonon coupled BCS superconductor

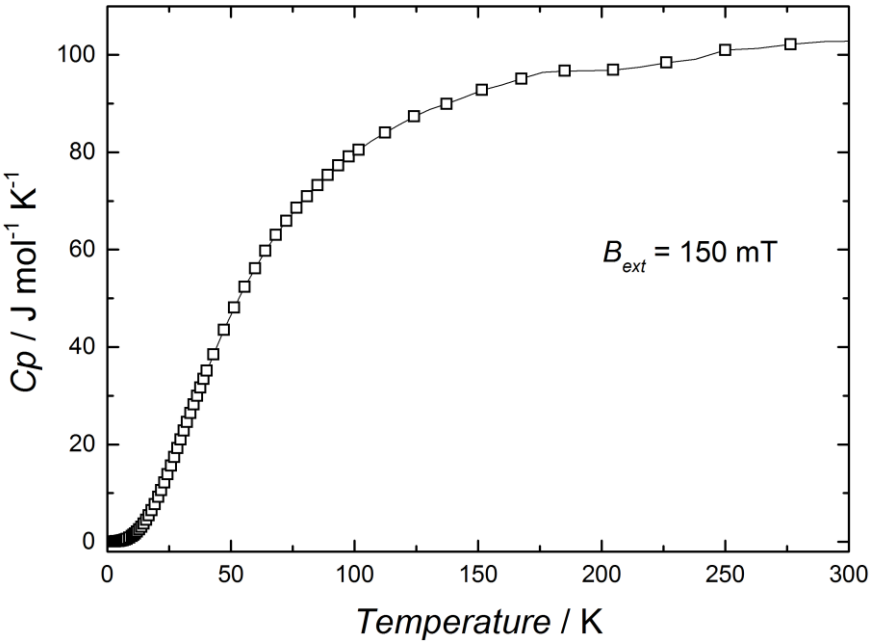

Figure 3.4.22 Specific heat of *h*-$BaGe_3$ in the temperature range 2 – 300 K, measured in an external magnetic field of 150 mT (normal-state). At high temperature, the specific heat behaves in agreement with the value predicted by the classical theory, C = 99.8 J mol^{-1} K^{-1} (Dulong-Petit´s law).

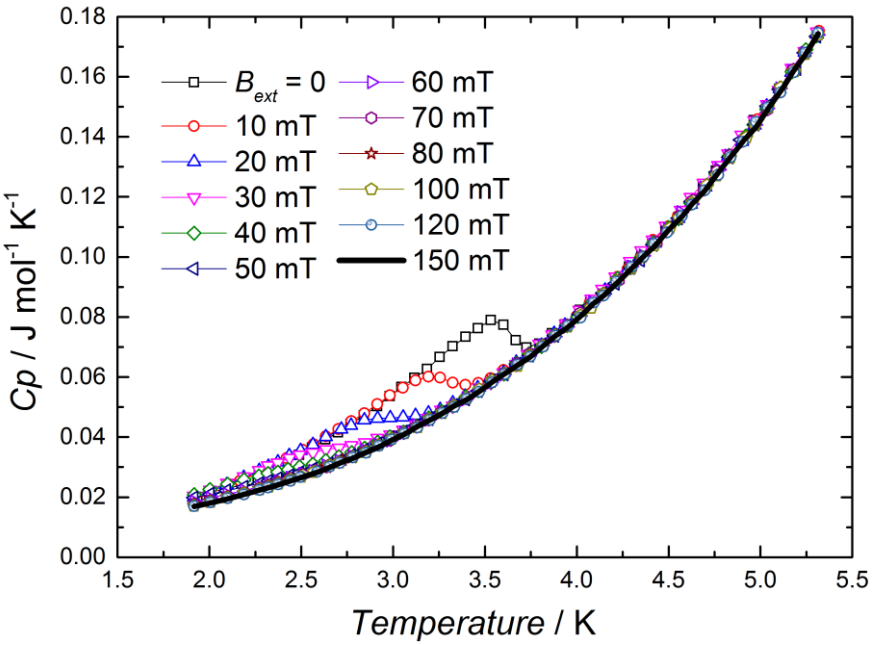

Figure 3.4.23 Specific heat measured from 2.0 to 5.5 K, at different magnetic fields. At 150 mT, the superconducting state seems to be fully vanished.

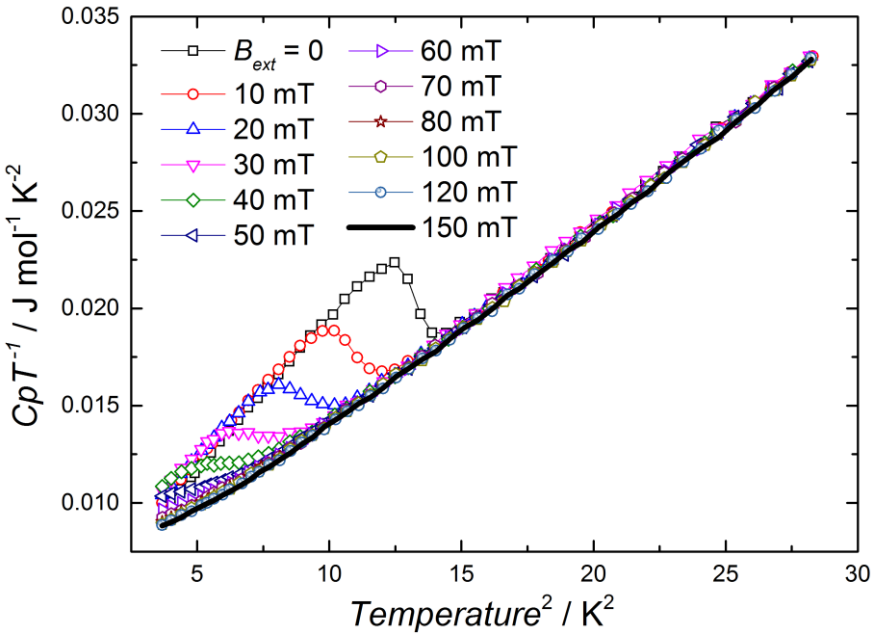

Figure 3.4.24 Specific heat in the form CpT^{-1} vs T^2. The normal-state data points show a straight line in the range 15 K^2 < T^2 < 28 K^2, and then deviates for T^2 < 15 K^2. An extra term is needed for the proper description of the data.

The upper critical field of the superconducting state of *h*-$BaGe_3$ at T = 0 K was determined by the WHH extrapolation, with *Tc* and magnetic field values derived from ΔCp plots (Figure 3.4.25). For the hexagonal case, the upper critical field was found to be $B_{c2}(0)$ = 120 mT.

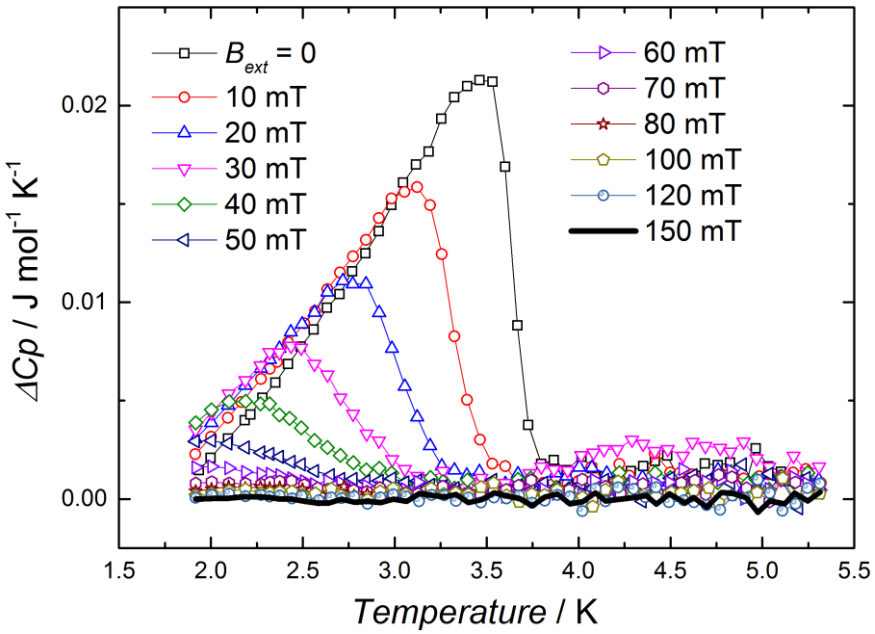

Figure 3.4.25 Difference specific heat of *h*-$BaGe_3$. The curves were modeled by a step-like function and their midpoints were extracted as *Tc* for the WHH extrapolation.

3.4.6 Comparison of both modifications

Summarizing the results; *h*-$BaGe_3$ is obtained in the pressure range 3 – 13 GPa, crystallizes in the hexagonal crystal system and its crystal structure is composed of Ge-columns oriented parallel to [001]. It is a metal and becomes superconducting at *Tc* = 3.9 K. *t*-$BaGe_3$ is obtained at 15 GPa pressure, it adopts a tetragonal unit cell with a layered crystal structure of Ge atoms with Ba in between the layers. It is also a metal and becomes a superconductor at *Tc* = 6.5 K.

Example of pressure-induced structural transitions which causes the appearance of superconductivity or increases the superconducting transition temperature is elemental silicon (see Introduction). The sequence diamond → β-Sn → simple hexagonal, which occurs at pressures ~12 and ~16 GPa, modifies the electronic structure in such a way that it start being an insulator, then becomes a metal with *Tc* = 6.3 K (measured at 6.3 GPa) and then a metal again with *Tc* = 8.2 K (measured at 15.2 GPa) [104].

Similar trends were observed in binary compounds like $CaSi_2$ [105], Figure 3.4.26. Under normal pressure, $CaSi_2$ adopts a rhombohedral crystal structure (*hR18*) which was reported to be a semimetal. Annealing at 1100 K and quenching under 8 GPa of pressure of the *hR18* form results in the well-known α-$ThSi_2$ modification (*tI12*), which is a metal with *Tc* = 1.5 K. On the other hand, applying pressure to the *hR18* two phase transitions occur at 9 and 16 GPa, involving a trigonal crystal structure ($EuGe_2$-like, *hP3*) and an AlB_2-like structure (*hR3*), respectively. Both high-pressure phases are metallic and become superconductors with *Tc* = 3 and 14 K, respectively. Then again, increase in *Tc* is achieved by increasing the pressure.

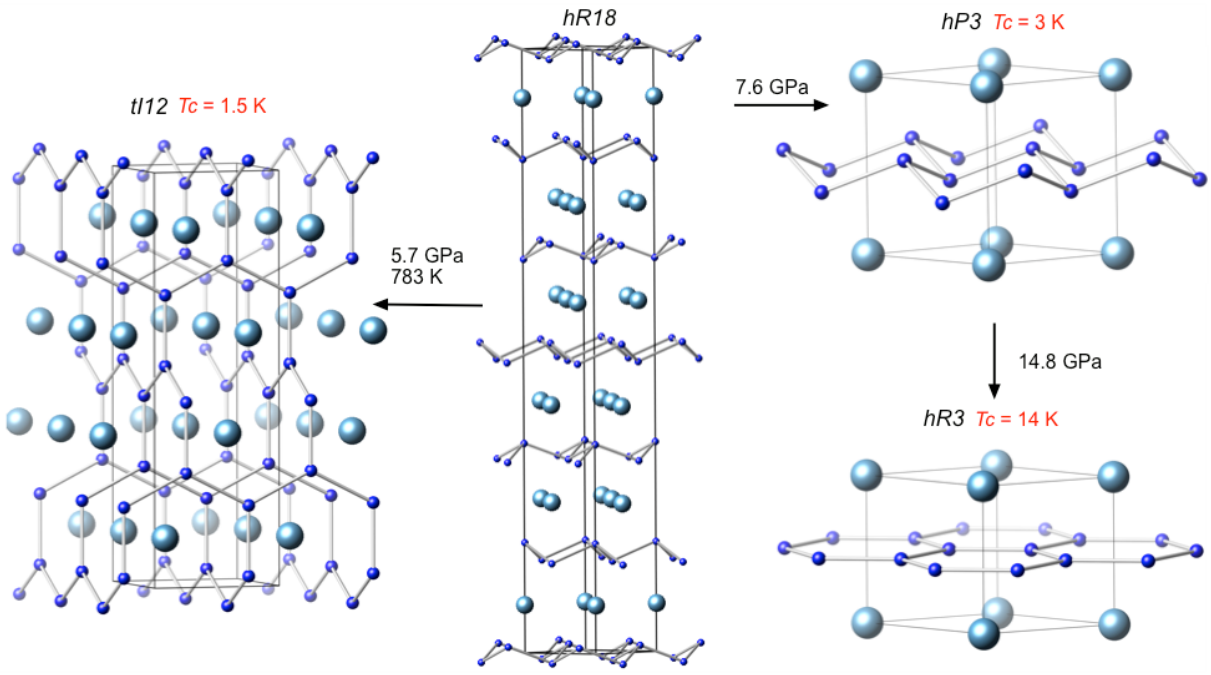

Figure 3.4.26 Crystal structures $CaSi_2$ at room temperature and different pressures. The large available space between the layers in ambient pressure *hR18* makes the pressure a suitable parameter for structural changes. At high-pressure and high-temperature, the polymorph with the α-$ThSi_2$ structure appears.

In the last example, the crystal structures differ mainly in the Si sublattice. The three structures consist of simple lattices formed by alternate metal and Si layers. In *hR18*, single three-dimensional Si layers alternate with planar Ca sheets along the [001], in the stacking sequence *AABBCC*. By applying pressure, the transformation into the *hP3* involves a shortened *c* axis, with a short stacking sequence, *AA*, with the planar layers of metal atoms separated by three-dimensional layers of Si. On further increasing pressure, the three-dimensional layer of Si becomes flat, similar to graphite-like honeycombs, resulting in the *hR3* structure. According to theoretical calculations, the enhancement in the *Tc* from 3 to 14 K, during the transition *hP3* $\rightarrow$ *hR3*, is mainly due to the enhancement in the electron-phonon interaction (*hR3* has higher DOS at the Fermi level than *hP3*). However, the flattering of the Si layer plays an important role too, due to the appearance of a high-frequency peak in the phonon DOS, coming from the alternate oscillation of neighboring Si atoms in the Si layers. In summary, all the required conditions for high *Tc* are met in the *hR3* structure.

When looking for new superconductors, the first inspection of the electronic structure concerns the appearance of high DOS at E_F. Both modifications of $BaGe_3$ have non-zero DOS at E_F (Figure 3.4.27) and thus are expected to be metallic (confirmed by measurements) and supposed to become superconducting at low temperatures. The calculated DOS for both structures are very similar, not only in the overall shape but also in the partial contribution. For instance, the valence and conduction band are mainly composed of Ge, with Ba becoming significant in the conduction band. The Ba contribution to the DOS comes mostly from the *d* states in the whole range, while the Ge contributes mainly with *p* states, and a non-negligible character of *s* orbitals is present in the conduction band. Then, the main difference is the number of states, with 1.32 and 1.85 states eV^{-1} $f.u.^{-1}$ at the Fermi level for *h*-$BaGe_3$ and *t*-$BaGe_3$, respectively. Obviously, in the vicinity of E_F, Ge *p* states and Ba *d* states hybridize, in agreement with the finding concerning the participation of Ba in multicenter bonding, as observed by ELI-D.

It is noteworthy to comment on the band structure (Figure 3.4.28) and its interpretation according to the different Ge-substructures in the two modifications. In *h*-$BaGe_3$ for instance, nearly flat bands are observed in paths along the (001) plane, while strong band dispersion, or bands with large slope, are detected parallel to the [001] direction. The opposite situation is observed in *t*-$BaGe_3$, where few bands change their slope along paths parallel to the [001] direction while most of them disperse strongly through the (001) plane. Such band structure behavior is in agreement with the Ge-sublattices in both structures: columns in *h*-$BaGe_3$ and layers in *t*-$BaGe_3$.

In the framework of the BCS theory and according to the McMillan's formula [106]:

$$Tc = \frac{\langle\omega\rangle}{1.2} exp\left[\frac{-1.04(1+\lambda)}{\lambda - \mu^*(1+0.62\lambda)}\right]$$

Tc depends on the electron phonon coupling parameter λ, the average phonon energy $<\omega>$, and the coulomb pseudopotential μ^*. The three variables can be accurately measured with tunneling experiments [107]. Nevertheless, μ^* is an almost constant value for metallic systems ranging from 0.10 to 0.15, and is not expected to change much from one polymorph to another, and thus for the sake of a qualitative analysis, it can be neglected. In order to present his equation in terms of easily measurable

quantities, $<\omega>$ is replaced by θ_D and the preexponential term rescaled to give the approximated equation [106,108]:

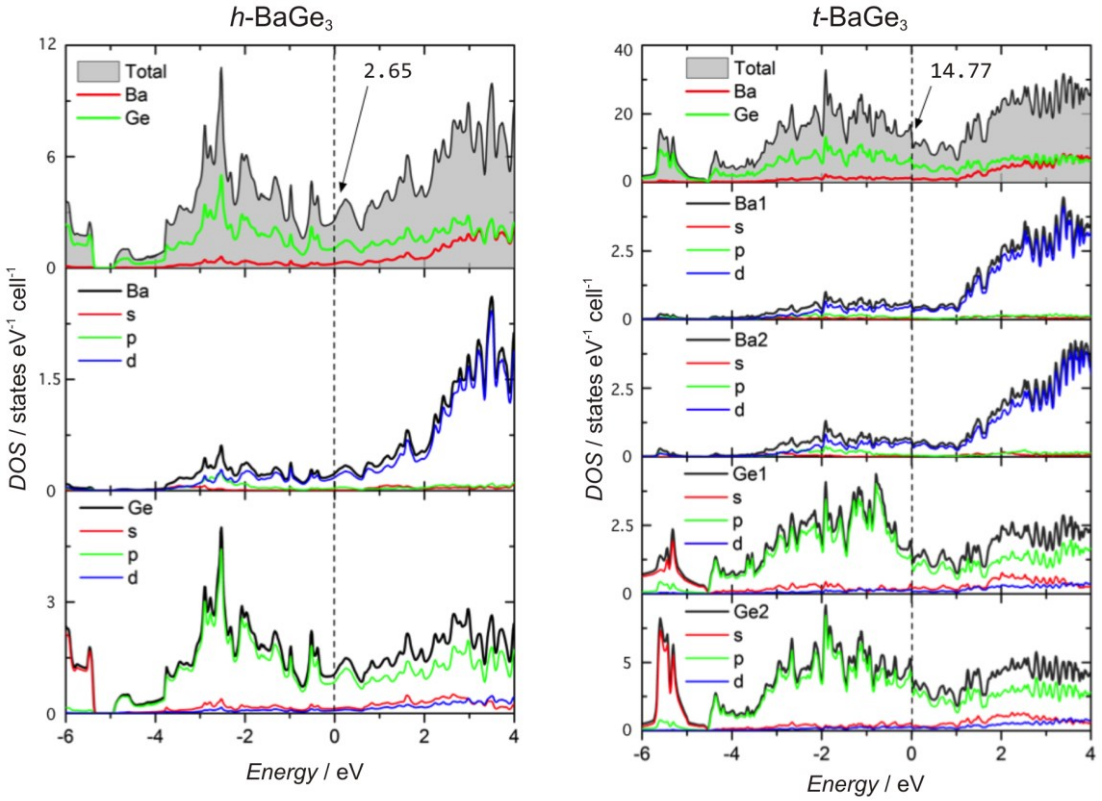

Figure 3.4.27 Electronic density of states, DOS, of *h*-$BaGe_3$ (left) and *t*-$BaGe_3$ (right). The total DOS together with Ba and Ge contributions are displayed in the first plot. The following plots contain orbital resolved DOS of every inequivalent atom.

$$Tc = \frac{\theta_D}{1.45} exp\left[\frac{-1.04(1+\lambda)}{\lambda - \mu^*(1+0.62\lambda)}\right]$$

Large λ and $<\omega>$ (or alternatively, θ_D) are favorable for high *Tc*. Regarding the electron-phonon coupling parameter, a very crude approximation [109] can be done by the relation $\gamma_N = (1+\lambda)\gamma_B$, where γ_N is the Sommerfeld coefficient derived from the specific heat in the normal state, and γ_B is the "bare" Sommerfeld coefficient estimated with the aid of theoretical calculations of DOS (Figure 3.4.27). They result in low values, and as a consequence *Tc* < 1 K is calculated in both cases, confirming the crude approximation of λ. Therefore, λ is calculated with the above formula, using only experimental thermodynamic data, resulting in 0.71 and 0.74 for *h*-$BaGe_3$ and *t*-$BaGe_3$, respectively.

Considering the Ge substructures in both modifications, the interatomic distances found in *h*-$BaGe_3$ amount to 2.618 Å (intra-triangle) and 2.934 Å (inter-triangle), for *t*-$BaGe_3$ the shortest Ge – Ge distances range from 2.515 Å to 2.278 Å for Ge1 and from 2.513 Å to 2.837 Å for Ge2. Strong bonds will give rise to high phonon frequencies [110] so that the higher *Tc* of the tetragonal modification is in accord with the crystal structure and the coupling parameters.

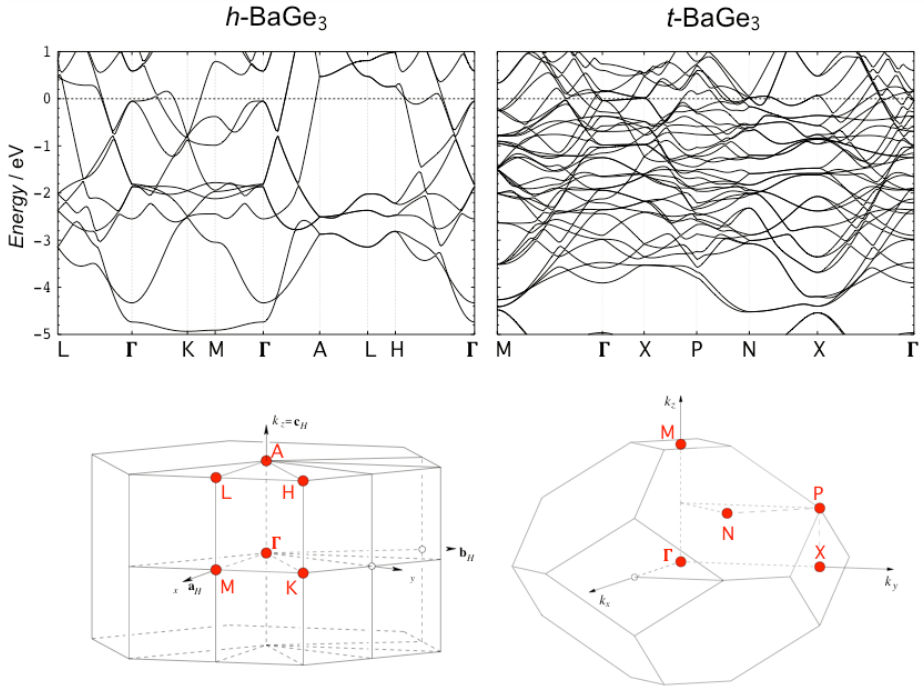

Figure 3.4.28 Band structure of *h*-$BaGe_3$ (left) and *t*-$BaGe_3$ (right) along high symmetrically selected paths. The Brillouin zones are showed at the bottom.

3.4.7 Conclusions

The new high-pressure metastable tetragonal modification of $BaGe_3$ was synthesized, characterized and compared with the hexagonal one. The pressure range for the synthesis was found to be from 3 to 12 GPa for the *h*-$BaGe_3$ and >15 GPa, for the *t*-$BaGe_3$. Both crystal structures are characterized by different Ge building units: triangles in *h*-$BaGe_3$, which give rise to columns made of face-sharing octahedrons, and dumbbells in *t*-$BaGe_3$, which are oriented perpendicular to each other, resulting in layers. Classical counting rules are not satisfied and analysis of the chemical bonding by means of direct space indicators revealed strong 2c2e covalent bonds within the dumbbells and weak interactions for *inter*-dumbbells contacts, with significant participation of the Ba atoms via multicenter bonding. Both phases are metallic and become superconducting with transition temperatures of 3.9 K and 6.5 K for *h*-$BaGe_3$ and *t*-$BaGe_3$, respectively. The finding that the reduced specific heat jump $\Delta Cp/\gamma Tc$, amounts to a value of approximately 1.3 only for *t*-$BaGe_3$ is rather attributed to the fair sample quality than indicating deviation from the value 1.43 predicted by the BCS theory for weak electron-phonon coupling in a single band scenario. The increased transition temperature found in the tetragonal polymorph can be attributed to the higher DOS at E_F together with the stronger electron-phonon coupling, which are originated because of the different topology of the covalent framework.

3.5 $SrGe_3$

Since the previously reported $BaGe_3$ was found to be isostructural to $CaGe_3$ [36], the likely existence of another member in the family was $SrGe_3$. Its synthesis succeeded at high-pressure conditions, similarly to the other two trigermanides, and was fully characterized. Even when most of the structural and physical features of $SrGe_3$ are, to some extent, in between of $CaGe_3$ and $BaGe_3$, it is interesting to note the tendencies among the three high-pressure phases and link their structural trends with their physical properties, particularly with the superconductivity. With this objective in mind, the aim of the present chapter is to report the similarities (or differences) and comparison of the previously described $BaGe_3$ and the already published $CaGe_3$ with the new $SrGe_3$.

3.5.1 Synthesis

The synthesis of $SrGe_3$ was investigated at high-pressure in the range 8 – 15 GPa, and 1173 K of annealing temperature. The optimal conditions were established to 9.45 GPa and one hour of annealing, which produced well crystalline samples. For Rietveld refinement high-resolution synchrotron X-ray diffraction data were collected at ID22 of ESRF (Figure 3.5.1, left and Table 5.25), employing the crystal structure model of $BaGe_3$. The refined crystal structure is shown in Figure 3.5.1, left and the structural data are in Tables 5.24 – 5.26.

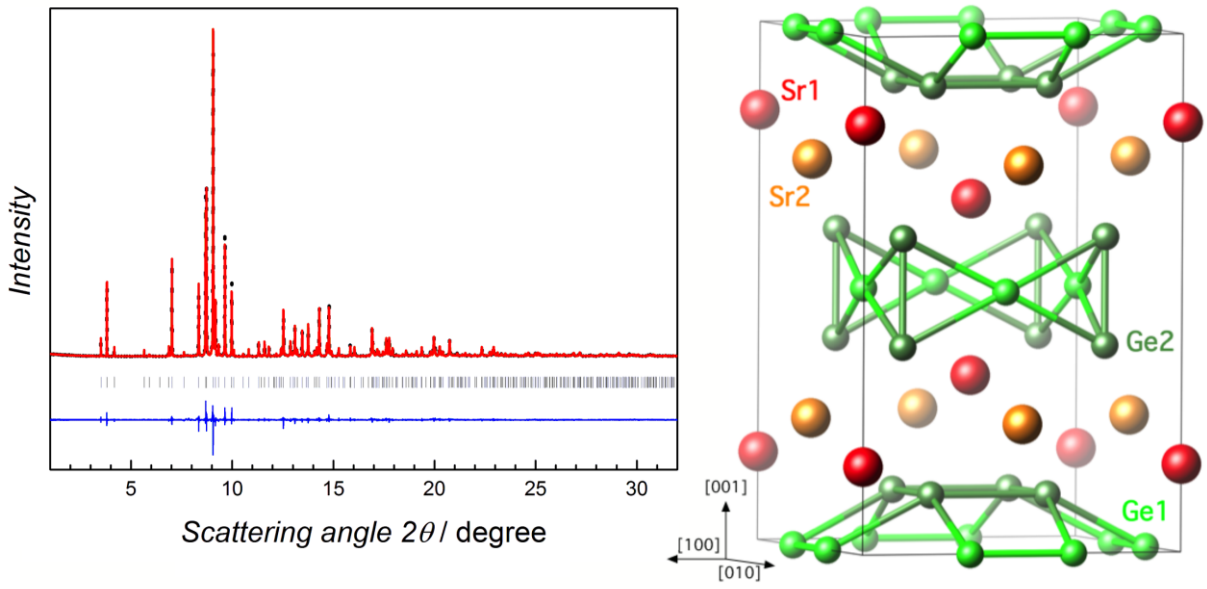

Figure 3.5.1 X-ray powder diffraction pattern of $SrGe_3$ (high-resolution x-ray synchrotron radiation data). Black points and red lines correspond to the observed and calculated profiles, respectively. Reflection positions are marked by vertical ticks and the difference between observed and calculated intensities is shown as blue line (left). The refined model is isostructural to $BaGe_3$ and $CaGe_3$ (right).

The first difference between $BaGe_3$ (Figure 3.4.1) and $SrGe_3$ is found in their X-ray powder pattern: $SrGe_3$ shows sharper reflections. Since both samples were measured with the same experimental setup, the wider reflections of $BaGe_3$ are attributed to smaller domain sizes of the crystallites. This is

supported by the synthesis conditions (much higher pressure and temperature in case of *t*-$BaGe_3$) causing strain in the sample and broadening the peaks.

3.5.2 Thermal behavior and crystal structure

The thermal stability was investigated by means of DSC measurements (Figure 3.5.2). The metastable character of $SrGe_3$ is evidenced by the exothermic effect at 612 K during the heating segment (labeled as I in Figure 3.5.2) that is absent on its cooling counterpart.

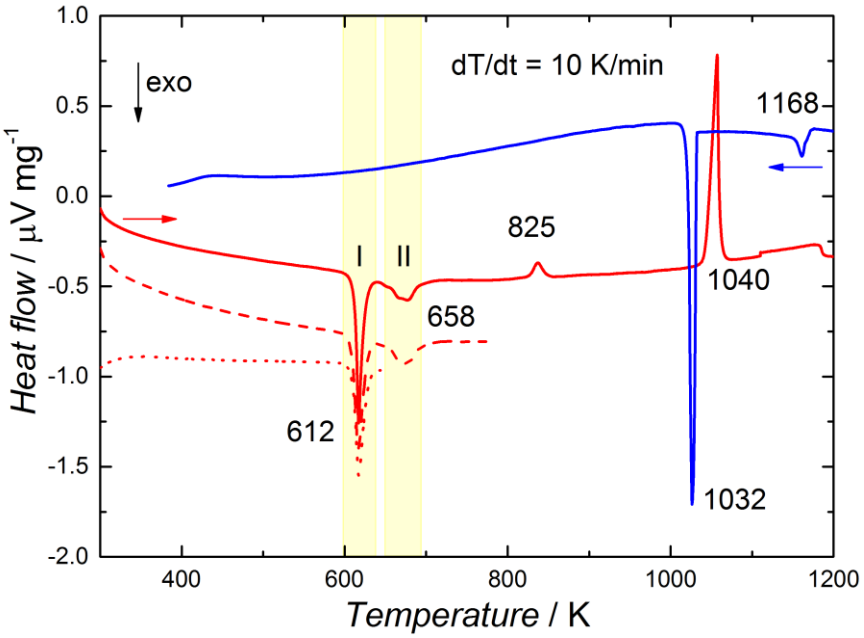

Figure 3.5.2 DSC data of $SrGe_3$ consisting of heating (red line) and cooling (blue line) segments. The dotted and dashed lines represent measurements up to temperatures above both exothermic peaks.

A second wider and weak exothermic effect is detected at 658 K (labeled as II in Figure 3.5.2). In order to investigate the reactions involved during the decomposition process of $SrGe_3$, two additional measurements were performed at temperatures slightly higher than the end of both exothermic peaks (dotted and dashed lines in Figure 3.5.2, corresponding to reaction I and II respectively) and their products were identified by X-ray diffraction. Additionally, in-situ high-temperature X-ray diffraction patterns were collected for $SrGe_3$.

The first exothermic effect corresponds to the reaction $SrGe_3 \rightarrow$ *hp*-$SrGe_2$ + Ge, *hp*-$SrGe_2$ being a high-pressure modification [111]. No additional phases or transformations were detected before, during or after the second broad exothermic effect, as evidenced by in-situ XRD (Figure 3.5.3). The reason for that might be that this intermediate and metastable product decomposes quite fast, impeding in this way to be detected by the XRD experiment. The endothermic effect at 825 K corresponds to the transformation of *hp*-$SrGe_2$ into the ambient pressure form [112]. Even though *hp*-$SrGe_2$ is expected to be metastable due to its preparation route, as reported in [111], its transformation is represented

by an endothermic effect. This fact together with the observation of reflections belonging to this phase in the diffraction pattern measured after cooling back, strongly suggest that *hp*-$SrGe_2$ is most probably the low-temperature modification of strontium digermanide, and the accepted phase diagram [113] needs the reconsideration in this respect.

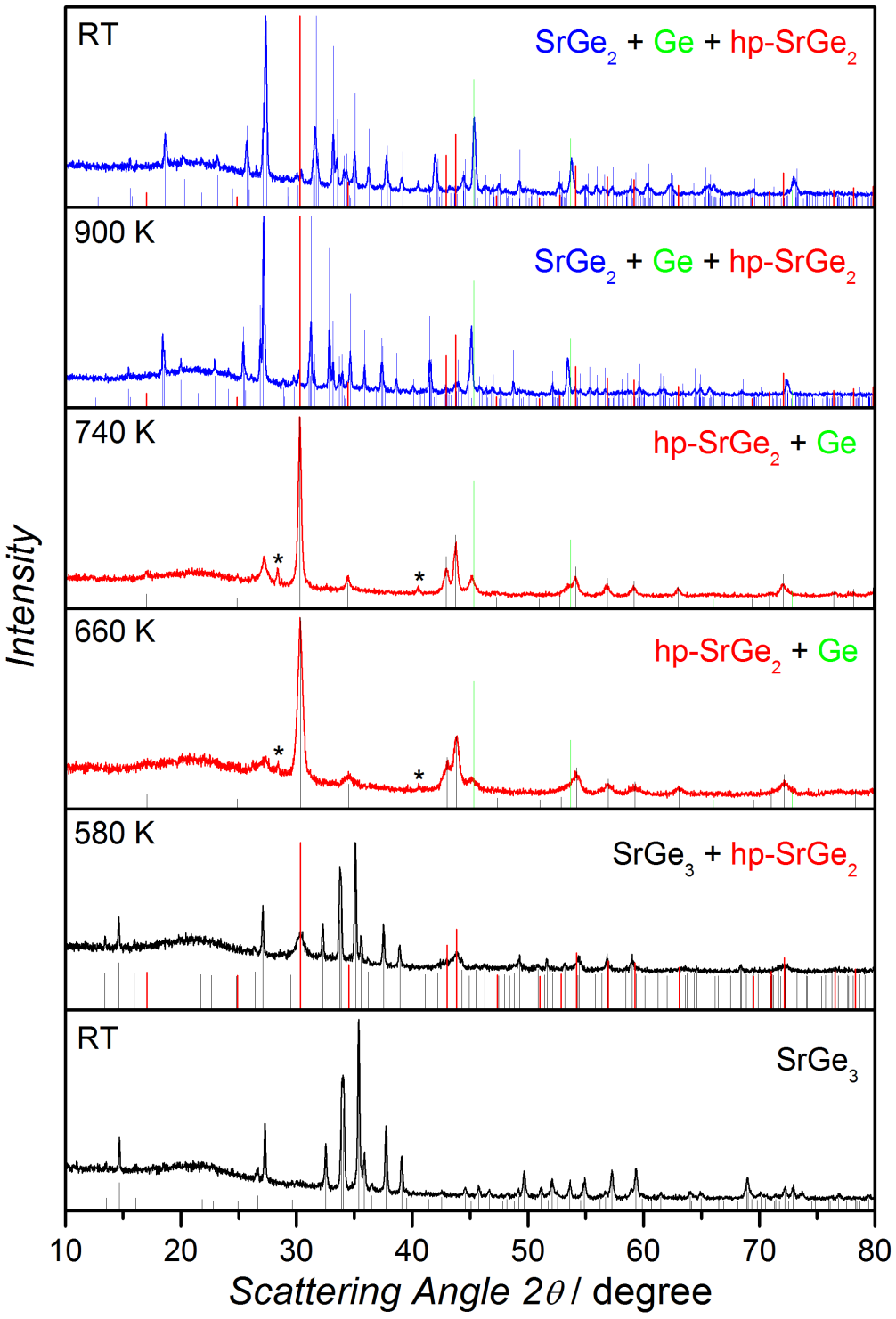

Figure 3.5.3 In-situ X-ray powder diffraction pattern of SrGe3 sample upon heating. The measured diffraction intensities and the reflection positions of different phases are marked by different colors.

The thermal stability of the three trigermanides are compared in Figure 3.5.4. A correlation between the decomposition temperature and the size of the metal atom is apparent. This correlation might be a consequence of the required pressure for the synthesis of each phase (8, 10, and 15 GPa for $CaGe_3$, $SrGe_3$, and $BaGe_3$, respectively) indicating that with increasing synthesis pressure the decomposition temperature decreases.

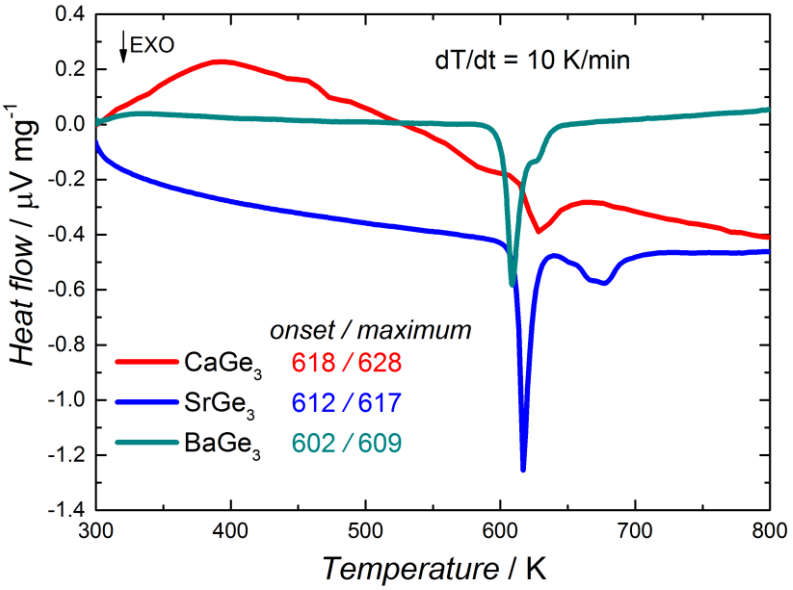

Figure 3.5.4 Comparison of the decomposition temperatures of the three MGe_3 phases. The first exothermic peak onset and maximum temperature values are given. The data points of $CaGe_3$ were extracted from the published data.

The structural parameters of MGe_3 (*M* = Ca, Sr and Ba) are plotted against the ionic radii of *M* (Ca^{2+} = 1.06 Å, Sr^{2+} = 1.27 Å, Ba^{2+} = 1.43 Å) [114] in Figure 3.5.5. The increment of the lattice parameter *a* is very small (in $SrGe_3$ it is 0.09 Å larger than $CaGe_3$ and in $BaGe_3$ it is 0.04 Å larger than $SrGe_3$) in contrast to the increase in the lattice parameter *c* (in $SrGe_3$ it is 0.73 Å larger than $CaGe_3$ and in $BaGe_3$ it is 0.72 Å larger than $SrGe_3$). Consequently, the ratio *c/a* increases almost constantly when the alkaline-earth element is replaced from Ca to Ba, and so does the volume, as shown in Figures 3.5.5 a-d.

The interatomic distances Ge – Ge and *M* – Ge are summarized in Figure 3.5.6. Huge differences are observed for the case of $CaGe_3$, in line with the changes in the lattice parameters. For instance, Ge1 – Ge1 and the short Ge2 – Ge2 contacts in the plot correspond to the dimer units, and the main effect of replacing the metal atom, in the sequence Ca – Sr – Ba, is the shortening of the interatomic distance within both dimers. For Sr and Ba the Ge2 dimers are 0.003 Å shorter than the Ge1 dimers and for Ca it is almost 0.05 Å longer. Recalling that the Ge1 – Ge1 dimer is perpendicularly oriented to the [001] direction and the Ge2 – Ge2 dimer is parallel to the same direction, one would expect a shorter distance in the Ge2 dimer for the $CaGe_3$ that has the lowest *c/a* ratio (Figure 3.5.5, c). For longer Ge – Ge contacts, the opposite situation is observed, changing the metal atom (Ca – Sr – Ba) increases the interatomic distances. The *M* – Ge contacts are affected in a systematic manner according to the nature of *M*, that is, the larger the metal atom, the longer the *M* – Ge distance.

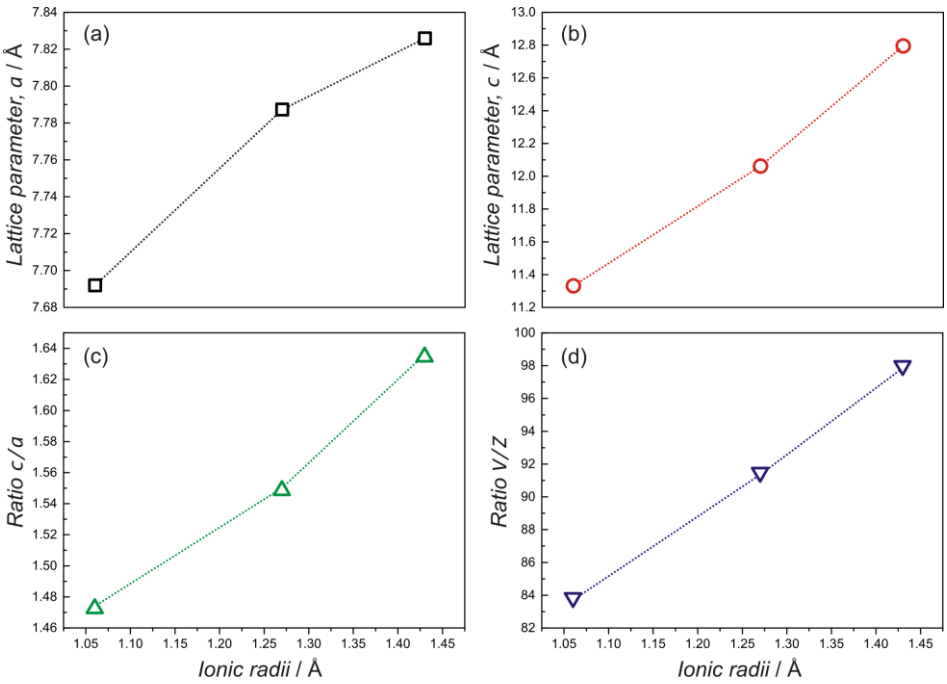

Figure 3.5.5 Structural parameters trends in $CaGe_3$, $SrGe_3$ and $BaGe_3$. As a function of the ionic radii of the alkaline-earth atoms.

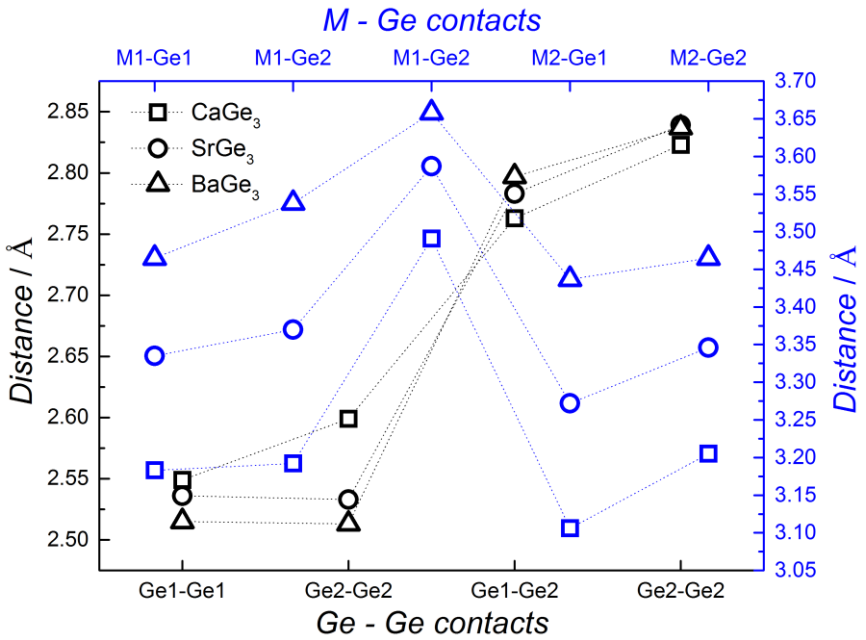

Figure 3.5.6 Interatomic Ge – Ge distances (black axis and data points) and *M* – Ge distances (blue axis and data points) in MGe_3 (*M* = Ca, Sr, Ba).

All these observations give evidence of the strength of the bonds within the dumbbells: If the size of metal atom increases, the interlayer space is expanded, keeping the intralayer distances along the (001) plane almost constant. Additional information into the nature of the different interactions between the short and long Ge – Ge contacts in $SrGe_3$ is gained by quantum chemical calculations.

3.5.4 Chemical bonding

Electronic structure calculations performed on $SrGe_3$ (Figure 3.5.7, left) reveal similar features in the density of states, DOS, to those of $BaGe_3$ (and the reported data of $CaGe_3$). It indicates a metallic behavior in the electronic transport properties, with major contributions to both, valence and conduction bands being attributed to the Ge atoms, and strong admixture of Sr and Ge states are reached at the vicinity of the Fermi level, involving Sr *d*- and Ge *p*-states.

The DOS was computed for $CaGe_3$ too in order to compare it with the present data. For that purpose, the same parameters were employed for the calculation (GGA with PBE, cut-off energies, convergence criteria, *k*-points). The results, together with the DOS of $SrGe_3$ and $BaGe_3$ are shown in Figure 3.5.7, right. The pattern resembles essentially the published data. However, for the present calculation the DOS at E_F is 0.22 states higher than the reported data, a difference which may be attributed to the code and functional employed (LDA vs GGA).

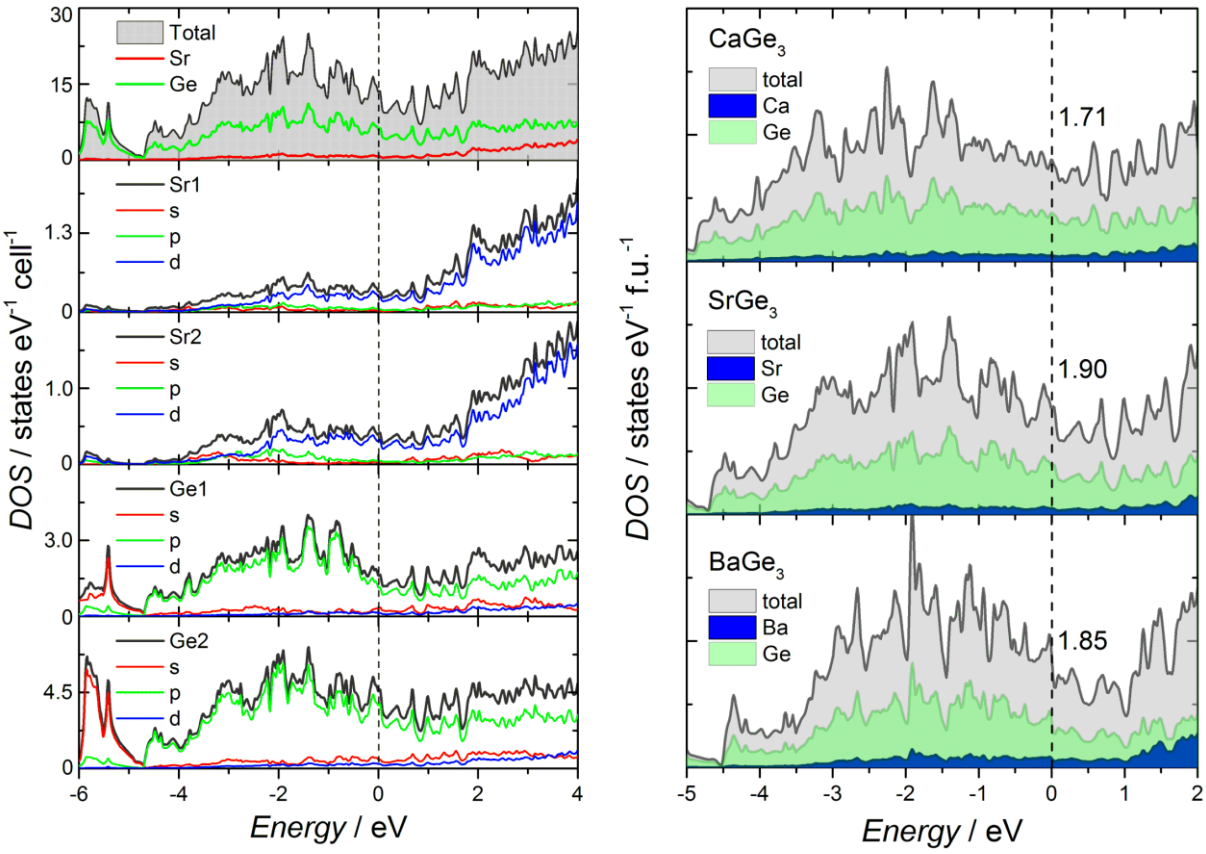

Figure 3.5.7 Total and orbital resolved DOS of $SrGe_3$ (left) and total and atom resolved DOS of $CaGe_3$, $SrGe_3$, and $BaGe_3$ (right). The number of states at Fermi level ($E - E_F = 0$) are specified.

First glance on the MGe_3 DOS does not evidence any systematic change in the number of states at E_F. $CaGe_3$ has the lowest and $SrGe_3$ the highest number of states, and $BaGe_3$ lies in between. The probable reason for that is the size effect of the metal atom. As the size of the metal increases, the states are shifted to higher energies, and since the region around E_F is composed of several peaks, the E_F matches different sections of those peaks, leading to different number of states. A second important

observation is the proportion of the atomic contributions. The ratio *M/Ge* which corresponds to the number of states belonging to the metal atoms over those belonging to the germanium atoms, both at E_F, amounts to 0.126, 0.119, and 0.200 for $CaGe_3$, $SrGe_3$, and $BaGe_3$, respectively. These numbers represent, to some extent, the hybridization degree of the *M d*-states with the Ge *p*-states, and it is much higher for $BaGe_3$.

Analysis of the electron density within the framework of the QTAIM performed on $SrGe_3$ reveals a complex pattern due to the huge number of critical points, and for the sake of clarity only the bond critical points (BCPs) are plotted for further analysis. Figure 3.5.8 shows the molecular graph in the unit cell of $SrGe_3$ and the color legend for each BCP. They are found between different Ge – Ge and Sr – Ge contacts, and no BCP between Sr – Sr contacts was detected.

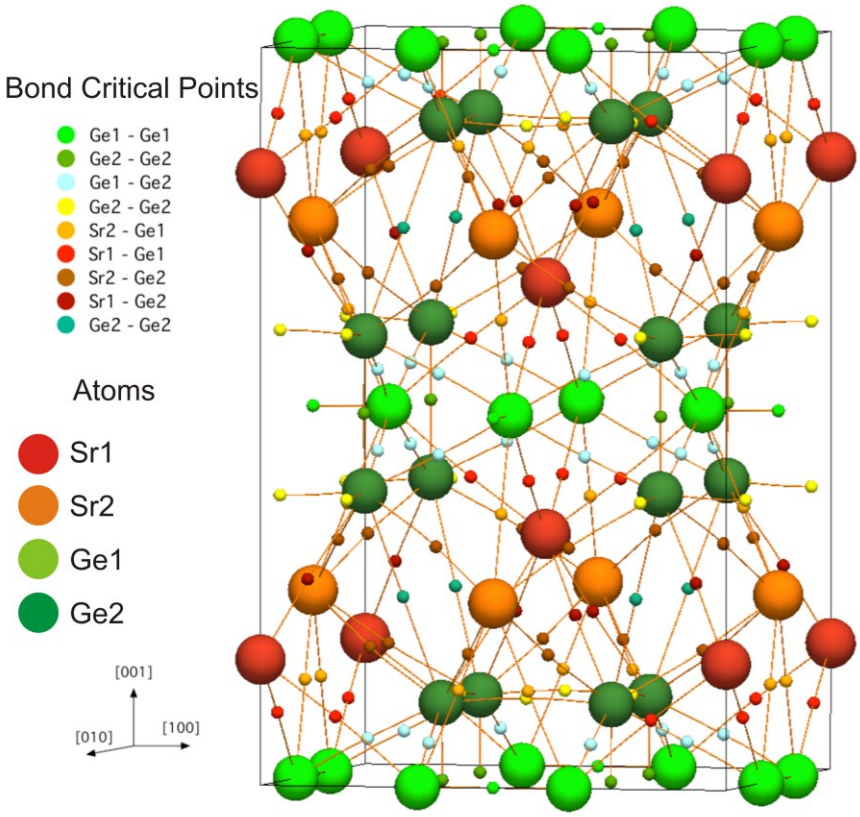

Figure 3.5.8 Unit cell of $SrGe_3$ showing the bond critical points (see legend for color code) and the bond paths (orange line between BCP and atoms).

The evaluation of the main topological properties (electron density $\rho(r)$, Laplacian of the electron density $\nabla^2\rho$, and the ellipticity ε) at the BCPs for $SrGe_3$ ($CaGe_3$ and $BaGe_3$ are included for comparison) are summarized in Table 3.5.1. For the different Ge – Ge contacts, $\rho(r)$ decreases as the distance increases, possessing the highest density the BCPs situated between the dimer units. It is remarkable to note that these dimers are the only contacts with a negative value of $\nabla^2\rho$, indicating covalent bonded atoms ($\nabla^2\rho < 0$ indicates that ρ is locally concentrated) and with a highly cylindrical distribution of ρ, (or strong σ character in the bond) as suggested by the low value of ε (the ellipticity

is defined as $\varepsilon = \lambda_1/\lambda_2 - 1$, with $\lambda_1 < \lambda_2 < 0$) [59,115]. The next short distance involving germanium atoms is Ge1 – Ge2 which still have noticeable electron density at the BCP but with depletion of charge which strongly deviates from the "cylindrical" shape, pointing to a delocalized bonding situation. The nature of the BCPs situated in between Sr and Ge is marked by the low electron density and a highly ionic component, presumably related to the expected charge transfer.

Table 3.5.1 Topological parameters at bond critical points in the topology of the electron density of $CaGe_3$, $SrGe_3$, and $BaGe_3$.

BCP	*Distance / Å*	$\rho(r)$ /e Å^{-3}	$\nabla^2\rho$ / e Å^{-5}	ε
Ge1 – Ge1 dimer	2.549(2)	0.4278	-0.3904	0.23
	2.538(4)	0.4407	-0.5157	0.19
	2.515(6)	0.4582	-0.6675	0.16
Ge2 – Ge2 dimer	2.599(1)	0.3799	-0.0010	0.07
	2.534(3)	0.4265	-0.3470	0.06
	2.515(4)	0.4420	-0.4964	0.05
Ge1 – Ge2	2.763(2)	0.2801	0.5856	0.41
	2.784(2)	0.2706	0.6049	0.52
	2.798(3)	0.2645	0.6073	0.56
Ge2 – Ge2	2.823(1)	0.2618	0.4796	0.06
	2.839(2)	0.2537	0.4555	0.08
	2.837(4)	0.2544	0.4193	0.08
M2 – Ge1	3.106(3)	0.1208	1.0387	0.32
	3.272(1)	0.1113	0.9326	0.25
	3.437(2)	0.1100	0.7928	0.20
M1 – Ge1	3.183(2)	0.1093	0.8459	0.01
	3.335(3)	0.1032	0.7760	0.05
	3.465(4)	0.1080	0.6892	0.11
M2 – Ge2	3.205(3)	0.1026	0.8772	1.01
	3.346(2)	0.0992	0.8001	0.63
	3.465(3)	0.1059	0.7278	0.37
M1 – Ge2	3.192)2)	0.1012	0.8772	0.54
	3.370(3)	0.0918	0.7615	0.47
	3.538(4)	0.0911	0.6531	0.36
Ge2 – Ge2 interlayer	3.390(1)	0.1255	0.4410	0.17
	3.801(3)	0.0823	0.2892	0.17
	3.791(4)	0.0601	0.1976	0.25
Ba1 – Ge2	3.491(2)			
	3.587(2)			
	3.658(3)	0.0823	0.5591	1.62

Although the Table 3.5.1 reveals a nearly constant variation of $\rho(r)$ with respect to the interatomic distances, there are two nonsystematic changes: One additional BCP with non-negligible value of $\rho(r)$ is found in $BaGe_3$, involving the Ba1 and Ge2 atoms. Interestingly, this observation supports the much higher degree of hybridization between the metal atom and the Ge states found for $BaGe_3$, in comparison to $SrGe_3$ and $CaGe_3$, as estimated by the DOS. The second interesting remark is the higher value of $\rho(r)$ found for the interlayer Ge2 – Ge2 BCP in $CaGe_3$, which is much larger than in $SrGe_3$ and $BaGe_3$. The reason for the relatively high $\rho(r)$ at this BCP is attributed to the small size of the Ca^{2+} ion

which allows the layers to be closer, and is in agreement with the smaller *c/a* ratio (Figure 3.5.5 c) observed in $CaGe_3$.

Interestingly, one particular ring critical point, RCP, with $\rho(r)$ was found in the three compounds at the center of the triangle made of Ge1 and the Ge2 dimer. The electron density (in e Å^{-3}) for this RCP are 0.2281, 0.2308, and 0.2288 for $CaGe_3$, $SrGe_3$, and $BaGe_3$ respectively. These numbers are not far from the values found in BCPs between the Ge2 – Ge2 contacts and supports the idea of a delocalized multicenter bonding.

According to the analysis of the saddle points, the bonding interactions in the crystal structure of MGe_3 compounds can be decomposed into an ionic component (*M* – Ge), covalent (Ge – Ge dumbbells) and delocalized (long Ge – Ge contacts). The ionic interaction is confirmed by integration of the electron density within the atomic QTAIM basins, which are summarized in Table 3.5.2.

Table 3.5.2 Volumes of the atomic basins (V_M and V_{Ge}), charge transfer and Pauling electronegativity differences ($\chi_M - \chi_{Ge}$) [116] of the high-pressure trigermanides.

Compound	V_{M1}	V_{M2}	V_{Ge1}	V_{Ge2}	$M1 \rightarrow$ Ge	$M2 \rightarrow$ Ge	$\chi_M - \chi_{Ge}$
	Atomic Basin Volume / Å^3				Charge transfer / Electrons		
$CaGe_3$	14.89	14.15	22.92	23.18	1.33	1.29	-1.01
$SrGe_3$	20.24	19.29	23.38	24.05	1.32	1.28	-1.06
$BaGe_3$	27.90	26.78	22.85	23.89	1.16	1.12	-1.12

As expected, the basin volume increases as the size of *M* is larger, with *M*2 being always slightly smaller than *M*1. On the other hand, the size of *M* does not seem to have any systematic effect on the basin volume of the Ge atoms. The electrons delivered from the electropositive metal are not fully the estimated valence electrons, 2 e^-, and are contrary to the expected trend from electronegativity differences; Ca transfers 1.31 e^- and Ba 1.14 e^- while the larger electronegativity difference is found in the barium compound. This disagreement was investigated in more detail by means of electron localizability indicators. ELI-D has proven to be an invaluable tool in the analysis of chemical bonding in solids, especially when multicenter interactions are present [117].

Alike to $BaGe_3$ (chapter 3.4.2), the absence of the last shell in Sr indicates the charge transfer and the structuring of its penultimate shell suggests interactions with the Ge layers (Figure 3.5.9, left). The topology of the ELI-D isosurfaces can be decomposed into two types: core and valence attractors. Beside the core attractos, five valence ELI-D attractors are found in $SrGe_3$ (Figure 3.5.9, right): two well localized disynaptic attractors lying in between the atoms of each dumbbell, two lone-pair like attractors located around Ge atoms in the bond opposite region, and one around the long Ge2 – Ge2 contact. Surprisingly, no attractor was detected along the Ge1 – Ge2 contact, which is shorter than the long Ge2 – Ge2 interatomic distance. Interestingly, both lone-pair like attractors can be decomposed into smaller attractors. For Ge1 the splitting results in three attractors, one of them remains along the bond axis and the other two are shifted towards the Sr1 atoms. In the case of Ge2, the splitting gives rise to two attractors, located at the center of Ge2-Sr1-Sr1-Sr2 and Ge2-Sr1-Sr2-Sr2 tetrahedrons.

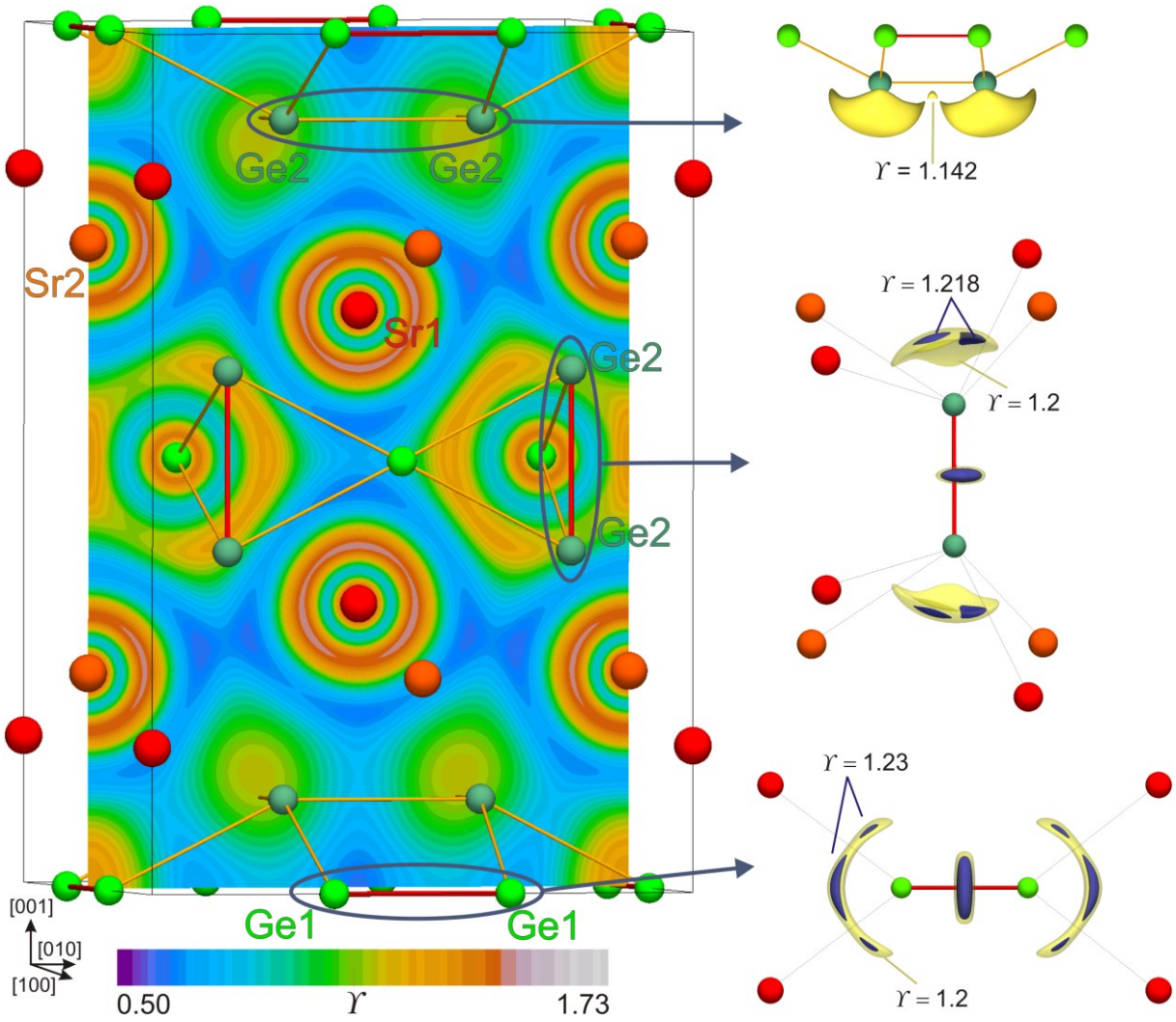

Figure 3.5.9 Distribution of the ELI-D in $SrGe_3$. The structuring of the penultimate shell of both Sr atoms are clearly visible from the slice parallel to [001] (left). The ELI-D isosurfaces, at different values of Υ, are shown separately (right) for the valence region of both Ge atoms. The lone-pair like attractor of both Ge atoms (yellow isosurfaces) splits at slightly higher values of Υ (blue isosurfaces), revealing clearly the interaction between Ge and Sr atoms.

Integration of the electron density within the ELI-D basins yields nearly two electrons for the attractors in both dumbbells, while a population of almost four and three electrons is detected for the lone-pair like attractor around the Ge1 and Ge2, respectively. When the integration is performed on the split basins, it results in 2x 1.7 electrons + 0.9 electrons for the lone-pair like on Ge1 and 2x 1.54 electrons for the lone-pair like on Ge2, thus they conserve the number of electrons as in the big lone-pair like attractor. For the small attractor located in the vicinity of the bond region involving the long Ge2 – Ge2 contact, the integration amounts to half-electron. By intersecting the QTAIM atoms with the ELI-D basins, the corresponding atomic contribution to the valence ELI-D basins is obtained. In the case of the dumbbells, the two electrons are equally shared by the atoms. The same sharing is obtained in the long Ge2 – Ge2 basin. For the lone-pair like basin in Ge2, 89% is contributed by the Ge2 atom and the remaining is attributed to the Sr atoms. For the lone-pair in Ge1, 80% belong to the Ge1, 10% to Ge2 and the remaining share comes from the Sr. Since the Ge2 contributes significantly to this basin, the

Ge1 – Ge2 interaction can be considered as multicenter with participation of the Sr atoms. Although the dumbbells have technically the same interatomic distance, the surrounding Sr atoms are distributed around them in a significant different manner: four Sr1 atoms on the same plane with the Ge atoms in Ge1-Ge1 dumbbell (two around each Ge1 atom) and four Sr atoms (two Sr1 and two Sr2) around each Ge2 in Ge2-Ge2 dumbbell. These different environments are responsible for the different electron counts on each dumbbell, which results in the species: $(Ge1\text{-}Ge1)^{-2.8}$ and $(Ge2\text{-}Ge2)^{-0.6}$, by adding all basin populations around each dumbbell. Finally, the electron balance in $SrGe_3$ according to the ELI-D picture can be written as $[Sr^{+2}]_2[(Ge1\text{-}Ge1)]^{-2.8}[(Ge2\text{-}Ge2)^{-0.6}]_2$, which illustrates the Zintl-like nature of the bonding in this compound. The complete set of results for $CaGe_3$ and $BaGe_3$ are summarized in Table 3.5.4

Table 3.5.4 Population of the ELI-D valence basins (in electrons) and atom contribution to the lone-pair basins.

ELI-D Basin	**$CaGe_3$**	**$SrGe_3$**	**$BaGe_3$**
Ge1-Ge1 dumbbell	2.05	2.15	2.21
Ge2-Ge2 dumbbell	1.70	1.91	1.95
Ge2-Ge2 long	0.50	0.49	0.66
Lone-pair in Ge1	4.66	4.35	4.11
Lone-pair in Ge2	3.01	3.07	2.88
Contributions in Lone-pair of Ge1	78.0% Ge1 13.4% Ge2 5.6% Ca1 3.0% Ca2	80.6% Ge1 10.2% Ge2 6.0% Sr1 3.2% Sr2	81.7% Ge1 10% Ge2 5.6% Ba1 2.8% Ba2
Contributions in Lone-pair in Ge2	90.8% Ge2 5.6% Ca2 4.2% Ca1	89.0% Ge2 5.6% Sr2 5.0% Sr1	87.9% Ge2 6.4% Ba2 5.4% Ba1

The bonding picture is quite similar in the three compounds, although minor differences are observed in the number of electrons. Interestingly, the largest amount of electrons within the bonding basins belongs to $BaGe_3$, while in $CaGe_3$ are concentrated the highest negative charge within the lone-pair like basins. This fact can be attributed to the interatomic distances: the shortest Ge – Ge (and shortest *M* – Ge) distances belong to $BaGe_3$ and the shortest *M* – Ge (and longest Ge – Ge) distances are observed in $CaGe_3$. The polar nature of the MGe_3 compounds is evidenced by the significant contribution of *M* to the bonds, especially within the lone-pair like attractor in Ge2, which has larger participation of Ba. This is in agreement with the unexpected observation in the electronegativity and the QTAIM charges.

3.5.5 Magnetic susceptibility and electrical resistivity

Low-temperature magnetic susceptibility measurements (B_{ext} = 0) are shown in Figure 3.5.10 left. The compound becomes a superconductor below 5.3(5) K as observed by the Meissner effect, with a shielded volume close to 100% (unaccounted for geometrical factors), however, it reaches only 5% of

-1/4π, which is typical for type-II superconductors. High-field magnetic susceptibility measured from room temperature down to 2 K (not shown) indicates diamagnetic behavior of $SrGe_3$ in the whole investigated range, after correction for paramagnetic impurities. Electrical resistivity measurements at high-temperature and in the normal state ($B_{ext} > B_{c2}$) reveal the metallic character of the sample, similar to $BaGe_3$ (chapter 3.4) and $CaGe_3$ [36]. In the low-temperature range and without the presence of an external magnetic field, the compound enters in the superconducting state at *Tc* = 5.7(3) K (Figure 3.5.10 right). Although *Tc* differs in the different measurements, the values agree within the standard deviation. It is worthy to mention that *Tc* estimated from magnetic susceptibility has a larger standard deviation because the amount of sample employed was very small (< 10 mg).

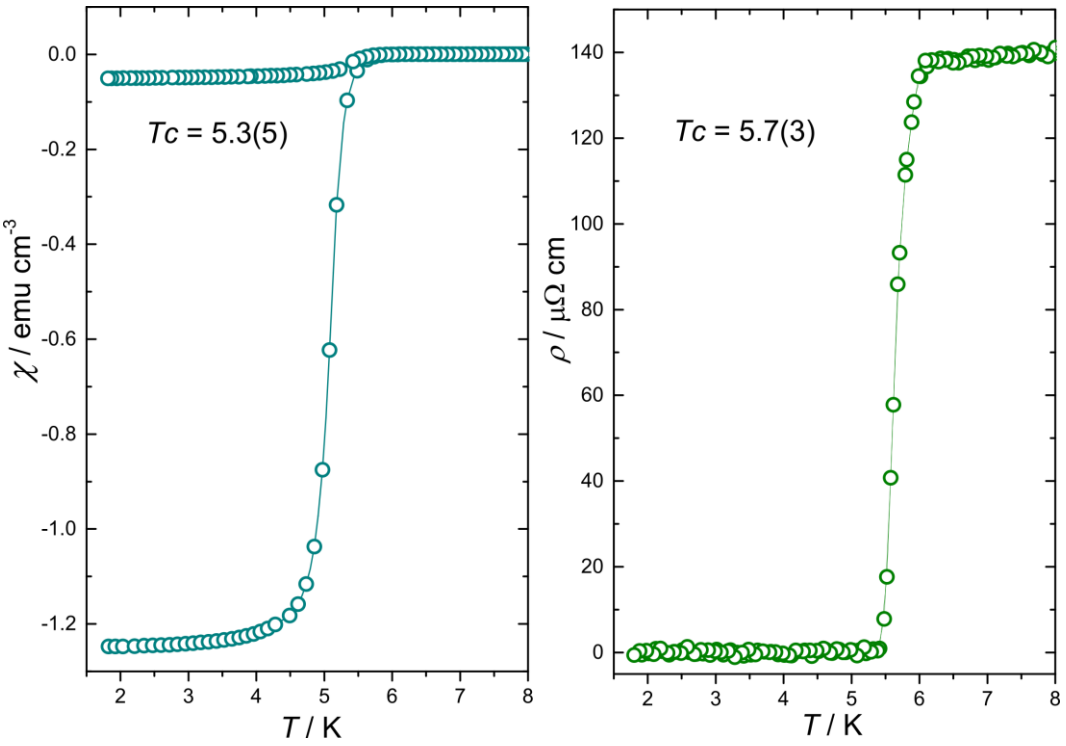

Figure 3.5.10 Low-temperature magnetic susceptibility (left) and electrical resistivity (right) of $SrGe_3$ at B_{ext} = 0. From the Meissner effect and a superconducting volume fraction of ~1.2 (unaccounted for geometrical factors) is estimated. The transition temperatures are the same within the standard deviations.

3.5.6 Specific heat

The specific heat of $SrGe_3$ in the low temperature region is shown in Figure 3.5.11 left. The broad anomaly observed at zero magnetic field (black squares) is completely vanished at 1 T (green circles). In the high-temperature region, the specific heat approaches quite well the value of the Dulong-Petit law (Figure 3.5.11 left, inset).

Similar to $BaGe_3$ and $CaGe_3$, a fit to the data in the form CpT^{-1} *vs* T^2 of $SrGe_3$ in the normal state (Figure 3.5.11, right) is performed in a standard way according to the expansion:

$$Cp_n(T \to 0) = \gamma_n T + \sum_{n=1}^{2} \beta_{2n+1} T^{2n+1}$$

Where the first term is the electronic contribution, with $\gamma = 1/3\pi^2 k_B^2(1+\lambda_{ep})N(E_F)$, k_B Boltzmann´s constant, λ_{ep} the electron-phonon coupling constant and $N(E_F)$ the density of states at the Fermi level. The second term is the low-temperature expansion of the lattice specific heat, $\beta_3 = 12/5 N_A k_B^4 \theta_D^{-3}(0)$, with N_A = Avogadro´s number and $\theta_D(0)$ the initial Debye temperature. A fit to normal-state data from 1.9 to 6.3 K results in γ = 5.04 mJ mol^{-1} K^{-2} and an initial Debye temperature $\theta_D(0)$ = 287 K.

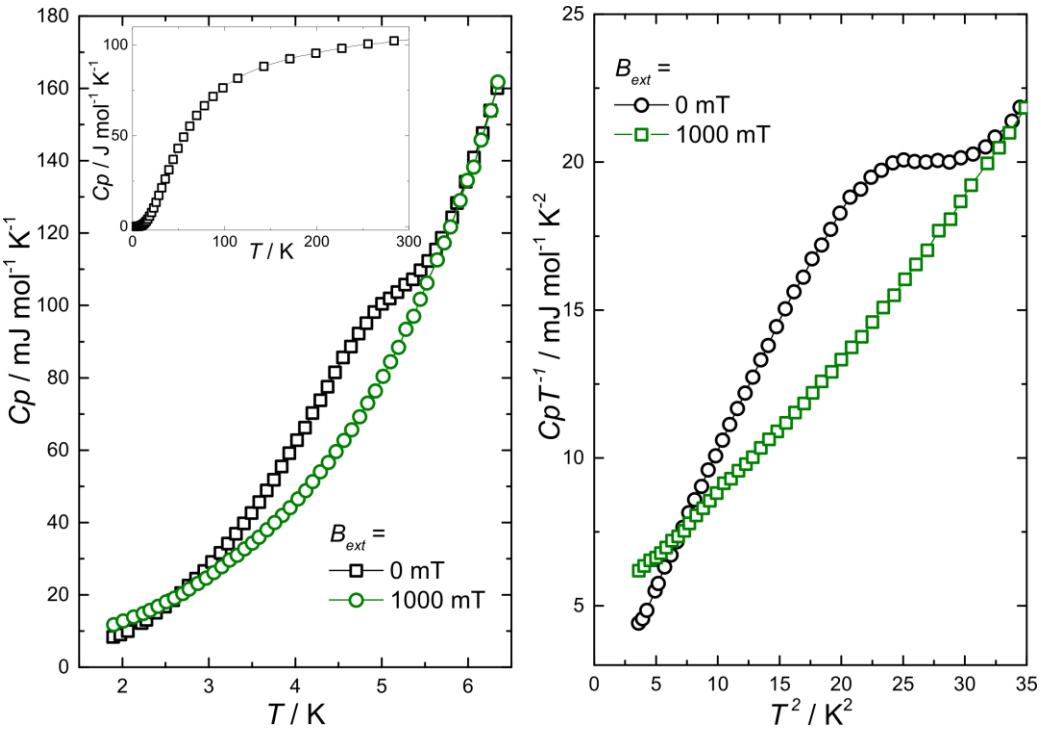

Figure 3.5.11 Low temperature specific heat of $SrGe_3$ in the form *Cp vs T* (left) and CpT^{-1} *vs* T^2 (right). Both, the superconducting state (black squares) and in the normal state (green circles) are shown at the indicated external magnetic field. Inset shows the high temperature region.

The difference in the specific heat, defined as the specific heat in the superconducting state (B_{ext} = 0) minus the specific heat in the normal state ($B_{ext} > B_{c2}$) for $SrGe_3$ is shown in Figure 3.5.12. By using the local entropy balance method around the phase transition, the transition temperature is found to be Tc = 5.2(2) K and $\Delta Cp/\gamma Tc$ = 1.3, which indicates weak electron-phonon coupling close to the BCS limit ($\Delta Cp/\gamma Tc$ = 1.43) [118].

The difference in the specific heat for $SrGe_3$ at different magnetic fields is shown in Figure 3.5.13. By using the WHH extrapolation [103], the critical magnetic field was determined to be B_{c2} = 300 mT, which lies in between the estimated values of $CaGe_3$ and $BaGe_3$. Table 3.5.5 contains the summary of the parameters determined from specific heat measurements on $SrGe_3$ and are compared with those of $CaGe_3$ and $BaGe_3$.

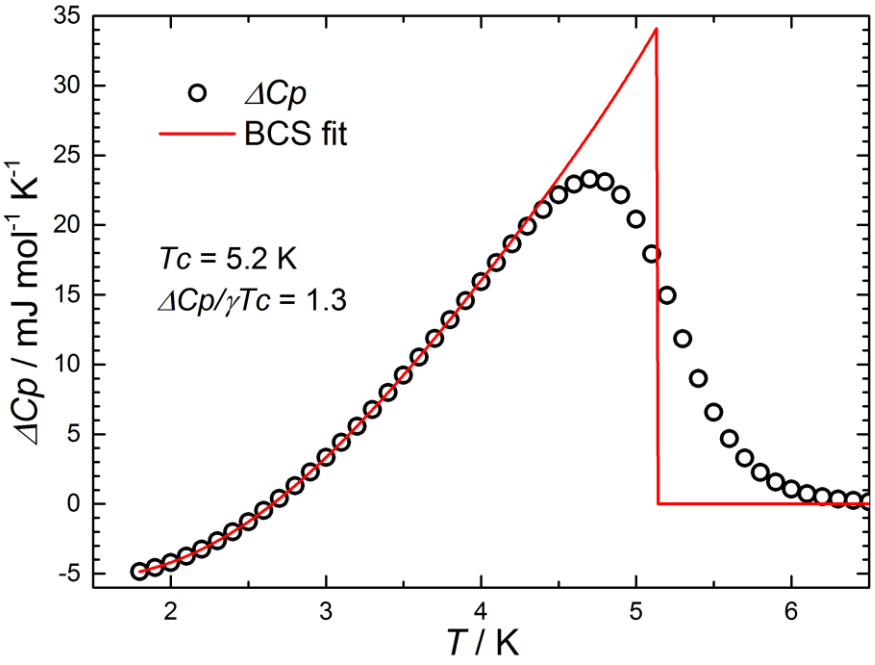

Figure 3.5.12. Temperature dependence on the difference in the specific heat for $SrGe_3$. The BCS theory resembles well the experimental data and is in agreement with the entropy conservation method.

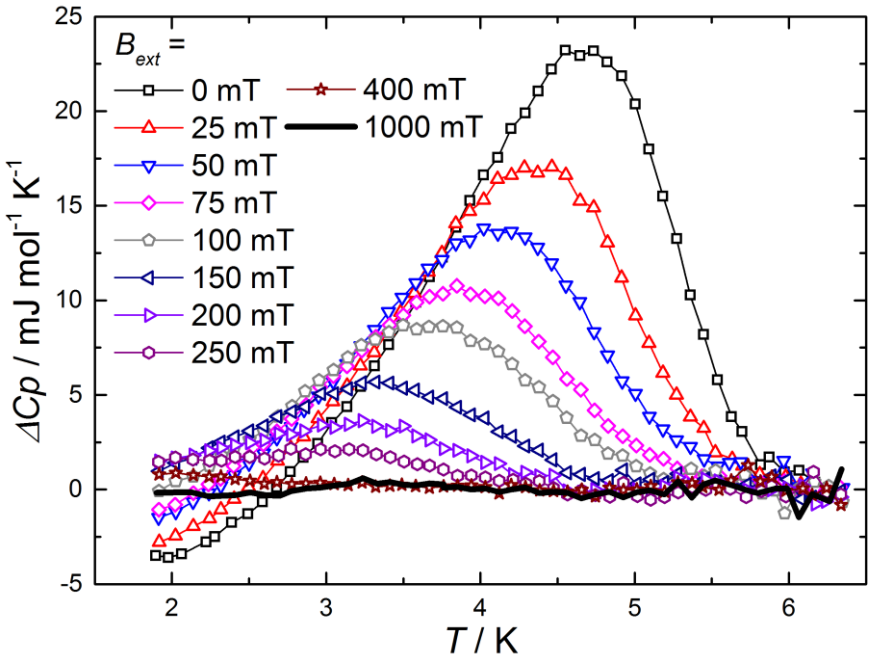

Figure 3.5.13 Difference specific heat plot for $SrGe_3$. The *Tc* values extracted at each magnetic field were used for the WHH extrapolation.

First glance into Table 3.5.5 reveals different transition temperatures and different trends on them depending on the measurements they were obtained. For this reason, only the *Tc* values obtained from specific heat measurements, will be discussed.

There is no apparent relation between the nature of the metal atom and *Tc* in this family of isostructural compounds. In order to find an explanation for such behavior, examination of the remaining parameters is essential. An estimation of the electron coupling parameter, λ_{ep}, was performed by using the McMillan´s formula [106]:

$$Ln\left(1.45\frac{Tc}{\theta_D}\right) = \frac{-1.04\left(1+\lambda_{ep}\right)}{\lambda_{ep} - \mu^*\left(1+0.62\lambda_{ep}\right)}$$

Table 3.5.5 Summary of the superconducting parameters obtained by specific heat measurements on *M*Ge_3.

Parameter	**$CaGe_3$**	**$SrGe_3$**	**$BaGe_3$**
***Tc* / K (from χ)**	6.8	5.3	6.5
***Tc* / K (from ρ)**	6.2	5.7	6.8
***Tc* / K (from *Cp*)**	6.5	5.2	5.6
γ / mJ mol^{-1} K^{-2}	6.31	4.64	6.32
θ_D / K	330	287	266
***N*(E_F) / states eV^{-1} $f.u.^{-1}$ (from γ)**	2.68	2.14	2.68
***N*(E_F) / states eV^{-1} $f.u.^{-1}$ (from band structure)**	1.49	1.97	1.85
λ_{ep} (from McMillan)	0.72	0.70	0.74
ΔCp/γTc	1.6	1.4	1.3
B_{c2} / mT	290	300	315

Employing a value of μ^* = 0.15 (typical for metals) and using the *Tc* from specific heat data, λ_{ep} results in 0.72, 0.70 and 0.74 for $CaGe_3$, $SrGe_3$ and $BaGe_3$, respectively. These values together with the reduced specific heat jump $\Delta Cp/\gamma Tc$, which classifies the superconductor according to the coupling strength, clearly favor the highest *Tc* in $CaGe_3$ among the three compounds.

3.5.7 Conclusions

The new compound $SrGe_3$ was successfully characterized and its properties were discussed and compared to those of $CaGe_3$ and $BaGe_3$. Concerning the structural features, replacing the alkaline-earth atom in the *M*Ge_3 family affects strongly the *c* axis of the unit cell, while minor changes occur for the lattice parameter *a*. A consequence of this is the strong interlayer interaction observed in $CaGe_3$, according to the BCP with considerable electron density found in between Ge atoms of adjacent layers. In the same sense, $BaGe_3$ is characterized by the appearance of additional *M* – Ge interactions that are

absent in the other two compounds. This observation was supported by the DOS calculations, in which a higher degree of hybridization of *M-d* states with Ge-*p* states was estimated.

Bonding analysis in real space revealed strong covalent bond within each Ge dimer (2c2e), weak and multicenter interactions with marked contributions of the metal atoms are present for the long Ge-Ge contacts. The lone-pair like attractors contained most of the alkaline-earth metal contributions. In fact, these lone-pair like attractors turned out to be well localized attractors which involved Ge-Sr in both dumbbells.

Regarding the superconducting properties, it was shown that high density of states at E_F is not the only nor the main conditions for high *Tc*. For this family of compounds, the main parameter that governs the superconductivity seems to be the reduced specific heat ratio, $\Delta Cp/\gamma Tc$, followed by the electron-phonon coupling constant, λ_{ep}. Although $SrGe_3$ has the highest DOS at E_F, it shows the lowest *Tc*, while $CaGe_3$ has considerably lower DOS at E_F, but higher values of $\Delta Cp/\gamma Tc$ and λ_{ep}, it shows the highest *Tc* among the three isostructural compounds.

3.6 $EuGe_3$

With the finding of $BaGe_{5.5}$ which is isotypic to $SrGe_{5.5}$, and taking into account the often similar chemistry of Ba or Sr with Eu, a compound with target composition $EuGe_{5.5}$ was attempted under similar conditions to $BaGe_{5.5}$ (chapter 3.2). Three experiments carried out on mixtures with composition $EuGe_{5.5}$ yielded well-resolved reflections in the X-ray powder diffraction pattern, from which the high-pressure form of germanium *(tP12)* was identified (black ticks in Figure 3.6.1), while the rest of the reflections did not coincide with any of the known phases in the Eu – Ge system. The samples were prepared for metallographic analysis, and together with WDX, a phase with composition $EuGe_{3.10(1)}$ was identified to be present in a matrix of germanium (Figure 3.6.2, a and b).

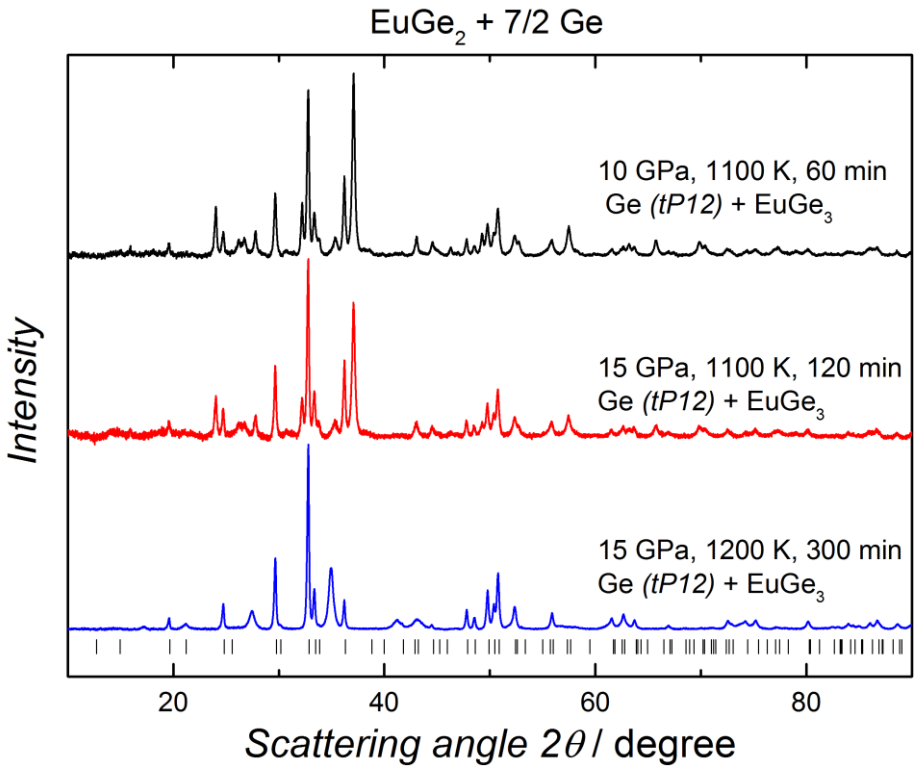

Figure 3.6.1 X-ray powder diffraction patterns of the product obtained from three HPHT experiments done on a mixture with composition $EuGe_{5.5}$. Black vertical ticks indicate the reflection position of Ge *(tP12)*.

3.6.1 Preparation

Knowing the composition of the unidentified phase, a new set of experiments was performed. The synthesis of the new germanide starts with arc-melting of the elements in the approximate ratio 1:3 and subsequent application of high-pressure high-temperature conditions to the as-cast product. In order to account for the mass loss during the melting process, an excess of 1% europium was added. Synthesis at 8 GPa and 1000 K, obtained the earlier reported $BaPb_3$-type modification *(hR36)* $EuGe_3$ [119]. Starting from 10 GPa on, the yielded products are the new hexagonal form *hP8*, together with the *h*R36 isomorph. At 12 GPa single-phase *hP8* is observed (Figure 3.6.3) and at 15 GPa new set of broad reflections appeared and became dominant when the annealing time is longer (Figure 3.6.1,

blue line). These new pattern may indicate another modification. Thus, the selected pressure for the synthesis of the hexagonal modification of $EuGe_3$ *(hP8)* was 12 GP. This Mg_3Cd-type [120] atomic pattern is isotypic to one of the high-pressure phases of $BaGe_3$ [98]. Metallographic inspection of the new sample revealed a single phase, with composition $EuGe_{3.03(6)}$, as determined by WDX analysis (Figure 3.6.2, c and d). The x-ray powder diffraction patterns obtained at 12 GPa and different temperatures are showed in Figure 3.1. It can be seen that as the temperature increases, the crystallinity of the sample is improved, as well as some impurity reflections observed at low temperature, vanishes at high temperatures.

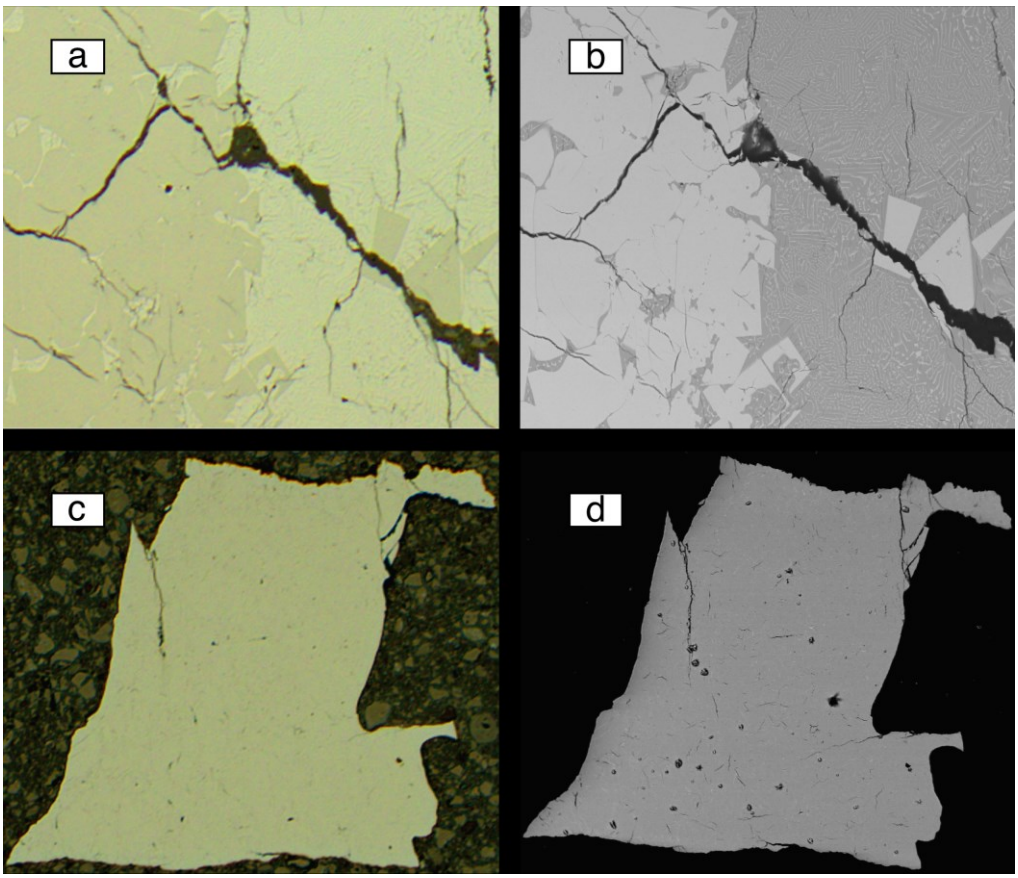

Figure 3.6.2 Microstructure of samples with nominal composition $EuGe_{5.5}$ as revealed by (a) bright field optical microscope and (b) BSE, and samples with nominal composition $EuGe_3$ in (c) bright field optical microscope and (d) BSE.

The thermal stability of $EuGe_3$ at ambient pressure was investigated by differential thermal analysis measurements (Figure 3.6.4). The data reveal a single exothermal effect upon heating at 573 K (onset), and this signal does not have any equivalent in the cooling curve. X-ray powder diffraction data collected on the products obtained after the heating cycle, and on a sample which was annealed at 773 K for two days evidence decomposition of $EuGe_3$ into $EuGe_2$ [121] and α-Ge (Figure 3.6.5). These findings clearly indicate that $EuGe_3$ is a high-pressure high-temperature phase, which is metastable at ambient pressure.

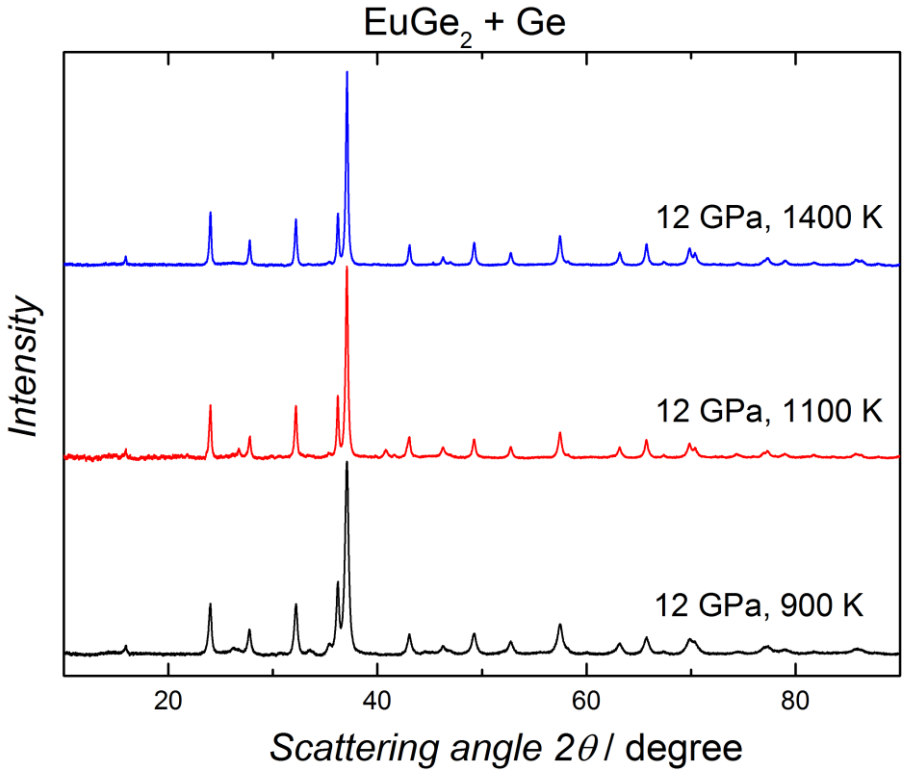

Figure 3.6.3 X-ray powder diffraction patterns of samples with nominal composition $EuGe_3$ synthesized at 12 GPa and different annealing temperature.

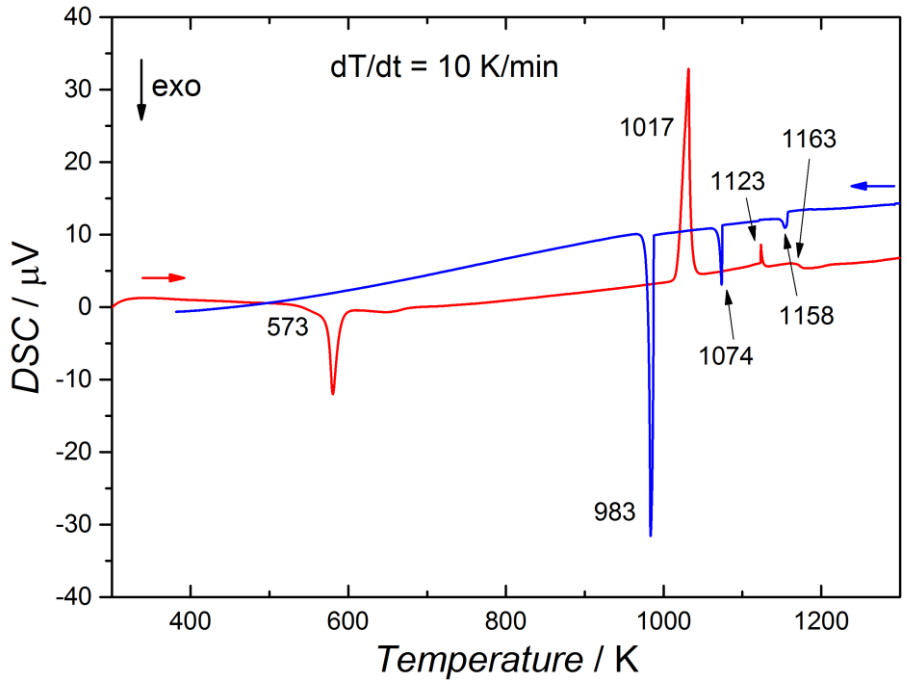

Figure 3.6.4 Thermal behavior of $EuGe_3$ at ambient pressure. The exothermic effect indicates the decomposition reaction $EuGe_3 \rightarrow EuGe_2 + Ge$, with an onset temperature of 573 K.

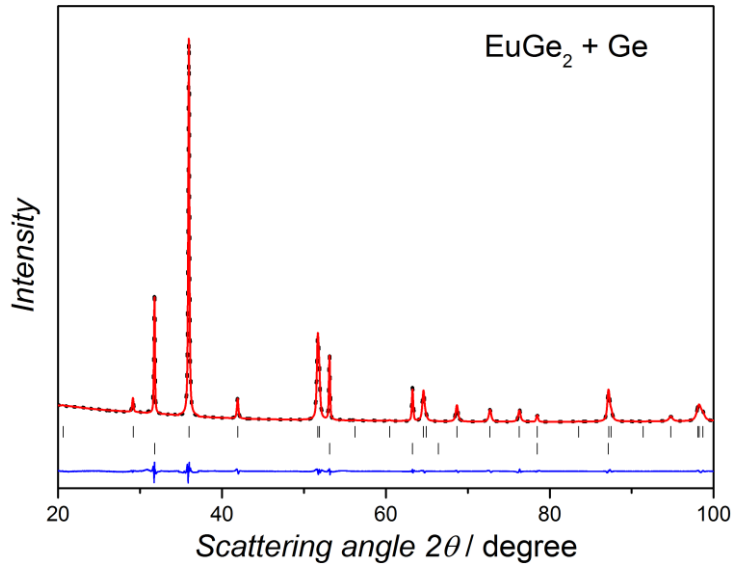

Figure 3.6.5 X-ray powder diffraction pattern of $EuGe_3$ sample annealed at 773 K for 2 days: Black points and red lines correspond to the observed and calculated profiles, respectively. Reflection positions are marked by vertical ticks (upper row: $EuGe_2$, bottom row: Ge) and the difference between observed and calculated intensities is shown as blue line.

3.6.2 Crystal structure

The crystal structure of (*h*P8) $EuGe_3$ is refined first in the centrosymmetric space group $P6_3/mmc$ by the Rietveld method using high-resolution synchrotron X-ray powder diffraction data, employing the model of the hexagonal phase of $BaGe_3$ (Figure 3.6.6). The crystallographic information is presented in Table 5.27, atomic positions and displacement parameters are listed in Table 5.28 and 5.30.

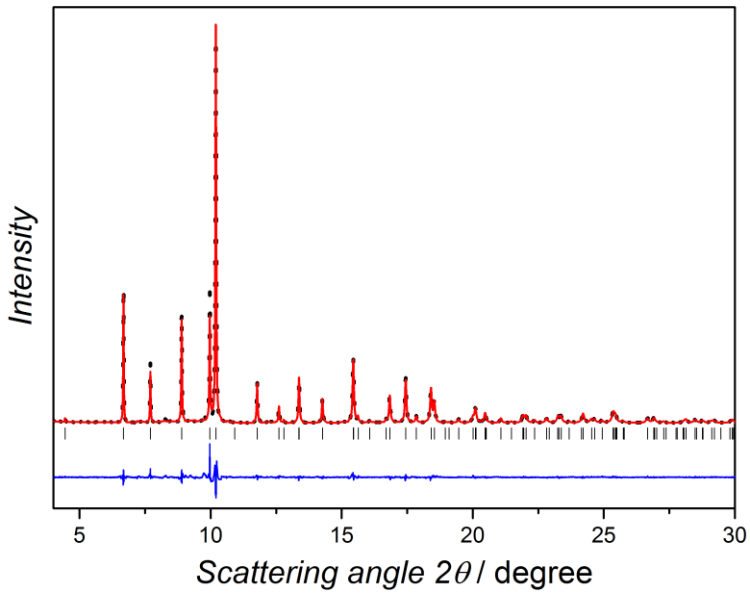

Figure 3.6.6 X-ray powder diffraction pattern of $EuGe_3$ *(hP8)* (high-resolution x-ray synchrotron radiation data). Black points and red lines correspond to the observed and calculated profiles, respectively. Reflection positions are marked by vertical ticks and the difference between observed and calculated intensities is shown as blue line.

The extreme anisotropy of the atomic displacement of europium B_{33} >> B_{11} = B_{22} indicates that the atoms have a significant probability of being located outside the mirror plane which is oriented normal to the hexagonal axis of the crystal structure. The improved model takes into account this disorder of the europium atoms, thereby reducing the anisotropy of the atomic displacement factors significantly (Figure 3.6.7). Final values for the atomic coordinates and atomic displacement parameters are listed in Tables 5.31 and 5.33.

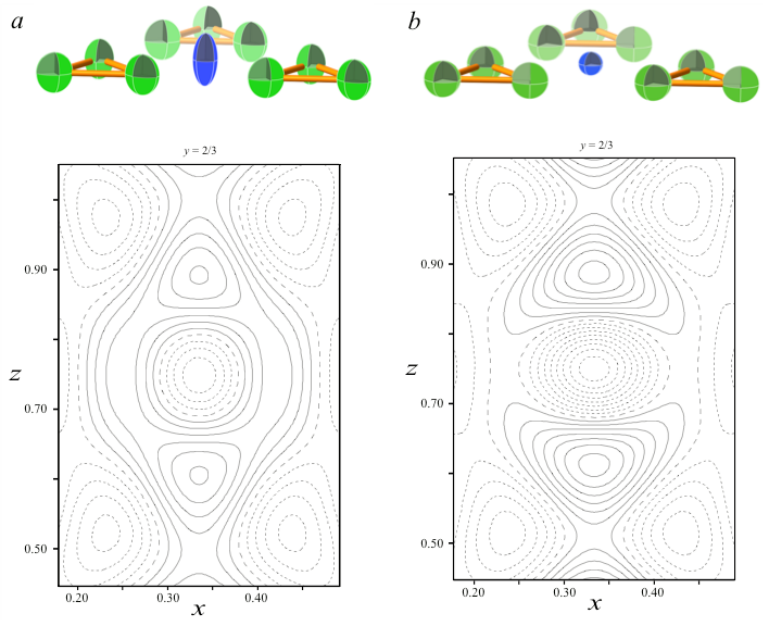

Figure 3.6.7 Atomic displacement ellipsoids of Eu and its neighbors in the ab plane (top) and difference Fourier map projected in the *zx* plane (bottom) for the models refined in (a) the centrosymmetric space group *P6₃/mmc* and in (b) the non-centorsymmetric space group *P6₃mc*.

The ideal structure of $EuGe_3$ with Eu atoms located well within the mirror planes perpendicular to the [001] direction can be assigned to the Mg_3Cd-type [120] of crystal structure. In a first approximation this structure pattern represents an ordered derivative of the hexagonal close packing, i.e. layers with a component ratio of 1:3 are stacked in a sequence …ABABA… along the [001] direction. The coordination number of the europium atoms corresponds to twelve with interatomic distances *d*(M-Ge) of 3.220(7) Å to 3.290(6) Å. In an undistorted decoration variety of atoms with equal radii, the majority component germanium would occupy a position with the coordinates (1/6 1/3 1/4). In the crystal structure of $EuGe_3$, the germanium atoms are located at (0.1384, 0.2768, 1/4) and thus, are strongly shifted from the ideal position. The displacement corresponds to a differentiation of the distances *d*(Ge–Ge) into short 2.663(7) Å and long 3.748(9) Å contacts yielding discrete equilateral triangles of germanium. The Ge_3 units of adjacent layers are rotated by 60° against each other (Figure 3.6.8a). The resulting infinite columns are often described as an ensemble of face-sharing octahedral (Figure 3.6.8b), but the shortest distances *d*(Ge–Ge) between the layers are markedly longer 2.916(7) Å than the contacts within the Ge_3 groups. For comparison, the short contact *d*(Ge–Ge) within the Ge_3

groups of the high-pressure phase $LaGe_3$ [122] amounts to 2.635(3) Å. Here, the distances *d*(Ge–Ge) between units in adjacent layers fall into the range from 2.944(4) Å to 3.031(7) Å. In $LaGe_3$ and $EuGe_3$, the coordination number of the rare-earth element atoms corresponds to twelve with interatomic distances *d*(*M*–Ge) (*M* = Eu, La) of 3.175(4) Å to 3.230(4) Å in the lanthanum and 3.2198(4) Å to 3.2881(3) Å in the europium compound. Similar arrangements of triangular tetrel units are present in the related $BaPb_3$-type crystal structure [123].

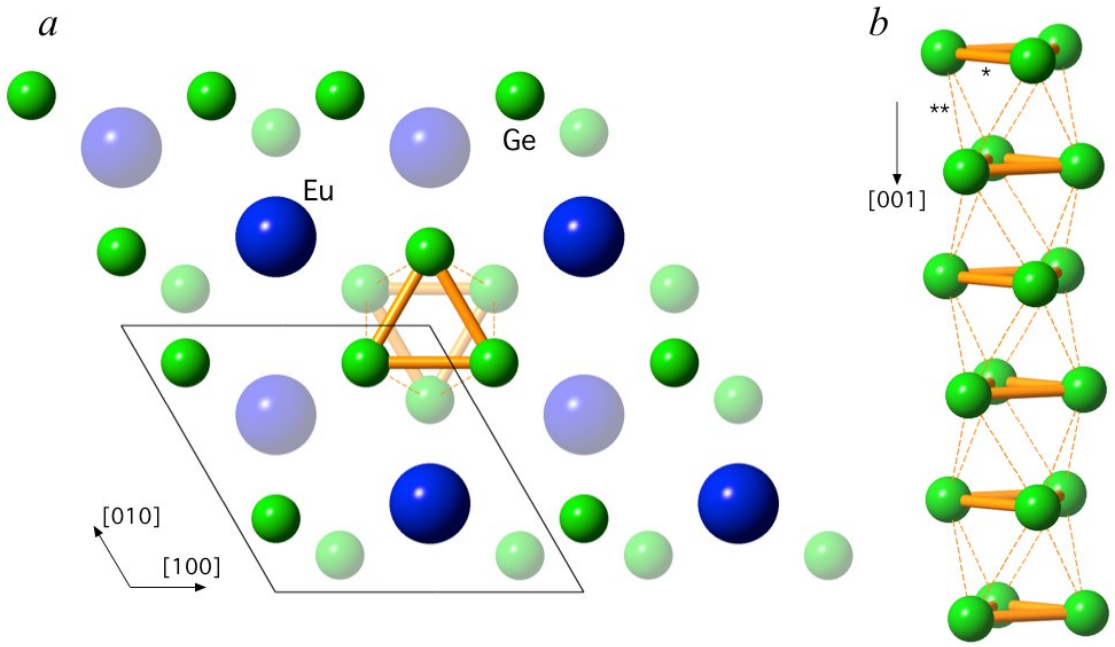

Figure 3.6.8 (a) Crystal structure of $EuGe_3$ in a projection along [001]. Light- and dark-colored atoms represent the layers at z = ¼ and ¾, respectively. Black lines indicate the unit cell. (b) Column of face-sharing octahedrons made of Ge3 units parallel to [001]. Intra- and interatomic Ge – Ge distances indicated by * and **, respectively, amount to 2.663(7) Å and 2.916(7) Å.

The distances *d*(Ge–Ge) within the triangular germanium units are significantly longer than those in diamond-type germanium (2.449 Å) and those of classic two-center two-electron bonds in Zintl-compounds like $EuGe_2$ [121] (2.556(5) Å) or Eu_5Ge_3 [124] (2.5603(8) Å), and even longer are the distances between Ge atoms of adjacent layers, to be considered as bonded. Moreover, completely isolated Ge_3 units would stand for two-bonded species Ge^{2-} according to the *8–N* rule. However, in $EuGe_3$ a transfer of only two electrons per triangular unit or $Ge^{2/3-}$ is evidenced by X-ray absorption spectroscopy measurement of europium L_{III}-edge indicating that the oxidation state of the rare-earth metal is mainly +2 with only a minor amount of Eu^{+3} (Figure 3.6.9).

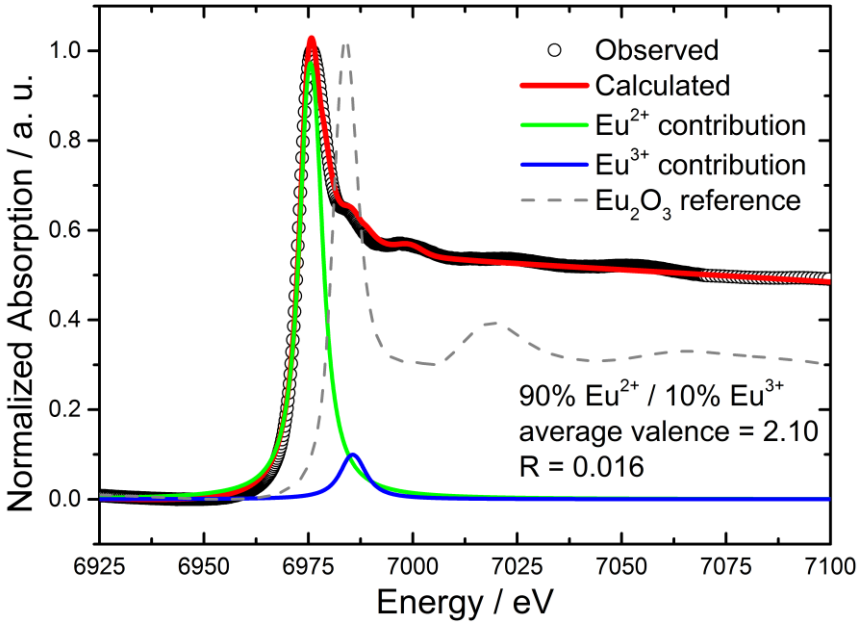

Figure 3.6.9 X-ray absorption spectroscopy of the Eu L_{III}-edge on $EuGe_3$. According to the Eu_2O_3 reference and the profile fitting, a small amount of Eu^{3+} is present, probably indicating a mixed valence situation.

3.6.3 Chemical bonding

A more elaborated model of the chemical bonding in direct space is realized by calculating the electron localizability indicator and electron density within the electron localizability approach.

The topological analysis of the ELI-D for both configurations of Eu atoms (inside and outside the mirror plane perpendicular to [001]) shows the presence of three kinds of attractors (Figure 3.6.10a, top and bottom). Attractors of the first type are local maxima close to the bond lines revealing two-center Ge – Ge interactions within the triangles. Similar covalent bonds have been found in triangular Sn_3 units of $BaSn_3$ [99] and in Ge_3 species of $LaGe_3$ [122]. Altogether, the spatial organization of the bonding within the triangles bears some similarities to that of cyclopropane [125] (Figure 3.6.10b), even despite different electron counts of the valence shells (18 e^- in C_3H_6, 14 e^- in $EuGe_3$). However, a closer inspection to the bond paths of both, triangular Ge3 units and carbon ring of cyclopropane, reveal that the bond critical point between two germanium atoms is curved towards the triangle center (Figure 3.6.10c), while in cyclopropane exhibits outward bends. This kind of topology revealing the direct interaction of the cationic component with its environment was observed earlier in the compounds of the late transition metals. So the dative bonding Au – Ba and Rh – Mg was found in $Ba_8Au_{5.3}Ge_{40.7}$ [68f], $Mg_3Rh_5B_3$ and $Mg_{11}Rh_{18}B_8$ [126]. Along the bond lines Eu – Ge, ring critical points occur in the penultimate (5^{th}) shell of europium (shell structuring) accompanied by a maximum toward germanium. This topology is a fingerprint for the participation of electrons of the penultimate shell (most probably semi-core 5d states) in the interactions within the valence region [127] and is interpreted as additional covalent interactions involving europium and germanium atoms, which for interactions including a *p* element is observed for the first time. This observation is well in agreement with the QTAIM charges of europium and germanium atoms: +0.77 for Eu and -0.26 for Ge for the in-mirror-plane configuration and +0.76 for Eu and -0.25 for Ge for the out-of-mirror-plane configuration. Despite the 6^{th} shell of

europium is essentially indiscernible, the charge transfer from Eu to Ge is remarkably low, being e.g. even lower than in $EuRh_2Ga_8$ (Eu+1.1) where direct interaction of Eu with the surrounding atoms was identified [128].

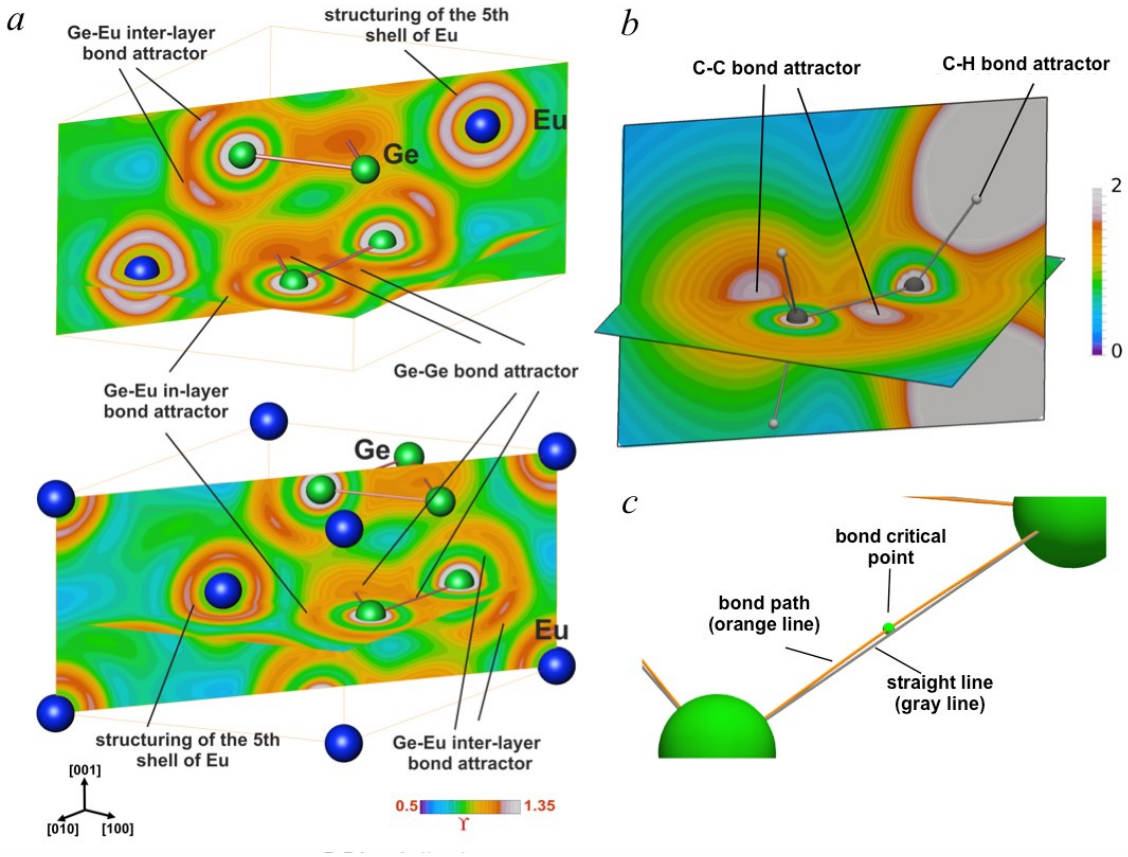

Figure 3.6.10 Electron localizability indicator (ELI-D) in $EuGe_3$ with the europium atom located in (a, top) and out of the horizontal mirror plane (a, bottom), respectively. The atomic arrangements exhibit different ELI-D distribution in regions of the Ge – Ge and Eu – Ge bonds, respectively. The ELI-D distribution of cyclopropane is shown in b for comparison. Part of the molecular graph is shown in c, indicating the concave shape of Ge-Ge bond path (orange) with bond critical point (small green sphere) on it, which deviates from the straight line (gray) between two Ge atoms (large green spheres) indicating the multicenter character of the bonding within the Ge3 triangle.

The disorder of the rare-earth metal atoms implies shifting of the Eu atoms along [001]. Thereby, half of the inter-layer attractors disappears; the intra-layer Eu – Ge attractors become less pronounced i.e. the local maximum value of ELI-D decreases. Simultaneously, the remaining inter-layer attractors become more pronounced, i.e., the local maximum value of ELI-D increases. The Ge – Ge attractors are not markedly affected by the europium shift.

Integration of the ELI-D basins for the different structure models yields practically the same electron populations for the arrangements in which the europium atoms are placed in and out the mirror planes (Figure 3.6.11). One electron is located inside a disynaptic basin which corresponds to the Ge – Ge bond of the triangle and 4.0 electrons per germanium atoms are located in the Eu – Ge basins. This

amounts to a total of 15 valence electrons per Ge unit. The core basins of germanium are populated with 27.75 electrons for both arrangements of Eu. This yields the electron localizability-based oxidation number (ELIBON) [129] of 32-(27.75+15/3) = -0.75 for germanium. In total this would give the balance $Eu^{+2.25}[Ge_3]^{-2.25}$, being in rough agreement with the XAS data.

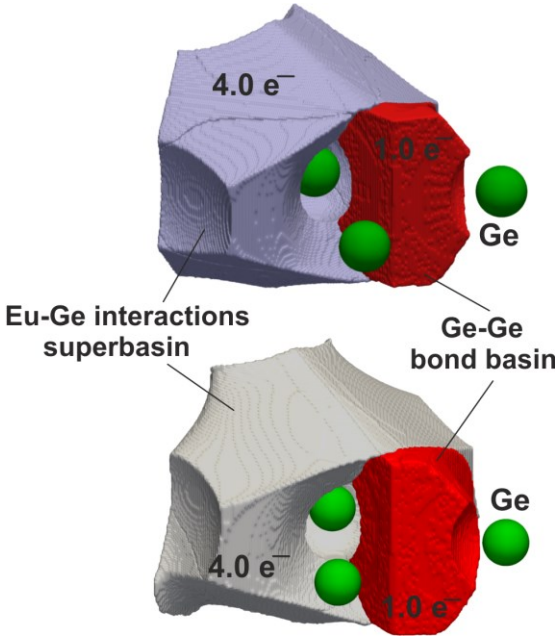

Figure 3.6.11 ELI-D basins and charges calculated for the configuration of europium atoms being located in (top) and out of the mirror planes (bottom) of $EuGe_3$.

3.6.4 Magnetic susceptibility, specific heat and electrical resistivity

The inverse of the magnetic susceptibility of $EuGe_3$ shows an almost linear dependence on temperature between 60 and 400 K (Figure 3.6.12). A fit to the data in this range follows a Curie-Weiss law $\chi = C(T - \theta)^{-1}$, with a Curie constant $C = N_A\mu_{eff}/3k_B$, and results in an effective magnetic moment, μ_{eff} = 7.89 μ_B for the Eu atom, which is consistent with a $^8S_{7/2}$ ground state of europium in the $4f^7$ configuration (Eu^{2+}, 7.94 μ_B), together with a Weiss parameter of θ = 32.7(4). The positive and low value may indicate a weak interaction of the europium magnetic moments (d(Eu-Eu) = 4.4541(6) Å). The cusp assigned to antiferromagnetic ordering of the europium moments is observed at the Néel temperature, T_N = 36(1) K. The magnetic susceptibility is also field dependent, as shown in the inset of Figure 3.6.12, which is a characteristic behavior for antiferromagnetic materials.

Specific heat measurements at low temperatures and zero magnetic field for $EuGe_3$, in the form of $C_p(T)$ and $c_pT^{-1}(T)$, are shown in Figure 3.6.13, top (black and blue circles, respectively). The λ-shape peak at 36 K is associated to the transition into the antiferromagnetic phase. This transformation exhibits a characteristic temperature shift in magnetic fields (inset of Figure 3.6.13, top). The specific heat of $EuGe_3$ $C_p(T)$ may be described as a sum of the terms $C_p(T) = C_{ph} + C_{el} + C_{mag}$ accounting for the contributions of phonons, electrons and magnetic interactions. Aiming to estimate the magnitude of the magnetic contribution C_{mag}, the isostructural diamagnetic reference compound $BaGe_3$ has been synthesized and measured (triangles in Figure 3.6.13, top). A fit to the $BaGe_3$ data in the range from 2 K to 8 K can be performed with a standard Debye model, resulting in the parameters γ = 4.4 mJ×mol^{-}

$^1K^{-2}$, β = 0.9 mJ×mol^{-1}K^{-4} and θ_D = 205 K. After subtraction of the phonon and electron terms, C_{ph} and C_{el}, of the reference compound $BaGe_3$, the magnetic specific heat of $EuGe_3$ is obtained (gray dashed curve in Figure 3.6.13, bottom). By integration of $C_{mag}T^{-1}$, the magnetic entropy is determined to 2.0 *R* (dark green in Figure 3.6.13, bottom). This value is in good agreement with the expected value of *R* ln8 for the free Eu^{2+} ion.

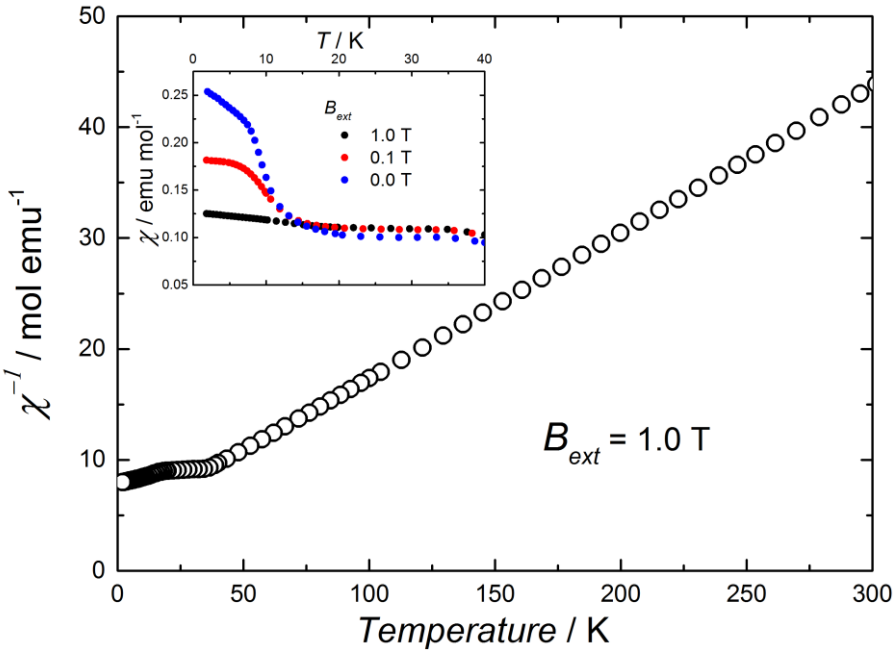

Figure 3.6.12 Inverse magnetic susceptibility of $EuGe_3$ at B_{ext} = 1.0 T. The almost linear comportment above 50 K is well fitted to the Weiss-Curie law. The field dependence at low temperatures is shown in the inset.

Because of the large anisotropy of the ADP of the europium atom in the ideal model (*$P6_3/mmc$*), an Einstein term (which relates the thermal motions to vibrations of atoms) was included to the Debye description of phonon contribution, $C_{ph} = \beta T^3 + \varepsilon E(T/\theta_E)$. However, it does not improve the modeling of the data. This may be an indication that, in the most likely model of the crystal structure, the ADP of the europium atoms are rather spherical than asymmetric, which is well correlated with the refined model including the split of the europium positions (*$P6_3mc$*).

The electrical resistivity, $\rho(T)$ of $EuGe_3$ (Figure 3.6.14) exhibits linear temperature dependence above 40 K with a positive slope indicating metal-like behavior. A fit to the data in the range 40 – 300 K results in the equation $\rho = 1043(4) + 9.14(2)\times T$ (R^2 = 0.998). The value of 3.785 mΩ×cm for $\rho(T)$ at 300 K appears to be unusually large for metallic conductivity since the common limit corresponds to ~0.1 mΩ×cm, however similar values have been observed for europium-tetrel compounds like Eu_3Si_4 [130], $EuSi_6$ [24a], $EuGe_2$ [121]. The extrapolated resistivity to 0 K amounts almost to a quarter of the value at 300 K, indicating weak magnetic disorder scattering.

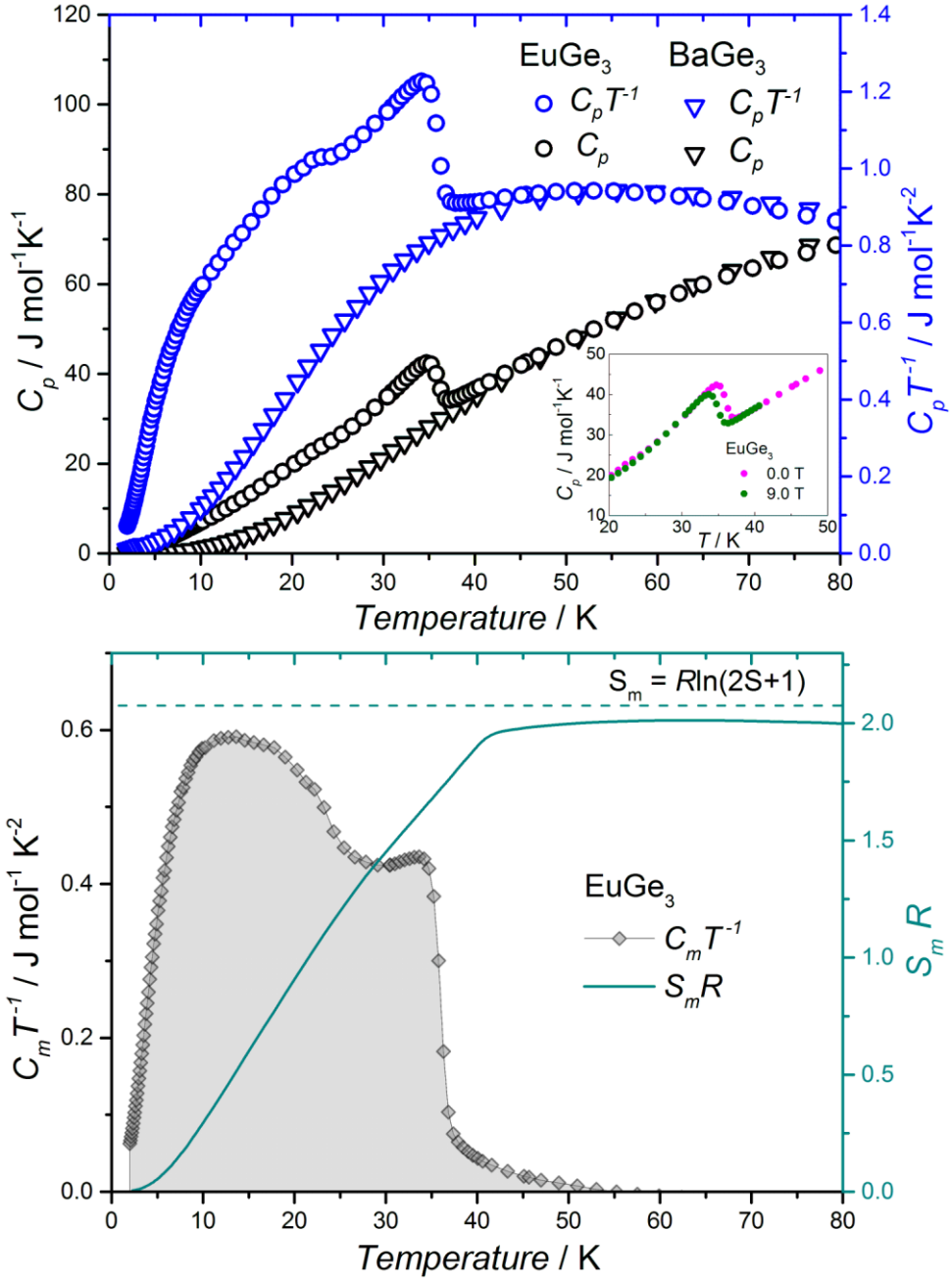

Figure 3.6.13 (top) Specific heat $C_p(T)$ (blue) and $C_pT^{-1}(T)$ (gray) for $BaGe_3$ and $EuGe_3$. The λ-peak is shown for clarity in the inset. (bottom) Magnetic specific heat $C_mT^{-1}(T)$ (gray) and integral of $C_mT^{-1}(T)$ (dark green) of $EuGe_3$.

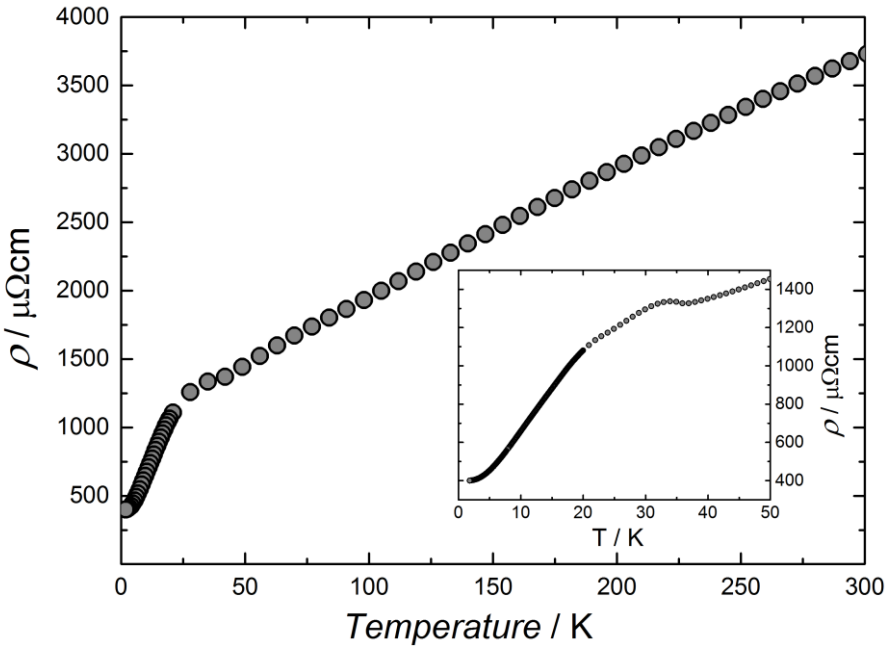

Figure 3.6.14 Electrical resistivity of $EuGe_3$ measured at zero magnetic fields. The transition to the antiferromagnetic ordering is observed at 32 K, as shown in the inset for clarity.

3.6.5 Conclusions

The new high-pressure modification *(hP8)* $EuGe_3$ was synthesized and characterized. Its X-ray powder diffraction pattern seemed to be similar to *h*-$BaGe_3$ but nevertheless, the crystal structure model was not fully correct, as evidenced by the marked anisotropy of the ADP of the europium. Better description of the crystal structure included a split of the europium position, making the ADP physically reasonable. This was further corroborated by the interpretation of the specific heat data, where the addition of an Einstein term to the phonon contribution did not improve the description of the data, and resulted in an insignificant degree of freedom for the whole crystal structure. According to the Zintl concept and in agreement with quantum chemical calculations, the crystal structure comprises covalently bonded triangular units Ge_3^{2-}. The rare-earth metal europium forms additional multi-center Eu-Ge bonds involving states of the 5th shell.

Chapter 4
Summary and Outlook

High-pressure high-temperature conditions demonstrated to be an invaluable tool for the synthesis of new materials. Even in well-known binary system like Ba – Ge, extreme condition revealed several new phases in a narrow composition range. The metastable compounds obtained in this work are characterized mainly by the occurrence of unusual crystal structures and atomic arrangements. Such uncommon structure patterns violate classical electron counting schemes like the *8-N* rule and/or do not follow always the predictions based on the Zintl concept. Beside the intriguing physical properties that they can convey, these unique features made the reported compounds attractive candidates for detailed quantum chemical studies. In this respect, it was shown that the chemical bonding situation is, to some extent, responsible for some physical properties.

The main focus of the present work was the Ge-rich part of the binary Ba – Ge system, in which by inspecting the behavior of the clathrate-I Ba_8Ge_{43} under pressure, several new phases were found. The new phases in this system have the following compositions: $BaGe_3$ (with two modifications), $BaGe_5$, $BaGe_{5.5}$ and $BaGe_6$, therefore they are quite close in composition range: 75% - ~85% at. Ge, as indicated in Figure 4.1. Although each of these is discussed in the respective subchapters, a brief review of all of them together with possible dependence of physical properties with composition is still missing.

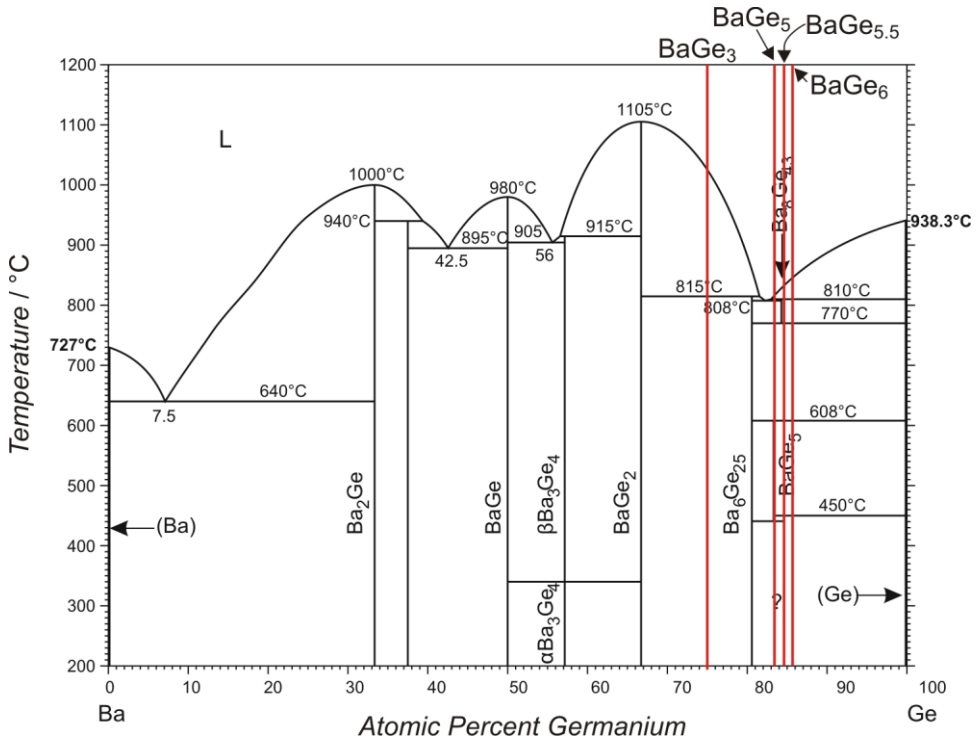

Figure 4.1 The phase diagram of the binary Ba – Ge system with the new phases found in that system included with red lines. Taken from JPED vol. 30 no. 1 2009.

Concerning the conditions required for the synthesis of each phase, several combinations of temperature and pressure were employed in order to find a stability range. It was possible to establish

such a formation range for all phases, as shown by the elliptic areas in Figure 4.2. These areas encompass the pressure and temperature range in which a single phase was obtained, represented by the big symbols within them. In some cases, two phases were found, represented by medium-size symbols and in many other cases three or more phases were found to coexist, and those cases are represented by small-size symbols in Figure 4.2. It must be highlighted that $BaGe_6$ could never by synthesized as a single phase, as discussed in chapter 3.2.

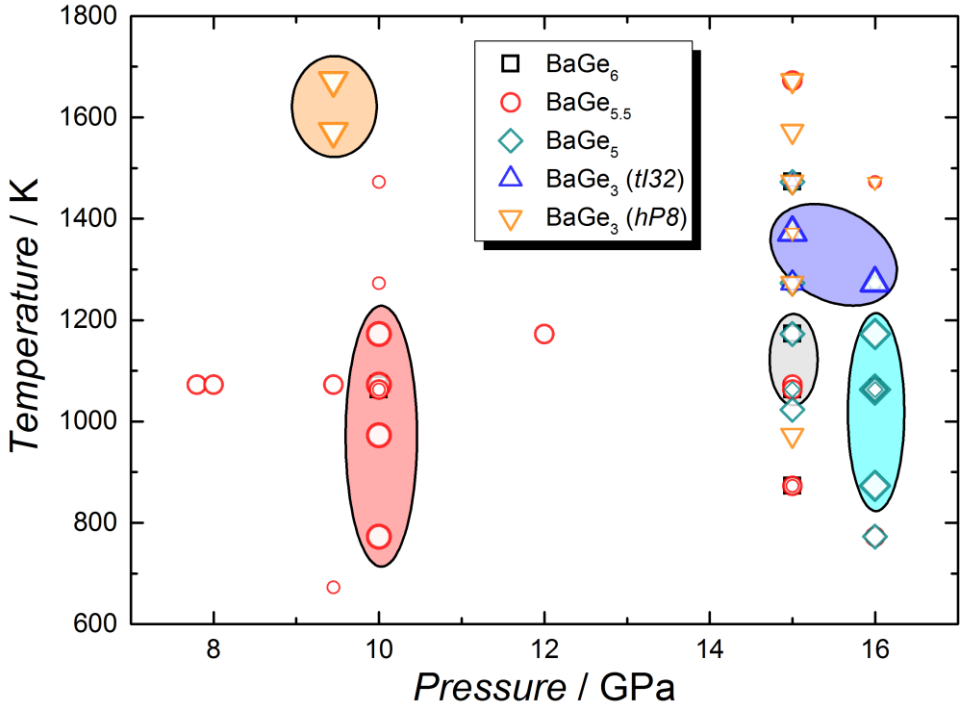

Figure 4.2 Temperatures and pressures at which the different phases were detected. The color legend is inside the figure and the meaning of the symbol´s size is: big when single phase was found, medium when two phases coexist and small when three or more phases are present. $BaGe_6$ was never found as a single phase.

Besides the already discussed trends between $BaGe_6$ and $BaGe_{5.5}$ with pressure and the trends found in $BaGe_3$ and its two modifications, in both examples affecting the physical properties, there is no systematic relation between the required pressure and the Ge content. However, by inspecting some structural features, for instance the interatomic distances, it is found that the average of the Ge – Ge distances change in line with the composition, i.e. the shorter contacts belong to $BaGe_6$ while the longer distances are present in $BaGe_3$ (any modification). An opposite trend is observed for the calculated density of each phase (neglecting the *tI32* form of $BaGe_3$): the lower density is found for $BaGe_3$ and the denser compound is found to be $BaGe_6$. Of course this is not coincidence, since due to the Ge content, $BaGe_6$ has the largest molar mass. Another way of analyze Figure 4.3 is by examining the density as a function of the interatomic distance. In such case, the denser compound is characterized by shorter Ge – Ge contacts, while the less dense phase holds the longest Ge – Ge contacts. This is in agreement with the building motifs within each crystal structure: columns in $BaGe_3$

(open framework) passing through layers in $BaGe_5$, ending in a three-dimensional network (closed framework) in $BaGe_6$.

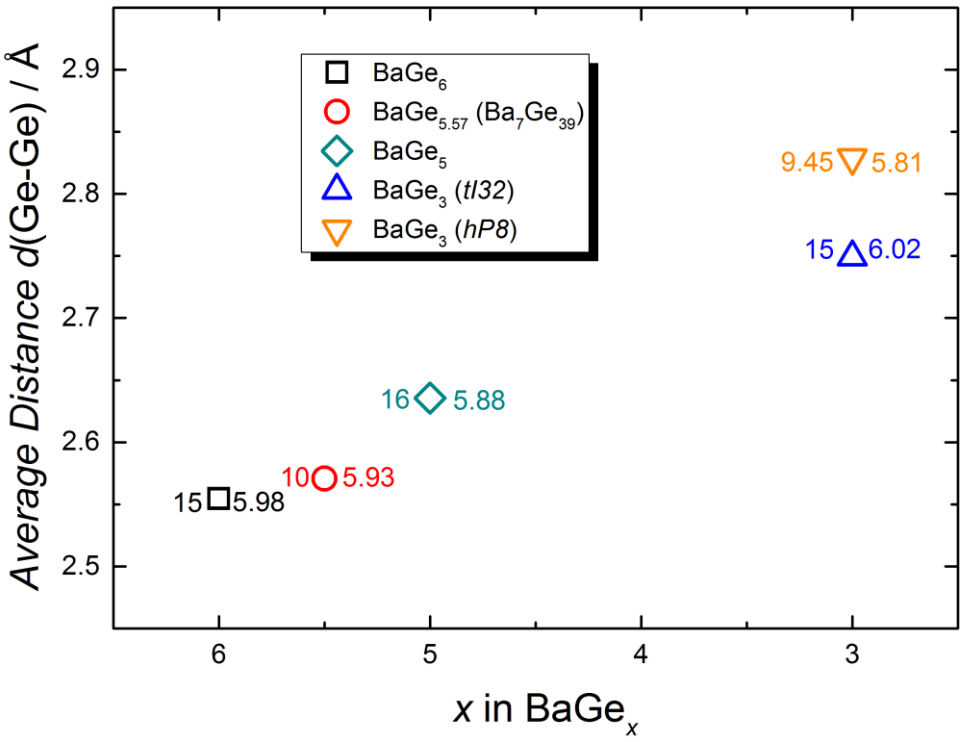

Figure 4.3 Average interatomic Ge – Ge distances found in the high-pressure Ba-Ge compounds. The pressure (in GPa) and the calculated density (in g cm^{-3}) are indicated at the left and right of each symbol, respectively.

Although a systematic study was performed and the compounds were fully characterized, some important points could be considered for further research. These are related basically to the doping of the binary phases, alter the number of electrons and affect the structure and properties.

In the case of $BaGe_{6-x}$, replacing Ge by Ga may lead to situation with less electrons, or doping with a +3 element like La^{+3} would increase the excess of electrons, increasing the number of vacancies and affecting the modulation and the physical properties. All these changes could be easily visualized by using the reported crystal structure model as a starting reference.

Similarly, the metastable character of $BaGe_5$ can be related to the nature of its complicated bonding scheme and further experiments could examine to what extent the lone-pair behavior, which turned out to be a multicenter interaction involving the Ba atoms, can exist when the Ge3 is replaced by any electron-deficient element or if its charge is increased when it is replaced by a group-V element.

For $Ba_{8-x}Si_4$, a systematic study on the three variables that influence *x* would make possible the synthesis of the clathrate in a controlled manner regarding the Ba content and thus, its influence on the thermoelectric properties would be better understood. Additionally, replacing silicon with Au in a short range will help to justify the conclusion concerning the mechanism of lattice thermal conductivity reduction.

Finally, for the *M*Ge_3 superconductors, a lattice dynamics study would complement in a great manner the results regarding the mechanism involved in the superconductivity. Similarly, solid solutions of the form $Ca_{3-x}Sr_xGe_3$, $Sr_{3-y}Ba_yGe_3$ and $Ca_{3-z}Ba_zGe_3$, are interesting system to investigate what phenomena rises or suppress the transition temperature. In the case of the two high-pressure modifications of $BaGe_3$, the Fermi level is located below a maximum in the DOS, which means that by adding more states, i.e. electrons, the Fermi level will move accordingly and when matching the maximum, a considerable rise in Tc should be expected.

Chapter 5
Appendix

5.1 Effect of Pressure on the electronic structure

5.1.1 Pressure effect on elements

The basic Hamiltonian of an element, at the level of elementary nuclear and electronic charge, can be written as:

$$\hat{H} = \hat{H}_{nn} + \hat{H}_{en} + \hat{H}_{ee}$$

Here $\hat{H}_{nn}$ and $\hat{H}_{ee}$ are the kinetic energy of nuclei and electrons, respectively, and $\hat{H}_{en}$ represents the coulomb attraction. The whole assembly is confined to a volume *V*, and as a consequence of this boundary condition, the stationary states of the basic Schrödinger equation,

$$\hat{H}\psi(V) = E(V)\psi(V)$$

are visibly volume (*V)* dependent and hence, the electronic properties may be altered or modified by pressure.

Temperature is the most exploited variable in the study of condensed matter. However, the effect of pressure in the energetics of solids is much larger than the effect of temperature, as evidenced by the free energy vs atomic volume graph of CsI (Figure 5.1) [131]. The plot evidences that the same free energy is involved when the solid melts at ambient pressure and when it is compressed to 20 GPa at room temperature. Although the graph represents a particular case, similar relations hold for most solid materials.

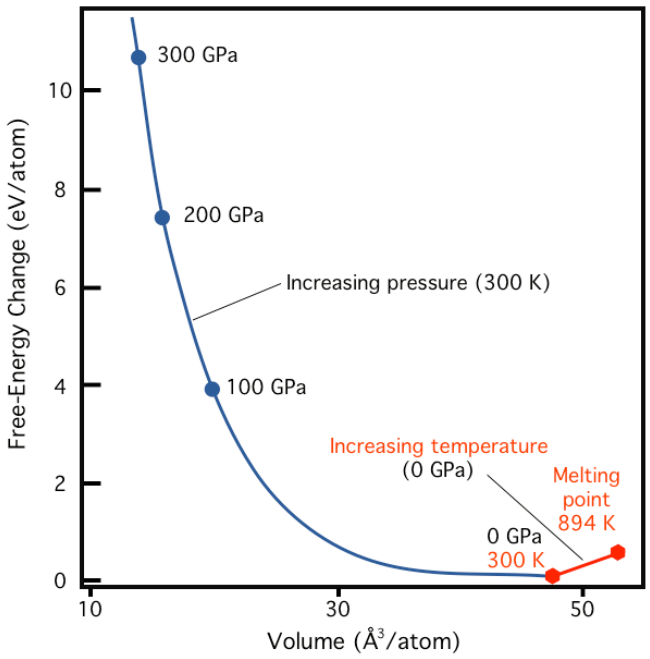

Figure 5.1 Absolute value of the Helmholtz free energy of CsI as a function of volume, either upon compression at 300 K (isotherm curve) or upon heating at zero pressure. Original data from R. Jeanloz (Ann. Rev. Phys. Chem. (1989) 40, 237-259), and R. J. Hemley and N. W. Ashcroft (Physics Today (1998) 51, 26) are combined to highlight important features.

The main result of pressure application is the compression. The material´s constituent particles are brought closer under pressure. This increases the overlap of the electron clouds and leads to a rearrangement of the electronic structure, reflected in changes of the optical and electrical properties [132]. This means, pressure has an effect intimately related to the electronic properties of atoms, being able even to modify the electronic behavior and to give rise to often exotic and rather unusual chemical systems, with unexpected physical properties and chemical bonding situations.

The qualitative picture of a phase transition of a substance under pressure is simple to understand. During compression of a chemical system, the interatomic distances (*d*) become shorter and the attractive part of the bonding energy increases as d^{-1} or d^{-2}. On the other hand, the repulsive energy (due to the overlap of electron clouds of nearest atoms) grows more sharply, as d^{-12}. At some point the repulsion becomes bigger than the attraction and the initial chemical system can no longer exist under the new thermodynamic conditions. The structure experiences an abrupt rearrangement of atoms in order to reduce the electronic repulsion. This can be achieved in one way only, namely, by increasing the coordination number in the structure leading to an increase of the packing density (but also, paradoxically, of the *nearest* interatomic distances), in accordance with Le Chatelier's principle.

From the point of view of orbital interactions, high-pressures have considerable effect on the electronic properties. The best-known examples are heavy alkaline and alkaline earth metals, which undergo the so-called *s-to-d* (*s-to-p* for Li [133], Be, Na [134] and Mg [135]) transition so that they behave like transition metal elements [136] because of the strong orbital overlap caused by high pressure. These transitions are easily observed by band structure calculations performed on compressed alkali metals [137], however, experimental evidence for that have been found, for instance, alkaline and alkaline-earth metals react with transitions metals to form alloys under high pressures [138,139]. According to some empirical rules for intermetallic compound formation, such compounds are not stable. Indeed, they have not been observed at ambient pressure, because of large difference in size and electronic structure (Miedema´s rules [140]). Exceptions are gold and platinum, which are the most electronegative transition metals.

5.1.2 Pressure effect on physical properties

The general tendency in a group of elements is that they adopt the structure of the heavier homologue when subjected to pressure (Table 1.2), so it is logic to ask if this is also true for the physical properties. Silicon and germanium are semiconductors; they have an optical band-gap around 1 eV. The next element in the group is tin, which is a metal and has a different crystal structure. When Si and Ge transform to the β-Sn structure by effects of pressure, they also become metals. At higher pressure, they can even reach the superconducting state [141]. Metallization occurs as the atoms come closer to each other and the valence and conduction bands broaden and overlap with each other. The above solids undergo semiconductor-metal transition and then become superconductors. Thus, we come across the phenomenon of pressure-induced superconductivity exhibited by metals, semiconductors, intermetallic compounds and alloys [142]. The same effect is observed for other kind of solids, like ionic compounds, in which closure of the band-gap has been measured, for instance, CsI, a transparent salt that under pressure shows insulator-semiconductor-metal transitions [131]. The large band-gap of CsI at ambient conditions (E_g = 6.3 eV) and its large compressibility (or low bulk modulus, B_0 = 11.9

GPa) allow an almost linear reduction of the band-gap, estimated by in-situ optical experiments, when increasing the pressure and becoming metal at around 110 GPa [143]. This is noted by the changes in the sample´s color, from transparent to yellow-orange-red and finally opaque around 55 GPa [144]. Electrical transport and magnetic measurements at pressures above 180 GPa, show a drop in the resistance at about 2 K, characteristic of the superconductivity state [145]. The accepted phase transition sequence in CsI is as follow; a continuous distortion from the B2 structure (CsCl type) to an hcp-like structure [146] with an orthorhombic intermediate structure above 40 GPa [147]. Theoretical calculations together with crystal structure predictions algorithms on CsI show that indeed the transition from cubic to orthorhombic structure occurs; with the last one having a hexagonal pattern being stable up to 300 GPa [148] and that may explain the experimental data.

5.1.3 Pressure effects predicted by electronic structure calculations

Electronic structure calculations are nowadays a common complement of the experimental work. One advantage of solid-state chemistry experiments under HPHT conditions is that they can be accompanied by quantum chemical calculations with quite good reproducibility of the experimental observations.

The characteristic example of the link between the experimental work and the theoretical calculations is the *density of states* (DOS), and specifically the number of states at the Fermi level (E_F), usually represented as $N(E_F)$. This number (in units of eV states^{-1} cell^{-1}) can be obtained from different temperature-dependent (the approximations in electronic structure calculations are taken at 0 K) experimental measurements, like magnetic susceptibility, electrical resistivity and specific heat [149]. In the case of the last one, the electronic contribution in the low temperature range, represented by the Sommerfeld term, γ, depends linearly on the temperature; $C_{el}(T) = \gamma T$, with $\gamma = (\pi^2/3)k_B^2 N(E_F)$, according to the free electron theory of metals. Good agreement between both, calculated and experimentally obtained $N(E_F)$ have been found [150]. Especially for high-pressure research, electronic structure calculations are very useful and reliable, because the application of pressure can relatively be easy simulated by a reduction of the unit cell parameters and energies for different volume can be computed. Total energy calculations based on the density functional theory allow us to derive free energies, and in this way determine the atomic positions in a solid such that the structure is the most stable at given conditions and even predict the pressure range at which the transition can occur to the next stable structure [151,152,27]. In Figure 5.2 the example of silicon is shown [153], which was the first element on which electronic structure calculations were able to estimate the transition from the diamond-type structure at ambient pressure to the beta-tin modification at high pressure and demonstrated why other possible phases are not observed, at least in the low-pressure range.

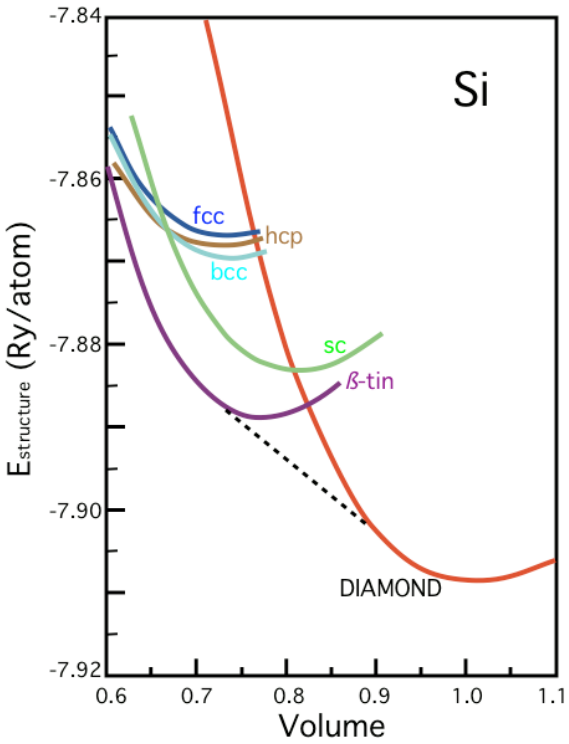

Figure 5.2 Total energy of silicon plotted as a function of volume. Data taken from reference [153] and modified in order to highlight important features.

From these parabolic curves, the bulk modulus can be estimated with high accuracy, and be compared with the experimentally obtained value from Pressure vs Volume curves, $P(V)$, probing the reliability of electronic structure calculations for high-pressure phases [154,155]. An important fact related with this subject, the fcc phase of silicon was first predicted from DFT calculations years before it could be experimentally observed.

The effect of pressure can be monitored *in-situ* with the diamond anvil cell (DAC) assembly [156], employed normally at synchrotron sources, by recording X-ray patterns at different pressures. Subsequent refinement of the lattice parameters and the volume of the unit cell for each pressure will result in a bent curve for a Pressure vs Volume plot with negative slope (as a solid is compressed, it becomes harder and more difficult to be further compressed). From such kind of plot, one can fit the points to different equations of states, for instance, the Murnaghan equation of state [157] (*eos*):

$$P(V) = \frac{K_0}{K_0'}\left[\left(\frac{V}{V_0}\right)^{-K_0'} - 1\right]$$

This is one of the first *eos* proposed and its simple form is still useful to get a first impression of the behavior of the material. It relates the volume of a body and the pressure to which it is subjected. It involves two adjustable parameters, the modulus of incompressibility k_0 and its first derivatives with

respect to the pressure, k_0', both measured at ambient pressure. They are determined by a regression on experimentally obtained values of *V* as a function of *P*, knowing the volume at ambient pressure.

In connection with *ab initio* calculations, an expression of energy as a function of volume is preferred, which is obtained by integration of the previous equation according to *P = -dE/dV* [158]:

$$E(V) = E_0 + K_0 V_0 \left[\frac{1}{K_0'(K_0' - 1)} \left(\frac{V}{V_0} \right)^{1-K_0'} + \frac{1}{K_0'} \frac{V}{V_0} - \frac{1}{K_0' - 1} \right]$$

The fact that an intrinsic and mechanical property of a material, like the bulk modulus, can be estimated by quantum chemistry calculations, demonstrates the intimate connection between the theory and the reproducibility of high-pressure experiments. Figure 5.3 shows the phase transitions of Si with increasing pressure, by using the DAC setup [159]. Many other properties can be determined in the same manner, like elastic constants, unit cell parameters, cohesive energy, phonon spectra and other static properties [160]. A short review to some values obtained for the bulk modulus by both, experimentally and theoretically, for some elements and compounds of interest in this work, are summarized in Table 5.1. A huge list of compounds comparing both and with different methods is available in the literature [161]. The excellent agreement is evident, in the case of silicon, one of the first element studied by *ab initio* methods [162], the lattice parameters and bulk moduli differ from the experimental values in 0.4 and -1% respectively [163].

Table 5.1 Experimental and calculated bulk moduli for selected compounds.

Compound	Structure	B_{exp} (GPa)	B_{cal} (GPa)
C	Diamond	442[a]	435[b]
Si	Diamond	100[a]	98[b]
Ge	Diamond	78[a]	79[b]
Sn	Diamond	55	56[c]
BN	Diamond	369	368[d]

a: Kamran, S.; Chen, K.; Chen, L. *Phys. Rev. B.* (2008) **77,** 094109

b: Cohen, M. *Phys. Rev. B.* (1985) **32,** 7988-7991

c: Svane, A.; Antoncik, E. *Solid State Commun.* (1986) **58**, 541

d: Knittle, E.; Wentzcovitch, R. M.; Jeanloz, R.; Cohen, M. L. *Nature* (1989) **337,** 349

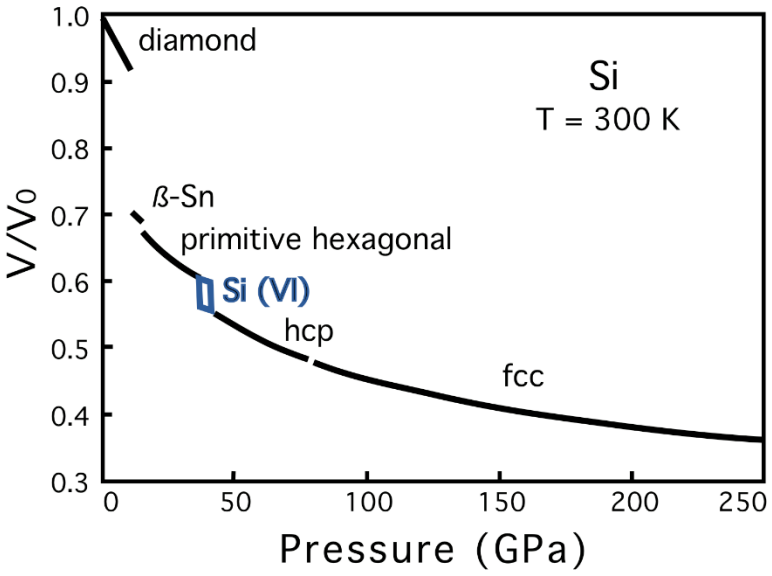

Figure 5.3 Compressibility of silicon at ambient temperature and pressure up to 248 GPa. Taken and modified from reference [159]

5.2 Crystallographic data

Table 5.1 Details on data collection of $Ba_{8-x}Si_{46}$.

Composition	$Ba_{7.27(1)}Si_{46}$
Pearson symbol	*cP(54-0.83)*
Crystal system, space group	Cubic, *Pm-3n* (no. 223)
Unit cell parameters	a = 10.3051(1) Å
Unit cell volume	V = 1094.35(3) Å^3
Formula units per cell	Z = 1
Calculated density	ρ_{calc} = 3.48 g cm^{-3}
Temperature	293(2) K
Measurement device	STOE STADI MP Bragg-Brentano setup Zero-background sample holder Step width: 0.02°
Radiation	Cu $K_{\alpha 1}$, λ = 1.540562 Å
Profile function	Pseudo-Voigt
Measurement range	$10° \leq 2\theta \leq 120°$ $0 \leq h < 13, 0 \leq k \leq 13, 0 \leq l \leq 13$
Number of points / reflections	5500 / 135
Number of parameters crystal structure / profile	10 / 36
Structure refinement	Full profile method, WinCSD
Residuals and GoF	R_P = 0.108, R_F = 0.027, GoF = 1.01

Table 5.2 Atomic coordinates and displacement parameters of $Ba_{8-x}Si_{46}$.

Atom	*Site*	*Occupancy*	*x*	*y*	*z*	B_{iso}
Ba1	2*a*	0.636(6)	0	0	0	1.2(1)
Ba2	6*d*	1	1/4	1/2	0	1.38(5)
Si1	6*c*	1	1/4	0	1/2	1.2(2)
Si2	16*i*	1	0.1847	*x*	*x*	1.2(1)
Si3	24*k*	1	0	0.3044(5)	0.1217(5)	1.1(1)

Table 5.3 Selected interatomic distances in $Ba_{8-x}Si_{46}$.

Ba1 –	8x Si2	3.296(2)	Si1 –	4x Si3	2.411(4)
	12x Si3	3.378(5)		4x Ba2	3.643(1)
Ba2 –	8x Si3	3.503(4)	Si2 –	1x Si2	2.336(3)
	4x Si1	3.643(1)		1x Si3	2.359(4)
				1x Si3	2.359(5)
				1x Si3	2.359(5)
				1x Ba1	3.296(2)
			Si3 –	2x Si2	2.359(4)
				1x Si1	2.411(4)
				1x Si3	2.508(7)
				1x Ba1	3.378(5)

Table 5.4 Details on data collection of $BaGe_6$.

Composition	*$BaGe_6$*
Pearson symbol	*oC28*
Crystal system, space group	Orthorhombic, *Cmcm* (no. 63)
Unit cell parameters	a = 4.7690(7) Å b = 10.777(2) Å c = 12.385(2) Å
Unit cell volume	V = 636.6(2) Å^3
Formula units per cell	Z = 4
Calculated density	ρ_{calc} = 5.98 g cm^{-3}
Temperature	293(2) K
Measurement device	Huber G670 Reflection geometry Step width: 0.005°
Radiation	Cu $K_{\alpha 1}$, λ = 1.540562 Å
Profile function	Pseudo-Voigt
Measurement range	$10° \leq 2\theta \leq 100°$ $0 \leq h < 4$, $0 \leq k \leq 10$, $0 \leq l \leq 12$
Number of points / reflections	18000 / 201
Number of parameters crystal structure / profile	11 / 24
Structure refinement	Full profile method, Jana 2006
Residuals and GoF	R_P = 0.057, R_F = 0.029, GoF = 3.45

Table 5.5 Structural parameters of $BaGe_6$.

Atom	*Site*	*Occupancy*	*x*	*y*	*z*	*B_{iso}*
Ba	4*c*	1	0	0.270(2)	1/4	1.1(4)
Ge1	8*f*	1	0	0.249(3)	0.536(1)	1.3(2)
Ge2	8*f*	1	0	0.446(2)	0.644(2)	B_{iso}(Ge1)
Ge3	8*f*	1	0	0.023(2)	0.598(2)	B_{iso}(Ge1)

Table 5.6 Selected interatomic distances in $BaGe_6$.

Ba –	2x Ge2	3.33(3)	Ge2 –	1x Ge1	2.51(4)
	2x Ge1	3.55(1)		2x Ge3	2.59(1)
				1x Ge2	2.63(3)
Ge1 –	1x Ge2	2.51(4)		1x Ba	3.33(3)
	2x Ge1	2.543(8)			
	1x Ge3	2.55(4)	Ge3 –	1x Ge3	2.48(3)
	1x Ge3	3.37(4)		1x Ge1	2.55(4)
				2x Ge2	2.59(1)
				1x Ge1	3.37(4)

Table 5.7 Details on data collection of $BaGe_{6-x}$ in a commensurate model.

Composition	*$BaGe_{5.57}$ (Ba_7Ge_{39})*
Pearson symbol	*oC184*
Crystal system, space group	Orthorhombic, *Cmc2₁* (no. 36)
Centering	(0, 0, 0), (1/2, 1/2, 0)
Unit cell parameters	a = 29.5729(8) Å b = 11.2228(3) Å c = 12.7992(3) Å
Unit cell volume	V = 4247.9(4) Å^3
Formula units per cell	Z = 28 (4)
Calculated density	ρ_{calc} = 5.93 g cm^{-3}
Temperature	293(2) K
Measurement device	Rigaku AFC7 CCD detector (Saturn 724)
Radiation	Mo K_α, λ = 0.71073 Å
Absorption correction	Multiscan
Measurement range	$-42 \le h < 45$ $-17 \le k \le 14$ $-8 \le l \le 19$
Number of reflections: measured / unique	12063 / 4416
Refinement	$F \ge 5.9\sigma(F)$
Refined parameters	217
Software	WinCSD
Residuals (reflns) and GoF	R_F = 0.039, R_W = 0.041 (1708), GoF = 1.01
$\Delta\rho_{min}$, $\Delta\rho_{max}$ / e Å^3	-2.67, 3.63

Table 5.8 Structural parameters of Ba_7Ge_{39}.

Atom	*Site*	*Occupancy*	*x*	*y*	*z*	B_{iso}
Ba1	4*a*	1	0	0.2858(4)	1/4	1.1(1)
Ba2	8*b*	1	0.4295(1)	0.2852(2)	0.2589(5)	1.11(8)
Ba3	8*b*	1	0.1416(1)	0.2915(3)	0.2689(4)	0.84(7)
Ba4	8*b*	1	0.28665(8)	0.2943(3)	0.2550(6)	0.85(9)
Ge1	4*a*	1	0	0.5638(7)	0.3565(7)	0.5(2)
Ge2	4*a*	1	0	0.0348(9)	0.9145(8)	1.1(3)
Ge3	4*a*	1	0	0.5815(8)	0.1536(8)	0.7(3)
Ge4	4*a*	1	0	0.2452(8)	0.9739(7)	0.8(2)
Ge5	4*a*	1	0	0.0490(8)	0.6033(8)	1.2(3)
Ge6	8*b*	1	0.0723(2)	0.0672(5)	0.3590(6)	0.9(2)
Ge7	8*b*	1	0.3551(2)	0.0820(5)	0.3618(6)	0.8(1)
Ge8	8*b*	1	0.3548(1)	0.2508(4)	0.0415(5)	0.9(1)
Ge9	8*b*	1	0.4283(3)	0.0324(8)	0.9135(7)	1.6(2)
Ge10	8*b*	1	0.2135(3)	0.0768(5)	0.3553(6)	1.4(2)
Ge11	8*b*	1	0.0714(3)	0.0743(6)	0.1556(6)	0.8(2)
Ge12	8*b*	1	0.1434(3)	0.0273(5)	0.6001(6)	1.0(1)
Ge13	8*b*	1	0.4275(2)	0.0396(5)	0.6005(6)	0.8(2)
Ge14	8*b*	1	0.1428(4)	0.0434(6)	0.9160(6)	1.0(1)
Ge15	8*b*	1	0.2859(2)	0.0296(6)	0.9207(6)	0.5(2)
Ge16	8*b*	1	0.3568(3)	0.0681(5)	0.1622(5)	0.5(1)
Ge17	8*b*	1	0.2147(2)	0.0732(7)	0.1581(7)	1.1(2)
Ge18	8*b*	1	0.2859(2)	0.0331(5)	0.6024(6)	0.6(2)
Ge19	8*b*	1	0.2772(2)	0.2576(5)	0.9776(6)	1.4(2)
Ge20	8*b*	1	0.0865(2)	0.2569(4)	0.0384(6)	1.4(1)
Ge21	8*b*	1	0.1902(1)	0.2454(4)	0.0264(5)	1.3(1)
Ge22	8*b*	1	0.4435(2)	0.2516(6)	0.9809(6)	1.2(1)

Table 5.9 Anisotropic ADP of Ba_7Ge_{39}.

Atom	*B11*	*B22*	*B33*	*B12*	*B13*	*B23*
Ba1	0.8(2)	1.1(2)	1.2(2)	0	0	-0.1(2)
Ba2	0.9(2)	1.1(1)	1.3(1)	0.1(1)	-0.2(1)	-0.2(1)
Ba3	0.8(1)	0.9(1)	0.9(1)	0.1(2)	0.3(2)	-0.0(1)
Ba4	0.8(2)	0.9(1)	0.8(1)	-0.1(1)	0.1(1)	0.1(1)
Ge1	0.5(4)	0.4(4)	0.6(4)	0	0	0.0(3)
Ge2	0.8(4)	1.2(5)	1.5(4)	0	0	0.0(3)
Ge3	1.3(6)	0.3(4)	0.5(3)	0	0	0.1(3)
Ge4	0.2(3)	1.3(4)	0.8(3)	0	0	0.2(3)
Ge5	1.5(5)	0.9(5)	1.2(4)	0	0	0.3(3)
Ge6	1.1(5)	0.7(3)	0.8(3)	0.3(2)	0.0(2)	0.0(2)
Ge7	0.4(3)	1.1(3)	0.9(2)	0.5(2)	0.1(2)	0.1(2)
Ge8	1.3(2)	0.5(2)	0.7(2)	0.0(2)	0.0(1)	0.0(2)
Ge9	1.3(4)	2.2(4)	1.3(3)	0.2(3)	0.2(2)	0.1(2)
Ge10	1.4(4)	1.5(3)	1.2(3)	0.2(3)	0.1(3)	0.0(2)
Ge11	0.8(4)	0.6(3)	0.9(2)	0.3(3)	0.3(2)	0.2(2)
Ge12	0.7(3)	1.3(2)	1.0(2)	0.0(3)	0.0(3)	0.1(1)
Ge13	0.8(3)	0.9(3)	0.7(2)	0.3(2)	0.2(2)	0.1(2)
Ge14	0.9(3)	1.3(3)	0.9(2)	0.2(3)	0.2(3)	0.1(2)
Ge15	0.8(4)	0.2(4)	0.4(2)	0.1(2)	0.0(2)	0.1(2)
Ge16	0.6(2)	0.6(3)	0.5(2)	0.2(3)	0.4(3)	0.2(2)
Ge17	0.4(4)	1.9(4)	1.1(3)	0.4(3)	0.3(2)	0.0(3)
Ge18	0.5(3)	0.6(3)	0.6(2)	0.1(2)	0.1(2)	0.0(2)
Ge19	1.9(3)	1.2(3)	1.1(3)	0.1(3)	0.5(2)	0.1(2)
Ge20	1.8(3)	1.1(3)	1.3(2)	0.1(3)	0.5(2)	0.0(2)
Ge21	2.4(2)	0.8(2)	0.7(2)	0.1(2)	0.7(1)	0.1(1)
Ge22	1.6(2)	0.9(3)	1.2(2)	0.1(3)	0.1(2)	0.1(2)

Table 5.10 Selected interatomic distances in Ba_7Ge_{39}.

Ba1 –	2x Ge11	3.399(8)	Ge11 –	1x Ge12	2.52(1)
	1x Ge1	3.405(9)		1x Ge20	2.579(9)
	2x Ge22	3.421(7)		1x Ge6	2.60(1)
				1x Ge5	2.61(1)
Ba2 –	1x Ge3	3.375(8)			
	1x Ge6	3.415(7)	Ge12 –	1x Ge14	2.49(1)
	1x Ge5	3.432(9)		1x Ge17	2.50(1)
				1x Ge11	2.52(1)
Ba3 –	1x Ge16	3.392(7)		1x Ge8	2.601(8)
	1x Ge20	3.393(9)			
	1x Ge10	3.399(8)	Ge13 –	1x Ge20	2.453(8)
				1x Ge9	2.53(1)
Ba4 –	1x Ge17	3.367(9)		1x Ge16	2.54(1)
	1x Ge7	3.412(7)		1x Ge3	2.628(8)
	1x Ge10	3.421(7)			
			Ge14 –	1x Ge12	2.49(1)
Ge1 –	2x Ge9	2.489(9)		1x Ge6	2.53(1)
	1x Ge3	2.61(1)		1x Ge10	2.61(1)
	1x Ge4	2.62(1)			
			Ge15 –	1x Ge18	2.43(1)
Ge2 –	1x Ge4	2.48(1)		1x Ge7	2.515(9)
	2x Ge6	2.527(8)		1x Ge10	2.59(1)
	1x Ge5	2.59(1)		1x Ge19	2.673(9)

Ge3 –	1x Ge1	2.60(1)	Ge16 –	1x Ge18	2.50(1)
	2x Ge13	2.628(8)		1x Ge13	2.54(4)
				1x Ge7	2.56(1)
Ge4 –	1x Ge2	2.48(1)		1x Ge8	2.568(8)
	1x Ge1	2.62(1)			
	2x Ge20	2.691(7)	Ge17 –	1x Ge12	2.50(1)
				1x Ge18	2.523(9)
Ge5 –	1x Ge2	2.59(1)		1x Ge10	2.52(1)
	2x Ge11	2.62(1)		1x Ge21	2.66(1)
Ge6 –	1x Ge2	2.527(8)	Ge18 –	1x Ge15	2.43(1)
	1x Ge14	2.53(1)		1x Ge16	2.50(1)
	1x Ge11	2.61(1)		1x Ge17	2.523(9)
	1x Ge22	2.61(1)		1x Ge21	2.761(8)
Ge7 –	1x Ge15	2.515(9)	Ge19 –	1x Ge8	2.437(7)
	1x Ge16	2.56(1)		1x Ge10	2.445(9)
	1x Ge9	2.60(1)		1x Ge21	2.651(7)
				1x Ge15	2.673(9)
Ge8 –	1x Ge19	2.437(7)			
	1x Ge16	2.568(8)	Ge20 –	1x Ge13	2.453(8)
	1x Ge12	2.601(8)		1x Ge11	2.579(9)
	1x Ge22	2.735(7)		1x Ge4	2.691(7)
Ge9 -	1x Ge1	2.49(1)	Ge21 –	1x Ge19	2.651(7)
	1x Ge13	2.53(1)		1x Ge17	2.66(1)
	1x Ge7	2.60(1)		1x Ge18	2.761(8)
	1x Ge22	2.65(1)			
			Ge22 –	1x Ge6	2.61(1)
Ge10 –	1x Ge19	2.445(9)		1x Ge9	2.65(1)
	1x Ge17	2.52(1)		1x Ge8	2.735(7)
	1x Ge15	2.59(1)			
	1x Ge14	2.61(1)			

Table 5.11 Details on data collection of $BaGe_{6-x}$ in an incommensurate model.

Composition	*$BaGe_{5.5}$*
Pearson symbol	*oC26*
Crystal system, superspace group	Orthorhombic, *Cmcm(α00)00s* (no. 5250)
Modulation wave vector	$q = 0.5700(1)a^*$
Centering	(0, 0, 0, 0), (1/2, 1/2, 0, 0)
Unit cell parameters	$a = 4.2251(2)$ Å $b = 11.2208(5)$ Å $c = 12.7992(5)$ Å
Unit cell volume	$V = 606.79(8)$ Å^3
Formula units per cell	$Z = 4$
Calculated density	$\rho_{calc} = 5.88$ g cm^{-3}
Temperature	293(2) K
Measurement device	Rigaku AFC7 CCD detector (Saturn 724)
Radiation	Mo K_α, $\lambda = 0.71073$ Å
Absorption correction	Multiscan
Measurement range	$0 \le h < 5$ $0 \le k \le 15$ $0 \le l \le 17$ $0 \le m \le 3$
Number of reflections: measured / unique	12063 / 2872
Refinement	$F \ge 4\sigma(F)$
Refined parameters	72
Software	WinCSD
R(F), R(w) [all], reflns	0.034, 0.036 (991)
R(F), R(w) [hkl0]	0.025, 0.027 (586)
R(F), R(w) [hkl1]	0.063, 0.065 (340)
R(F), R(w) [hkl2]	0.070, 0.071 (63)
R(F), R(w) [hkl3]	0.057, 0.059 (2)
GoF	1.01
$\Delta\rho_{min}$, $\Delta\rho_{max}$ / e Å^3	-1.26, 1.83

Table 5.12 Structural parameters of the incommensurate model of $BaGe_{6-x}$.

Atom	*Site*	*Occupancy*	*x*	*y*	*z*	B_{iso}
Ba	4*c*	1	0	0.28989(5)	1/4	1.03(2)
Ge1	8*f*	0.618(4)	0	0.2476(5)	0.5362(3)	0.80(4)
Ge2	8*f*	1	0	0.57333(6)	0.35025(5)	0.81(2)
Ge3	8*f*	1	0	0.03511(6)	0.59242(5)	0.71(4)
Ge4	16*h*	0.067(2)	0.186(2)	0.2556(7)	0.5131(5)	1.0(3)

Table 5.13 Anisotropic ADP of the incommensurate model of $BaGe_{6-x}$.

Atom	*B11*	*B22*	*B33*	*B12*	*B13*	*B23*
Ba	0.92(2)	1.14(2)	1.03(4)	0	0	0
Ge1	0.78(8)	0.97(5)	0.64(4)	0	0	-0.01(2)
Ge2	0.79(4)	0.86(5)	0.79(3)	0	0	0.02(2)
Ge3	0.49(8)	0.93(8)	0.71(6)	0	0	0.13(2)
Ge4	1.1(7)	1.0(3)	0.8(4)	-0.1(3)	-0.1(2)	0.2(2)

Table 5.14 Modulation parameters for the atomic displacement of $BaGe_{6-x}$ in the incommensurate description.

Atom	$\cos(2\pi x_4)$	$\sin(2\pi x_4)$	$\cos(4\pi x_4)$	$\sin(4\pi x_4)$	$\cos(6\pi x_4)$	$\sin(6\pi x_4)$
Ba				$-0.0011(5)_x$		
			$-0.0013(3)_y$			
		$0.0093(1)_z$				$0.0036(7)_z$
Ge1	$0.0904(9)_x$			$-0.001(2)_x$	$0.039(2)_x$	
		$0.0048(9)_y$	$0.0037(7)_y$			$0.001(1)_y$
		$-0.0099(6)_z$	$-0.00115(4)_z$			
Ge2	$0.0023(4)_x$			$-0.0047(6)_x$	$0.005(4)_x$	
		$0.0061(2)_y$	$-0.0021(3)_y$			$-0.0055(9)_y$
		$0.0033(1)_z$	$-0.0002(4)_z$			$0.001(2)_z$
Ge3	$0.0030(4)_x$			$-0.0020(6)_x$	$0.023(3)_x$	
		$-0.0059(2)_y$	$-0.0019(4)_y$			$-0.0078(9)_y$
		$-0.0015(1)_z$	$-0.0005(3)_z$			$0.0051(8)_z$
Ge4	$0.007(6)_x$	$0.008(7)_x$				
	$-0.006(3)_y$	$-0.008(2)_y$				
	$0.003(3)_z$	$-0.003(2)_z$				

Table 5.15 Details on data collection of $BaGe_5$.

Composition	*$BaGe_5$*
Pearson symbol	*oI24*
Crystal system, space group	Orthorhombic, *Imma* (no. 63)
Unit cell parameters	a = 8.3421(8) Å b = 4.8728(5) Å c = 13.7202(9) Å
Unit cell volume	V = 557.72(9) Å^3
Formula units per cell	Z = 4
Calculated density	ρ_{calc} = 5.96 g cm^{-3}
Temperature	293(2) K
Measurement device	ESRF ID31 Glass capillary ϕ = 0.5 mm 9 detectors stage Step width: 0.001°
Radiation	Synchrotron, λ = 0.430459(5) Å
Profile function	Pseudo-Voigt
Measurement range	$3° \leq 2\theta \leq 34°$ $0 \leq h < 11, 0 \leq k \leq 6, 0 \leq l \leq 18$
Number of points / reflections	31000 / 437
Number of parameters crystal structure / profile	12 / 23
Structure refinement	Full profile method, Jana 2006
Residuals and GoF	R_P = 0.057, R_F = 0.029, GoF = 0.8

Table 5.16 Structural parameters of $BaGe_5$.

Atom	*Site*	*Occupancy*	*x*	*y*	*z*	U_{iso}
Ba	4*e*	1	0	1/4	0.7826(3)	0.010(1)
Ge1	4*e*	1	0	1/4	0.0397(6)	0.010(2)
Ge2	8*i*	1	0.1534(5)	1/4	0.5576(3)	0.010(1)
Ge3	8*i*	1	0.2754(6)	1/4	0.1274(3)	0.009(1)

Table 5.17 Selected interatomic distances in $BaGe_5$.

Ba –	2x Ge2	3.342(6)	Ge2 –	1x Ge2	2.559(6)
	2x Ge1	3.447(7)		1x Ge3	2.607(6)
	1x Ge1	3.528(9)		2x Ge3	2.684(3)
	4x Ge3	3.569(4)			
	2x Ge2	3.629(5)	Ge3 –	1x Ge1	2.593(6)
	4x Ge3	3.739(3)		1x Ge2	2.607(6)
				2x Ge2	2.684(3)
Ge1 –	2x Ge3	2.593(6)			
	2x Ge1	2.669(5)			

Table 5.18 Details on data collection of $BaGe_3$ in the tetragonal modification.

Composition	*$BaGe_3$*
Pearson symbol	*tI32*
Crystal system, space group	Tetragonal, *I4/mmm* (no. 139)
Unit cell parameters	a = 7.8259(5) Å c = 12.7952(9) Å
Unit cell volume	V = 783.6(2) Å^3
Formula units per cell	Z = 8
Calculated density	ρ_{calc} = 6.02 g cm^{-3}
Temperature	293(2) K
Measurement device	ESRF ID22 Glass capillary ϕ = 0.5 mm 9 detectors stage Step width: 0.002°
Radiation	Synchrotron, λ = 0.40066 Å
Profile function	Pseudo-Voigt
Measurement range	$1° \leq 2\theta \leq 32°$ $0 \leq h < 10, 0 \leq k \leq 10, 0 \leq l \leq 17$
Number of points / reflections	15500 / 359
Number of parameters crystal structure / profile	16/33
Structure refinement	Full profile method, WinCSD
Residuals and GoF	R_P = 0.09, R_F = 0.03, GoF = 1.47

Table 5.19 Structural parameters of $BaGe_3$.

Atom	*Site*	*Occupancy*	*x*	*y*	*z*	B_{iso}
Ba1	4*e*	1	0	0	0.1739(3)	0.62(9)
Ba2	4*d*	1	1/2	0	1/4	0.51(9)
Ge1	8*i*	1	0.3393(6)	0	0	0.62(14)
Ge2	16*m*	1	0.3188(3)	*x*	0.0983(3)	1.15(7)

Table 5.20 Selected interatomic distances

Ba1 –	4x Ge1	3.465(4)	Ge1 –	1x Ge1	2.515(6)
	4x Ge2	3.538(4)		4x Ge2	2.798(3)
	4x Ge2	3.658(3)			
			Ge2 –	1x Ge2	2.515(4)
Ba2 –	4x Ge1	3.437(2)		2x Ge1	2.798(3)
	8x Ge2	3.465(3)		2x Ge2	2.837(4)

Table 5.21 Details on data collection of $BaGe_3$, in the hexagonal modification.

Composition	*$BaGe_3$*
Pearson symbol	*h*P8
Crystal system, space group	Hexagonal, *$P6_3/mmc$* (no. 194)
Unit cell parameters	*a* = 6.8288(3) Å *c* = 5.0303(3) Å
Unit cell volume	*V* = 203.15(3) Å^3
Formula units per cell	*Z* = 2
Calculated density	ρ_{calc} = 5.81 g cm^{-3}
Temperature	293(2) K
Measurement device	Huber G670 Reflection geometry Step width: 0.005°
Radiation	Cu $K_{\alpha 1}$, λ = 1.540562 Å
Profile function	Pseudo-Voigt
Measurement range	$10° \leq 2\theta \leq 90°$ $0 \leq h < 6, 0 \leq k \leq 6, 0 \leq l \leq 4$
Number of points / reflections	16000 / 46
Number of parameters crystal structure / profile	4/11
Structure refinement	Full profile method, WinCSD
Residuals and GoF	R_P = 0.10, R_F = 0.03, GoF = 1.33

Table 5.22 Structural parameters of $BaGe_3$.

Atom	*Site*	*Occupancy*	*x*	*y*	*z*	B_{iso}
Ba	2*d*	1	1/3	2/3	3/4	1.3(1)
Ge	6*h*	1	0.1278(3)	2*x*	1/4	1.4(1)

Table 5.23 Selected interatomic distances in $BaGe_3$.

Ba –	6x Ge	3.4452(4)
	6x Ge	3.4980(3)
	6x Eu	4.6765(1)
Ge –	2x Ge	2.6181(5)
	4x Ge	2.9344(3)
	2x Ge	3.4452(4)

Table 5.24 Details on data collection of $SrGe_3$.

Composition	*$SrGe_3$*
Pearson symbol	*t*I32
Crystal system, space group	Tetragonal, *I4/mmm* (no. 139)
Unit cell parameters	a = 7.7873(1) Å c = 12.0623(2) Å
Unit cell volume	V = 731.48(3) Å^3
Formula units per cell	Z = 8
Calculated density	ρ_{calc} = 5.55 g cm^{-3}
Temperature	293(2) K
Measurement device	ESRF ID22 Glass capillary ϕ = 0.5 mm 9 detectors stage Step width: 0.002°
Radiation	Synchrotron, λ = 0.40066 Å
Profile function	Pseudo-Voigt
Measurement range	$1° \leq 2\theta \leq 32°$ $0 \leq h < 11, 0 \leq k \leq 11, 0 \leq l \leq 18$
Number of points / reflections	15500 / 427
Number of parameters crystal structure / profile	16/33
Structure refinement	Full profile method, WinCSD
Residuals and GoF	R_P = 0.09, R_F = 0.05, GoF = 1.64

Table 5.25 Structural parameters of $SrGe_3$.

Atom	*Site*	*Occupancy*	*x*	*y*	*z*	B_{iso}
Sr1	4*e*	1	0	0	0.1706(3)	0.88(7)
Sr2	4*d*	1	1/2	0	1/4	0.76(7)
Ge1	8*i*	1	0.3370(4)	0	0	0.92(8)
Ge2	16*m*	1	0.3177(2)	*x*	0.1051(1)	1.35(5)

Table 5.26 Selected interatomic distances in $SrGe_3$.

Sr1 –	4x Ge1	3.335(3)	Ge1 –	1x Ge1	2.538(4)
	4x Ge2	3.370(3)		4x Ge2	2.784(2)
	4x Ge2	3.587(2)			
			Ge2 –	1x Ge2	2.534(3)
Sr2 –	4x Ge1	3.272(1)		2x Ge1	2.784(2)
	8x Ge2	3.346(2)		2x Ge2	2.839(2)

Table 5.27 Details on data collection of $EuGe_3$.

Composition	*$EuGe_3$*
Pearson symbol	*h*P8
Crystal system, space group	Hexagonal, *P6₃/mmc* (no. 194)
Unit cell parameters	a = 6.4092(4) Å c = 4.9532(4) Å
Unit cell volume	V = 176.21(3) Å^3
Formula units per cell	Z = 2
Calculated density	ρ_{calc} = 6.97 g cm^{-3}
Temperature	293(2) K
Measurement device	ESRF ID31 Glass capillary ϕ = 0.5 mm 9 detectors stage Step width: 0.001°
Radiation	Synchrotron, λ = 0.430459(5) Å
Profile function	Pseudo-Voigt
Measurement range	$4° \leq 2\theta \leq 30°$ $0 \leq h < 7, 0 \leq k \leq 7, 0 \leq l \leq 6$
Number of points / reflections	26000 / 78
Number of parameters crystal structure / profile	Ordered model: 7/21 Disordered model: 10 / 33
Structure refinement	Full profile method, WinCSD
Residuals and GoF	Ordered model: R_P = 0.072, R_F = 0.023, GoF = 0.98 Disordered model: R_P = 0.098, R_F = 0.022, GoF = 1.26

Table 5.28 Structural parameters of the ordered model of $EuGe_3$.

Atom	*Site*	*Occupancy*	*x*	*y*	*z*	*B_{iso}*
Eu	2*d*	1	1/3	2/3	3/4	0.7(1)
Ge	6*h*	1	0.1383(4)	2*x*	1/4	0.7(1)

Table 5.29 Anisotropic ADP of the ordered model of $EuGe_3$.

Atom	*B11*	*B22*	*B33*	*B12*	*B13*	*B23*
Eu	0.3(1)	*B*11	1.5(2)	1/2 *B*11	0	0
Ge	0.5(2)	0.5(2)	1.0(2)	1/2 *B*22	0	0

Table 5.30 Selected interatomic distances of the ordered model of $EuGe_3$.

Eu –	6x Ge	3.220(2)
	6x Ge	3.289(2)
	6x Eu	4.4527(2)
Ge –	2x Ge	2.660(3)
	4x Ge	2.914(2)
	2x Ge	3.749(3)

Table 5.31 Structural parameters of the disordered model of $EuGe_3$.

Atom	*Site*	*Occupancy*	*x*	*y*	*z*	*B_{iso}*
Eu1	2*d*	0.87(3)	1/3	2/3	3/4	0.28(15)
Eu2	4*f*	0.06(2)	1/3	2/3	0.82(1)	0.3(4)
Ge	6*h*	1	0.1384(4)	2*x*	1/4	0.6(2)

Table 5.32 Anisotropic ADP of the disordered model of $EuGe_3$.

Atom	*B11*	*B22*	*B33*	*B12*	*B13*	*B23*
Eu1	0.2(2)	*B*11	0.3(3)	1/2 *B*11	0	0
Ge	0.4(2)	0.4(2)	1.0(3)	1/2 *B*22	0	0

Table 5.33 Selected interatomic distances of the disordered model of $EuGe_3$.

Eu1 –	6x Ge	3.220(3)
	6x Ge	3.288(2)
	6x Eu2	4.25(2)
	6x Eu1	4.4527(1)
Ge –	2x Ge	2.662(4)
	4x Ge	2.915(2)
	2x Ge	3.747(4)

References

[1] Bridgman, Percy, W., *Collected Experimental Papers.* Cambridge, Harvard University Press.

[2] **R**öntgen, W. C. *Nature* **1896,** *53,* 274-276 (b) Bragg, W. H. T. *Roy. Soc. South Aust.* **1907,** *31,* 94–98.

[3] Wang, J. in *Modern Thermodynamics,* 2011, Springer-Verlag, Berlin, pp v-vii.

[4] Lewis, G. N. *J. Am. Chem. Soc.* **1916,** *38,* 762-785.

[5] (a) Moseley, H. G. J. *Philos. Mag. Series 6* **1913,** *26,* 1024-1034; (b) Moseley, H. G. J. *Philos. Mag. Series 6* **1914,** *27,* 703-713.

[6] Bridgman, Percy, W.: *The physics of high pressure.* London : Bell, 1931.

[7] Degtyareva, O. *High Pressure Res.* **2010,** *30,* 581-619.

[8] Stampfl, C.; Soon, A.; Piccinin, S.; Shi, H.; Zhang, H. *J. Phys.: Condens. Matter* **2008,** *20,* 184021.

[9] Winter, R.; Gabke, A.; Erbes, J.; Czeslik, C. in *High Pressure Molecular Science*, 1998, Winter, R. and Jonas, J. Eds. Springer, Il Ciocco, Italy, pp 369-404.

[10] Silva, J. L.; Oliveira, A. C.; Vieira, T. C. R. G.; de Oliveira, G. A. P.; Suarez, M. C.; Foguel, D. *Chem. Rev.* **2014,** *114,* 7239-7267.

[11] Anzellini, S.; Dewaele, A.; Mezouar, M.; Loubeyre, P.; Morard, G. *Science* **2013,** *340,* 464-466.

[12] Holzapfel, W. B. *Acta Crystallogr. B* **2014,** *70,* 1-7.

[13] Tse, J. *Z. Kristallogr.* **2005,** *220,* 521-530.

[14] Katzke, H., & Tolédano, P. *J. Phys.: Condens. Matter* **2007,** *19,* 275204.

[15] McMahon, M. I.; Nelmes, R. J.; Wright, N. G.; Allan, D. R. *Phys. Rev. B* **1994,** *50,* 739-743.

[16] Wosylus, A.; Rosner, H.; Schnelle, W.; Schwarz, U. *Z. Anorg. Allg. Chem.* **2009,** *635,* 700-703.

[17] Hanfland, M.; Schwarz, U.; Syassen, K.; Takemura, K. *Phys. Rev. Lett.* **1999,** *82,* 1197-1200.

[18] Chen, X.-J.; Zhang, C.; Meng, Y.; Zhang, R.-Q.; Lin, H.-Q.; Struzhkin, V. V.; Mao, H.-k. *Phys. Rev. Lett.* **2011,** *106,* 135502.

[19] Mujica, A.; Radescu, S.; Muñoz A.; Needs, R. J. *J. Phys.: Condens. Matter* **2000,** *13,* 35-42.

[20] McMahon, M. I.; Nelmes, R. *J. Chem. Soc. Rev.* **2006,** *35,* 943-963.

[21] Oganov, A. R.; Ma, Y.; Xu, Y.; Errea, I.; Bergara, A.; Lyakhov, A. O. *Proc. Natl. Acad. Sci. U.S.A.* **2010,** *107,* 7646-7651.

[22] (a) Jiang, Q.; Li. C. J.; Wilde, G. *J. Phys.: Condens. Matter* **2000,** *12,* 5623-5627. (b) Sung, J. *J. Mater. Sci.* **2000,** *35,* 6041-6054 (c) Day, H. W. *Am. Mineral.* **2012,** *97,* 52-62.

[23] (a) Trucano, P.; Chen, R. *Nature* **1975,** *258,* 136-137. (b) Hom. T; Kiszenik, W.; Post, B. *J. Appl. Crystallogr.* **1975,** *8,* 457-458.

[24] (a) Wosylus, A.; Prots, Yu.; Burkhardt, U.; Schnelle, W.; Schwarz, U.; Grin, Yu. *Solid State Sci.* **2006,** *8,* 773-781. (b) Hubbard, C. R.; Swanson, H. E.; Mauer, F. A. *J. Appl. Crystallogr.* **1975,** *8,* 45-48.

[25] Evers, J.; Oehlinger, G.; Weiss, A. *J. Less-Common Met.* **1983,** *90,* 19-23.

[26] (a) Evers, J. *J. Solid State Chem.* **1980,** *32,* 77-86. (b) Evers, J. *J. Solid State Chem.* **1979,** *28,* 369-377. (c) Evers, J.; Oehlinger, G.; Sextl, G. Eur. *J. Solid State Chem.* **1997,** *34,* 773-784. (d) Evers, J.; Oehlinger, G.; Weiss, A. *J. Solid State Chem.* **1977,** *20,* 173-181.

[27] Evers, J. in *Zintl Phases. Principles and Recent Developments.* Structure and Bonding Series, Volume 139. 2011, Fässler, T. Ed. Springer-Verlag, Berlin - Heidelberg, pp 57-96.

[28] Kasper, J. S.; Hagenmuller, P.; Pouchard, M.; Cros, C. *Science* **1965,** *150,* 1713-1714.

[29] Martin, J.; Nolas, G. S.; Wang, H.; Yang, J. *J. Appl. Phys.* **2007,** *102,* 103719.

[30] Tritt, T. M. *Annu. Rev. Mater. Res.* **2011,** *41,* 433-448.

[31] Nolas, G. S.; Cohn, J. L.; Slack, G. A.; Schujman, S. B. *Appl. Phys. Lett.* **1998,** *73,* 178-180.

[32] Nolas, G. S.; Morelli, D. T.; Tritt, T. M. *Annu. Rev. Mater. Res.* **1999,** *29,* 89-116.

[33] (a) Wosylus, A.; Prots, Yu.; Burkhardt, U.; Schnelle, W.; Schwarz, U.; Grin, Yu. *Z. Naturforsh. B* **2006,** *61,* 1485-1492. (b) Wosylus, A.; Prots, Yu.; Burkhardt, U.; Schnelle, W.; Schwarz *Sci. Technol. Adv. Mater.* **2007,** *8,* 383-388.

[34] Carrillo-Cabrera, W.; Paschen, S.; Grin, Yu. *J. Alloys Compd.* **2002,** *333,* 4-12.

[35] Schwarz, U.; Wosylus, A.; Rosner, H.; Schnelle, W.; Ormeci, A.; Meier, K.; Baranov, A. I.; Nicklas, M.; Leipe, S.; Müller, C. J.; Grin, Yu. *J. Am. Chem. Soc.* **2012,** *134,* 13558-13561.

[36] Schnelle, W.; Ormeci, A.; Wosylus, A.; Meier, K.; Grin, Yu.; Schwarz, U. *Inorg. Chem.* **2012,** *51,* 5509-5011.

[37] Wosylus, A.; Meier, K.; Prots, Yu.; Schnelle, W.; Rosner, W.; Schwarz, U.; Grin, Yu. *Ang. Chem. Int. Ed.* **2010,** *49,* 9002-9006.

[38] Fukuoka, H.; Yamanaka, S. *Phys. Rev. B* **2003,** *67,* 094501.

[39] (a) Meier, K.; Cardoso-Gil, R.; Schnelle, W.; Rosner, H.; Burkhardt, U.; Schwarz, U. *Z. Anorg. Allg. Chem.* **2012,** *636,* 1466-1473. (b) Fukuoka, H.; Baba, K.; Yoshikawa, M.; Ohtsu, F.; Yamanaka, S. *J. Solid State Chem.* **2009,** *182,* 2024-2029.

[40] Meier, K.; Wosylus, A.; Cardoso-Gil, R.; Burkhardt, U.; Curfs, C.; Hanfland, M.; Grin, Yu.; Schwarz, U. *Z. Anorg. Allg. Chem.* **2012,** *638,* 1446-1451.

[41] Forbes, J. W. *Shock Wave Compression of Condensed Matter,* 2012, Springer-Verlag, Berlin, Germany, pp 1-11

[42] Walker, D.; Carpenter, M. A.; Hitch, C. M. *Am. Mineral.*, **1990,** *75,* 1020.

[43] Max Voggenreiter GmbH, Industriestraße 9-10, 95336 Mainleus, mavo@voggenreiter-gmbh.de

[44] Huppertz. H. *Z. Anorg. Allg. Chem.* **2004,** *219,* 330-338.

[45] (a) Boldyreva, E. *High-Pressure Crystallography: From Fundamental Phenomena to Technological Applications*, 2010, Springer-Verlag, Berlin, Germany, pp. 264–265 (b) Decker, D. L.; Bassett, W. A.; Merrill, L.; Hall, H. T.; Barnett, J. D. *J. Phys. Chem. Ref. Data* **1972,** *1*, 773.

[46] Program WinXPOW v2.22, Stoe & Cie GmbH, Darmstadt (2005).

[47] S. W. Freiman, N. M. Trahey, *"NIST Certificate, SRM 660a Lanthanum Hexaboride Powder, Line Position and Line Shape Standard for Powder Diffraction",* NIST Gaithersburg, MD 2000

[48] Akselrud, L.; Grin, Yu. *J. Appl. Crystallogr.* **2014,** *47,* 803-805.

[49] Petricek, V.; Dusek, M.; Palatinus, L. *Z. Kristallogr.* **2014,** *229,* 345-352.

[50] ATOMS V6.3.4, by Shape Software, 2008.

[51] Brandenburg, K.: DIAMOND 3.2k – Visual crystal structure information system. Program for drawing crystal structures. University of Bonn, 2014

[52] CrystalMaker®: a crystal and molecular structures program for Mac and Windows. CrystalMaker Software Ltd, Oxford, England (www.crystalmaker.com)

[53] Sheldrick, G. M. *Acta Crystallogr. Sect. A* **2008,** *64,* 112-122.

[54] L. J. Farrugia, *J. Appl. Cryst.* **2012,** *45,* 849-854.

[55] Kolb, U.; Mugnaioli, E.; Gorelik, T. E. *Cryst. Res. Technol.* **2011,** *46,* 542-554.

[56] Brown, M. E. *Introduction to Thermal Analysis. Techniques and Applications.* Kluwer Academic Publishers, Dordrecht, 2001, pp 13-17.

[57] elk code version 1.4.22 http://elk.sourceforge.net

[58] Jepsen, O.; Burkhardt, A.; Andersen, O. K. The Program TB-LMTO-ASA, Version 4.7, Max-Planck-Institut für Festkörperforschung, Stuttgart, 1999.

[59] Bader, R. F. W. *Atoms in Molecules: A Quantum Theory*, Oxford University Press, Oxford, 1999.

[60] Kohout, M. *Int. J. Quantum Chem.* **2004,** *135,* 43-54.

[61] Kohout, M. DGrid, version 4.6, Radebeul, 2011.

[62] Singh, D. J. and Nordström L. *Planewaves, Pseudopotentials and the LAPW Method.* Springer-Verlag, Berlin, 2006.

[63] Ambrosch-Draxl, C. *Phys. Scr.* **2004,** *T109,* 48-53.

[64] Skriver, H. L. *The LMTO Method. Muffin-Tin Orbitals and Electronic Structure.* Cardona, M. and Fulde, P. Eds. Springer-Verlag, Berlin, 1984.

[65] (a) Tanigaki, K.; Shimizu, T.; Itoh, K. M.; Teraoka, J.; Moritomo, Y.; Yamanaka, S. *Nature Materials*, **2003,** *2,* 653. (b) Yamanaka, S. *Dalton Trans.* **2010,** *39,* 1901. (c) Yamanaka, S.; Enishi, E.; Fukuoka, H.; Yasukawa, M. *Inorg. Chem.* **2000,** *39,* 56-58.

[66] (a) Yamanaka, S.; Horie, H.-O.; Nakano, H.; Ishikawa, M. *Fullerene, Sci. Tech.* **1995,** *3,* 21. (b) Kawaji, H.; Horie, H.-O.; Yamanaka, S.; Ishikawa, M. *Phys. Rev. Lett.* **1995,** *74,* 1427.

[67] Stefanoski, S.; Beekman, M.; Nolas, G. S. In: *The Physics and Chemistry of Inorganic Clathrates*, Springer, 2014, p. 169.

[68] (a) Martin, J.; Wang, H.; Nolas, G. S. *Appl. Phys. Lett.* **2008,** *92,* 222110. (b) Toberer, E. S.; Christensen, M.; Iversen, B. B.; Snyder, G. *J. Phys. Rev. B* **2008,** *77,* 075203. (c) May, A. F.; Toberer, E. S., Saramat, A.; Snyder, G. J. *Phys. Rev. B* **2009,** *80,* 125205. (d) Shi, X.; Yang, J., Bai, S.; Yang, J.; Wang, H.; Chi, M.; Salvador, J. R.; Zhang, W.; Chen L.; Wong-Ng, W. *Adv. Funct. Mater.* **2010,** *20,* 755. (e) Anno, H.; Hokazono, M.; Takakura, H.; Matsubara, K. IEEE Proc. 24th International Conference on Thermoelectrics (ICT 05), Clemson, USA, 2005, p. 102. (f) Zhang, H.; Borrmann, H.; Oeschler, N.; Schnelle, W.; Candolfi, C.; Schmidt, M.; Burkhardt, U.; Baitinger, M.; Zhao, J. T.; Grin, Yu. *Inorg. Chem.* **2011,** *50,* 1250-1257. (g) Liang, Y.; Böhme, B.; Reibold, M.; Schnelle, W.; Schwarz, U.; Baitinger, M.; Lichte, H.; Grin, Yu. *Inorg. Chem.* **2011,** *50,* 4523-4528.

[69] (a) Fukuoka, H.; Kiyoto, J.; Yamanaka, S. *Inorg. Chem.* **2003,** *42,* 2933-2937. (b) Fukuoka, H.; Kiyoto, J.; Yamanaka, S. *J. Phys. Chem. Solids* **2004,** *65,* 333-336. (c) Toulemonde, P.; Adessi, Ch.; Blase, X.; San Miguel, A.; Tholence, J. L. *Phys. Rev. B* **2005,** *71,* 094504.

[70] Pailhès, S.; Euchner, H. ; Giordano, V. M.; Debord, R.; Assy, A.; Gomès, S.; Bosak, A.; Machon, D.; Paschen, S.; De Boissieu, M. *Phys. Rev. Lett.* 2014, 113, 025506.

[71] Liang, Y.; Boehme, B.; Vasylechko, L.; Baitinger, M.; Grin, Yu. *J. Phys. Chem. Solids* **2013,** *74,* 225.

[72] Kitano, A.; Moriguchi, K.; Yonemura, M.; Munetoh, S.; Shintani, A.; Fukuoka, H.; Yamanaka, S.; Nishibori, E.; Takata, M.; Sakata, M. *Phys. Rev. B* **2001,** *64,* 045206.

[73] Selwood, P.W. *Magnetochemistry*, 2nd Ed., Interscience, New York, 1956.

[74] Landoldt-Börnstein, New Series II/16, *Diamagnetic Susceptibility*, Springer-Verlag, Heidelberg, 1986.

[75] Cros, C.; Pouchard, M.; Hagenmüller, P. *J. Solid State Chem.* **1970,** *2,* 570.

[76] Paschen, S.; Tran, V. H.; Baenitz, M.; Carrillo-Cabrera, W.; Grin, Yu.; Steglich, F. *Phys. Rev. B* **2002,** *65,* 134435.

[77] Lortz, R.; Viennois, R.; Petrovic, A.; Wang, Y.; Toulemonde, P.; Meingast, C.; Koza, M. M.; Mutka, H.; Bossak, A.; San Miguel, A. *Phys. Rev. B* **2008,** *77,* 224507.

[78] Padamsee, H.; Neighbor, J. E.; Shiffman, C. A. *J. Low Temp. Phys.* **1973,** *12,* 387.

[79] Takabatake, T.; Suekuni, K.; Nakayama, T.; Kaneshita, E. *Rev. Mod. Phys.* **2014,** *86,* 669-716.

[80] Beekman, M.; Schnelle, W.; Borrmann, H.; Baitinger, M.; Grin, Yu.; Nolas, G. S. *Phys. Rev. Lett.* **2010,** *104,* 018301.

[81] Bhattacharya, A.; Carbogno, C.; Scheffler, M. Verhandl. Deutsch. Phys. Gesellsch. – DPG Meeting, 2014, HL49.7.

[82] Nguyen, L. T. K.; Aydemir, U.; Baitinger, M.; Bauer, E.; Borrmann, H.; Burkhardt, U.; Custers, J.; Haghighirad, A.; Hoefler, R.; Luther, K. D.; Ritter, F.; Assmus, W.; Grin, Yu.; Paschen S. *Dalton Trans.* **2010,** *39,* 1071-1077.

[83] Candolfi, C.; Aydemir, U.; Baitinger, M.; Oeschler, N.; Steglich, F.; Grin. Yu. *J. Appl. Phys.* **2012,** *111,* 043706.

[84] *CRC Handbook of Chemistry and Physics*, 84th Edition. David.

[85] Fukuoka, H.; Yamanaka, S.; Matsuoka, E.; Takabatake, T. *Inorg. Chem.* **2005,** *44,* 1460-1465.

[86] Aydemir, U.; Akselrud, L.; Carrillo-Cabrera, W.; Candolfi, C.; Oeschler, N.; Baitinger, M.; Steglich, F.; Grin, Yu. *J. Am. Chem. Soc.* **2010,** *132,* 10984-10985.

[87] Janssen, T.; Janner, A.; Looijenga-Vos, A.; de Wolff, P. M. *Incommensurate and Commensurate Modulated Structures*. In *International Tables for Crystallography*, third edition; Prince, E., Ed; Volume C, chapter 9.8, 907-955; Kluwer Academic Publisher: Dordrecht, 2004.

[88] Petricek, V.; van der Lee, A.; Evain, M. *Acta Crystallogr. A* **1995,** *51,* 529-535.

[89] Baitinger, M.; Böhme, B.; Ormeci, A.; Grin, Yu. *Solid state chemistry of clathrate phases: crystal structure, chemical bonding and preparation routes*. In: *Clathrates*, Nolas, G. S.; Ed; Springer, 2014.

[90] Wang, Z.; Wan, W.; Sun, J.; Carrillo-Cabrera, W.; Grüner, D.; Yin, X.; Qiu, S.; Zhu, G.; Zou, X. *Cryst. Eng. Comm.* **2012,** *14,* 2204.

[91] Burla, M. C.; Caliandro, R.; Camalli, M.; Carrozzini, B.; Cascarano, G. L.; Giacovazzo, C.; Mallamo, M.; Mazzone, A.; Polidori, G.; Spagna, R. *J. Appl. Crystallogr.* **2012,** *45,* 357.

[92] (a) Gemmi, M.; Galanis, A.; Karavassili, F.; Das, P. P.; Calamiotou, M.; Gantis, A.; Kollia, M.; Margiolaki, I.; Nicolopoulos, S. *Microscopy and Analysis,* **2013,** *27,* 24–29. (b) Samuha, S.; Krimer, Y.; Meshi, L. *J. Appl. Crystallogr.* **2014,** *47,* 1032. (c) Kolb, U.; Mugnaioli, E.; Gorelik, T. *Cryst. Res. Technol.* **2011,** *46,* 542.

[93] Leoni, S.; Carrillo-Cabrera, W.; Schnelle, W.; Grin, Y. *Solid State Sci.* **2003,** *5,* 139.

[94] Guloy, A. M.; Ramlau, R.; Tang, Z.; Schnelle, W.; Baitinger, M.; Grin, Yu. *Nature* **2006,** *443*, 320-323.

[95] von Schnering, H. G.; Zürn, A.; Chang, J.-H.; Baitinger, M.; Grin, Yu. *Z. Anorg. Allg. Chem.* **2007,** *633,* 1147-1153.

[96] Carrillo-Cabrera, W.; Budnyk, S.; Prots, Yu.; Grin, Yu. *Z. Anorg. Allg. Chem.* **2004,** *630,* 2267-2276.

[97] Carrillo-Cabrera, W.; Curda, J.; von Schnering, H. G.; Paschen, S.; Grin, Yu. *Z. Kristallogr. NCS* **2000,** *215,* 207-208.

[98] Fukuoka, H.; Tomomitsu, Y.; Inumaru, K. *Inorg. Chem.* **2011,** *50,* 6372-6377.

[99] (a) Fässler, T. F.; Kronseder, C. *Ang. Chem. Int. Ed.* **1997,** *36,* 2863. (b) Ponou, S.; Fässler, T. F.; Kienle, L. *Ang. Chem. Int. Ed.* **2008,** *47,* 3999. (c) Wendorff, M.; Röhr, C. *Z. Anorg. Allg. Chem.* **2011,** *637,* 1013.

[100] (a) Meier, K.; Cardoso-Gil, R.; Schwarz, U. *Z. Kristallogr.* **2011,** *226,* 297-298. (b) Wosylus, A.; Prots, Y.; Schwarz, U. *Z. Kristallogr.* **2011,** *226,* 295-296.

[101] Brunner, G. O.; Schwarzenbach, D. *Z. Kristallogr.* **1971,** *133,* 127.

[102] Müller, U. *Inorganic Structural Chemistry*, second edition, Wiley, chapter 2, 2007.

[103] Werthamer, N. R.; Helfand, E.; Hohenberg, P. C. *Phys. Rev. B* **1966,** *147,* 295.

[104] (a) Chang, K. J.; Dacorogna, M. M.; Cohen, M. L.; Mignot, J. M.; Chouteau, G.; Martinez, G. *Phys. Rev. Lett.* **1985,** *54,* 2375-2378. (b) Erskine, D.; Yu, P. Y.; Chang, K. J.; Cohen, M. L. *Phys. Rev. Lett.* **1986,** *57,* 2741-2744. (c) Lin, T. H.; Dong, W. Y.; Dunn, K. J.; Wagner, C. N. J. *Phys. Rev. B* **1986,** *33,* 7820-7822. (d) Martinez, G.; Mignot, J. M.; Chouteau, G.; Chang, K. J.; Dacorogna, M. M.; Cohen, M. L. *Physica Scripta,* **1986,** *13,* 226-229.

[105] (a) Bordet, P.; Affronte, M.; Sanfilippo, S.; Núñez-Regueiro, M.; Laborde, O.; Olcese, G. L.; Palenzona, A.; LeFloch, S.; Levy, D.; Hanfland, M. *Phys. Rev. B* **2000,** *62,* 392-397. (b) Sanfilippo, S.; Elsinger, H.; Núñez-Regueiro, M.; Laborde, O.; LeFloch, S.; Affronte, M.; Olcese, G. L.; Palenzona, A. *Phys. Rev. B* **2000,** *61,* 3800-3803. (c) Nakanishi, A.; Ishikawa, T.; Nagara, H.; Kusakabe, K. *J. Phys. Soc. Jpn* **2008,** *77,* 104712.

[106] (a) McMillan, W. L. *Phys Rev.* **1968,** *167,* 331-344. (b) Allen, P. B.; Dynes, R. C. *Phys. Rev. B* **1975,** *23,* 905-922.

[107] Rowell, J. M.; McMillan, W. L.; Anderson, P. W. *Phys. Rev. Lett.* **1965,** *14,* 633-634.

[108] Dynes, R. C. *Solid State Commun.* **1972,** *10,* 615-618.

[109] Allen, Philip B. *The electron-phonon coupling constant λ.* In: *Handbook of Superconductivity*, Poole, C. P.; Ed; chapter 9, Sec. G, pp. 478-483. Academic Press, New York, 1999.

[110] Buckel, W.; Kleiner, R. *Superconductivity. Fundamentals and Applications,* second edition; chapter 3, 146-149; Wiley-VCH, Weinheim, 2004.

[111] Evers, J.; Oehlinger, G.; Weiss, A. *Z. Naturforsch. B* **1979,** *34,* 524.

[112] Betz, A.; Schäfer, H.; Weiss, A.; Wulf, R. *Z. Naturforsch. B* **1968,** *23,* 879.

[113] Palenzona, A.; Pani, M. *J. Alloys Compd.* **2005,** *402,* 136-140.

[114] Shannon, R. D. *Acta Cryst. A* **1976,** *32,* 751-767.

[115] Gatti, C. *Z. Kristallogr.* **2005,** *220,* 339-457.

[116] Emsley, J. *The Elements,* Walter de Gruyter, 1994.

[117] (a) Dashjav, E.; Prots, Y.; Kreiner, G.; Schnelle, W.; Wagner, F. R.; Kniep, R. *J. Solid State Chem.* **2008,** *181,* 3121-3130. (b) Ormeci, A.; Simon, A.; Grin, Yu. *Ang. Chem. Int. Ed.* **2010,** *49,* 8997-9001. (c) Ormeci, A.; Grin, Yu. *Isr. J. Chem.* **2011,** *51,* 1349-1354. (d) Ormeci, A.; Rosner, H.; Wagner, F. R.; Kohout, M.; Grin, Yu. *J. Phys. Chem. A* **2006,** *110,* 1100-1105.

[118] Bardeen, J.; Cooper, L. N.; Schrieffer, J. R. *Phys. Rev.* **1957,** *108,* 1175.

[119] Fukuoka, H.; Baba, K.; Yoshikawa, M.; Yamanaka, Y. *Evolution of New Quantum Phenomena Realized in the Filled Skutterudite Structure*. http://www2.kobe-u.ac.jp/~hh/skutterud/activities/absrtarct27S.pdf (accessed Dec. 2, 2013).

[120] (a) Edwards, D. A.; Wallace W. E.; Craig R. S. *J. Amer. Chem. Soc.* **1952,** *74,* 5256-5261. (b) Watanabe, Y. *J. Phys. Soc. Jpn* **1975,** *38,* 141-149. (c) Shastry, C. R.; Bhan, S. *Z. Metallkd.* **1975,** *66,* 56-58.

[121] (a) Gladyshevskii, E. I. *Dopovidi Akademii Nauk Ukrains'koi RSR* 1964, 209-212. (b) *Journal of Structural Chemistry*, translated from *Zhurnal Strukturnoi Khimii* **1964,** *5,* 523-529. (c) Bobev, S.; Bauer, E. D.; Thompson, J. D.; Sarrao, J. L.; Miller, G. J.; Eck, B.; Dronskowski, R. *J. Sol. St. Chem.* **2004,** *177,* 3545-3552.

[122] Fukuoka, H.; Suekuni, K.; Onimaru, T.; Inumaru, K. *Inorg. Chem.* **2011,** *50,* 3901-3906.

[123] Sands D. E.; Wood D. H.; Ramsey W. J. *Acta Cryst.* **1964,** *17,* 986-989. (b) Bruzzone G.; Franceschi E. *J. Less-Common Met.* **1977,** *52,* 211-216.

[124] Poettgen, R.; Simon, A. *Z. Anorg. Allg. Chem.* **1996,** *622,* 779-784.

[125] Wagner, F. R.; Kohout, M.; Grin, Yu. *J. Phys. Chem. A.* **2008,** *112,* 9814.

[126] Alekseeva, A.; Abakumov, A.; Leither-Jasper, A. *Chem. Eur. J.* **2013,** *19,* 17860.

[127] (a) Wagner, F. R.; Bezugly, V.; Kohout, M.; Grin, Yu. *Chem. Eur. J.* **2007,** *13,* 5724. (b) Kohout, M.; Wagner, F. R.; Grin, Yu. *Theor. Chem. Acc.* **2002,** *108,* 150.

[128] Sichevych, O.; Kohout, M.; Schnelle, W.; Borrmann, H.; Cardoso-Gil, R.; Schmidt, M.; Burkdardt, U.; Grin, Yu. *Inorg. Chem.* **2009,** *48,* 6261.

[129] Veremchuk, I.; Mori, T.; Prots, Yu.; Schnelle, W.; Leithe-Jasper, A.; Kohout, M.; Grin, Yu. *J. Solid State Chem.* **2008,** *181,* 1983.

[130] Weitzer, F.; Prots, Yu.; Schnelle, W.; Hiebl, K.; Grin, Yu. *J. Sol. St. Chem.* **2004,** *177,* 2115.

[131] Jeanloz, R. *Annu. Rev. Phys. Chem.* **1989,** *40,* 237-259.

[132] Bhardwaj, P.; Singh, S. *Cent. Eur. J. Chem.* **2012,** *10,* 1391-1422.

[133] Neaton, J. B.; Ashcroft, N. W. *Phys. Rev. B* **2001,** *86,* 2830-2833.

[134] Neaton, J. B.; Ashcroft, N. W. *Nature* **1999,** *400,* 141-144.

[135] Schilling, J. S. *High Pressure Res.* **2006,** *26,* 145-163.

[136] Feng, J.; Hennig, R. G.; Ashcroft, N. W.; Hoffmann, R. *Nature* **2008,** *451,* 445-448.

[137] Rousseau, B.; Xie, Y.; Ma, Y.; Bergara, A. *Eur. Phys. J. B* **2011,** *81,* 1-14.

[138] Parker, L. J.; Atou, T.; Badding, J. V. *Science* **1996,** *273,* 95-97.

[139] Lee, K. K. M.; Jeanloz, R. *Geophys. Res. Lett.* **2003,** *30,* 2212.

[140] Miedema, A. R.; Chatel, P. F.; Boer, F. R. *Physica B* **1980,** *100,* 1-28.

[141] Hirsch, J. E.; Hamlin, J. J. *Physica C* **2010,** *470,* S937-S939.

[142] Asokamani, R. *Solid State Physics, Principles and Applications*, 2007, Anamaya Publishers, New Dheli, India, pp 272-324.

[143] Williams, Q.; Jeanloz, R. *Phys. Rev. Lett.* **1986,** *56,* 163-164.

[144] Asaumi, K.; Vohra, E. *Solid State Commun.* **1981,** *40,* 715-718.

[145] Eremets, M. I.; Shimizu, K.; Kobayashi, T. C.; Amaya, K. *J. Phys.: Condens. Matter.* **1998,** *10,* 11519-11523.

[146] Mao, H. K.; Wu, Y.; Hemley, R. J.; Chen, L. C.; Shu, J. F.; Finger, L. W.; Cox, D. E. *Phys. Rev. Lett.* **1990,** *64,* 1749-1752.

[147] Asaumi, K. *Phys. Rev. B.* **1984,** *29,* 1118-1120.

[148] Xu, Y.; Tse, J. S.; Oganov, A. R.; Cui, T.; Wang, H. Ma, Y.; Zou, G. *Phys. Rev. B.* **2009,** *79,* 144110.

[149] (a) Asokamani, R. *Solid State Physics, Principles and Applications*, 2007, Anamaya Publishers, New Dheli, India, pp 126-147. (b) Heiniger, H.; Bucher, E.; Muller *J. Phys.kondens. Materie* **1966,** *5,* 243-284.

[150] (a) Ibach H., Lüth, H. *Solid-State Physics, An Introduction to Principles of Materials Science,* 2009, Springer-Verlag, Berlin, Germany, pp 145-150. (b) Kim, J. S.; Kremer, R. K.; Boeri, L.; Razavi, F. S. *Phys. Rev. Lett.* **2006,** *96,* 217002. (c) Levin, E. M.; Pecharsky, V. K.; Gschneider, K. A.; Miller, G. J. *Phys. Rev. B.* **2001,** *64,* 235103.

[151] Miller, G. J.; Wang, F. *Inorg. Chem.* **2011,** *50,* 7625-7636.

[152] Evers, J.; Oehlinger, G. *Inorg. Chem.* **2000,** *39,* 628-629.

[153] Cohen, M. L. *Ann. Rev. Mat. Sci.* **2000,** *30,* 1-26.

[154] Raju, S.; Mohandas, E.; Raghunathan, V. S. *J. Phys. Chem. Solids* **1997,** *58,* 1367-1373.

[155] Gerward, L.. *J. Phys. Chem. Solids* **1985,** *46,* 925-927.

[156] Katrusiak, A. *Acta Cryst. A* **2008,** *64,* 135-148.

[157] Murnaghan, F. D. *Proc. Natl. Acad. Sci.* **1944,** *30,* 244-247.

[158] Tyuterev, V. G.; Vast, N. *Comp. Mater. Sci.* **2006,** *38,* 350-353.

[159] Duclos, S. J.; Vohra, Y. K.; Ruoff, A. L. *Phys. Rev. B* **1990,** *41,* 12021-12028.

[160] (a) Mermin, N. D. *Phys. Rev.* **1965,** *137,* A1441-A1443. (b) Parlinski, K.; Kawazoe, Y. *Phys. Rev. Lett.* **1997,** *78,* 4063-4066. (c) Grabowski, B.; Hickel, T.; Neugebauer, *J. Phys. Rev. B* **2007,** *76,* 024309. (c) Yu, C-J.; Ri, G-C.; Jong, U-G.; Choe, Y-G.; Cha, S-J. *Physica B* **2014,** *434,* 185-193. (d) Stoffel, R. P.; Dronskowski, R. *Z. Anorg. Allg. Chem.* **2012,** *638,* 1403-1406.

[161] (a) Xu, B.; Wang, Q.; Tian, Y. *Scientific Reports* **2013,** *3,* 3068 (b) Al-Douri, Y.; Abid, H.; Aourag, H. *Mater. Lett.* **2005,** *59,* 2032-2034. (c) Li, K.; Ding, Z.; Xue, D. *Phy. Status Solidi B* **2011,** *248,* 1227-1236.

[162] Yin, T. M.; Cohen, M. L. *Phys. Rev. Lett.* **1980,** *45,* 1004-1007.

[163] Hu, J. Z.; Merkle, L. D.; Menoni, C. S.; Spain, I. L. *Phys. Rev. B.* **1986,** *34,* 4679-4684.

Publications

L. Akselrud, A. Wosylus, R. Castillo, U. Aydemir, Y. Prots, W. Schnelle, Yu. Grin, U. Schwarz, *"$BaGe_6$ and $BaGe_{6-x}$: Incommensurately Ordered Vacancies as Electron Traps"*, *Inorg. Chem.* **2014,** *53,* 12699-12705.

R. Castillo, W. Carrillo-Cabrera, U. Schwarz, Yu. Grin, *"Classical and Nonclassical Germanium Environments in High-Pressure $BaGe_5$"*, *Inorg. Chem.* **2015,** *54,* 1019-1025.

R. Castillo, A. I. Baranov, U. Burkhardt, Yu. Grin, U. Schwarz, "Triangular Ge3 Units in a New Modification of $EuGe_3$", *Z. Anorg. Allg. Chem.* **2015,** *641,* 355-361.

R. Castillo, W. Schnelle, M. Bobnar, U. Burkhardt, B. Böhme, M. Baitinger, U. Schwarz, Yu. Grin, *"The Clathrate $Ba_{8-x}Si_{46}$ Revisited: Preparation Routes, Electrical and Thermal Transport Properties"*, *Z. Anorg. Allg. Chem.* **2015,** *641,* 206-213.

R. Castillo, A. I. Baranov, R. Cardoso-Gil, W. Schnelle, M. Bobnar, U. Schwarz, "Germanium Dumbbells in a New Superconducting Modification of $BaGe_3$", *Inorg. Chem.* **2016,** *55,* 4498-4503.

R. Castillo, W. Schnelle, A. I. Baranov, U. Burkhardt, M. Bobnar, R. Cardoso-Gil, U. Schwarz, Yu. Grin, "Trigermanides *AE*Ge_3 (*AE* = Ca, Sr, Ba): Chemical Bonding and Superconductivity", *Z. Naturforsch.* **2016,** *71b,* 585-592.

Acknowledgments

I would like to express my gratitude to my advisor Prof. Yuri Grin, for giving me the opportunity to join his research group. His continuous support helped me in all the time of my research. It was a real privilege for me to take part in his renowned department “Chemical Metal Science” at the Max Planck Institute for Chemical Physics of Solids.

I would like to thank the rest of my thesis committee: Prof. Dr. Michael Ruck, Prof. Dr. Hans-Henning Klauss and Prof. Dr. Thorsten Stumpf.

My sincere thanks goes to Dr. Ulrich Schwarz, co-supervisor of my thesis and head of the high-pressure group. His kindly guidance and our discussions allowed me to propose aims, pursue and achieve them. This, together with his expertise in the field of high-pressure and his constant support, were an important part in the development of my PhD work.

I want to acknowledge all members of the competence group “Structure”, for providing careful measurement of the x-ray diffraction experiments and for the help and discussions in crystal structure analysis. In this respect, I have to thank to Dr. Lev Akselrud, for his support in the refinement of the modulated crystal structure, and Dr. Wilder Carrillo-Cabrera for his valuable work on electron diffraction and discussion.

My gratitude also to Dr. Walter Schnelle, Dr. Matej Bobnar and their collaborators for the great effort made performing measurements of the physical properties on the small pieces of samples resulted from the high-pressure experiments, and for fruitful discussions.

Thanks to Dr. Ulrich Burkhardt and the members of the competence group “Metallography”, for the careful preparation, characterization and analysis of the samples, in particular the elemental analysis, again, in the tiny pieces of samples.

To Dr. Marcus Schmidt and his assistants for the thermal analysis experiments, suggestions on how to improve the measurements and discussions of the results.

Thanks to the staff of the competence group “Chemical Bonding”, especially to Dr. Alexey I. Baranov, for introducing me in the field of electronic structure calculations and chemical bonding analysis, and for his constant support in the quantum chemical calculations.

Very special thanks goes to Susan Leipe for her valuable support in the high-pressure experiments.

To my family for the constant support.

I gratefully acknowledge CONICYT and the Max Planck Society for financial support.

Versicherung

Hiermit versichere ich, dass ich die vorliegende Arbeit ohne unzulässige Hilfe Dritter und ohne Benutzung anderer als der angegebenen Hilfsmittel angefertigt habe; die aus fremden Quellen direkt oder indirekt übernommenen Gedanken sind als solche kenntlich gemacht.

Die Arbeit wurde bisher weder im Inland noch im Ausland in gleicher oder ähnlicher Form einer anderen Prüfungsbehörde vorgelegt. Die Dissertation wurde von Prof. Juri Grin und Dr. Ulrich Schwarz am Max-Planck-Institut für Chemische Physik fester Stoffe betreut und im Zeitraum vom April 2011 bis März 2016 verfasst.

Ich erkläre hiermit, dass keine früheren erfolglosen Promotionsverfahren stattgefunden haben.

Die Promotionsordnung der Technischen Hochschule Dresden in der Version vom 23.02.2011 in geänderter Fassung vom 15.06.2011 und 18.06.2014 wird anerkannt.

Dresden, …… Rodrigo Esteban Antonio Castillo Rojas